IMAGE SEGMENTATION
WITH VARIATIONAL ACTIVE CONTOURS

THÈSE N^O 3283 (2005)

PRÉSENTÉE À LA FACULTÉ DES SCIENCES ET TECHNIQUES DE L'INGÉNIEUR

Institut de traitement des signaux

SECTION DE GÉNIE ÉLECTRIQUE ET ÉLECTRONIQUE

ÉCOLE POLYTECHNIQUE FÉDÉRALE DE LAUSANNE

POUR L'OBTENTION DU GRADE DE DOCTEUR ÈS SCIENCES TECHNIQUES

PAR

Xavier BRESSON

ingénieur diplômé de l'École Supérieure d'Électricité, Paris, France
et de nationalité française

acceptée sur proposition du jury:

Prof. J.-P. Thiran, directeur de thèse
Dr O. Cuisenaire, rapporteur
Prof. S. Osher, rapporteur
Prof. N. Paragios, rapporteur
Prof. P. Vandergheynst, rapporteur

Lausanne, EPFL
2005

All chapters of this dissertation are illustrated with the pictures of *Diego Porcel*[a], spanish artist. All pictures are protected by copyright.

Contents

Acknowledgments - Remerciements

Au terme de ce travail de recherche, j'aimerais remercier les personnes qui m'ont fait confiance et qui m'ont encouragé durant toutes ces années.

Mes premiers remerciements s'adressent à mon directeur de thèse, le Prof. Jean-Philippe Thiran, qui m'a accueilli dans son équipe de recherche. Je lui suis reconnaissant pour la confiance qu'il m'a donnée pour entreprendre des directions de recherche un peu "exotiques" sans remettre en question mes choix. Merci aussi, Jean-Phi, pour ton caractère chaleureux et humain.

Je voudrais aussi remercier le Prof. Murat Kunt, directeur de l'institut de recherche du Traitement du Signal, pour offrir un environnement de travail de haute qualité au ITS. J'ai aussi beaucoup aimé travailler dans l'atmosphère multi-culturelle du ITS, cela a été une expérience très enrichissante.

J'aimerais aussi remercier les autres membres de mon jury de thèse qui m'ont fait l'honneur d'être associé à ce travail de recherche.

I thank Prof. Nikos Paragios for having come in Lausanne the day of my private presentation, despite of his busy schedule. I would like to thank him for his observations and constructive critics, which helped me to improve the quality of this paper. Thanks also for your encouragements.

I also would like to thank Prof. Stanley Osher, firstly, for doing the presentation by video-conference in Los Angeles and secondly, for having accepted me last year for two months in UCLA. It was for me a great professional experience and I enjoyed a lot working with him.

Merci aussi au Prof. Pierre Vandergheynst d'avoir su me donner un peu de son temps pour des conseils mathématiques éclairés qui m'ont été très utiles.

Enfin, je remercie le dernier membre de mon jury, le Doc. Olivier Cuisenaire, qui a eu la patience de lire scrupuleusement ma thèse, m'a conseillé de manière avisée et m'encouragé aux moments difficiles. Merci aussi, Oli, pour les bons moments partagés autour d'une bonne bière... belge et les nombreuses activités sportives comme le beach volley ou le squash.

Merci aussi à Lisa, Olivier, Torsten, Jean-Phi et Karen pour avoir relu partiellement ou entièrement ma thèse.

Dans mon domaine de recherche, une place importante est consacré à l'informatique, alors j'aimerais aussi remercier Gilles Auric, Diego S.C. et Nicolas pour leur aide. Mais le plus grand remerciement s'adresse à Simon qui a eu une patience infinie pour me montrer, m'expliquer et résoudre mes nombreux problèmes informatiques, merci beaucoup Simon.

Merci aussi à Marianne et à Fabienne qui m'ont aidé et facilité la vie au quotidien du ITS. Sans elles, certaines procédures EPFLiennes seraient restées une équation sans solution.

J'aimerais aussi remercier la "promotion 2005" des doctorants: Rosa, Oscar et Lisa avec qui j'ai passé de bons moments aussi bien professionnels que personnels. Je n'oublierai pas la culture catalanne et les bons moments passés ensemble à Barcelone, à Paris et ailleurs. Merci aussi à Patricia pour son éternelle bonne humeur!

Abstract

An important branch of computer vision is image segmentation. Image segmentation aims at extracting meaningful objects lying in images either by dividing images into contiguous semantic regions, or by extracting one or more specific objects in images such as medical structures. The image segmentation task is in general very difficult to achieve since natural images are diverse, complex and the way we perceive them vary according to individuals.

For more than a decade, a promising mathematical framework, based on variational models and partial differential equations, have been investigated to solve the image segmentation problem. This new approach benefits from well-established mathematical theories that allow people to analyze, understand and extend segmentation methods. Moreover, this framework is defined in a continuous setting which makes the proposed models independent with respect to the grid of digital images.

This thesis proposes four new image segmentation models based on variational models and the active contours method. The active contours or snakes model is more and more used in image segmentation because it relies on solid mathematical properties and its numerical implementation uses the efficient level set method to track evolving contours.

The first model defined in this dissertation proposes to determine global minimizers of the active contour/snake model. Despite of great theoretic properties, the active contours model suffers from the existence of local minima which makes the initial guess critical to get satisfactory results. We propose to couple the geodesic/geometric active contours model with the total variation functional and the Mumford-Shah functional to determine global minimizers of the snake model. It is interesting to notice that the merging of two well-known and "opposite" models of geodesic/geometric active contours, based on the detection of edges, and active contours without edges provides a global minimum to the image segmentation algorithm.

The second model introduces a method that combines at the same time deterministic and statistical concepts. We define a non-parametric and non-supervised image classification model based on information theory and the shape gradient method. We show that this new segmentation model generalizes, in a conceptual way, many existing models based on active contours, statistical and information theoretic concepts such as mutual information.

The third model defined in this thesis is a variational model that extracts in images objects of interest which geometric shape is given by the principal components analysis. The main interest of the proposed model is to combine the three families of active contours, based on the detection of edges, the segmentation of homogeneous regions and the integration of geometric shape prior, in order to use simultaneously the advantages of each family.

Finally, the last model presents a generalization of the active contours model in scale spaces in order to extract structures at different scales of observation. The mathematical framework which allows us to define an evolution equation for active contours in scale spaces comes from string theory. This theory introduces a mathematical setting to process a manifold such as an active contour embedded

in higher dimensional Riemannian spaces such as scale spaces. We thus define the energy functional and the evolution equation of the multiscale active contours model which can evolve in the most well-known scale spaces such as the linear or the curvature scale space.

Version Abrégée

Un domaine de recherche important en vision artificielle est la segmentation d'image. L'objectif de la segmentation d'image est d'extraire les objects significatifs présents dans les images soit en divisant les images en régions sémantiques contigües, soit en extrayant un ou plusieurs objects spécifiques dans les images, telles que les structures médicales. La tâche de segmentation d'image est, en général, très difficile à réaliser puisque les images naturelles sont diverses, complexes et la manière de les percevoir varie selon les individus.

Depuis plus d'une décennie, un cadre mathématique prometteur, basé sur les modèles variationnels et les équations différentielles partielles, a été éxaminé pour résoudre le problème de la segmentation d'image. Cette nouvelle approche repose sur des théories mathématiques bien établies qui permettent d'analyser, de comprendre et de développer les méthodes de segmentation. De plus, ce cadre de travail s'inscrit dans une approche continue dont les modèles sont indépendants de la grille d'images numériques.

Cette thèse propose quatre nouveaux modèles de segmentation d'image basés sur des modèles variationnels et sur la méthode des contours actifs. Le modèle des contours actifs, ou "serpents", est de plus en plus utilisé en segmentation d'image car il repose sur des propriétés mathématiques solides et son implémentation numérique utilise la méthode efficace des courbes de niveaux pour faire évoluer des contours.

Le premier modèle défini dans cette dissertation propose de déterminer des minimiseurs globaux du modèle des contours actifs/serpents. Malgré ses grandes propriétés mathématiques, le modèle des contours actifs souffre de l'existence de minima locaux, qui rend la condition initiale critique et ne permet pas d'obtenir de résultats satisfaisants. Nous proposons de coupler le modèle des contours actifs géodésiques/géométriques avec la fonctionelle de la variation totale et la fonctionnelle de Mumford-Shah pour déterminer des minimiseurs globaux du modèle des serpents. Il est intéressant de remarquer que la fusion des modèles bien connus et "opposés" des contours actifs géodésiques/géométriques et des contours actifs sans bords fournit un minimum global à l'algorithme de segmentation d'image.

Le second modèle présente une méthode qui combine simultanément des concepts déterministes et statistiques. Nous définissons un modèle de classification d'image non supervisé et non paramétrique basé sur la théorie de l'information et la méthode du gradient de forme. Nous montrons que ce nouveau modèle de segmentation généralise, d'une manière conceptuelle, plusieurs modèles existants basés sur les contours actifs et des concepts issus de la statistique et de la théorie de l'information tels que l'information mutuelle.

Le troisième modèle défini dans cette thèse est un modèle variationnel qui extrait des images des objets d'intérêt dont la forme géométrique est donnée par l'analyse en composantes principales. L'intérêt principal du modèle proposé est de combiner les trois familles de contours actifs, qui se fondent sur la détection de bords, la segmentation de régions homogènes et l'intégration a priori de

formes géométriques, afin d'utiliser simultanément les avantages de chaque famille.

Finalement, le dernier modèle présente une généralisation du modèle des contours actifs dans les espaces échelles dans le but d'extraire des structures à différentes échelles d'observation. Le cadre de travail mathématique qui nous permet de définir une équation d'évolution pour les contours actifs dans les espaces échelles s'inscrit dans la théorie des cordes. Cette théorie présente un environnement mathématique qui traite une variété telle qu'un contour actif dans des espaces Riemanniens de dimension supérieure, comme les espaces échelles. Nous définissons ainsi la fonctionnelle énergétique et l'équation d'évolution du modèle des contours actifs multi-échelles qui peuvent évoluer dans les espaces échelles les plus connus comme l'espace échelle linéaire et de courbure.

List of Figures

Notations and Symbols

Abbreviations

w.r.t.	with respect to
s.t.	such that
a.e.	almost every(where)
PDE	Partial Differential Equation
MS	Mumford-Shah
KWT	Kass-Witkin-Terzopoulos
GAC	Geodesic/Geometric Active Contour
ZY	Zhu-Yuille
GAR	Geodesic Active Region
CV	Chan-Vese
VC	Vese-Chan
ACWE	Active Contour Without Edges
ABFJB	Aubert-Barlaud-Faugeras-Jéhan-Besson
KFYCW	Kim-Fisher-Yezzi-Cetin-Willsky
MI	Mutual Information
PDF	Probability Density Function
TYWTTFGW	Tsai-Yezzi-Wells-Tempany-Tucker-Fan-Grimson-Willsky
CTTHWG	Chen-Thiruvenkadam-Tagare-Huang-Wilson-Geiser
PRR	Paragios-Rousson-Ramesh
RPD	Rousson-Paragios-Deriche
HPM	Huang-Paragios-Metaxas
CTWS	Cremers-Tischhäuser-Weickert-Schnörr
CKS	Cremers-Kohlberger-Schnörr
CS	Cremers-Soatto
CSS	Cremers-Sochen-Schnörr
ROF	Rudin-Osher-Fatemi
CEN	Chan-Esedoḡlu-Nikolova
TV	Total Variation
RV	Random Variable
MRF	Markov Random Field
PCA	Principal Components Analysis
SDF	Signed Distance Function
ST	Spatial Transformations
SSD	Sum of Square Differences
ES	Euclidean Space
SS	Scale Space
MAC	Multiscale Active Contour
LSS	Linear Scale Space

Miscellaneous

Ω	Open subset of $\mathbf{R}^N$, usually the image domain
$\partial\Omega$	Boundary of Ω
$\bar{\Omega}$	Closure of set Ω
$\{\Omega_i\}_1^{N_R}$	Subsets of Ω s.t. $\Omega = \cup_{i=1}^{N_R}\Omega_i$ and $\Omega_i \cap \Omega_i = \emptyset, i \neq j$
$\partial\Omega_i$	Boundary of Ω_i
$|\Omega_i|$	Area of region Ω_i
$*$	Convolution operator
$\propto$	Symbol for proportional to

Functions

$\frac{\partial u}{\partial\zeta}, \partial_\zeta u, u_\zeta$	Differentiation of the function u w.r.t. the variable ζ, e.g. $\frac{\partial u}{\partial x}, \partial_y u, u_t$
$\frac{\partial^P u}{\partial\zeta_1...\partial\zeta_P}, \partial_{\zeta_1,...,\zeta_P} u, u_{\zeta_1,...,\zeta_P}$	Higher order differentiation of the function u, e.g. $\frac{\partial^2 u}{\partial x \partial y}, \partial_{xy} u, u_{xy}$
∇u	Gradient of the function u in $\mathbf{R}^N$ s.t. $\nabla u = (\partial_{x_1} u, \ldots, \partial_{x_N} u)$
$\nabla^2 u = \Delta u$	Laplacian of the function u in $\mathbf{R}^N$ s.t. $\Delta u = \sum_{i=1}^N \partial_{x_i}^2 u$
I_0	A given image s.t. $I : \mathbf{R}^N \to \mathbf{R}^M$, e.g. a gray-scale ($M = 1$), a color ($M = 3$) or a multi-dimensional ($M > 1$) image
I	Scale space representation or piecewise-smooth approximation of the given image I_0
C	Symbol for a curve in $\mathbf{R}^N$
Γ	Symbol for a curve/surface/hyper-surface in $\mathbf{R}^N$
G_σ	N-D Gaussian function s.t. $G_\sigma(\mathbf{x}) = \frac{1}{(2\pi\sigma^2)^{N/2}} \exp\left(-\sum_{i=1}^N x_i^2/2\sigma^2\right)$
ϕ	Symbol of a level set function embedding a curve/surface/hyper-surface Γ in $\mathbf{R}^N$
$\nabla.\mathbf{U}$	Divergence of the vector field $\mathbf{U} = (U_{x_1}, \ldots, U_{x_N})$ in $\mathbf{R}^N$ s.t. $\nabla.\mathbf{U} = \sum_{i=1}^N \partial_{x_i} U_{x_i}$
δ	Dirac function
H	Heaviside function
$\mathcal{H}_e$	Entropy
d_Γ	Signed distance function/representation of the closed curve/surface/hyper-surface Γ in $\mathbf{R}^N$ s.t. $d_\Gamma(\mathbf{x}) = \{\mathbf{x} \in \mathbf{R}^N | \pm \inf_{\mathbf{y}\in\Gamma}|\mathbf{x} - \mathbf{y}|\}$, with $\pm$ if $\mathbf{x}$ inside/outside Γ
$(u)^+$	$\max(u, 0)$
$(u)^-$	$\min(u, 0)$
$\chi_\Omega, \mathbf{1}_\Omega$	Characteristic/binary function of the set $\Omega \subset \mathbf{R}^N$ s.t. $\chi_\Omega(\mathbf{x}) = 1$ if $\mathbf{x} \in \Omega$ and 0 otherwise
$\text{sign}(\zeta)$	Sign function s.t. $\text{sign}(\zeta) = \pm 1$ if $\zeta > 0, \zeta < 0$ and $\text{sign}(\zeta) = 0$ if $\zeta = 0$

Functionals

$\frac{\partial F}{\partial u}$	First derivation of the functional F w.r.t. the function u called the Euler-Lagrange equation
$\mathbf{x}$	point in $\mathbf{R}^N$ s.t. $\mathbf{x} = (x_1, \ldots, x_N)$
$d\mathbf{x}$	Lebesgue measure in $\mathbf{R}^N$
$d\Omega$	
$\mathcal{H}^N$	N-dimensional Hausdorff measure
$L(C)$	Euclidean length of the curve C s.t. $L(C) = \int_{p_0}^{p_1} |C_p| dp = \int_0^{L(C)} ds$, with $p_0 = 0$ and $p_1 = 1$ without loss of generality
$\mathrm{Per}(\Omega)$	Perimeter of the region $\Omega \subset \mathbf{R}^N$ s.t. $\mathrm{Per}(\Omega) = \int_{\mathbf{R}^N} |\nabla \chi_\Omega| d\mathbf{x} = \int_{\partial\Omega} |\partial\Omega_p| dp$
$TV(u)$	Total variation of the function u s.t. $TV(u) = \int_{\mathbf{R}^N} |\nabla u|$

Spaces and Norms

$L^p(\Omega)$	Banach space with the norm $|u|_{L^p(\Omega)} = \left(\int_\Omega |u|^p dx\right)^{1/p} < +\infty$
$W^{m,p}$	Sobolev space
$\langle \cdot, \cdot \rangle$	Euclidean scalar product or inner product in $\mathbf{R}^N$
$|\cdot|$	Euclidean norm in $\mathbf{R}^N$

Differential Geometry

p	General curve parametrization
s	Specific parametrization of a curve C when $\left|\frac{dC}{ds}\right| = 1$, called Euclidean arc length
$[\cdot]$	Symbol of metric tensor
$[\delta_{ij}]$	Kronecker Delta for the Euclidean metric tensor in $\mathbf{R}^N$
$\mathcal{N}$	Unit normal vector to the curve/surface/hyper-surface in $\mathbf{R}^N$
$\mathcal{T}$	Unit normal vector to a curve in $\mathbf{R}^2$
κ	Mean curvature of a curve/surface/hyper-surface in $\mathbf{R}^N$
κ_i	Principal curvatures s.t. $\kappa = \frac{1}{N} \sum_{i=1}^{N} \kappa_i$
P_p	Projection operator onto the space normal to the vector p s.t. $P_p = I - \frac{p \otimes p}{|p|^2}$
$\mathcal{I}_n$	$n \times n$ identity matrix
Diag	Diagonal matrix s.t. $\mathrm{Diag}\,(\lambda_1, \ldots, \lambda_n) = \begin{pmatrix} \lambda_1 & & 0 \\ & \ddots & \\ 0 & & \lambda_n \end{pmatrix}$
Γ^i_{jk}	Levi-Civita connection coefficients in a Riemannian manifold defined by the metric tensor $[g_{ij}]$ s.t. $\Gamma^i_{jk} = \frac{1}{2} g^{il}(\partial_j g_{lk} + \partial_k g_{jl} - \partial_l g_{jk})$
$\Delta_g u$	Beltrami operator w.r.t. the metric tensor $[g_{ij}]$ s.t. $\Delta_g u = g^{-1/2} \partial_\mu (g^{1/2} g^{\mu\nu} \partial_\nu u)$, where g is the determinant of $[g_{ij}]$ and $[g^{ij}]$ is the inverse metric of $[g_{ij}]$

Numerical Analysis

$D_\zeta^+ u$	Forward difference operator s.t. $D_\zeta^+ u = (\phi(\zeta + \Delta\zeta) - \phi(\zeta))/\Delta\zeta$, with e.g. $\zeta = x, y, z, t$
$D_\zeta^- u$	Backward difference operator s.t. $D_\zeta^- u = (\phi(\zeta) - \phi(\zeta - \Delta\zeta))/\Delta\zeta$
$D_\zeta^0 u$	Central difference operator s.t. $D_\zeta^- u = (\phi(\zeta + \Delta\zeta) - \phi(\zeta - \Delta\zeta))/2\Delta\zeta$

Introduction and Preview

<div style="text-align:right;font-size:3em">1</div>

© *Diego Porcel*

1.1 Computer Vision and Image Segmentation

Computer vision is the field of research of this thesis. It is a branch of artificial intelligence that aims at giving *vision* to machines, which means to develop mathematical models, algorithms and technologies to build a machine with vision capabilities as advanced, at least, as human eyesight. More mathematically speaking, the purpose of computer vision is to process images acquired with cameras to produce a mathematical representation of *semantic* objects in the world. This is a high-challenging issue because images such as landscapes, medical images, astronomical images, paintings, can be very diverse and even the way we perceive them vary a lot according to individuals.

Computer vision is divided into many subfields including image processing, pattern recognition, graph theory, statistical learning, etc. which objectives are as varied as detection and recognition of objects in images, registration of different views of the same scene, tracking of objects through image sequences, searching for images by their content and so on. Thus, the range of computer vision applications is very large, the methods carried out can be very different, inspired from physics,

biology, statistics theory, functional analysis, etc.

This thesis will focus on a specific branch of computer vision called *image segmentation*. The objective of image segmentation is to extract the semantic objects lying in images either by dividing any given image into meaningful contiguous regions, or by extracting one or more important objects in images. This task is obviously very difficult to achieve and there exist many methods to realize it.

In two decades, several mathematical models have been developed to achieve image segmentation. The last promising models to solve the image segmentation problem are based on *variational approaches* and *partial differential equations* (PDE). These models benefit from well-founded mathematical theories that allow us to analyze, understand, improve the existing methods and to work in a continuous setting which makes the proposed models independent with respect to the grid of digital images. The next section introduces the general *paradigm* used throughout this thesis and coupled with other mathematical theories such as information theory and differential geometry to define new image segmentation models.

1.2   Variational Models and Partial Differential Equations

Digital images are representations of the visual world surrounding us. The common point between all digital images is the fact that they are defined in a *discrete* setting although they come from a *continuous world*. The transfer process is done by sampling and quantizing the "continuous images". Even if all image processing methods are developed for digital/discrete images, it is generally more powerful to use a continuous formulation of methods to analyze, understand, and solve the problems since continuous mathematics are more developed than their discrete version. At the beginning of image processing history, the techniques used to process images such as filter theory or spectral analysis were based on a discrete setting. Today, new techniques such as wavelets theory or variational models are based on a continuous setting.

In this thesis, we will therefore focus on partial differential equations and variational models to solve the image segmentation problem in different ways. PDEs, variational models, and functional analysis in general are mathematical theories closely related to physics such as propagation equations or conservation laws. PDEs and variational models are linked through an *optimization problem*. Indeed, let us assume that an image processing problem can be formulated as

$$u^\star = \min_{u \in S} F(u), \tag{1.1}$$

where $u^\star$, defined in an appropriate space S for the given problem, is an optimizer of a Functional/Energy $F(.)$ which gives the solution to the given image processing problem. If F is continuous and differentiable, it is possible to compute the first variation to determine the *Euler-Lagrange equation*:

$$\frac{\partial F}{\partial u} = 0, \tag{1.2}$$

which gives a necessary condition for $u^\star$ to be an optimizer of F such that $\frac{\partial F}{\partial u}\big|_{u^\star} = 0$. Then, a way

to compute an optimizer (usually a local optimizer) is to use the gradient descent/ascent method by introducing an artificial time t such that:

$$\frac{\partial u}{\partial t} = \pm\frac{\partial F}{\partial u},$$ (1.3)

and look for the steady state solution. In his book [158] Sapiro proposes a good example to illustrate the previous ideas. If we want to denoise an image, an example of variational model is:

$$I^\star = \min_{I\in L^2(\mathbf{R}^2)} F(I) = \int_{\mathbf{R}^2} |\nabla I|^2 d\mathbf{x},$$ (1.4)

where F is, in this case, the Dirichlet functional. The Euler-Lagrange equation of F provides us the famous isotropic/linear heat flow:

$$\frac{\partial I}{\partial t} = \Delta I.$$ (1.5)

Throughout this thesis, the previous paradigm will be applied to solve the image segmentation problem. The main difference between the proposed methods will rely on the definition of energy functionals. They will be defined from fundamental functionals such as the Rudin-Osher-Fatemi/Total Variation functional [155] and the Mumford-Shah functional [125] in Chapter 3, but also from information theory in Chapter 4, from a statistical shape model in Chapter 5 and finally from *string theory* introduced by Sochen-Kimmel-Malladi in image processing [167] in Chapter 6.

1.3   Organization of the Dissertation and Main Contributions

This thesis presents four new variational models to carry out the image segmentation task. All these models use the active contour/snake approach, which means that the boundaries of the meaningful objects in images are identified with a curve/surface which evolves according to a partial differential equation derived from the minimization of a given energy functional.

Chapter 2 introduces the state-of-the-art variational and PDE-based models used to segment images. The first part of Chapter 2 presents the three generations/families of active contours that have been defined since the original work of Kass-Witkin-Terzopoulos in [103]. The first generation of active contours localize the edges of objects lying in images, the second generation use region-based criteria to evolve the active contours toward smooth regions and the third generation incorporate prior shape information into the segmentation process. In this chapter, the most important models of these three families are reviewed, which is useful to introduce our first three image segmentation models in Chapters 3, 4 and 5.

Chapter 3 proposes an image segmentation model based on the first and second generation of active contours. More precisely, this model merges the geodesic/geometric active contours model of [35, 105], which detects edges, with Rudin-Osher-Fatemi's image denoising model [155] and Chan-Vese's image segmentation model of active contours without edges [42]. What makes our model interesting is that the merging is done in a global minimization framework where the global minimizers of the active contours/snakes model are determined. Usually, the active contours models

capture a local minimum, which is the main mathematical weakness of these approaches.

Chapter 4 introduces a new second-generation active contour model that uses at the same time determinist and statistical concepts. In this chapter, we use information theory to carry out segmentation by defining a non-parametric and non-supervised image classification model based on Butz-Thiran's information theory approach [32, 33]. Our classification framework includes most of the existing second-generation active contours model that use concepts of statistics and information theory such as mutual information.

Chapter 5 proposes a third-generation of active contours by defining a variational model to segment an object belonging to a given shape space and using the boundary-based active contours [35, 105], a geometric shape prior based on the principal components analysis (PCA) [113] and the Mumford-Shah functional [179] used by Vese-Chan [179]. This method integrates the three families of snakes in order to use simultaneously the advantages of each family.

Finally, the second part of Chapter 2 enables us to review some image denoising and enhancing models including the model of Sochen-Kimmel-Malladi [167] that proposes to denoise multidimensional images using string theory and differential geometry. This model is used in Chapter 6 to define a multiscale image segmentation model to simultaneously extract structures at different scales of observation/resolution. The approach of [167] is used to embed the active contours into multi-scale spaces derived from well-known diffusion equations used in image processing.

Thus, the main contributions presented in this dissertation are as follows:

- a novel method to determine global minimizers of the well-known active contours/snakes model, which allows us to merge the geodesic/geometric active contours model [35, 103, 105], the Rudin-Osher-Fatemi's model [155] and the models of Chan-Vese [42, 179] based on the Mumford-Shah functional [125].

- an image classification model that uses at the same time determinist and statistical concepts. The statistical part comes from information theory, with the promising approach of Butz-Thiran [32, 33] and the determinist part is based on the shape gradient method of Delfour-Zolesio [13, 69, 99].

- a variational model to segment an object of interest which geometric shape is a priori known thanks to a principal components analysis defined by Leventon [113]. We also benefit from the first and second generation of active contours by using the geodesic/geometric active contours model [35, 103, 105] and the Vese-Chan's model [179]. The proposed model simultaneously uses the advantages of three generations of snakes.

- a generalization of the geodesic/geometric active contours model to scale spaces in order to define a multiscale image segmentation model to capture structures at different scales of observation. We use the framework of Sochen-Kimmel-Malladi [167] who introduced the Polyakov action in image processing from string theory.

State of the Art

2

This chapter presents the state-of-the-art in the field of image segmentation using variational models and partial differential equations (PDEs). This restriction of image segmentation models to variational approaches and PDEs is voluntary for two main reasons. Firstly, the methods proposed in this thesis are all based on these mathematical concepts and secondly, an exhaustive review of all image segmentation models is not possible in a single chapter. The presentation of the state-of-the-art papers is organized like our thesis. First of all, the classical model of boundary-based snake/active contour is presented, then the region-based and the shape-based active contours and finally, the models of image denoising are introduced.

© *Diego Porcel*

2.1   Variational Image Segmentation Models

In image analysis, *image segmentation* is a fundamental component toward automated vision systems and useful to medical applications. Its main objective consists in determining the *semantically important parts of images*. Several approaches have been considered to perform the image segmentation process. The book of Sonka-Hlavac-Boyle [168] gives an exhaustive review of image segmentation models such as the thresholding approach, the region merging algorithm, the watershed segmentation and so on. Most of them are based on a discrete setting, which makes them dependent with respect to (w.r.t.) the parametrization. Moreover, they are not defined in a rigorous mathematical framework. Recently, new image segmentation models based on a *variational approach* have been introduced. These models are defined in a continuous setting and they are mathematically well studied. We propose to describe two well-known variational image segmentation models, namely the *Mumford-Shah model* [124, 125] and the *active contour method* [103].

(a) Original image I **(b)** Piecewise smooth image u **(c)** Boundaries C of u
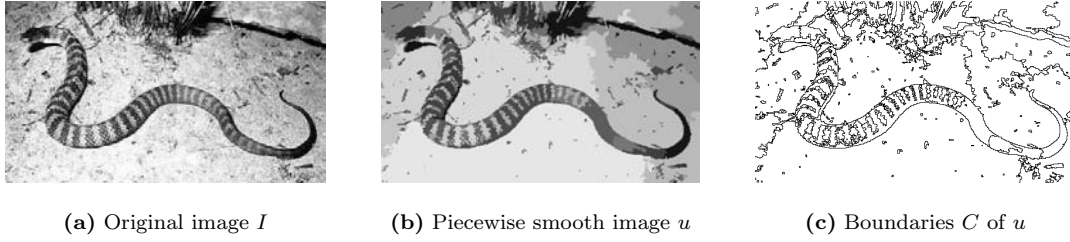
Figure 2.1: Image segmentation based on the Mumford-Shah model.

In the Mumford-Shah (MS) approach, the goal is to find *a partition of the image into distinct homogeneous regions.* This is realized by minimizing the Mumford-Shah functional [124, 125] which provides an optimal piecewise smooth approximation of a given image, in other words an image made up of homogeneous regions which common boundaries are sharp and piecewise regular [15]. The Mumford-Shah functional is defined as follows for any observed image $I_0 \in L^1(\Omega)$ and any positive parameters μ, ν:

$$F_{MS}(I, C) = \int_\Omega |I - I_0|^2 d\mathbf{x} + \mu \int_{\Omega \setminus C} |\nabla I|^2 d\mathbf{x} + \nu \mathcal{H}^{N-1}(C), \qquad (2.1)$$

where I_0 is defined on a domain Ω, I corresponds to a piecewise smooth approximation of the original image I_0, C is a discontinuity set (representing the edges of I) and the length of C is given by the (N-1)-dimensional Hausdorff measure $\mathcal{H}^{N-1}(C)$ (see [73] for an accurate definition but $\mathcal{H}^0$ is the counting measure, $\mathcal{H}^1$ the length and $\mathcal{H}^2$ the area). The first term of (2.1) is a fidelity term w.r.t. the given data I_0, the second term is a regularization term that constraints the function I to be smoothed inside the region $\Omega \setminus C$ and the last term imposes a regularization constraint on the discontinuity set C, i.e. the boundaries between smooth regions. Figure 2.1(b) shows the optimal piecewise constant approximation u of the original image I_0 presented on Figure 2.1(a) (I has been computed with the software *Megawave2* [126]).

Observing Figure 2.1(b), we notice that the Mumford-Shah model can not directly capture texture objects such as the snake because the snake-object is not composed of *one* smooth region but many. More generally speaking, the Mumford-Shah model efficiently realizes the segmentation of homogeneous *intensity* regions but not the segmentation of homogeneous *texture* regions.

The minimization of Functional (2.1), which belongs to the class of *free discontinuity problems*, is not easy to realize as explained in the books of Aubert-Kornprobst [15] and Morel-Solimi [122] and the paper of Vese-Chan [179]. Indeed, the Mumford-Shah functional needs to be reformulated to define a correct mathematical framework to prove the existence of minimizers (not unique in general). Thus, De Giorgi-Ambrosio in [6, 83] defines a new formulation of the Mumford-Shah functional, called the *weak formulation*, by replacing C by the set of jumps of I and defining SBV, the space of special functions of bounded variation. Then, Ambrosio in [6, 7, 8] established the equivalence between both formulations by proving that a solution of the weak formulation is also a minimizer of the initial Mumford-Shah functional. Having proved the existence of (at least) a minimizer, its computation is the next step. Unfortunately, this issue remains an open question in the general setting. Nevertheless, it is possible to determine a minimizer by introducing a constraint of connectedness. That was proposed in the original work of Mumford-Shah [124, 125] where the authors conjectured that their functional admits a minimizer satisfying two regularity hypotheses. Based on these two hypotheses and an hypothesis of connectedness, Mumford-Shah [125] and Bon-

(a) Initial active contour   **(b)** Final active contour   **(c)** Final active contour
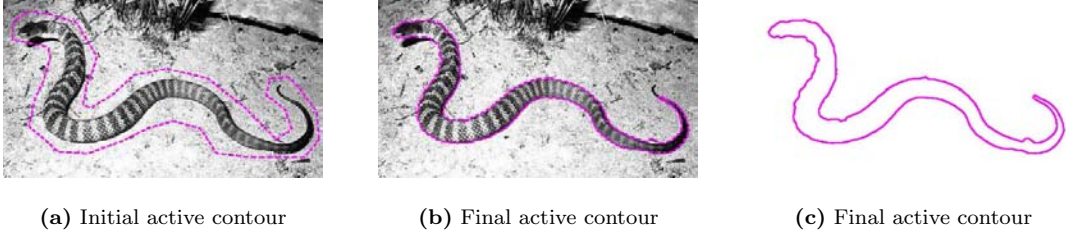
Figure 2.2: Image segmentation based on the active contour model.

net [22] established two theorems which characterize the properties of the minimizer. The numerical approximation of the Mumford-Shah functional is usually based on the technique of Euler-Lagrange equations. However, the term $\mathcal{H}^{N-1}(C)$ is not lower semi-continuous w.r.t. any compact topology ([15]) which prevents us from applying the calculus of variations. Hence, many authors proposed to approximate the functional $F_{MS}(I, C)$ by a sequence of regular functionals defined on Sobolev spaces. The sequence Γ-converges [84, 120] to the initial Mumford-Shah functional. Several approximation models of the Mumford-Shah functional were proposed in the literature [10, 23, 24, 38, 39]. Finally, Chan-Vese [42, 179] proposed to approximate the term $\mathcal{H}^{N-1}(C)$ by the length of a set of curves in order to use the Euler-Lagrange equations technique. This will provide the model of *active contours without edges* [42] that we will describe in Section 2.4.1.

Although the first segmentation model has proposed to extract all significant parts in images, some specific parts of images can be more important than others depending on applications such as in medical imaging. This makes the link with the second segmentation model, in the context of variational models, which aims at detecting *objects in images*. Indeed, the active contour model proposes to detect the closest contour(s) (such as the snake on Figure 2.2(b)) from an initial position (Figure 2.2(a)). The active contour/snake model was introduced by Kass-Witkin-Terzopoulos (KWT) in [103]. This model locates sharp image intensity variations by deforming, like a *snake*, a curve C toward the edges of objects. The evolution equation of the parametric planar curve $C(p) = (x(p), y(p)) \in \Omega, p \in [0, 1]$ is given by the minimization of the following energy functional defined for any observed image $I_0 \in L^1(\Omega)$ and any positive parameters α, β, λ:

$$F_{KWT}(C) = \alpha \int_0^1 \left| \frac{\partial C(p)}{\partial p} \right|^2 dp + \beta \int_0^1 \left| \frac{\partial^2 C}{\partial p^2} \right|^2 dp + \lambda \int_0^1 f^2(I_0(C))dp, \qquad (2.2)$$

where the first two terms are physics-based smoothness constraints on the geometry of the curve since the first term makes the snake act like a membrane and the second term makes it act like a thin plate. The sum of both terms is called the *internal energy*. The third term of (2.2), namely the *external energy*, attracts the curve toward the boundaries of objects using an edge detecting function f vanishing at infinity such as the function:

$$f(I_0) = \frac{1}{1 + \gamma |\nabla (I_0 * G_\sigma)|^2}, \qquad (2.3)$$

where G_σ is the Gaussian function with standard deviation σ, $I_0 * G_\sigma$ is a smoothed version of the original image I_0 and γ is an arbitrary positive constant. Figure 2.3(b) presents an edge-detecting function f.

It is interesting to note that the active contour model of Kass *et al.* allows us to use directly closed and *open* curves, which is not the case with the geodesic/geometric active contour model

[35, 105] that we present in the next section (even if the level set framework proposes a solution to evolve open curves in the context of the geodesic/geometric active contour model [30]).

The energy $F_{KWT}(C)$ admits at least a global minimum in the Sobolev space $(W^{2,2}(0,1))^2$, [15]. Unfortunately, F_{KWT} is not convex which implies no direct uniqueness result. However, a local minimum of F_{KWT} can be reached by solving the following Euler-Lagrange equations of F_{KWT}:

$$-\alpha\frac{\partial^2 C}{\partial p^2} + \beta\frac{\partial^4 C}{\partial p^4} + \lambda\nabla f^2(C) = 0. \tag{2.4}$$

In [103], Kass *et al.* numerically solved the fourth-order partial differential equation (2.4) with a finite differences method. This provides a fast numerical algorithm but, in the case of closed curves, it does not allow changes of topology since the final curve has the same topology as the initial one. In other words, it is not possible to detect more than one object as we can see on Figure 2.3(c-d).

(a) Original image I_0 **(b)** Associated edge detect-   **(c)**   **(d)**
                                ing function $f(I_0)$
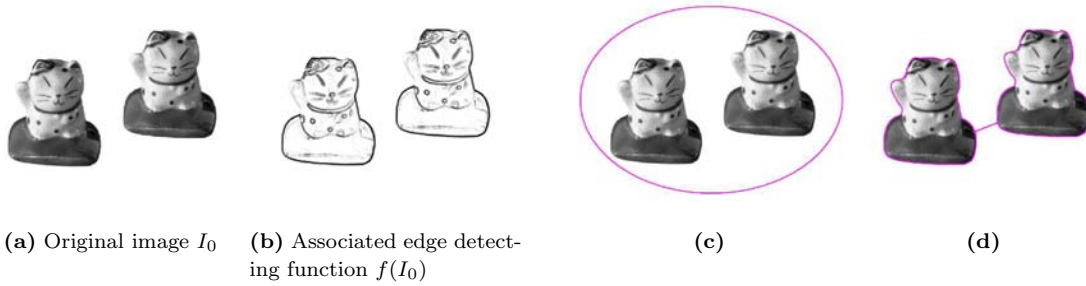
Figure 2.3: Figure (b) presents an edge detecting function from a given image (a). Figures (c-d) shows the snake at the beginning and at the end of the evolution process. Figure (d) proves that the snake model can not naturally change its topology during the evolution process since the final contour has captured only one object.

Another drawback of the snake segmentation model is the dependence of the functional F_{KWT} w.r.t. the parametrization of the curve C, in other words F_{KWT} is not intrinsic. This means that different parametrizations of the curve may give different solutions for the same initial condition, which is not satisfactory.

To overcome the limitation of the changes of topology, Osher-Sethian proposed the powerful *level set method* in [127, 129, 164] that we develop in Section 2.3. The curve C is then implicitly represented by a function of higher dimension ϕ, called the *level set function*, and the curve evolution equation can be re-written in a level set formulation.

Finally, the problem of local minimizers of the active contour model will be studied in Chapter 3. We will propose a method to determine global minimizers of the active contour/snake model.

2.2   The Geodesic/Geometric Active Contour Model

Caselles-Kimmel-Sapiro [35] and Kichenassamy-Kumar-Olver-Tannenbaum-Yezzi [104, 105] proposed a new energy, based on the Kass-Witkin-Terzopoulos model (2.2), that is invariant w.r.t. a new curve parametrization. The new *intrinsic* energy functional is

$$F_{GAC}(C) = \int_0^1 f(|\nabla I_0(C(p))|)|C_p|dp = \int_0^{L(C)} f(|\nabla I_0(C(s))|)ds, \tag{2.5}$$

where GAC stands for Geodesic/Geometric Active Contour, ds is the Euclidean element of length and $L(C)$ is the Euclidean length of the curve C defined by $L(C) = \int_0^1 |C_p|dp = \int_0^{L(C)} ds$. Hence,

the functional (2.5) is actually a new length obtained by weighting the Euclidean element of length ds by the function f which contains information concerning the boundaries of objects [15]. The function f is the edge detecting function introduced in the previous section and defined e.g. by Equation (2.3).

The equivalence between minimizing F_{GAC} and minimizing F_{KWT} was studied by Caselles *et al.* in [35] and Aubert-Blanc Féraud in [14]. They started from the energy F_{KWT} and remove the second-order smoothness component by setting $\beta = 0$. They justified this choice by the fact that the first two terms of F_{KWT} decrease the curvature, hence, they are redundant. Moreover, setting $\beta = 0$ allows second-order discontinuities as corners. Then, Caselles *et al.* used concepts of Hamiltonian theory and Aubert-Blanc-Féraud concepts of calculus of variations to prove the equivalence between minimizing F_{GAC} and F_{KWT}.

Caselles *et al.* also proved in [35] that the curve minimizing F_{GAC} is actually a geodesic in a Riemannian space which metric tensor is $[h_{ij}] = f(|\nabla I_0|)[\delta_{ij}]$ where f is the edge detecting function. This geodesic is computed by the calculus of variations. Let us introduce an artificial time t and let us consider a family of curves $C(t)$ such that:

$$F_{GAC}(t) = \int_0^1 f(|\nabla I_0(C(p,t))|)|C_p(p,t)|dp. \tag{2.6}$$

The first variation of the energy F_{GAC} is then:

$$\frac{dF_{GAC}}{dt} = \int_0^1 \left\langle \frac{\partial C}{\partial t}, \ \langle \nabla f, \mathcal{N} \rangle \mathcal{N} - \kappa f \mathcal{N} \right\rangle |C_p|dp, \tag{2.7}$$

see [35] for details. Hence, the direction for which F_{GAC} decreases most rapidly provides us the following minimization flow:

$$\frac{\partial C}{\partial t} = (\kappa f - \langle \nabla f, \mathcal{N} \rangle) \, \mathcal{N}, \tag{2.8}$$

where $\mathcal{N}$ is the unit normal to the curve C and κ is its curvature. The right hand side of the equation (2.8) corresponds to the Euler-Lagrange of Energy (2.5). The first term is the mean curvature motion, also called curve shortening flow, weighted by the edge detecting function f. It smoothes the curve shape by decreasing its total length as fast as possible. The second term of (2.8) attracts the curve toward the boundaries of objects by creating an attraction valley centered on the edges. Hence, the function f does not need to be equal to zero to stop the evolution of the snake on the contours of objects.

Cohen in [49] proposed to artificially introduce a constant force in the model (2.8), called a *balloon force*:

$$\partial_t C = (\kappa f - \langle \nabla f, \mathcal{N} \rangle + \alpha f) \, \mathcal{N}, \tag{2.9}$$

$\alpha > 0$. When $f = 1$, this flow minimizes the following functional:

$$F(C) = \int_0^1 f(|\nabla I(C(p))|)|C_p|dp + \alpha A, \tag{2.10}$$

where A is the *area* of the region inside the closed curve C, [15]:

$$A = -\frac{1}{2} \int_0^1 \left\langle C, \begin{pmatrix} -y_p \\ x_p \end{pmatrix} \right\rangle \, dp. \tag{2.11}$$

The two main reasons to use the balloon force is to significantly increase the speed of convergence toward the steady state solution and to allow the detection of non convex objects.

The geodesic/geometric active contours were extended to higher dimensions by Caselles *et al.* [36] and Kichenassamy *et al.* [104, 105]. In a 3-D Euclidean space, the curve becomes a surface and in higher dimensions a hyper-surface. In all situations, the problem is to find a curve, a surface, a hyper-surface which minimize the Euler functional that corresponds to the length, the area, the hyper-area of the associated curve, surface, hyper-surface. In differential geometry, they are called *harmonic maps*. We will come back on this concept at the end of Section 2.5.

To summarize this section, we started from the model of Kass *et al.* which is a physics-based deformable model which evolution equations are based on a *Lagrangian formulation*, i.e. a parametric formulation of the curve evolution. Then, we solved the problem of the dependence of the parametrization of the curve C in the energy functional F_{GAC}. In other words, F_{GAC} is invariant w.r.t. the way we parametrically represent the curve. In the next section, we introduce the powerful level set method which is based on an *Eulerian formulation*, i.e. an implicit formulation, of the curve. This will give us efficient and accurate numerical schemes to deal with propagating fronts and solving the problem of topology changes as seen on Figure 2.3 since we will be able to segment more than one object.

2.3   The Level Set Method

2.3.1   Generality

The level set method for tracking moving fronts was introduced by Osher and Sethian in [129]. This method have had a great success because it has been used in many applications from physics, by capturing multiphase fluid dynamics flows, to graphics, e.g. special effects in Hollywood, visualization, image processing, computer vision, control, epitaxial growth, visibility, ray tracing, segmentation, restoration and many others [116, 127, 164]. In this section, we introduce the level set method applied to the theory of curve/surface evolution. We show that the level set formulation of a curve/surface evolution equation allows us to efficiently solve the problem of moving fronts, in particular the problem of changes of topology.

The general evolution equation of a curve $C(p,t) : [0,1] \times [0,T] \to \mathbf{R}^2$, where p parametrizes the curve geometry and t parametrizes the family of evolving closed curves, is given by the PDE:

$$\begin{cases} \frac{\partial C}{\partial t} = V_{\parallel} \mathcal{T} + V_{\perp} \mathcal{N} \\ C(t=0) = C_0 \end{cases}, \qquad (2.12)$$

where $\mathcal{T}$ and $\mathcal{N}$ are respectively the unit tangential and the outward/inward (arbitrary choice) unit normal to the curve C and $V_{\parallel}$ and $V_{\perp}$ are respectively the tangential and normal velocities. Epstein-Gage showed in [72] that the geometry of the curve deformation is not affected by the tangential velocity $V_{\parallel}$. This result is due to the fact that the tangential velocity does not change the geometry of the curve but its parametrization. Hence, Equation (2.12) can be replaced by

$$\begin{cases} \frac{\partial C}{\partial t} = V_{\perp} \mathcal{N} \\ C(t=0) = C_0 \end{cases}, \qquad (2.13)$$

from a strict *geometric* point of view. The same result holds for surface and hyper-surface. Thus, the general geometric evolution equation of a curve/surface/hyper-surface Γ is:

$$\begin{cases} \frac{\partial \Gamma}{\partial t} = V_\perp \mathcal{N} \\ \Gamma(t=0) = \Gamma_0 \end{cases}, \tag{2.14}$$

where $\mathcal{N}$ is the unit normal to the curve/surface/hyper-surface Γ.

At this stage, we leave the parametric/explicit representation of a contour (curve, surface or hyper-surface) to get interest in the geometry/implicit representation of the contour. This leads to the level set representation which is independent to the parametrization of the contour. The core idea in the level set method is to *implicitly represent* an interface Γ in $\mathbf{R}^n$ as a level set of a function ϕ, called *level set function*, of higher dimension and compute the geometric characteristics and the motion of the front with this level set function. The level set function ϕ of the *closed* front Γ is defined as follows, [127]:

$$\begin{cases} \phi(\mathbf{x}, t) > 0 \text{ for } \mathbf{x} \in \Omega_{in}(t) \\ \phi(\mathbf{x}, t) < 0 \text{ for } \mathbf{x} \in (\Omega \setminus \Omega_{in})(t) \\ \phi(\mathbf{x}, t) = 0 \text{ for } \mathbf{x} \in \partial\Omega_{in} = \partial(\Omega \setminus \Omega_{in}) = \Gamma(t) \end{cases}, \tag{2.15}$$

where Ω is an open region in $\mathbf{R}^n$, Ω_{in} is a (multiply connected) region in Ω bounding by Γ.

As we said, the geometric characteristics of the interface can be computed with the level set function. The unit normal $\mathcal{N}$ and the mean curvature κ to $\Gamma(t)$ are given by

$$\begin{cases} \mathcal{N} = -\frac{\nabla\phi}{|\nabla\phi|} \\ \kappa = \nabla . \mathcal{N} = \nabla . \left(-\frac{\nabla\phi}{|\nabla\phi|}\right) \end{cases}. \tag{2.16}$$

The area/volume of the region $\Omega_{in}(t)$ bounding by Γ and the length/area of the interface $\Gamma(t)$ are

$$\begin{cases} \int_{\mathbf{R}^n} H(\phi)d\mathbf{x} \\ \int_{\mathbf{R}^n} |\nabla H(\phi)|d\mathbf{x} = \int_{\mathbf{R}^n} \delta(\phi)|\nabla\phi|d\mathbf{x} \end{cases}, \tag{2.17}$$

where δ and H are respectively the Dirac and the Heaviside functions.
The motion of the front $\Gamma(t)$ evolving according to Equation (2.14) is given by the evolution of the zero level set of $\phi(t)$ which is solution of the following PDE:

$$\begin{cases} \frac{\partial \phi}{\partial t} = V_\perp |\nabla\phi| \\ \phi(t=0) = d(\Gamma_0) = \phi_0 \end{cases}, \tag{2.18}$$

where d is a function (usually a signed distance function, d_{Γ_0}) which zero level set is the initial contour Γ_0. The equivalence between the front evolution given by Equation (2.14) and Equation (2.18) was shown e.g. by Caselles *et al.* in [35].

Equation (2.18) raises a number of comments:

- The zero level set of Γ and *all* its level sets follows the front evolution equation (2.14).

- The level set evolution is computed on a fixed coordinate system since the level set is a parametrization free formulation.

- The evolution of the contour is independent of the initial embedding ϕ_0, see e.g. [47, 74, 75, 76] and the *classical* solution, if it exists, of (2.14) coincides with the classical solution of (2.18).

- Singularities, called *kinks*, can arise with PDE (2.18).

The last comment raises the important issue of singularities which can happen even with the simplest velocity $V_\perp = 1$, i.e. when (2.18) is a nonlinear first order Hamilton-Jacobi equation. In this case, the front Γ at time t corresponds to the set of points at a distance t from the original front Γ_0. Singularities develop when we start with a square Γ_0 and move inward. The question is how to correctly do the propagation? The solution is given by the *theory of viscosity solutions* developed by Crandall-Lions-Evans [55, 56, 57]. In the case of development of discontinuities, the theory chooses the *unique Lipschitz continuous solution* which obeys to the *Hüygens principle* known in optics for the light propagation and in thermodynamics for the flame propagation. In the later situation, the front is seen as a burning front in a forest. Once a tree is burnt, it remains burnt and the front continues its propagation. In the case of *hyperbolic conservation laws*, the Hüygens principle is equivalent to choose the unique entropy solution that we numerically find with a special numerical scheme called *upwind scheme* that we will see in the next section. Finally, viscosity solutions are useful to prove the existence and uniqueness of non-smooth solutions of PDEs such that (2.18) for a large class of velocities $V_\perp$. They are consistent with classical smooth solutions since they coincide with them when classical solutions exist.

Finally, the level set method allows us natural curve topological changes, such as breaking or merging, as we can see on Figure 2.4 since the topology of the level set function remains unchanged. Hence, there is no need complementary functions to handle topological changes, and so *no emotional involvement* [127]!

The next section will be focused on the numerical implementation of PDE (2.18). We need special numerical schemes to compute the unique entropy solution satisfying (2.18).

2.3.2 Numerical Implementation of the Level Set Method

This section is devoted to the numerical implementation of PDE (2.18) which velocity field $V_\perp$ has the general form [127]:

$$V_\perp = \left\langle \boldsymbol{\Xi}(\mathbf{x}), \frac{\nabla \phi}{|\nabla \phi|} \right\rangle - \xi(\mathbf{x}) \nabla \cdot \left(\frac{\nabla \phi}{|\nabla \phi|} \right), \tag{2.19}$$

where $\boldsymbol{\Xi}(\mathbf{x})$ is a vector field and $\xi(\mathbf{x})$ a scalar field. Given the velocity $V_\perp$, PDE (2.18) is a Hamilton-Jacobi equation which solutions can develop kinks which are discontinuities defined by jumps in derivatives. Special numerical methods are necessary to handle these discontinuities. These schemes were presented by Osher-Sethian in [129] based on upwind differencing, then extended to higher-order accuracy with the essentially non-oscillatory (ENO) and weighted essentially non-oscillatory (WENO) schemes defined in [100, 130].
Putting the velocity (2.19) in Equation (2.18), we obtain:

$$\frac{\partial \phi}{\partial t} = \langle \boldsymbol{\Xi}, \nabla \phi \rangle - \xi |\nabla \phi| \nabla \cdot \left(\frac{\nabla \phi}{|\nabla \phi|} \right). \tag{2.20}$$

The first term of the right hand side of Equation (2.20) is a *convection term*. In the active contour framework, the function $\boldsymbol{\Xi}(\mathbf{x})$ represents either an attraction force toward the boundaries of objects, i.e. $\boldsymbol{\Xi} = \nabla f$ (see Section 2.2) or a balloon force such as $\boldsymbol{\Xi} = \Xi \mathcal{N} = -\Xi \frac{\nabla \phi}{|\nabla \phi|}$. The second term of the right hand side of Equation (2.20) is a contour smoothing term based on the curvature of level
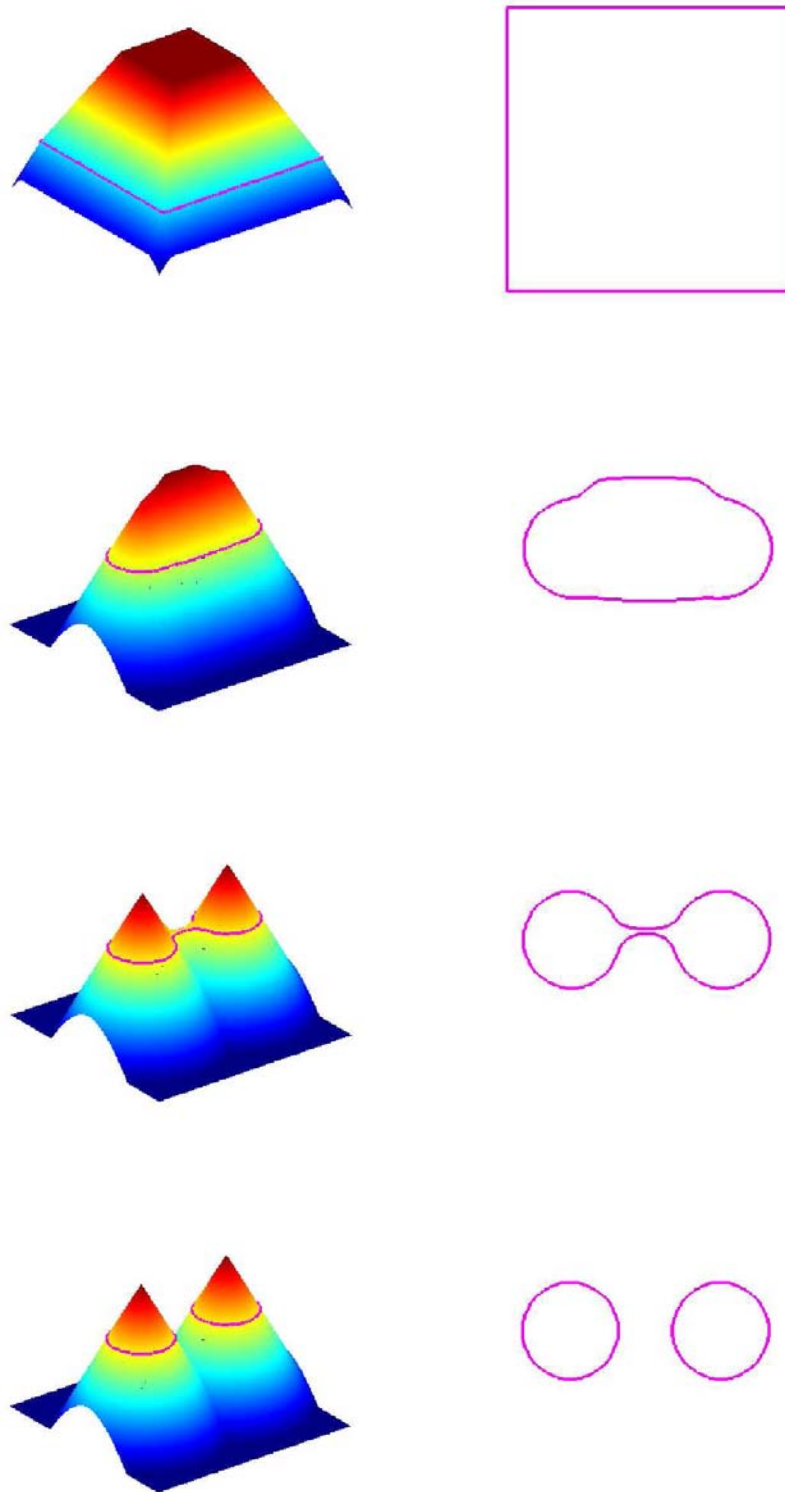
Figure 2.4: Natural changes of topology in the level set framework. The right column presents the evolution of the curve and the left column shows the evolution of the associated level set function. We note that the curve changed its topology but not the level set function.

sets of ϕ. In the following, we present the three corresponding discretization schemes.

The balloon force with the velocity $\boldsymbol{\Xi} = \Xi\mathcal{N}$ is approximated using the concept of *hyperbolic conservation laws* presented in the books of Osher-Paragios [128] (chapter 1), Sethian [164] (chapter 5) and Sapiro (chapter 1) [158]. We directly use their results: the balloon force term is equal to

$$\langle \boldsymbol{\Xi}, \nabla\phi \rangle = \langle -\Xi\frac{\nabla\phi}{|\nabla\phi|}, \nabla\phi \rangle = -\Xi|\nabla\phi| \tag{2.21}$$

and can be approximated by the first-order numerical scheme:

$$-\Xi(\mathbf{x})|\nabla\phi| = (-\Xi(\mathbf{x}))^+ \cdot \Delta^+ + (-\Xi(\mathbf{x}))^- \cdot \Delta^-, \tag{2.22}$$

where

$$\Delta^+ = \left[((D_x^-\phi)^+)^2 + ((D_x^+\phi)^-)^2 + ((D_y^-\phi)^+)^2 + ((D_y^+\phi)^-)^2 \right]^{1/2} \tag{2.23}$$

$$\Delta^- = \left[((D_x^+\phi)^+)^2 + ((D_x^-\phi)^-)^2 + ((D_y^+\phi)^+)^2 + ((D_y^-\phi)^-)^2 \right]^{1/2}, \tag{2.24}$$

and $(\zeta)^+ = \max(\zeta, 0)$, $(\zeta)^- = \min(\zeta, 0)$, $D_x^\pm\phi = \pm(\phi(x \pm \Delta x) - \phi(x))/\Delta x$ and $D_y^\pm\phi = \pm(\phi(y \pm \Delta y) - \phi(y))/\Delta y$. We illustrate this numerical scheme on Figure 2.5 by propagating a square curve inward and outward considering $\Xi(\mathbf{x}) = \pm 1$.

(a) $\Xi(\mathbf{x}) = -1$ (b) $\Xi(\mathbf{x}) = 1$
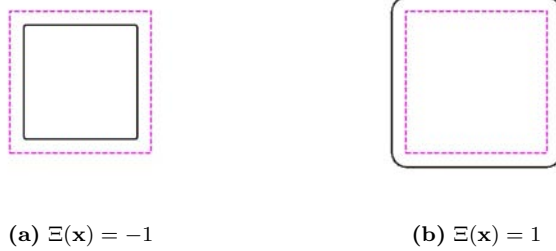
Figure 2.5: Evolution of a square curve inward and outward. The inward propagation, Figure 2.5(a), creates singularities (shocks) which are handled with the numerical scheme (2.22).

For a force different from the balloon force, the term $\langle \boldsymbol{\Xi}, \nabla\phi \rangle$ is a *pure passive advection term* [127, 164]. It can be computed using simple upwind schemes by choosing the correct difference scheme in the appropriate direction depending on the sign of each component of $\boldsymbol{\Xi}$:

$$\langle \boldsymbol{\Xi}, \nabla\phi \rangle = (\Xi_x)^+ \cdot D_x^-\phi + (\Xi_x)^- \cdot D_x^+\phi + (\Xi_y)^+ \cdot D_y^-\phi + (\Xi_y)^- \cdot D_y^+\phi, \tag{2.25}$$

with the vector field $\boldsymbol{\Xi} = (\Xi_x, \Xi_y)$.

Then, the second term of the right hand side of Equation (2.20) is a regularization term based on the mean curvature. This term is parabolic and therefore it does not need an upwind scheme which has been designed for hyperbolic advection term which needs to know the propagation direction. For a parabolic term, the propagation is in all direction, hence the central difference approximation scheme fits well to approximate the term $\xi|\nabla\phi|\nabla.\left(\frac{\nabla\phi}{|\nabla\phi|}\right)$ at a first-order of accuracy. In 2-D images, the curvature of the level sets is

$$\nabla.\left(\frac{\nabla\phi}{|\nabla\phi|}\right) = \frac{\phi_{xx}\phi_y^2 - 2\phi_x\phi_y\phi_{xy} + \phi_{yy}\phi_x^2}{(\phi_x^2 + \phi_y^2)^{3/2}} \tag{2.26}$$

and the associated numerical scheme is

$$\xi|\nabla\phi|\nabla.\left(\frac{\nabla\phi}{|\nabla\phi|}\right) = \xi\frac{D_{xx}^0\phi(D_y^0\phi)^2 - 2D_x^0\phi D_y^0\phi D_{xy}^0\phi + D_{yy}^0\phi(D_x^0\phi)^2}{((D_x^0\phi)^2 + (D_y^0\phi)^2)^{1/2}},\qquad(2.27)$$

where $D_x^0\phi = (\phi(x+\Delta x)-\phi(x-\Delta x))/2\Delta x$, $D_{xx}^0\phi = D_x^0 D_x^0\phi = (\phi(x+\Delta x)-2\phi(x)+\phi(x-\Delta x))/\Delta x^2$ and $D_{xy}^0\phi = D_x^0 D_y^0\phi = (\phi(x+\Delta x, y+\Delta y) + \phi(x-\Delta x, y-\Delta y) - \phi(x+\Delta x, y-\Delta y) - \phi(x-\Delta x, y+\Delta y))/4\Delta x\Delta y$. This smoothing term is illustrated on Figure 2.6.
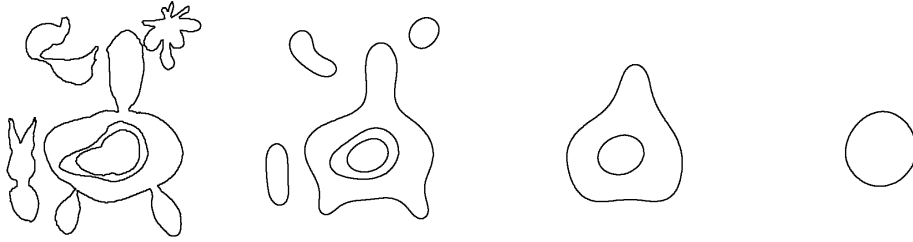
Figure 2.6: Smoothing of contours represented by the zero level set of a level set function

Finally, the three previous numerical schemes are combined to get the numerical model approximating the geodesic/geometric active contours (2.9) embedded in the level set formulation:

$$\frac{\partial\phi}{\partial t} = \left(\alpha + \nabla.\left(\frac{\nabla\phi}{|\nabla\phi|}\right)\right)f|\nabla\phi| + \langle\nabla f, \nabla\phi\rangle,\qquad(2.28)$$

where the first term is a balloon term approximated by the scheme (2.22), the second term is a curvature term implemented by (2.27) and the last term is a advection term computed by (2.25). Figure 2.7 presents the numerical model of the geodesic/geometric active contours which can naturally handle topological changes.

(a) (b) (c) (d)

Figure 2.7: Evolution of the geodesic/geometric active contour model in a level set formulation. Contrary to Figure 2.3(d) where the final contour captured only one object, Figure 2.7(d) shows that both objects have been successfully captured thanks to the level set method.

Finally, the model can be extended to 3-D images as seen on Figure 2.8.
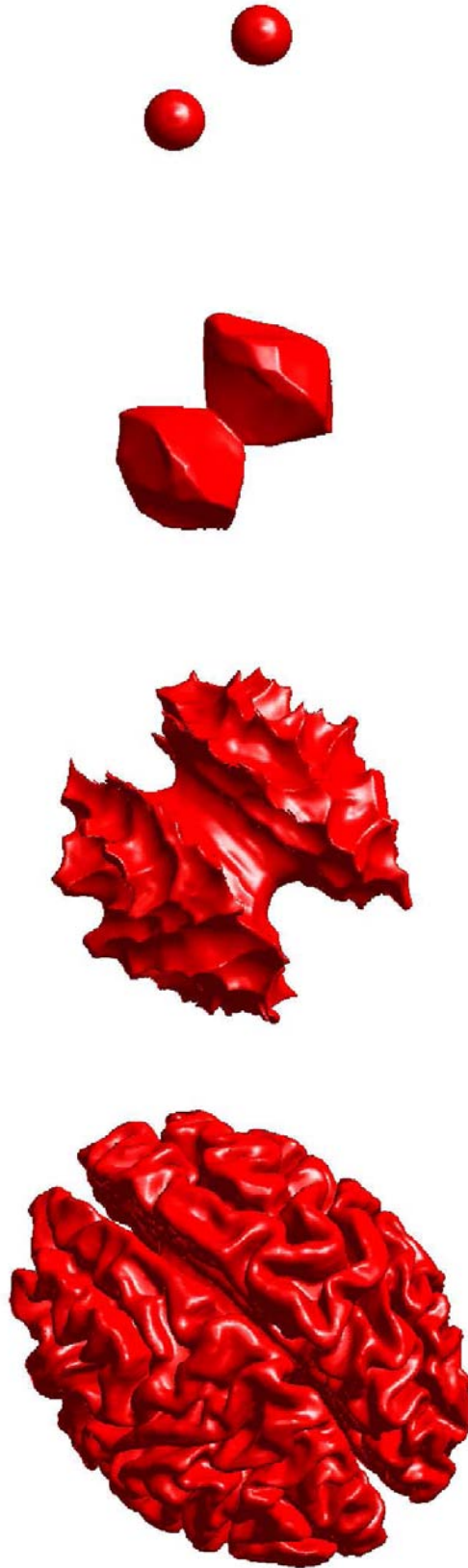
Figure 2.8: Minimal active surface model. This model is the extension of the geodesic/geometric active contour model to surface lying in 3-D images. These figures present the extraction of the cortical brain surface.

2.4 New Families of Active Contours

Section 2.2 presented the variational model of geodesic/geometric active contours which is basically based on the detection of edges in images. Combined with the level set method that provides efficient numerical schemes and natural extension to higher dimensions, this model have had great success to detect fine real-world shapes such as medical structures [101, 115, 188]. However, despite of their great advantages, these first-generation active contours, are highly sensitive to the presence of noise and poor image contrast, which can lead to bad segmentation results. To overcome this drawback, some authors incorporated *region-based evolution criteria* into active contour energy functionals built from intensity statistics and homogeneity requirements. We propose to review some of the well-known ones in Section 2.4.1. Yet the segmentation of *structures of interest* with these second-generation active contours is not able to deal with occlusion problems or presence of strongly cluttered background. Therefore the integration of *prior shape knowledge* about the objects in the segmentation task represents a natural way to solve these problems and can be considered as a third generation of active contours. Section 2.4.2 presents these active contours. As we will see in Chapter 4, we propose a segmentation model based on a region-based evolution criterion and information theory and in Chapter 5, a method that exploits the advantages of the three generations of active contours.

2.4.1 Region-Based Active Contours

In [192], Zhu-Yuille (ZY) proposed a variational and statistical image segmentation model based on the snake/balloon model and the region growing algorithm. They derived their evolution equation from a generalized Bayes/Minimum Description Length criterion, the Euler-Lagrange equations technique and the Green's theorem which states how to go from integrals defined over regions to functionals defined along contours. Their main contribution is the introduction of a region-based criterion into the snake model. However, the model does not use any boundary-based information such as in the original model and the active contour can not change its topology since it is based on a Lagrangian formulation. Their functional is a follows:

$$F_{ZY}(C, \{\alpha_i\}) = \sum_{i=1}^{N_R} \left\{ \frac{\mu}{2} \int_{\partial \Omega_i} ds - \int_{\Omega_i} \log P(I_0(\mathbf{x})|\alpha_i) d\mathbf{x} \right\}, \qquad (2.29)$$

where $C = \cup_{i=1}^{N_R} \partial \Omega_i$ is the segmentation boundaries, P is a Gaussian probability density distribution which $\{\alpha_i\}$ are the parameters and μ is a positive arbitrary parameter.

In [132, 133, 134, 139], Paragios-Deriche merged the previous model with the geodesic/geometric active contour model and the level set method to define the *geodesic active regions* (GAR) model. Their image segmentation method is able to unify boundary and region-based knowledge in a variational and statistical framework. Indeed, the boundary and the region information are based on a statistical estimation (Minimum Description Length criterion and Maximum Likelihood Principle) of the image histogram using a mixture of Gaussians distributions, each one representing an homogeneous region to be segmented. Their proposed energy functional is minimized using the Euler-Lagrange equations technique and the gradient descent method to get a set of PDEs, each PDE acting on a boundary, represented by a level set function, of a region to be segmented. Their method efficiently segments all homogeneous regions in images and presents a good robustness w.r.t. local minima. Moreover, the changes of topology are naturally handled with the level set formulation

of the evolution equations. The geodesic active region functional is as follows:

$$F_{GAR}(C) = \sum_{i=1}^{N_R} \left\{ (1-\alpha) \int_0^1 g_{B,i}(I_0(\partial\Omega(p_i))) |\partial\Omega_{p_i}| dp_i + \alpha \int_{\Omega_i} g_{R,i}(I_0(\mathbf{x})) d\mathbf{x} \right\}, \qquad (2.30)$$

where N_R is the number of homogeneous regions estimated from the image histogram, $C = \cup_{i=1}^{N_R} \partial\Omega_i$ are the boundaries between the different regions, $g_{B,i}$ is the boundary probability density functions of the region Ω_i and $g_{R,i}$ is the region probability density functions of the region Ω_i, p_i is the parametrization of the curve $\partial\Omega_i$ and α is a positive arbitrary parameter. See Figure 2.9 for an example of the geodesic active regions model. Finally, the authors extended their model to texture supervised segmentation [133] and video [134].

(a) Original image   (b) Image histogram and its approximation   (c) 4 Gaussian components

(d) Initial contours   (e) Final contours for Component 1   (f) Final contours for Component 2   (g) Final contours for Component 3
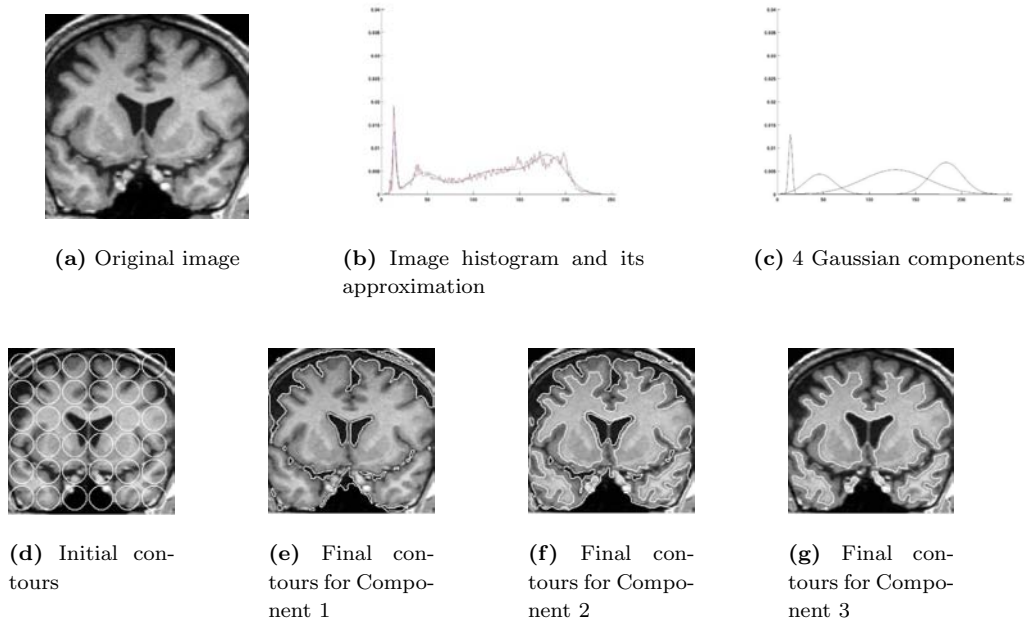
Figure 2.9: Segmentation model of geodesic active regions [132, 133, 134, 139]. Figure (b) presents the image histogram of Image (a) and its approximation. Figures (e-f) present the segmentation results for the first 3 Gaussian components.

More recently, Rousson-Deriche extended the model of geodesic active regions. In the original work, the statistical information concerning the homogeneous regions was estimated in an independent stage from the segmentation process. In [151, 152], they integrated this stage in the segmentation process. Finally, in [149, 150], Rousson-Brox-Deriche extended the *supervised* texture segmentation model [133] to an *unsupervised* texture segmentation by extracting a small set of features based on the structure image tensor $(I_0, I_{0x}^2, I_{0y}^2, I_{0x}I_{0y})$ and nonlinear diffusion, see Figure 2.10.

Samson-Blanc Féraud-Aubert-Zerubia in [156] presented a *supervised* classification model based on known intensity means and variances for each region to be segmented. They applied the multiphase level set model of Zhao-Chan-Merriman-Osher [191] to efficiently handled the evolution process of each regions to be classified, see Figure 2.11.

(a) Four smoothed components of the structure image tensor   (b) Segmentation result
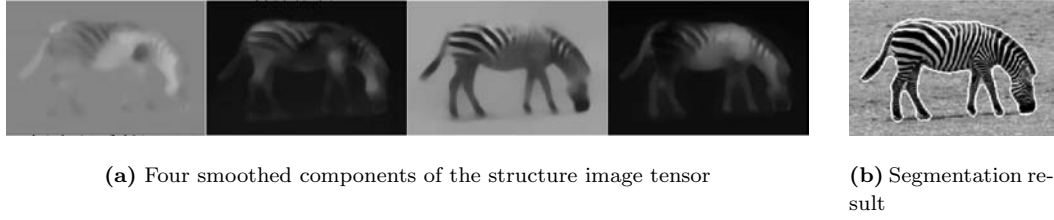
Figure 2.10: Figure (a) presents the 4 feature channels obtained by smoothing $(I_{0x}I_{0y}, I_{0y}^2, I_0, I_{0x}^2)$ from left to right and Figure (b) is the segmentation provided by the unsupervised texture segmentation model [149, 150] that use the 4 previous feature channels. Note that all figures are reproduced from [149].

(a) Original image   (b) Initial contours   (c) Final contours   (d) Classified image
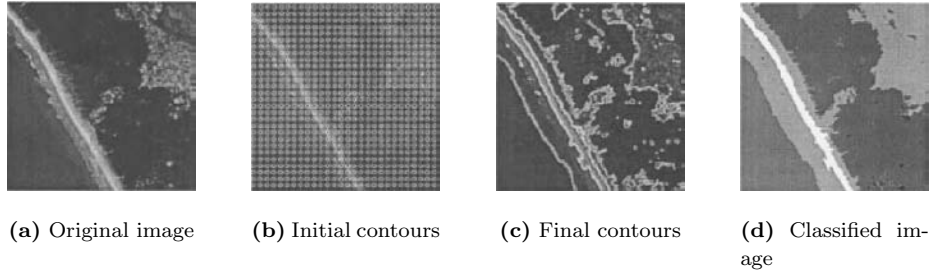
Figure 2.11: Supervised classification method of Samson *et al.* [156]. Figure (a) is a SPOT satellite image, Figures (b) and (c) show the initial and final active contours and Figure (d) the four classified homogeneous regions. Note that all figures are reproduced from [156].

As we explained in Section 2.1, the variational segmentation problem of Mumford-Shah [124, 125] for segmentation and partition is difficult to solve for many reasons. In [42, 178, 179], Chan-Vese proposed a method to minimize the Mumford-Shah functional in the context of active contours. Indeed, the active contour framework is useful to define a mathematical framework suitable to determine a solution to a variational model thanks to the calculus of variations. Moreover, PDEs computed from the Euler-Lagrange equations technique naturally use geometric regularization constraints such as the ones conjectured by Mumford-Shah in [125]. Finally, the last (and difficult) term of the Mumford-Shah functional (2.1) which imposes a smoothing constraint on the discontinuity set C between smooth regions can be approximated by the length of a set of curves. The Mumford-Shah (MS) functional in the approach of Chan-Vese (CV) is as follows:

$$F_{MS}^{CV}(I, C) = \int_\Omega |I - I_0|^2 d\mathbf{x} + \mu \int_{\Omega \setminus C} |\nabla I|^2 d\mathbf{x} + \nu \int_C ds, \qquad (2.31)$$

where I corresponds to a piecewise smooth approximation of the original image I_0, C represents the set of curves separating the smooth regions in the given image, $\int_c ds$ is the length of C and μ, ν are positive parameters.

In [42], Chan-Vese defined the model of *Active Contour Without Edges* (ACWE) based on a reduced form of the Mumford-Shah functional when the gradient-based term of (2.31) is removed. This case corresponds to the *piecewise-constant case* of the Mumford-Shah model, also called the *minimal partition problem*, since the optimal solution is an image composed of regions of approximatively constant intensities equal to the mean value of intensities in the corresponding region. The general

case (2.31) is called the *piecewise-smooth case*. In what follows, we consider only two regions Ω_{in} and $\Omega \setminus \Omega_{in}$ even if Chan and Vese have solved the complete image partitioning problem. The variational segmentation model of active contours without edges, i.e. the two-phase piecewise constant Mumford-Shah segmentation model, is as follows:

$$\min_{\Omega_{in}, c_1, c_2} F_{ACWE}(\Omega_{in}, c_1, c_2) = \text{Per}(\Omega_{in}) +$$
$$\lambda \left(\int_{\Omega_{in}} (c_1 - I_0(\mathbf{x}))^2 \, d\mathbf{x} + \int_{\Omega \setminus \Omega_{in}} (c_2 - I_0(\mathbf{x}))^2 \, d\mathbf{x} \right), \tag{2.32}$$

where the region $\Omega_{in} \subset \Omega$, $c_1, c_2 \in \mathbf{R}$ and $\text{Per}(\Omega_{in})$ is the perimeter of the region Ω_{in}.

The variational model (2.32) determines the best approximation, in the L^2 sense of the image I_0 as a set of regions with only two different values, c_1 and c_2. If Ω_{in} is fixed, the values of c_1 and c_2 which minimize Energy F_{ACWE} are the mean values inside and outside Ω_{in}. Finally the term $\text{Per}(\Omega_{in})$ imposes a smoothness constraint on the geometry of the set Ω_{in} which separates the piecewise constant regions. Functional (2.32) can be re-written in a level set formulation by representing the regions Ω_{in} and $\Omega \setminus \Omega_{in}$ with the Heaviside function H of a level set function (which models a characteristic function). Hence Energy F_{ACWE} can be written w.r.t. a level set function ϕ as follows:

$$F_{ACWE}(\phi, c_1, c_2) = \int_{\Omega} |\nabla H_\epsilon(\phi(\mathbf{x}))| d\mathbf{x} +$$
$$\lambda \int_{\Omega} \left(H_\epsilon(\phi) \left(c_1 - I_0(\mathbf{x}) \right)^2 + H_\epsilon(-\phi) \left(c_2 - I_0(\mathbf{x}) \right)^2 \right) d\mathbf{x}, \tag{2.33}$$

where H_ϵ is a regularization of the Heaviside function which allows us to differentiate F_{ACWE}. To minimize F_{ACWE}, the natural way is a two-steps method. Firstly, ϕ is fixed and $F_{ACWE}(\phi, c_1, c_2)$ is minimized w.r.t. the constants c_1 and c_2, we get:

$$c_1 = \frac{\int_\Omega I_0(\mathbf{x}) H_\epsilon(\phi(\mathbf{x})) d\mathbf{x}}{\int_\Omega H_\epsilon(\phi) d\mathbf{x}}, \quad c_2 = \frac{\int_\Omega I_0(\mathbf{x}) H_\epsilon(-\phi) d\mathbf{x}}{\int_\Omega H_\epsilon(-\phi) d\mathbf{x}}. \tag{2.34}$$

Secondly, c_1, c_2 are fixed and $F_{ACWE}(\phi, c_1, c_2)$ is minimized w.r.t. ϕ to provide the following minimization flow:

$$\frac{\partial \phi}{\partial t} = \delta_\epsilon(\phi) \left\{ \nabla . \left(\frac{\nabla \phi}{|\nabla \phi|} \right) - \lambda \left((c_1 - I_0(\mathbf{x}))^2 - (c_2 - I_0(\mathbf{x}))^2 \right) \right\}, \tag{2.35}$$

where $\delta_\epsilon(\phi) = H'_\epsilon(\phi)$.

Figure 2.12(c) underlines well the name of the Chan-Vese's model that is able to stop the curve evolution even in the absence of boundary (2.12(c)) whereas the standard snake model fails to stop (Figure 2.12(b)). This is due to the fact that the active contours without edges use a *global* stopping criterion which measures the homogeneity of both regions whereas the standard active contours use a *local* stopping criterion which measures the presence of an edge. Another advantage of the Chan-Vese model is the robustness in the presence of noise and the detection of interior contours with a *non-compactly* supported smooth strictly monotone approximation $H_\epsilon(.)$ of the Heaviside function.

In [102], Jonasson-Hagmann-Bresson-Thiran-Wedeen applied the previous segmentation model to the extraction of white matter tracts in high angular resolution diffusion magnetic resonance images [181]. The segmentation is done in a 5-*dimensional space* of position and orientation to separate crossing fiber tracts that merge in 3-D position space. The level set formulation of active contours without edges is easily extensible to a 5-D space. The only implementation issue is the

(a) Initial contour

(b) Standard active contour

(c) Active contour without edges
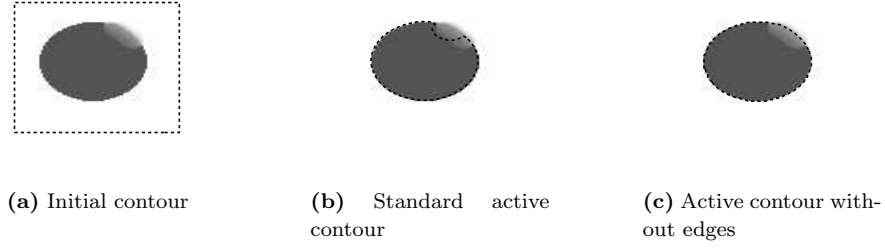
Figure 2.12: Comparison between the standard model of active contours [35, 103, 105] (b) and the model of active contours without edges [42] (c). Standard snake fails to stop on the borders of the ellipse (b) because edges do not exist whereas the Chan-Vese model separates the image into two homogeneous regions (c) which boundary is represented by an active contour.

computation of the mean curvature in this high-dimensional space. Fortunately, a lot of work has already been done for N-D mean curvature flows such as Ambrosio-Soner in [9] who determine the mean curvature of level sets of a function $\phi : \mathbf{R}^N \to \mathbf{R}$ as the mean value of the principal curvatures $\kappa_i, i = 1, \ldots, N-1$ given by the $N-1$ smallest eigenvalues of the $N \times N$ matrix $\frac{1}{|\nabla \phi|^2} P_{\nabla \phi} \nabla^2 \phi P_{\nabla \phi}$ where P_p is a projection operator onto the space normal to the vector p: $P_p = I - \frac{p \otimes p}{|p|^2}$. Figure 2.13 illustrates the 5-D segmentation of crossing fiber tracts.

(a) High angular resolution diffusion magnetic resonance image

(b) Fibers tract segmentation
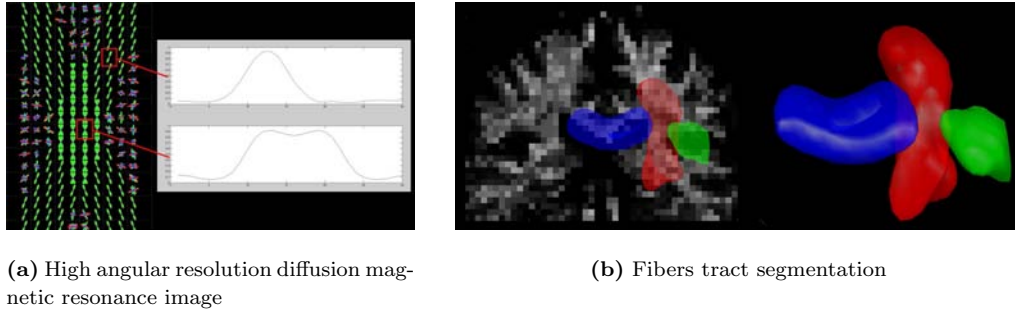
Figure 2.13: 5-D segmentation of crossing fibers [102]. Figure (a) is an example of high angular resolution diffusion magnetic resonance image and Figure (b) is the segmentation of fiber tracts obtained in a 5-D space where the red surface is a part of the cortical spinal tract, the blue surface is the corpus collosum and the green is the arcuate fasciculus.

In [178, 179], Vese-Chan considered the segmentation with the whole Mumford-Shah functional (2.31), i.e. the piecewise-smooth case. This model is also the extension of two-phase piecewise smooth Mumford-Shah segmentation model. In this situation, the variational problem to solve is given by:

$$
\min_{\Omega_{in}, s_1, s_2} F_{VC}(\Omega_{in}, s_1, s_2) = \mathrm{Per}(\Omega_{in}) +
$$
$$
\lambda \left(\int_{\Omega_{in}} (s_1(\mathbf{x}) - I_0(\mathbf{x}))^2 + \mu |\nabla s_1(\mathbf{x})|^2 d\mathbf{x} + \int_{\Omega \setminus \Omega_{in}} (s_2(\mathbf{x}) - I_0(\mathbf{x}))^2 + \mu |\nabla s_2(\mathbf{x})|^2 d\mathbf{x} \right), \tag{2.36}
$$

where the region $\Omega_{in} \subset \Omega$ and s_1 and s_2 are two C^1 functions on Ω_{in} and on $\Omega \setminus \Omega_{in}$ respectively.

The variational problem (2.36) determines the best approximation, in the L^2 sense, of the image I_0 as a set of smooth regions represented by the function $s(x)$ such that

$$s(x) = \begin{cases} s_1(x) \text{ if } x \in \Omega_{in}, \\ s_2(x) \text{ if } x \in \Omega \setminus \Omega_{in}, \end{cases} \tag{2.37}$$

and $\partial\Omega_{in} = \partial(\Omega \setminus \Omega_{in})$ is the boundary between the smooth regions. As in the previous model, both regions Ω_{in} and $\Omega \setminus \Omega_{in}$ are represented by the Heaviside function of a level set function. This leads to the following energy:

$$F_{VC}(\phi, s_1, s_2) = \int_\Omega |\nabla H_\epsilon(\phi(\mathbf{x}))| d\mathbf{x} +$$
$$\lambda \left(\int_\Omega H_\epsilon(\phi)((s_1 - I_0)^2 + \mu|\nabla s_1|^2) d\mathbf{x} + \int_\Omega H_\epsilon(-\phi)((s_2 - I_0)^2 + \mu|\nabla s_2|^2) d\mathbf{x} \right). \tag{2.38}$$

ϕ being fixed and minimizing E_{VC} w.r.t. the functions s_1 and s_2 using the calculus of variations gives us the evolution equations of s_i and their Neumann boundary conditions:

$$\begin{cases} s_1 - I_0 = \mu\Delta s_1 \text{ in } \Omega_{in}, \\ \frac{\partial s_1}{\partial \mathcal{N}} = 0 \text{ on } \partial\Omega_{in} \cup \partial\Omega, \end{cases} \qquad \begin{cases} s_2 - I_0 = \mu\Delta s_2 \text{ in } \Omega \setminus \Omega_{in}, \\ \frac{\partial s_2}{\partial \mathcal{N}} = 0 \text{ on } \partial(\Omega \setminus \Omega_{in}) \cup \partial\Omega. \end{cases} \tag{2.39}$$

The flow minimizing Energy (2.38) is as follows:

$$\begin{aligned} \frac{\partial\phi}{\partial t} &= H'_\epsilon(\phi) \left\{ \nabla.\left(\frac{\nabla\phi}{|\nabla\phi|}\right) - \right. \\ &\left. \lambda \left((s_1 - I_0)^2 - (s_2 - I_0)^2 + \mu|\nabla s_1|^2 - \mu|\nabla s_2|^2 \right) \right\} \end{aligned} \tag{2.40}$$

This model segments and also denoises objects in images as we can see on Figure 2.14.

(a) Initial contour   (b) Final contour   (c) Image denoising
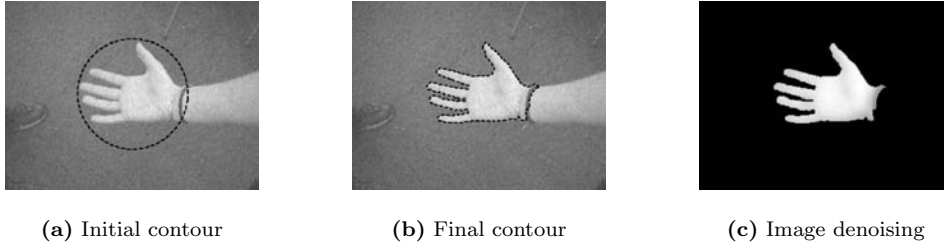
Figure 2.14: Figures (a-c) present the Vese-Chan model of active contours [179] based on the whole Mumford-Shah functional (2.31) that segmented Rosa's hand and denoised it simultaneously.

Chan-Vese also proposed to extend the 2-phase segmentation model to a higher number of regions to be segmented. In [178, 179], they defined a multiphase level set formulation which, by construction, automatically avoids the problems of vacuum and overlap. Only $\log n$ level set functions for n phases are necessary in the piecewise constant case and only two level set functions are needed to represent any partition based on the *Four-Color Theorem* [79] presented on Figure 2.15. These multiphase segmentation models can represent boundaries with triple junctions as shown on Figure 2.15. Concerning the coupling between the level set functions, Zhao-Chan-Merriman-Osher in [191] defined a variational level set approach to multiphase motion of junctions (of e.g. solid, liquid and grain boundaries) where each phase is represented by a level set function ϕ_i coupling by a term of the form $\int_\Omega (\sum_i H(\phi_i) - 1)^2 d\mathbf{x}$ which keeps the phases disjoint and avoids vacuum.

(a) Four color image   **(b)** Initial contours   **(c)** Final contours
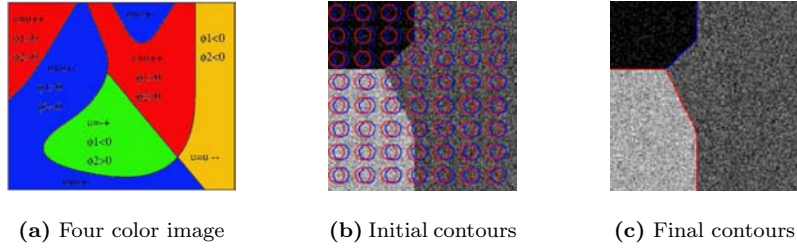
Figure 2.15: Figure (a) illustrates the Four Color Theorem [79]: all the regions in a partition can be "colored" using only four colors such that any two adjacent regions have different colors. Figures (b-c) shows the segmentation of a triple junction based on two level set functions [178, 179].

In [157], Sandberg-Chan-Vese extended the model of active contour without edges to *vector valued images* to segment texture images. They used a decomposition of the given image by the Gabor transforms and they chose in a supervised or unsupervised way the best Gabor transforms to realize the texture segmentation.

Finally, we mention that Tsai-Yezzi-Willsky [176] proposed (independently) a very similar work of Chan-Vese to segment and regularize images from the Mumford-Shah model and the curve evolution theory. The main differences between both works lie in the numerical implementations, the extraction of holes and triple points (which is done in a multiphase level set approach in Vese-Chan [178, 179]) and the extension of the model to missing data and magnification (which is not done in [178, 179]), see Figure 2.16.
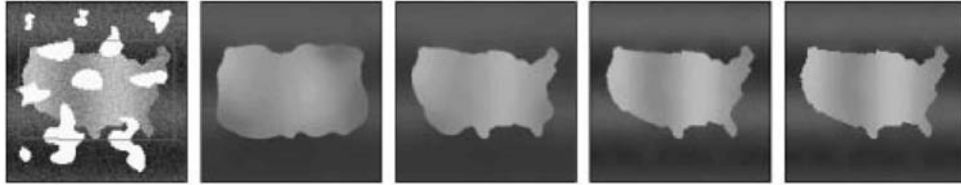
Figure 2.16: Segmentation and smoothing of an image given with regions of missing data with the model of Tsai *et al.* [176]. Note that all figures are reproduced from [176].

Contrary to the standard snake model, based on a *boundary (B) functional* s.t. $J_B(\partial\Omega) = \int_{\partial\Omega} f_B(\partial\Omega(s))ds$ where ds is the arc length/area element, all the previous region-based image segmentation models are based on a *region (R) functional* s.t. $J_R(\Omega) = \int_\Omega f_R(\mathbf{x}, \Omega)d\mathbf{x}$. Aubert-Barlaud-Faugeras-Jéhan-Besson (ABFJB) studied in [12, 13, 98, 99] the links between both types of functionals. They showed that boundary functionals are equivalent to region functionals by solving Poisson's or Helmotz's equation with well-chosen boundary conditions:

Theorem 1: (Transformation of region functionals into boundary functionals) *Let Ω be a bounded open set with regular boundary $\partial\Omega$. Let $f_R : \bar{\Omega} \to \mathbf{R}$ be a continuous function and u be the unique solution of Poisson's equation:*

$$\begin{cases} -\Delta u &= f_R \ in \ \Omega \\ u &= 0 \ on \ \partial\Omega. \end{cases} \tag{2.41}$$

Then we have the following equality:

$$\int_\Omega f_R(\mathbf{x}, \Omega) d\mathbf{x} = \int_{\partial\Omega} \nabla u \cdot \mathcal{N} ds, \qquad (2.42)$$

where $\mathcal{N}$ is the inside pointing unit normal to $\partial\Omega$.

Theorem 2: (Transformation of boundary functionals into region functionals) *Let Ω be a bounded open set with regular boundary $\partial\Omega$. Let $f_B : \bar{\Omega} \to \mathbf{R}$ be a continuous function and u be the unique solution of Helmotz's equation:*

$$\begin{cases} -\Delta u + u & = & 0 \ in \ \Omega \\ \frac{\partial u}{\partial \mathcal{N}} & = & -f_B \ on \ \partial\Omega. \end{cases} \qquad (2.43)$$

Then we have the following equality:

$$\int_{\partial\Omega} f_B(\partial\Omega(s)) ds = \int_\Omega u(\mathbf{x}, \Omega) d\mathbf{x}. \qquad (2.44)$$

Hence, image segmentation problems can be studied either through boundary functional by changing all region functionals into boundary functionals using Theorem 1 and applying standard methods of the calculus of variations to derive the corresponding Euler-Lagrange equations. The *dual approach* can also be used. Indeed, all boundary functionals can be transformed into region functionals using Theorem 2 and the tools of *shape derivatives* developed by Delfour-Zolesion [69] can be applied to derive an evolution equation of the boundary of regions to be found. This general framework can be applied to many image processing problems invoking contours or, by complementarity, regions of the corresponding contours that minimize a functional of the form:

$$F_{ABFJB}(\Omega_{in}, C) = \int_C f_B(C(s)) ds + \int_{\Omega_{in}} f_R^{in}(\mathbf{x}, \Omega_{in}) d\mathbf{x} + \int_{\Omega\setminus\Omega_{in}} f_R^{out}(\mathbf{x}, \Omega\setminus\Omega_{in}) d\mathbf{x}, \qquad (2.45)$$

where Ω_{in}, $\Omega\setminus\Omega_{in}$ are respectively the inner and the outer region of the closed active contour C, f_R^{in} and f_R^{out} are the *descriptors* of these regions and f_B is the boundary descriptor.

Applications of this general paradigm for the active contours derived from functionals including local and global measures concerning the regions to be segmented were proposed. In [12, 13], Aubert-Barlaud-Faugeras-Jéhan-Besson applied their framework to the problem of matching histograms and in [98, 99] the face segmentation in real video sequences. In [90, 91], Herbulot-Jéhan-Besson-Barlaud-Aubert (HJBBA) proposed an image segmentation model based on information theory (*entropy* and joint entropy) and non-parametric density probability estimations. Contrary to the model of geodesic active regions [132] which is based on the *parametric* assumption that all the regions in images follow a Gaussian density probability function (PDF), no particular hypothesis about the PDFs of the regions to be segmented is done such that they are *non-parametrically* estimated during the evolution process. One of the proposed functional is as follows:

$$F_{HJBBA}(\Omega_{in}, C) = \lambda \int_C ds + \mathcal{H}_e(\Omega_{in}) + \mathcal{H}_e(\Omega\setminus\Omega_{in}), \qquad (2.46)$$

where

$$\begin{cases} \mathcal{H}_e(\Omega_\zeta) = \int_{\Omega_\zeta} -q(I_0(\mathbf{x}), \Omega_\zeta) \ln q(I_0(\mathbf{x}), \Omega_\zeta) d\mathbf{x} \\ q(I_0(\mathbf{x}), \Omega_\zeta) = \frac{1}{|\Omega_\zeta|} \int_{\Omega_\zeta} G_\sigma(I_0(\mathbf{x}) - I_0(\hat{\mathbf{x}})) d\hat{\mathbf{x}} \end{cases} \ , \quad \Omega_\zeta = \Omega_{in} \ or \ \Omega\setminus\Omega_{in}, \qquad (2.47)$$

where $\mathcal{H}_e$ corresponds to the entropy to the regions Ω_{in} and $\Omega \setminus \Omega_{in}$ and G_σ is the Gaussian kernel. Then, they used shape derivatives tools [69] to derive the evolution equation of boundaries of the homogeneous regions. Their model was used to segment *one specific region* in multi-modal images. Indeed, they used a parametric representation of the contour based on the B-splines technique [144]. This allows to speed up the algorithm but it does not allow to segment more than one object. Figure 2.17 illustrates the segmentation model of Herbulot *et al.*.

(a) Initial contour   **(b)** Final contour   **(c)** Initial contour   **(d)** Final contour
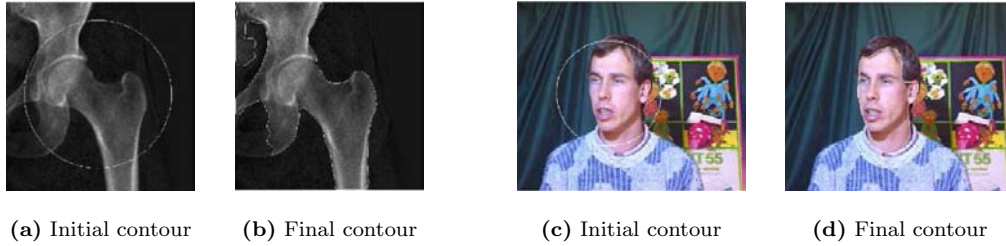
Figure 2.17: Segmentation using information theory-based models of Herbulot *et al.* [90, 91]. Figures (a-b) use Equations (2.46)-(2.47). Note that all figures are reproduced from [90, 91].

Another model based on information theory, non-parametric PDF and curve evolution theory was proposed for image segmentation by Kim-Fisher-Yezzi-Cetin-Willsky (KFYCW) in [106, 107]. They proposed to solve the segmentation problem by maximizing the mutual information (MI) between the image intensities $I_0(X)$ and the region labels $L(X)$ assuming that the probability distributions for each region is unknown and, therefore, is non-parametrically estimated during the evolution process:

$$F_{KFYCW}(C) = -MI(I_0(X); L(X)) + \alpha \int_C ds, \qquad (2.48)$$

which becomes after some computations [106]:

$$
\begin{aligned}
F_{KFYCW}(C) = \quad & \frac{1}{|\Omega_{in}|} \int_{\Omega_{in}} \log\left(\frac{1}{|\Omega_{in}|} \int_{\Omega_{in}} G_\sigma(I_0(\mathbf{x}) - I_0(\hat{\mathbf{x}}))d\hat{\mathbf{x}}\right) d\mathbf{x} + \\
& \frac{1}{|\Omega \setminus \Omega_{in}|} \int_{\Omega \setminus \Omega_{in}} \log\left(\frac{1}{|\Omega \setminus \Omega_{in}|} \int_{\Omega \setminus \Omega_{in}} G_\sigma(I_0(\mathbf{x}) - I_0(\hat{\mathbf{x}}))d\hat{\mathbf{x}}\right) d\mathbf{x} + \alpha \int_C ds,
\end{aligned}
$$

where $I_0(X)$ is the image intensity at a random location X, $L(X)$ is a binary label, $|\Omega_{in}|$ is the area of the region Ω_{in}, $\Omega \setminus \Omega_{in}$ is the complementary region, C is the boundary between Ω_{in} and $\Omega \setminus \Omega_{in}$, G_σ is Gaussian kernel coming from the non-parametric Parzen density estimate model [140], and α is a positive arbitrary parameter. Then, they derived the curve evolution equations that maximize the mutual information functional using the calculus of variations. Finally, they proposed a multiphase level set formulation to segment up to 2^m regions using m curves based on the approach of Vese-Chan. Experimental results demonstrate a very good behavior of the proposed segmentation approach as presented on Figure 2.18.

2.4.2 Shape-Based Active Contours

This section is dedicated to the identification of structures of interest which *geometric shape is given*. This topic is fundamental in the fields of computer vision and image processing since it is a core component toward e.g. automated vision systems and medical applications. We review the main variational models of active contours that use a geometric shape prior. In Chapter 5, we will propose

(a) Initial contour   **(b)** Final contour   **(c)** Initial contours   **(d)** Final contours
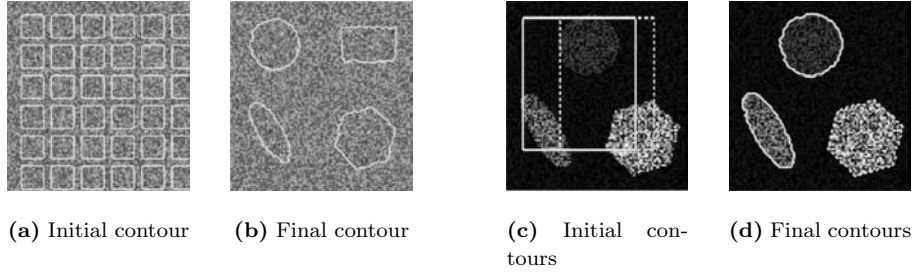
Figure 2.18: Segmentation using the information theory-based model of Kim *et al.* [106, 107]. Figures (a-b) presents the segmentation with Equations (2.48) and (2.49) of two regions having the same two first statistic moments, i.e. mean and variance, but different PDFs and Figures (c-d) show a multiphase segmentation of four regions with different intensity variances. Note that all figures are reproduced from [106, 107].

a variational model to extract structures of interest in images.

In [111, 113], Leventon-Grimson-Faugeras were the first authors to incorporate shape information into the segmentation process based on active contours intrinsically represented by a level set function. The shape model used by the authors is the *principal components analysis* (PCA) that aims at capturing the main variations of a training set while removing redundant information. In [51, 52], Cootes-Taylor used this technique on *parametric* active contours, called *deformable models*, to segment different kind of objects. The new idea proposed by Leventon *et al.* is to apply the PCA not on the parametric geometric contours but on the signed distance functions (SDFs) of these contours which are implicit and parameter free representations. They justified this choice in two ways. Firstly, SDFs provide a *stronger tolerance* than the parametric curves to slight misalignments during the alignment process of the training data since *the values of neighboring pixels are highly correlated in a SDF*. Secondly, this intrinsic contour representation improves the shape registration process in terms of robustness, accuracy and speed. Indeed, the problem of the point-wise correspondence of contours, *landmarks correspondence*, is replaced by a problem of intensity correspondence on grid points which is easier to solve. Thus, active contours defined by Leventon *et al.* evolve locally based on image gradients and curvature and globally towards the maximum a posteriori probability of position and shape of the prior shape model. However, this a posteriori probability is maximized at each iteration by an independent optimization process, which means that the final evolution equation is not a PDE since two independent stages are necessary to evolve the surface. The evolution equation is the following:

$$\phi(t+1) = \phi(t) + \lambda_1 \left(f(c+\kappa)|\nabla\phi(t)| + \langle \nabla\phi(t), \nabla f \rangle \right) + \lambda_2(\phi^\star(t) - \phi(t)), \tag{2.49}$$

where $\phi^\star$ is the shape prior and λ_1, λ_2 are positive parameters. The second term of the right-hand side of (2.49) weighted by λ_1 represents the classical term of the geodesic active contours. And the third term depending on λ_2 drives the shape of the active contour toward the shape prior given by the MAP estimation. They used their model in 2-D and 3-D synthetic and medical imagery data as shown on Figure 2.19.

In [111, 112], Leventon-Grimson-Faugeras-Wells presented a new method to incorporate prior knowledge concerning the intensity and curvature profile of a structure of interest from a training set of images and boundaries. More precisely, they defined a joint distribution between intensity value and distance to the boundaries given a distance function thanks to the Parzen non-parametric
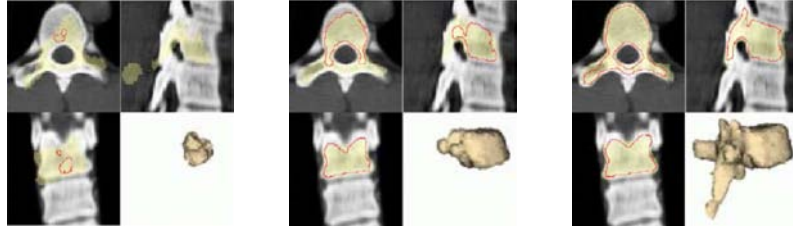
Figure 2.19: Segmentation with prior shape information [113], Equation (2.49). Evolution of a surface in 3-D and on three 2-D orthogonal slices. Note that all figures are reproduced from [113].

density estimation. They used a surface regularization term based on two statistic regularization processes, one in the local normal direction $\mathcal{N}$ and one in the tangent direction $\mathcal{T}$. Finally, the segmentation process estimates the signed distance function to the boundary of the object to be segmented by maximizing the maximum a posteriori probability:

$$P(\phi(\mathbf{x})|I_0(\mathbf{x}), \phi_{N(\mathbf{x})}) \propto P(I_0(\mathbf{x}), \phi(\mathbf{x}))P(\phi_{\mathcal{T}^+}, \phi_{\mathcal{T}^-}|\phi(\mathbf{x}))P(\phi_{\mathcal{N}^+}, \phi_{\mathcal{N}^-}|\phi(\mathbf{x})), \tag{2.50}$$

where $\phi(\mathbf{x})$ is the height of the surface (the signed distance function) at location $\mathbf{x}$, $I_0(\mathbf{x})$ is the intensity value at $\mathbf{x}$, $N(\mathbf{x})$ is the neighborhood of $\mathbf{x}$, $\phi_{\mathcal{T}^\pm}$ is the height of the surface at location $\mathbf{x} \pm \mathcal{T}$ and $\phi_{\mathcal{N}^\pm}$ is the height of the surface at location $\mathbf{x} \pm \mathcal{N}$. Their model presented good segmentation results on 2-D synthetic and magnetic resonance imagery data.

In [173, 174, 175], Tsai-Yezzi-Wells-Tempany-Tucker-Fan-Grimson-Willsky (TYWTTFGW) integrated the shape model of Leventon *et al.* [113] into region-based segmentation energy functionals to identify 3-D images containing known medical object types. In the three papers, the implicit shape prior, namely $\phi[\mathbf{v_S}, \mathbf{v_T}]$, depends on a shape vector $\mathbf{v_S}$ for the shape variations and a pose vector $\mathbf{v_T}$ for the spatial transformations. For example, in [174, 175], Tsai *et al.* defined a functional based on the reduced version of the Mumford-Shah functional proposed by Chan and Vese in [42]:

$$F_{TYWTTFGW}^1(\mathbf{v_S}, \mathbf{v_T}) = -(\frac{S_{in}^2}{A_{in}} + \frac{S_{out}^2}{A_{out}}), \tag{2.51}$$

where $A_{in} = \int_{\Omega_{in}} H(-\phi[\mathbf{v_S}, \mathbf{v_T}])d\mathbf{x}$, $S_{in} = \int_{\Omega_{in}} I_0.H(-\phi[\mathbf{v_S}, \mathbf{v_T}])d\mathbf{x}$ are the area and the sum intensity (I is the given image) in the region $\Omega_{in} = \{\mathbf{x} \in \mathbf{R}^2 | \phi(x,y) > 0\}$ and $A_{out} = \int_{\Omega_{out}} H(\phi[\mathbf{v_S}, \mathbf{v_T}])d\mathbf{x}$, $S_{out} = \int_{\Omega_{out}} I_0.H(\phi[\mathbf{v_S}, \mathbf{v_T}])d\mathbf{x}$ are the area and the sum intensity in the region $\Omega_{out} = \Omega \setminus \Omega_{in} = \{\mathbf{x} \in \mathbf{R}^2 | \phi(x,y) < 0\}$. Parameters $\mathbf{v_S}$ and $\mathbf{v_T}$ that optimize the segmentation energy functional (2.51) are given by two gradient descents.

In [175], Tsai *et al.* also proposed two other segmentation energies, coming from Yezzi *et al.* in [187], which use the image mean and the image variance to partition an image into two homogeneous regions. Figure 2.20 illustrates the energy based on the image variance.

Finally, they proposed in [173] to extend their segmentation model to a multiple segmentation of shapes and to a mutual information-based functional proposed by Kim *et al.* in [106, 107] (see Section 2.4.1):

$$F_{TYWTTFGW}^2(\mathbf{v_S}, \mathbf{v_T}) = -MI(I_0(X); L(X)) \tag{2.52}$$

$$\sim \left(\sum_{i=1}^{N_R} P_{\Omega_i}\hat{h}(I_0|L = \Omega_i)\right) + P_{\Omega_c}\hat{h}(I_0|L = \Omega_c), \tag{2.53}$$

(a) Original image   **(b)** Image surrounded by line clutter   **(c)** Image (b) with noise   **(d)** Initial contour   **(e)** Final contour
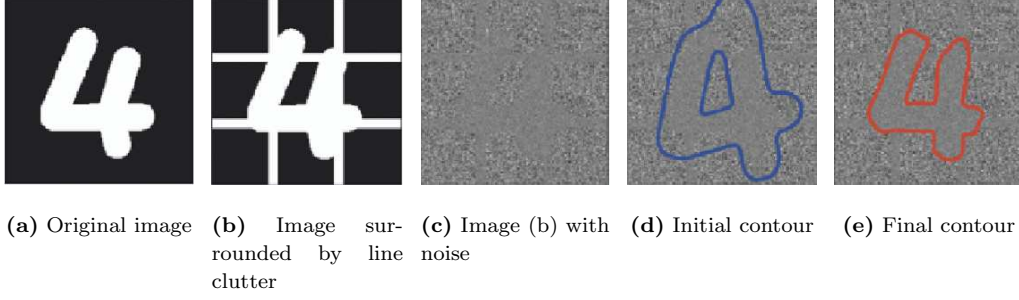
Figure 2.20: Segmentation of a noisy number four using the model [175]. Note that all figures are reproduced from [175].

where $MI(I_0(X); L(X))$ is the mutual information between the image pixel I_0 and the segmentation label L at a random location X, $N_R + 1$ is the number of regions handled with this segmentation model, P_{Ω_i} denotes the prior probability of pixel values in the i-th region Ω_i, P_{Ω_c} is the prior probability of pixel values in Ω_c (the area outside of the N_R regions), $\hat{h}(.|.)$ denotes the estimate of the conditional entropy which is estimated using the non-parametric Parzen density estimation method [140] to compute these densities from the training data as proposed by Kim *et al.* [106, 107]:

$$\begin{cases} \hat{h}(I_0|L = \Omega_i) = -\frac{1}{|\Omega_i|} \int_\Omega \log(\hat{p}_{\Omega_i}(I_0(\mathbf{x}))) H(-\phi_i(\mathbf{x})) d\mathbf{x} \\ \hat{h}(I_0|L = \Omega_c) = -\frac{1}{|\Omega_c|} \int_\Omega \log(\hat{p}_{\Omega_c}(I_0)) H(\phi_i(\mathbf{x})) d\mathbf{x} \end{cases}, \qquad (2.54)$$

where $\hat{p}_{\Omega_i}(I_0)$ and $\hat{p}_{\Omega_c}(I_0)$ are estimates of the probability density functions of I_0 in regions Ω_i and Ω_c, $|\Omega_i|$ and $|\Omega_c|$ are the areas of Ω_i and Ω_c, ϕ_i is the level set function of region Ω_i and H is the Heaviside function. Finally, the shape vector $\mathbf{v_S}$ and the pose vector $\mathbf{v_T}$ are determined by two gradient descents.

In [45, 46], Chen-Thiruvenkadam-Tagare-Huang-Wilson-Geiser (CTTHWG) designed a variational model that incorporates prior shape knowledge into the geometric/geodesic active contours which detect edges from the image gradient. Contrary to Leventon-Grimson-Faugeras-Wells' approach [113], the shape prior of Chen *et al.* only uses the first geometric moment: the mean. Indeed, the prior is given by the *average shape* of a training set of rigidly aligned parametric curves. However, the variational approach of Chen *et al.* is mathematically justified by the proof of the existence of a solution to the energy minimization problem. This mathematical justification is not possible with the probabilist approach of Leventon *et al.*. The energy functional of *et al.* which is minimized once the active contour has captured high image gradients and formed a shape close to the prior model of the object to be segmented is as follows [45, 46]:

$$F^1_{CTTHWG}(C, \mu, \theta, T) = \int_0^1 \left(f(|\nabla I_0(C(p))|) + \frac{\lambda}{2} d^2_{C^\star}(\mu R_\theta C(p) + T) \right) |C_p| dp, \qquad (2.55)$$

where C is the active contour, (μ, θ, T) are the parameters of a rigid transformation (scale, orientation and translation), R_θ is the rotation matrix, f is an edge detecting function, $d^2_{C^\star}(\mathbf{x}) = d^2(C^\star, \mathbf{x})$ is the square distance of the point $\mathbf{x}$ from $C^\star$, the target shape and $\lambda > 0$ a parameter. They also presented a level set formulation of the energy functional (2.55):

$$F^1_{CTTHWG}(\phi, \mu, \theta, T) = \int_\Omega \left(f(|\nabla I_0(\mathbf{x})|) + \frac{\lambda}{2} d^2_{C^\star}(\mu R_\theta \mathbf{x} + T) \right) \delta(\phi(\mathbf{x})) |\nabla \phi| d\mathbf{x}, \qquad (2.56)$$

Their model showed a good ability to extract real-world structures in 2-D ultrasound and fMRI images in which the complete boundary was either missing or had low resolution and bad contrast. In [44], they incorporated in the previous variational segmentation model prior fixed locations of a small number of points which can be given e.g. by a medical expert. The new variational model is as follows:

$$
\begin{aligned}
F^2_{CTTHWG}(\phi, \mu, \theta, T) &= \int_\Omega \left(f(|\nabla I_0(\mathbf{x})|) + \frac{\lambda}{2} d^2_{C^\star}(\mu R_\theta \mathbf{x} + T) \right) \delta(\phi(\mathbf{x})) |\nabla \phi| d\mathbf{x} \\
&\quad + \frac{\alpha}{2} \int_\Omega g_\sigma(\mathbf{x}) \phi^2(\mathbf{x}) d\mathbf{x},
\end{aligned} \tag{2.57}
$$

where g_σ is equal to the convolution of g and G_σ, g being a function taking value 1 on the prior points and 0 elsewhere and G_σ is the standard Gaussian kernel. The two first terms constraint the active contour being on the location where the magnitude of image gradient is high and forming a shape similar to the prior. Finally, the last term forces the interface passing through the given points. Figure 2.21 illustrates the segmentation of an endocardium image without and with a set of prior points.

(a) Minimization of F^1_{CTTHWG}

(b) Minimization of F^2_{CTTHWG}
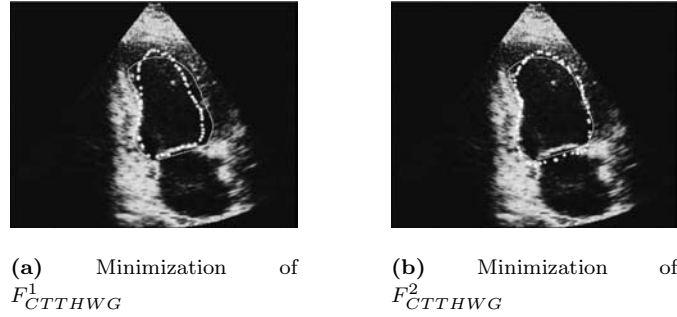
Figure 2.21: Figures (a-b) presents the segmentation of an endocardium image using the models [44, 45, 46]. Figure (a) is given by the model [45, 46], the solid contour is the expert's contour and the dotted contour is the contour minimizing F^1_{CTTHWG}, Equation (2.55). Figure (b) shows the result provided by the model [44], solid contour is the expert's contour and the dotted contour is the contour minimizing F^2_{CTTHWG}, Equation (2.57). Energy F^2_{CTTHWG} is better than F^1_{CTTHWG} since it uses a set of prior points given e.g. by a medical expert. Note that all figures are reproduced from [44].

In [135, 137, 138], Paragios-Rousson-Ramesh (PRR) defined a variational framework to perform a rigid-invariant registration of level set-based geometric shapes. Indeed, they used the level set representation to represent shapes and to register them globally (with a rigid transformation) and locally (thanks to a local deformation field). The optimization matching criterion is the sum of square differences and the definition of this criterion is invariant w.r.t. translation, rotation and scaling:

$$
\begin{aligned}
F^1_{PRR}(\mu, \theta, T, (U, V)) &= \alpha \int_\Omega N_{\delta_1}(\phi_D, \phi_S)(\mu \phi_D - \phi_S(A))^2 d\mathbf{x} \\
&\quad + (1 - \alpha)\beta \int_\Omega N_{\delta_2}(\phi_D, \phi_S)(\mu \phi_D - \phi_S(A - (U, V)))^2 d\mathbf{x} \\
&\quad + (1 - \alpha)(1 - \beta) \int_\Omega N_{\delta_2}(U_x^2 + U_y^2 + V_x^2 + V_y^2) d\mathbf{x}, \tag{2.58}
\end{aligned}
$$

where (μ, θ, T) are the parameters (scale, angle and translation) of a global rigid deformation between S, the shape source, and D, the shape target represented by two signed distance functions ϕ_S and ϕ_D, $A = \mu R_\theta \mathbf{x} + T$, (U, V) is a local deformation field (non-rigid deformation), N_δ is a binary function such that $N_\delta(\phi_1, \phi_2) = 1$ for $\min(|\phi_1|, |\phi_2|) \geq \delta$ and 0 otherwise. Paragios *et al.* interpreted Energy (2.58) in [138]. The first term of the energy aims at finding pixel-wise intensity correspondences according to a global motion model (rigid transformation). The second term has the objective to correct the correspondences in the pixel level using a local deformation field on top of the existing global model, while the third term constrains these deformations to be locally smooth. Paragios *et al.* demonstrated the efficiency of their registration model on synthetic results which exhibit large global motions as well as important local deformations, see Figure 2.23 as example.

Figure 2.22: Global-to-local registration with Equation (2.58) given in [138]. Note that all figures are reproduced from [138].

They also considered the registration process between a shape and a shape target with local degrees of variability. This shape model can be built from a training set of N_s aligned signed distance functions ϕ_i representing the shape of interest. They estimated a mean (M) shape image $\phi_M(\mathbf{x})$ and a map of local shape deformations $\sigma_S(\mathbf{x})$ from a variational minimization model as follows:

$$
\begin{aligned}
F_{PRR}^2(\phi_S, \sigma_S) &= \alpha \sum_{i=1}^{N_s} \int_\Omega \log[p_S(\phi_i(\mathbf{x}))]d\mathbf{x}, \\
&\quad + (1-\alpha) \int_\Omega \left[\left(\frac{\partial \sigma_S(\mathbf{x})}{\partial x} \right)^2 + \left(\frac{\partial \sigma_S(\mathbf{x})}{\partial y} \right)^2 \right] d\mathbf{x}, \quad (2.59)
\end{aligned}
$$

$$
p_S(\phi(\mathbf{x})) = \frac{1}{\sqrt{2\pi}\sigma_S(\mathbf{x})} \exp\left[-\frac{(\phi(\mathbf{x}) - \phi_M(\mathbf{x}))^2}{2\sigma_S^2(\mathbf{x})} \right], \quad (2.60)
$$

subject to the constraint: $\quad |\nabla\phi_M(\mathbf{x})|^2 = 1 \quad \forall \mathbf{x} \in \Omega.$ $\quad (2.61)$

Figure 2.23 illustrates this statistical shape model. And in [136], they used the previous statistical shape model to segment the left ventricle in Magnetic Resonance images with a modified version of the geodesic active regions defined in [132].

In [153, 154], Rousson-Paragios-Deriche (RPD) integrated the active shape model of Cootes *et al.* [52] into the level set framework. More precisely, they applied the principal components analysis on the level set functions embedding the training contours of an object of interest as Leventon *et al.* did in [113]. This allows them to represent variations of shapes with complex topologies such as the left ventricle over a cardiac cycle composed by two separated objects [153] or the two brain ventricles [154]. The functional proposed by the authors to realize the shape registration is as follows:

$$
F_{RPD}(\phi, \mathbf{v_S}, \mathbf{v_T}) = \int_\Omega \delta_\epsilon(\phi) \left(\mu\phi - \left(\phi_M(\mathbf{v_T}) + \sum_{i=1}^{N_s} v_{Si} \, \phi_{V_i}(\mathbf{v_T}) \right) \right)^2 d\mathbf{x}, \quad (2.62)
$$

(a) Training samples   (b) Aligned train- (c) Mean shape (d) Variance func-
ing shapes $\{\phi_i =$ function $\phi_M(\mathbf{x})$ tion $\sigma_S(\mathbf{x})$
$0\}$
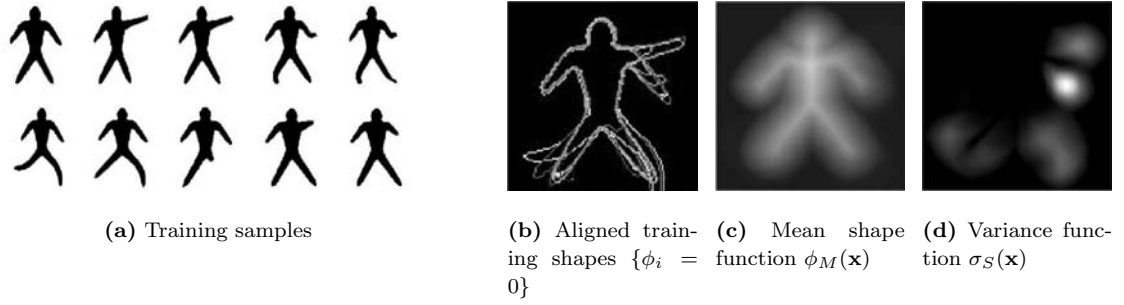
Figure 2.23: Shape prior model determined by Equations (2.59)-(2.61) in [135, 138]. Note that all figures are reproduced from [135].

where ϕ is the level set function embedding the evolving interface, $\delta_\epsilon(.)$ is an approximation of the Dirac function, $\mathbf{v_T} = (\mu, \theta, T)$ models a rigid transformation, $\mathbf{v_S} = (v_{S1}, \ldots, v_{SN_s})$ are the weight factors of the eigenmodes of variation (V) $(\phi_{V_1}, \ldots, \phi_{V_{N_s}})$ determined by the PCA on the training set of the object of interest and ϕ_M is an approximation of the mean (M) shape of the level set functions embedding the training data subject to the constraint that ϕ_M is a true signed distance function.

The energy functional (2.62) is minimized using two flows: one minimizing flow for the level set function ϕ and one minimizing flow for the parameters of the global rigid transformation $\mathcal{A}$. Finally, the shape weights λ are optimally estimated by solving a linear system. The variational formulation of the registration process allows them to combine it with variational segmentation models such as the geodesic/geometric active contour model [35, 105] or the geodesic active region model [132] to simultaneously realized the registration/segmentation tasks, which gives promising experimental results in 2-D and 3-D images, see Figure 2.24.
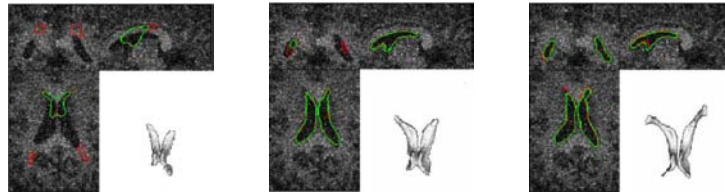
Figure 2.24: Segmentation of lateral Brain ventricles with shape prior of a noisy MR image using Equation (2.62) from [153, 154]. Evolution of a surface in 3-D and three 2-D orthogonal slices. Surface cuts are in green and their projection in the shape space in red. Note that all figures are reproduced from [154].

In [93, 94], Huang-Paragios-Metaxas (HPM) proposed a global-to-local registration method that integrates statistical and variational techniques. They used a distance functions to implicitly represent shapes and the mutual information is considered as a global registration criterion:

$$F^1_{HPM}(A(\mathbf{v_T})) = -MI(\phi_S, \phi_T(A)) = -\int_\Omega p_{\phi_S,\phi_T}(\zeta_1, \zeta_2) \log \frac{p_{\phi_S,\phi_T}(\zeta_1, \zeta_2)}{p_{\phi_S}(\zeta_1)p_{\phi_T}(\zeta_2)} d\zeta_1 d\zeta_2 \quad (2.63)$$

$$p^{\phi_S,\phi_T}(\zeta_1, \zeta_2) = \alpha \int_\Omega G_\sigma(\zeta_1 - \phi_S(\mathbf{x}), \zeta_2 - \phi_T(A(\mathbf{v_T}; \mathbf{x}))) d\mathbf{x}, \quad (2.64)$$

where $\mathbf{v_T}$ is the vector of parameters of a parametric global transformation A such as a rigid, affine, homographic or quadratic transformation, $MI(\phi_S, \phi_T(A))$ is the mutual information between ϕ_S and $\phi_T(A)$ where ϕ_S and ϕ_T are the distance representations of the shape source (S) and the shape target (T), p_{ϕ_S}, p_{ϕ_T} and p_{ϕ_S,ϕ_T} correspond to the probability density in ϕ_S, in $\phi_T(A)$ and the joint density, G_σ is a 2-D Gaussian kernel and α is a normalization constant.

The local correspondences are recovered by a B-spline approximation of grid within a free-from deformation criterion that guarantees a one-to-one mapping:

$$F^2_{HPM}(\Theta) = \int_\Omega (\phi_T(A(\mathbf{x})) - \phi_S(L(\Theta; \mathbf{x})))^2 d\mathbf{x} \tag{2.65}$$

$$L(\Theta; \mathbf{x}) = \mathbf{x} + \delta L(\Theta; \mathbf{x}) = \sum_{k=0}^{3} \sum_{l=0}^{3} B_k B_l (P^0_{i+k,j+l} + \delta P_{i+k,j+l}), \tag{2.66}$$

where ϕ_S and $\phi_T(A)$ are the implicit representations of the source shape S and the transformed target shape T, L is the local deformation field, $P^0_{m,n}$ and $\delta P_{m,n}$ are the control point (m, n) on the grid and the deformation of the control point (m, n), $\Theta = (\delta P^x_{m,n}, \delta P^y_{m,n})$ is the deformation of the control points in x and y directions and B_k is the kth basis function of a Cubic B-spline (B_l is similarly defined).

Hence, their registration model benefits to the advantages of implicit representations, i.e. the robustness w.r.t. noise, the extension to higher dimensions and the handling of complex shapes with e.g. occlusions, missing parts and strong local variations. Figure 2.25 shows an example of registration.

| (a) | (b) | (c) | (d) | (e) |
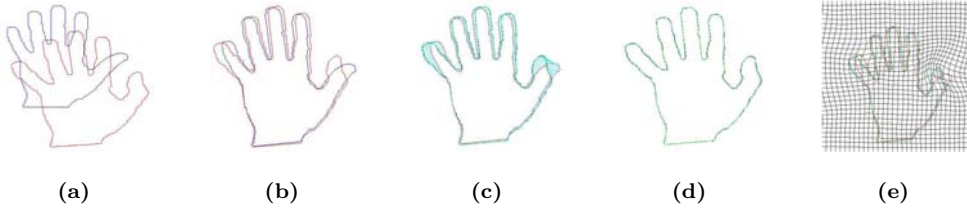
Figure 2.25: Registration of structures defined in [93, 94]. Figure (a) presents the initial contours. Figure (b) shows the global alignment using mutual information, Equations (2.63) and (2.64). Figure (c) establishes correspondences with B-splines free-form deformations and Figure (d) is the local registration. Finally, Figure (e) presents the grid deformation. Note that all figures are reproduced from [94].

Their method also deals with *open contours* since they used a distance function to represent contours and not a signed distance function. Finally in [93], the authors demonstrates the efficiency of their alignment method to solve the correspondence problem in systolic left ventricle in ultrasonic images.

In [62, 66, 67], Cremers-Tischhäuser-Weickert-Schnörr (CTWS) modified the Mumford-Shah functional and its cartoon limit to segment known object types in a variational framework. They proposed to add a quadratic shape energy to "convexify" the Mumford-Shah functional which has, in general, a non-convex dependency w.r.t. the contour. The shape energy is as follows:

$$F_{CTWS}(C) = -\log(P(C)) + \text{const.} \tag{2.67}$$

$$P(C) \propto \exp\left(-\frac{1}{2}(C - C_M)^t \Sigma_\perp^{-1} (C - C_M)\right), \tag{2.68}$$

where $C = (x_1, y_1, \ldots, x_N, y_N)$ represents the contour *parametrized* by a vector of N control points, $P(C)$ is a Gaussian probability distribution defined by a mean (M) control point vector C_M and a

covariance matrix Σ estimated from a training set of the object of interest. We notice that Cremers *et al.* used a parametric formulation of the contour which is numerically implemented with a quadratic B-spline technique. This contour formulation is faster than an intrinsic formulation but it decreases the degree of variation and does not allow changes of topology. The shape energy (2.68) is then modified to be invariant to rigid transformation (translation, rotation and scale) and it is added to the following modified Mumford-Shah energy:

$$F_{MS}^{CTWS}(I, C) = \frac{1}{2} \int_{\Omega} (I - I_0)^2 d\mathbf{x} + \lambda^2 \frac{1}{2} \int_{\Omega} w_c(x) |\nabla I|^2 d\mathbf{x} + \nu L(C), \qquad (2.69)$$

where I is the piecewise-smooth approximation of the given image I_0, C is the contour of the smooth regions, $L(C)$ is the length of the contour C and w_c is an indicator function such that $w_c(\mathbf{x}) = 0$ if $\mathbf{x} \in C$ and 1 otherwise. The flow minimizing F_{MS}^{CTWS} w.r.t. u is given by the following inhomogeneous diffusion process:

$$\frac{\partial I}{\partial t} = \nabla.(w_c \nabla I) + \frac{1}{\lambda^2}(I_0 - I), \qquad (2.70)$$

which gave rise to the term *diffusion snake* by the authors [62, 66]. Experimental results show that the proposed model efficiently segment known 2-D objects in presence of misleading information due to noise, occlusion and strongly cluttered background as we can see on Figure 2.26.
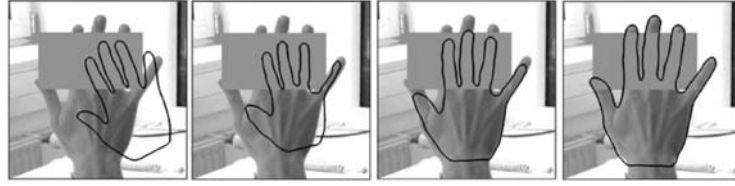
Figure 2.26: Contour evolution with a statistical shape prior based on the model of Cremers *et al.* [62, 66]. The segmentation model can deal with occlusion. Note that all figures are reproduced from [66].

Equation (2.68) implicitly makes the assumption that the probability density function of the shape of interest is Gaussian which can be limited in some situations. In [58, 59, 67], Cremers-Kohlberger-Schnörr (CKS) extended the linear shape model of [62, 66] to a nonlinear statistic model. The nonlinear statistic shape model is computed from a training set by a new method of density estimation which can be considered as an extension of kernel PCA to a probabilistic framework. More precisely, Cremers *et al.* applied a nonlinear mapping to the training data in order to represent them in a higher-dimensional feature space where the training data are supposed to form a Gaussian distribution. If $C_1, \ldots, C_{N_s} \in \mathbf{R}^n$ is a given set of training data and ω is a nonlinear mapping from the input space to a higher-dimensional space Y. The mean and the covariance matrix of the mapped training data are given by

$$\omega_M = \frac{1}{N_s} \sum_{i=1}^{N_s} \omega(C_i), \qquad (2.71)$$

$$\tilde{\Sigma}_\omega = \frac{1}{N_s} \sum_{i=1}^{N_s} (\omega(C_i) - \omega_M)(\omega(C_i) - \omega_M)^t, \qquad (2.72)$$

and the new shape energy is defined by

$$F_{CKS}(C) \;=\; \tilde{\omega}(C)^t \, \Sigma_\omega^{-1} \, \tilde{\omega}(C), \tag{2.73}$$

$$= \; \sum_{k=1}^{r} \left(\sum_{i=1}^{N_s} \alpha_i^k \tilde{k}(C_i, C) \right)^2 \cdot (\lambda_k^{-1} - \lambda_\perp^{-1}) + \lambda_\perp^{-1} \cdot \tilde{k}(C, C), \tag{2.74}$$

where $\tilde{\omega}(C) = \omega(C) - \omega_M$, Σ_ω is a regularized covariance matrix obtained by replacing all zero eigenvalues of the matrix $\tilde{\Sigma}_\omega$ by a constant $\lambda_\perp$, $\tilde{k}(.,.) := (\tilde{\omega}(.), \tilde{\omega}(.))$ denotes the corresponding scalar product in Y by the Mercer kernel [53], r is the number of nonzero eigenvalues λ_k of the covariance matrix $\tilde{\Sigma}_\omega$ and α_i^k are the expansion coefficients obtained in terms of eigenvalues and eigenvectors of a kernel matrix given in [59]. Applications of the proposed method in segmentation and tracking of 2-D and 3-D objects shows the ability of the nonlinear shape model to segment different complex real-world shapes in presence of noise, clutter, occlusion and misleading information as shown on Figure 2.27.

(a)   Aligned contours   **(b)**   Single Gaussian   **(c)** Mixture of Gaussians   **(d)**   Feature space Gaussian   **(e)** Segmentations with prior
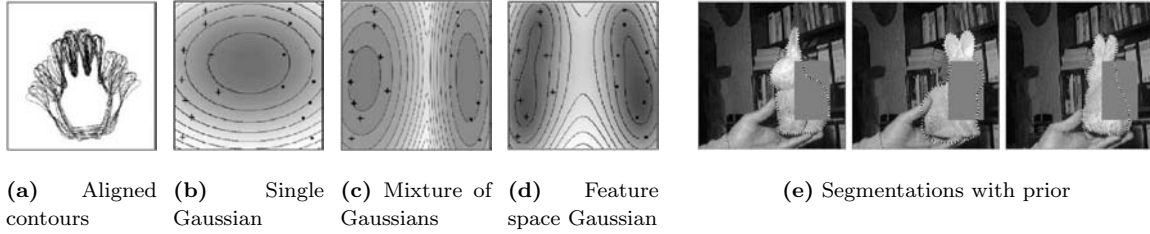
Figure 2.27: Figures (b-d) compares different models of density estimation. Figure (d) presents the density estimation in the feature space and produces level lines which are not necessary ellipses as in the case of Gaussians. Figure (e) shows three contours from a tracking sequence in the presence of occlusion. Note that all figures are reproduced from [59].

In [63], Cremers-Soatto (CS) proposed a novel dissimilarity measure for shapes implicitly represented by the signed distance function. It has the main advantage to be symmetric compared to previous presented measures in this Section which allows them to segment corrupted images of known objects which consist of multiple components, see Figure 2.28. Their *symmetric* dissimilarity measure, not biased toward small areas, is defined as follows:

$$d_{CS}^2(\phi_1, \phi_2) \;=\; \int_\Omega (\phi_1 - \phi_2)^2 \, \frac{f(\phi_1) + f(\phi_2)}{2} d\mathbf{x}, \tag{2.75}$$

$$f(\phi) \;=\; \frac{H(\phi)}{\int_\Omega H(\phi) d\mathbf{x}}, \tag{2.76}$$

where $H(.)$ is the Heaviside function. Finally, the measure (2.75) is a pseudo-distance since it does not satisfy the triangle inequality.

In [60, 61], Cremers-Osher-Soatto (COS) dealt with the problem of image segmentation with statistical shape priors in the level set framework. They defined a shape dissimilarity measure invariant w.r.t. translation and scaling, which avoid to compute them by gradient flows that are local optimization methods that require appropriate time steps. Then, they proposed a new statistical shape measure based on Parzen-Rosenblatt [140, 148] density estimation in the level set domain

(a) Initial contour

(b) Final contour with asymmetric measure

(c) Final contour with symmetric measure
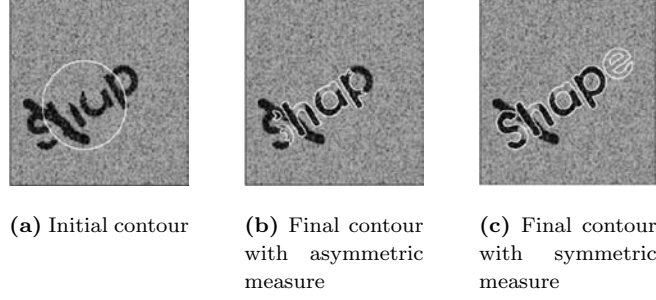
Figure 2.28: Figure (c) presents the advantage of using a symmetric dissimilarity measure compared to a asymmetric measure on Figure (b). The asymmetric measure is not able to propagate the shape information outside the initial shape area. Note that all figures are reproduced from [63].

such that:

$$P_{COS}(\phi) \quad \propto \quad \frac{1}{N_s} \sum_{i=1}^{N_s} \exp\left(-\frac{1}{2\sigma^2} d^2(H\phi, H\phi_i)\right), \tag{2.77}$$

$$d^2(H\phi_1, H\phi_2) \quad = \quad \int_\Omega (H(\phi_1(\mathbf{x})) - H(\phi_2(\mathbf{x})))^2 d\mathbf{x}, \tag{2.78}$$

where $\phi_{i=1,\ldots,N}$ are the N training shapes, σ is the kernel width of the Parzen-Rosenblatt method, $H\phi$ is the Heaviside function applied to the level set function ϕ and d is a symmetric difference measure. Their segmentation model is formulated in the Bayesian framework, hence the segmentation process is seen as maximizing the conditional probability:

$$P(\phi|I_0) = \frac{P(I_0|\phi)P(\phi)}{P(I_0)} \tag{2.79}$$

with respect to the level set function ϕ which is equivalent to minimizing the negative log-likelihood:

$$F_{COS}(\phi) = \frac{1}{\alpha}F_{ACWE}(\phi) + F_{shape}(\phi) \tag{2.80}$$

with $\alpha > 0$ and $F_{shape}(\phi) = -\log P_{COS}(\phi)$ and F_{ACWE} is the energy of Chan-Vese given by Equation (2.32). They successfully applied their segmentation method to track a walking person partially occluded, see Figure 2.29.

In [64, 65], Cremers-Sochen-Schnörr (CSS) defined a variational approach based on the level set representation for integrating multiple shape priors in the segmentation task. For this, they introduced a *labeling function* which indicates *where* to apply *which* prior. This function is simultaneously optimized with the level set function to jointly segment and partition the image domain between the objects of interest. The energy functional proposed in [65] to encode N_R different regions is:

$$F_{CSS}(\phi, \mathbf{L}) = \sum_{i=1}^{N_R-1} \int_\Omega \frac{(\phi - \phi_i)^2}{\sigma_i^2} \chi_i(\mathbf{L}) d\mathbf{x} + \int_\Omega \lambda^2 \chi_{N_R}(\mathbf{L}) d\mathbf{x} + \gamma \sum_{i=1}^{N_R} \int_\Omega |\nabla H(L_i)| d\mathbf{x}, \tag{2.81}$$

where ϕ is the level set function, $\mathbf{L}(\mathbf{x}) = (L_1(\mathbf{x}), \ldots, L_n(\mathbf{x})), \mathbf{x} \in \Omega, L_j \in \{+1, -1\}$ is the vector-valued labeling function such that $N_R = 2^n$, $\chi_i, i = 1, \ldots, N_R$ correspond to the indicator function for each label region and each ϕ_i corresponds to a particular known shape with its variance given by σ_i. Experimental results demonstrate the performance of their approach since it allows them to
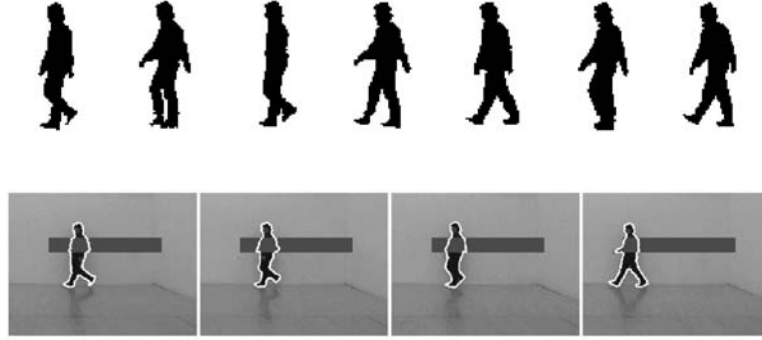
Figure 2.29: Segmentation given by minimizing Energy (2.80) defined in [60, 61]. The first row represents the sample training shapes and the second row shows the segmentation of a sequence of a walking person using a prior shape information. Note that all figures are reproduced from [61].

(a) Initial contour   (b) Final contour without prior   (c) Final contour with prior in yellow
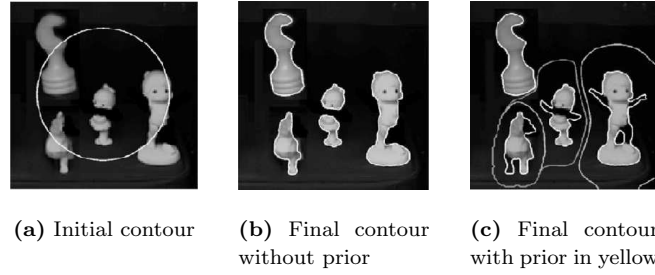
Figure 2.30: Evolution of the segmentation with multiple dynamic labeling given by Equations (2.81) in [65]. Figure (c) presents the final active contours in yellow and the final labeling contours in blue. Note that all figures are reproduced from [65].

segment multiple independent objects in an image as we can see on Figure 2.30.

Let us finally mention the paper [147] of Riklin Raviv-Kiryati-Sochen which addresses the problem of general *projective transformations* between a prior shape and an image to be segmented in the level set framework.

2.5 Variational Models and Partial Differential Equations for Image Denoising/Enhancing

Since fifteen years, partial differential equations (PDEs) and variational models have been more and more used to perform image restoration. As we said in Section 1.2, one of the main reasons to use PDEs in image analysis is to work in the *continuous* domain to become grid-independent and isotropic. Before that, the signal/image processing had been done with filters, i.e. in the *discrete* domain. The link between both approaches is to see PDEs as the iteration of local filters with an infinitesimal neighborhood [158]. This novel view of image analysis proposes two main advantages. Firstly, the continuous approach is independent w.r.t. the grid. Secondly, PDEs are well-founded mathematical domains, which allows us to generalize classical methods, classify and create PDEs according to conditions of causality, regularity, morphological invariance, affine invariance, locality, etc. [4].

The original idea to use PDEs in image analysis started with Gabor in 1965 [80] who noticed that the difference between the original and the blurred image is roughly proportional to its Laplacian [87]. If we call G_h the Gaussian blur kernel with the scale parameter h and the given image $I_0 \in L^1(\Omega \subset \mathbf{R}^2)$, then

$$\frac{I_0 * G_h(x) - I_0(x)}{h} \propto \Delta I_0(x), \tag{2.82}$$

where $*$ stands for the convolution operator. Hence, when h gets smaller, the blur process (2.82) looks more and more like the *linear isotropic heat diffusion equation*:

$$\begin{cases} \frac{\partial I}{\partial t} = \Delta I & (t > 0) \\ I = I_0 & (t = 0) \end{cases} \tag{2.83}$$

In 1983-1984, Witkin [185] and Koenderink [109] proposed to formalize the smoothing process in image analysis by introducing the notion of *scale space* which generally corresponds to the representation of images at different levels/scales of observation. In their work, the multiple representation of images is obtained by applying the simplest diffusion flow (2.83) to the original image. In [97], Hummel defined a scale space as an evolution equation that satisfies the *maximum principle* which basically states that the maximum of the solution of a certain class of PDEs is obtained at the spatial or the temporal boundaries of the PDE domain [145, 158]. This principle is useful to prove the uniqueness of solutions and other properties. In the case of parabolic PDEs (2.83), the maximum principle states that [184]:

$$\inf_{x \in \Omega} I_0 \leq I(t) \leq \sup_{x \in \Omega} I_0, \ \forall t > 0 \tag{2.84}$$

In a general way, analytic solutions do not exist for all PDEs. However, there exists an analytic solution for the image smoothing PDE (2.83):

$$\begin{cases} I = G_{\sqrt{2t}} * I_0 & (t > 0) \\ I = I_0 & (t = 0) \end{cases} \tag{2.85}$$

where G_σ is the Gaussian kernel with standard deviation σ. In other words, the Gaussian convolution (2.85) and the linear diffusion flow (2.83) are equivalent when $\sigma = \sqrt{2t}$.

Recently, Weickert-Ishikawa-Imiya in [183] discovered that the previous linear scale space was determined by Iijima in 1962 using 5 axioms: linearity, translation invariance, scale invariance, semi-group property and positive preservation.

In fact, the linear/Gaussian scale space has been deeply studied and widely used in image processing not only to regularize images but also to detect edges by the zero-crossings of the Laplacian of a Gaussian, see the work of [119].

We apply the linear heat diffusion flow (2.83) on Figure 2.31.

| **(a)** Original Image | **(b)** scale s_1 | **(c)** scale $s_2 > s_1$ |
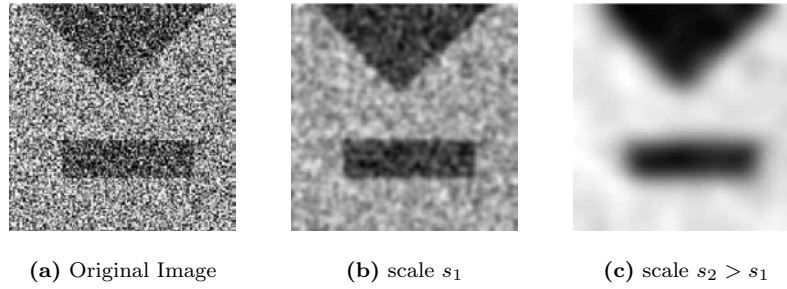
Figure 2.31: Scale space produced by the linear isotropic diffusion equation (2.83). The noise has been removed but the location of edges have been lost at the same time.

It is interesting to notice here that the smoothing equation (2.83) is actually a *diffusion equation* based on a physical process. The analogy between physics and image processing is done as the following way. The image intensity (grey-level, color, etc.) I is seen as a physical variable such as temperature. The existence of a concentration gradient ∇I creates a flux according to the *first Fick/diffusion law* in order to equilibrate the concentration differences in the diffusing medium Ω:

$$J = D \cdot \nabla I, \tag{2.86}$$

where D is the diffusion tensor which characterizes the diffusing medium and which determines the type of diffusion processes we apply on images. It is reasonable to think that the quantity of image intensities remains unchanged in Ω, in other words, the *mass conservation* hypothesis is valid. Hence, the temporal variation of I inside Ω is equal to the flux of I across the boundary of Ω:

$$\frac{\partial}{\partial t} \iint_\Omega I \, d\mathbf{x} = \int_{\partial \Omega} J \cdot \mathcal{N} \, ds = \iint_\Omega \nabla \cdot J \, d\mathbf{x}, \tag{2.87}$$

$$\Longrightarrow \iint_\Omega \left(\frac{\partial I}{\partial t} - \nabla \cdot (D \cdot \nabla I) \right) d\mathbf{x} = 0, \tag{2.88}$$

thanks to the *Navier-Stokes equation*, which implies the *second Fick/diffusion law*:

$$\frac{\partial I}{\partial t} = \nabla \cdot (D \cdot \nabla I), \tag{2.89}$$

which is the general diffusion equation in physics (up to the density function equal to 1).

In the context of diffusion equations, the smoothing flow (2.83) is obtained when the diffusion matrix D is reduced to a scalar. Thus, the flux J is parallel to ∇I which means that the diffusion is *isotropic* [184]. Despite of many advantages of the linear heat flow (2.83), this one presents two main shortcomings: it blurs everything in images, the noise but also the edges as we can see on Figure 2.31, then it can create new extrema for signals N-D, $N \geq 2$. The solution of both drawbacks is to extend the linear isotropic diffusion equation (2.83) to *nonlinear anisotropic* ones.

In this direction, Perona-Malik in [141] proposed a PDE-based model to denoise images while keeping edges well-localized. They chose a scalar-valued diffusion matrix $D = f(|\nabla I|^2)$ such that the diffusion equation is equal to:

$$\frac{\partial I}{\partial t} = \nabla \cdot (f(|\nabla I|^2)\nabla I), \tag{2.90}$$

where f is called the diffusivity function, e.g. $f(\zeta) = \frac{1}{1+\zeta/\lambda}$. The diffusion process defined by Equation (2.90) is *anisotropic* since the diffusion intensity depends on the direction. Indeed, if (ξ, η) denotes the local orthogonal coordinate system, where the η-axis indicates the direction parallel to the gradient ∇I and the ξ-axis is orthogonal to the gradient direction, then the diffusion equation (2.90) can be re-written [15, 158]:

$$\frac{\partial I}{\partial t} = f(|\nabla I|^2)I_{\eta\eta} + (|\nabla I|f(|\nabla I|^2))'I_{\xi\xi}. \tag{2.91}$$

Thus, the diffusion process (2.91) does not diffuse in the same way in the ξ-direction and the η-direction. In general, the diffusion flow (2.90) is bad-posed but one solution consists of introducing a slight Gaussian convolution in the diffusivity function f such that:

$$f(|\nabla I_\sigma|^2) = \frac{1}{1 + |\nabla(G_\sigma * I)|^2/\lambda}. \tag{2.92}$$

The PDE-based denoising flow using (2.92) is well-posed since Catté-Coll-Lions-Morel proved in [5, 37] the existence, the uniqueness and the stability w.r.t. the initial image of a solution. Figure 2.32 shows the scale space produced by the *regularized* version of the Perona-Malik model.

(a) Original Image   (b) scale s_1 (c) scale $s_2 > s_1$
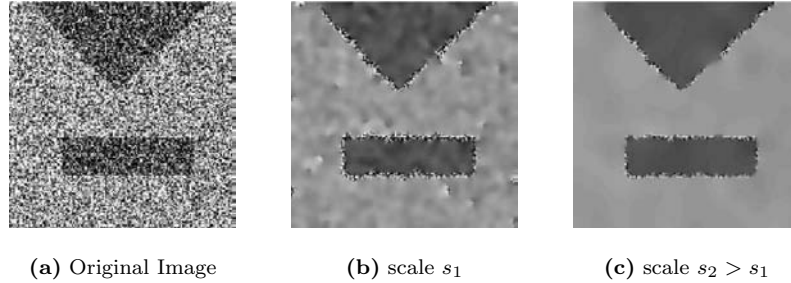
Figure 2.32: Scale space produced by the regularized nonlinear diffusion equation (2.90) of Perona-Malik [141]. The noise has been removed from homogeneous regions while preserving the location of edges. However, the edges are still noised since there is no diffusion on these locations.

In the model of Perona-Malik, the edges between homogeneous regions are well preserved thanks to the function f. However, even if homogeneous regions are efficiently denoised, noisy edges are badly/not regularized since the diffusivity function f is null on the edges. Hence, Weickert [184] proposed to take into account the direction of local structures instead of the edge localization in the diffusion process. He considered the whole diffusion tensor D in Equation (2.89) which is decomposed into eigenvectors and eigenvalues with the fundamental theorem of *singular values decomposition*:

$$D = \Sigma \cdot \Lambda \cdot \Sigma^T, \qquad \Sigma = (\mathbf{v}_1; \mathbf{v}_2) \quad \text{and} \quad \Lambda = \text{Diag}(\lambda_1, \lambda_2). \tag{2.93}$$

The unit eigenvectors $(\mathbf{v}_1; \mathbf{v}_2)$ are respectively parallel and orthogonal to the gradient ∇I_σ and the eigenvalues are, for example, equal to $\lambda_2 = 1$ and $\lambda_1 = 1 - \exp\left(\frac{-3.31488}{(|\nabla I_\sigma|/\lambda)^8}\right)$ if $|\nabla I_\sigma| > 0$ and $\lambda_1 = 1$

if $|\nabla I_\sigma| = 0$ [184]. The scale space produced by the diffusion equation (2.89) with D given by (2.93) is illustrated on Figure 2.33. We can see that this diffusion denoises homogeneous regions and also edges while keeping them well localized. Weickert also proposed a new nonlinear anisotropic diffusion equation in [182, 184] to regularize and enhance coherent flow-like structures, see Figure 2.34.

(a) Original Image **(b)** scale s_1 **(c)** scale $s_2 > s_1$
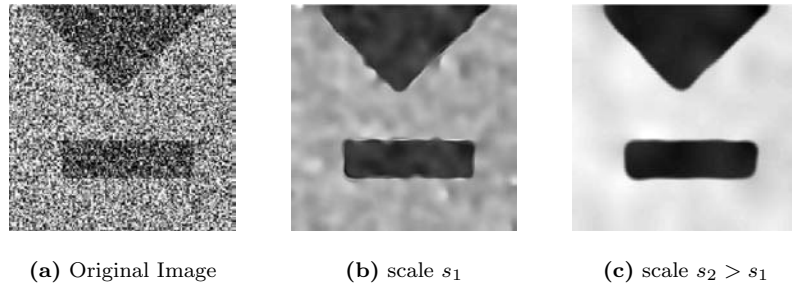
Figure 2.33: Scale space produced by the edge-enhancing diffusion equation defined by Weickert [184] and the diffusion tensor (2.93). The noise has been removed from homogeneous regions and edges while keeping them well localized..

(a) Original Image **(b)** Regularized Image **(c)** Original **(d)** Regularized
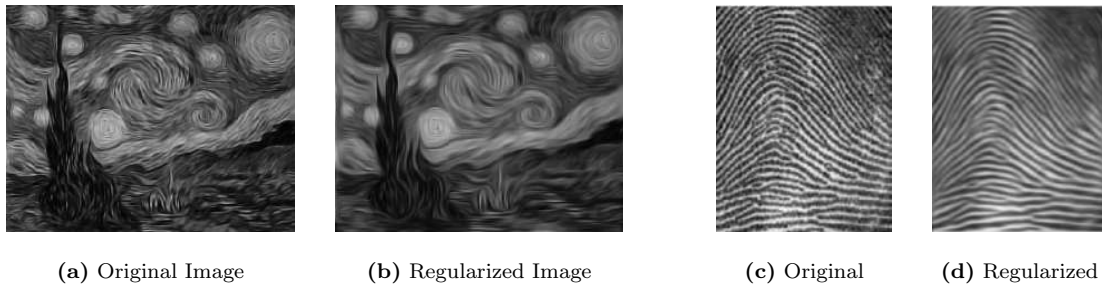
Figure 2.34: Scale space produced by the coherence-enhancing diffusion model of Weickert [182] which applies a 1-D smoothing along flow-like structures.

The previous models were extended to higher dimensions to process e.g. color images [82, 184]. The generalization does not introduce difficulties in the theory and the new PDEs are also well posed. Nevertheless, there are different ways to extend the models to higher dimensions and the simplest solution to extend to vector-valued images is to diffuse each channel separately and recombine them after the denoising process. However, the coupling between channels is a better approach since structures can be constructed by different channels which do not appear at each channel. For example, the m vector-valued formulation of the Perona-Malik's model is as follows [82]:

$$\frac{\partial I_i}{\partial t} = \nabla \cdot \left(f \left(\sum_{j=1}^{M} |\nabla I_{j,\sigma}|^2 \right) \nabla I_i \right), \qquad i = 1, \ldots, M, \tag{2.94}$$

where I_i is the ith component of the vector-valued image I.

Before presenting the mean curvature flow which satisfies the *morphological invariance* which is equivalent to the contrast invariance, we review the link between PDEs and the mathematical

morphology. Mathematical morphology is a well-established domain in image processing from a theoretical and a numerical points of view [89, 121, 162]. Although all mathematical morphology definitions and theorems are established in the continuous setting, the application of the theory is often done in the discrete setting for binary images. The continuous/grey-scale morphology is more difficult to implement. However, a novel way of processing *continuous mathematical morphology* is to use PDEs through continuous flows which has a sub-pixel accuracy and are well posed. For example, the PDE-based dilatation/erosion tool, which structuring element is a disk, is achieved with the flow:

$$\frac{\partial I}{\partial t} = \pm|\nabla I|, \tag{2.95}$$

which is implemented with the level set method of Osher-Sethian based on hyperbolic upwind techniques, Equation (2.22).

In the following, we present the fundamental work of Alvarez-Guichard-Lions-Morel [4] who defined and classified the PDEs used in image processing according to mathematical properties and invariances [4, 158]: causality/semi-group property, regularity, linearity, locality, Euclidean invariance, affine invariance and morphological invariance. They deduced that the flow which satisfies the properties of causality, regularity, Euclidean invariance and morphological invariance is as follows:

$$\frac{\partial I}{\partial t} = F\left[t, \nabla \cdot \left(\frac{\nabla I}{|\nabla I|}\right)\right] |\nabla I|, \tag{2.96}$$

which provides the dilatation/erosion flow when $F = \pm 1$ and the famous mean curvature flow when $F = \nabla \cdot \left(\frac{\nabla I}{|\nabla I|}\right)$:

$$\frac{\partial I}{\partial t} = \nabla \cdot \left(\frac{\nabla I}{|\nabla I|}\right) |\nabla I|, \tag{2.97}$$

which is equivalent to evolve all isophotes (the level sets) of I according to the Euclidean shortening flow $\partial_t C = \kappa \mathcal{N}$. They also derived the unique flow, called *affine morphological scale space* and which has more invariances than other scale spaces, which satisfies the properties of causality, regularity, affine invariance and morphological invariance:

$$\frac{\partial I}{\partial t} = \left[t\nabla \cdot \left(\frac{\nabla I}{|\nabla I|}\right)\right]^{1/3} |\nabla I|, \tag{2.98}$$

which means that each level set of the image I evolves according to $\partial_t C = [t\kappa]^{1/3}\mathcal{N}$ which is the affine invariant heat flow or affine shortening flow, defined by Sapiro-Tannenbaum in [159, 160], which propagates isophotes in the inner direction to smooth them.

The previous flows and their level set version are related to the active contour model presented in Section 2.2. Indeed, the mean curvature flow of isophotes $\partial_t C = \kappa \mathcal{N}$ is the minimizing gradient flow of the Euclidean arc-length of the curve C: $L(C) = \int |C_p| dp = \int ds$. This flow decreases as fast as possible the length of C. The link with the active contour model is done when the edge detecting function $f(|\nabla I|)$ weights the Euclidean arc-length of the curve C: $\int f(|\nabla I(C(p))|)|C_p| dp = \int f(|\nabla I(C(s))|) ds$ which produces the flow $\partial_t C = f\kappa\mathcal{N} - <\nabla f, \mathcal{N} > \mathcal{N}$ which level set version is

$$\frac{\partial I}{\partial t} = \nabla \cdot \left(f(|\nabla I|)\frac{\nabla I}{|\nabla I|}\right) |\nabla I|, \tag{2.99}$$

which is close to the Perona-Malik flow (2.90) and becomes the level set-based mean curvature flow (2.97) when f is equal to 1.

We now arrive to the well-known variational and PDE-based denoising model in image processing, the Rudin-Osher-Fatemi's model proposed in [155]. This denoising technique removes the noise while preserving the edges in images and without arbitrarily choosing some parameters as in (2.92). The convex Rudin-Osher-Fatemi (ROF) energy is as follows:

$$F_{ROF}(I, \lambda) = \int_\Omega |\nabla I| + \lambda \int_\Omega (I - I_0)^2 \, d\mathbf{x}, \tag{2.100}$$

where $\Omega \subset \mathbf{R}^N$ is an open set, I_0 is a given (possibly noisy) image, λ is an arbitrary positive parameter related to the scale of observation of the solution and $\int_\Omega |\nabla I| := TV(I)$ is the total variation (TV) norm. The PDE minimizing Energy (2.100) is the following one:

$$\frac{\partial I}{\partial t} = \nabla \cdot \left(\frac{\nabla I}{|\nabla I|} \right) + 2\lambda \left(I - I_0 \right), \tag{2.101}$$

where $\nabla \cdot \left(\frac{\nabla I}{|\nabla I|} \right) = \kappa$ is the curvature of the level sets of I. The first term of the flow is the mean curvature flow weighted by the inverse of the norm of the gradient of I. Indeed, if I evolves according to $\partial_t I = \nabla \cdot \left(\frac{\nabla I}{|\nabla I|} \right)$, its isophotes evolve according to the curve flow $\partial_t C = \frac{\kappa}{|\nabla I|} \mathcal{N}$. Therefore, homogeneous regions, for which $|\nabla I| \to 0$, are smoothed according to the mean curvature flow weighted by $1/|\nabla I|$ and the localization of edges is preserved since there is no flow when $|\nabla I| \to \infty$. Then, the second term of the flow (2.101) is a data fidelity term which λ can be computed with the Lagrange multiplier technique to remove the estimated noise. Finally, the ROF model can also be multi-dimensional using the generalized TV-norm proposed by Blomgran in [21]:

$$TV_{N,M}(I) := \sqrt{\sum_{i=1}^M [TV(I_i)]^2}, \qquad I : \mathbf{R}^N \to \mathbf{R}^M. \tag{2.102}$$

Figure 2.35 presents the scale space produced by a color image using the multi-dimensional TV-norm.

Figure 2.35: Scale space produced by the multi-dimensional TV-norm (2.102).

At the stage, two observations can be made. Firstly, there is again a relation between the different PDEs used in image denoising/restoration. For example, the TV-flow (2.101) can be obtained by choosing $g = \frac{1}{|\nabla I|}$ in the Perona-Malik flow (2.90). Secondly, like in the ROF model, a data fidelity term, such as $\lambda(I - I_0)$, can also be added to the Flows (2.83), (2.90), (2.94) and (2.99).

In the previous cases, we have considered smoothing-enhancing flows. We now present a pure edge enhancement flow called the *shock filter model* proposed by Osher-Rudin in [131]. This model is based on a nonlinear hyperbolic PDE which tries to propagate the color information from homogeneous regions toward the edges of these regions. One of the shock model proposed for 2-D images is

$$\frac{\partial I}{\partial t} = -|\nabla I| F(L(I)), \tag{2.103}$$

where F is a Lipschitz function satisfying $F(0) = 0$, $\text{sign}(s)F(s) > 0 (s \neq 0)$, for example $F(s) = \text{sign}(s)$, and L is a nonlinear elliptic operator such that zero crossings define the edges on images such that $L(I) = \frac{\nabla I}{|\nabla I|}.H_I.\frac{\nabla I}{|\nabla I|} = \frac{1}{|\nabla I|^2}(I_x^2 I_{xx} + 2I_{xy}I_x I_y + I_y^2 I_{yy})$ where H_I is the Hessian of I, in other words $L(I)$ is the second derivative of I in the direction of $\frac{\nabla I}{|\nabla I|}$. We illustrate the shock flow (2.103) on Figure 2.36 to deblur an image.

(a) Original image   **(b)** Blurred image   **(c)** Restored image
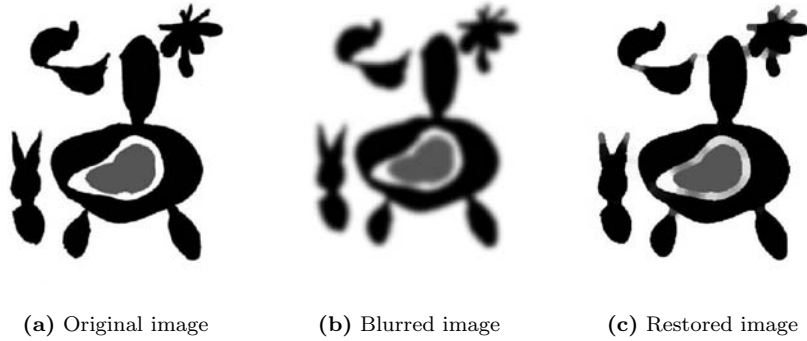
Figure 2.36: Blurred image restored with the shock flow (2.103).

In [166, 167], Sochen-Kimmel-Malladi proposed a new framework to consider low level processing in vision. This novel point of view is based on the field of *high energy physics* where researchers look for determining a mathematical framework, called *string theory* [86], to unify the four basic forces of nature and reconcile gravity and quantum mechanics. In their work, Sochen-Kimmel-Malladi used the approach of string theory in image processing to define images as *surfaces embedded in higher dimensional space*. This new point of view has deep consequences in the processing of images since their approach does not consider anymore images as *collections of level sets* which evolve with the same dynamics. However, the authors showed the links between their approach and several existing scale space/smoothing models, which proves the generalization of their model to many low level vision models. They also defined a new denoising/regularization flow, called the *Beltrami flow*, which can be applied indifferently on multi-valued signals such as gray-level, color and texture images [108].

In their approach, differential geometry is an essential tool to define their energy functional. In their work, (gray-level, color, texture, etc) images are considered as 2-D Riemannian surfaces embedded in higher dimensional Riemannian manifolds. For example, let u^1, u^2 be the local coordinates on the image surface, see Figure 2.37, and $X^i(u^1, u^2), i = 1, \ldots, n_M$ be the coordinates of the embedding space. Hence, we have defined a mapping X between a surface, namely Σ, and the embedding manifold, called M. Figure 2.37 illustrates $X : \Sigma \to M = \mathbf{R}^3$, a gray-level image viewed as a surface embedded in $\mathbf{R}^3$.

Riemannian differential geometry defines the concept of *intrinsic metric* on manifolds, i.e. the concept of *distance*. Distances on manifolds are measured using the *first fundamental form* of
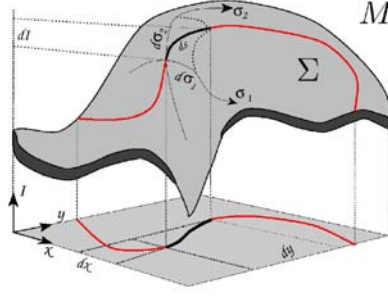
Figure 2.37: Surfaces Σ embedded in higher dimensional spaces M. Images can be considered as 2-D Riemannian/non-flat surfaces embedded in higher dimensional manifolds. Note that the figure is reproduced from [167].

differential geometry [110]. For example, the squared distance between two close points on the surface 2.37 is given by the metric:

$$ds^2 = g_{\mu\nu}d\sigma^\mu d\sigma^\nu, \tag{2.104}$$

where $[g_{\mu\nu}]$ is the first fundamental form, also called the *metric tensor*, which is a positive definite symmetric bilinear form. In Equation (2.104), the *Einstein summation* convention is used since identical indices that appear one up and one down are summed over.

Let $(\Sigma, g_{\mu\nu})$ be the image manifold characterized by the Riemannian metric $[g_{\mu\nu}]$ and (M, h_{ij}) the embedding manifold geometrically represented by the metric tensor $[h_{ij}]$. Then, Polyakov in [143] defines for the map $X : \Sigma \to M$ the following weight functional:

$$P(X, \Sigma, M) = \int d^{n_\Sigma}\sigma \ g^{1/2}g^{\mu\nu}\partial_\mu X^i \partial_\nu X^j h_{ij}(X), \tag{2.105}$$

where n_Σ is the dimension of Σ, n_M the dimension of M, $[g^{\mu\nu}]$ is the inverse metric of $[g_{\mu\nu}]$, g is the determinant of $[g_{\mu\nu}]$, $\mu, \nu = 1, ..., n_\Sigma$, $i, j = 1, ..., n_M$ and $\partial_\mu X^i = \partial X^i / \partial\sigma^\mu$.

If the Euler-Lagrange equation of the Polyakov functional (2.105) is computed w.r.t. an embedding coordinate X^i and multiplied by a strictly positive function and a positive definite matrix to be re-parametrization invariant, we get the following flow:

$$\frac{\partial X^i}{\partial t} = -\frac{1}{2g^{1/2}}h^{il}\frac{\partial P}{\partial X^i} = g^{-1/2}\partial_\mu(g^{1/2}g^{\mu\nu}\partial_\nu X^i) + \Gamma^l_{jk}\partial_\mu X^j \partial_\nu X^k g^{\mu\nu} \quad \text{for } 1 \le i \le n_M, \tag{2.106}$$

where Γ^l_{jk} is the Levi-Civita connection coefficient. Given the Polyakov functional (2.105) and its minimizing flow (2.106), Sochen-Kimmel-Malladi proved in [166, 167] that different choices of the metric tensor $[g_{\mu\nu}]$ in Equation (2.106) give the most well-known scale spaces: the linear scale space, the scale space of Perona-Malik, the mean curvature scale space and the total variation scale space. When the embedding space M is Euclidean, the flow (2.106) is reduced to:

$$\frac{\partial X^i}{\partial t} = g^{-1/2}\partial_\mu(g^{1/2}g^{\mu\nu}\partial_\nu X^i) = \Delta_g X^i, \tag{2.107}$$

where Δ_g is the *Beltrami operator* [110] which is a generalization of the Laplacian operator to non-flat manifolds. They used this flow to denoise multi-dimensional signal such as texture images in a natural way without coupling artificially the different channels [108]. Let $X : (x, y) \to (x, y, I(x, y))$ then $\partial_t I = \Delta_g I = \kappa\mathcal{N}_I$ where κ is the mean curvature of the surface Σ and $\mathcal{N}_I$ is the unit normal in the I-direction, see Figure 2.37. The Beltrami flow (2.107) works as follows: each point on the

n_Σ-dimensional surface moves with a velocity that depends on the mean curvature and the angle between the I-component and the normal component to the surface. More precisely, I does not change along edges since the I-component is orthogonal to the normal surface component and I changes a lot for the rest of the image. Indeed, the rest of the image tends toward a minimal surface at the most rapid rate. This is explained with the concept of *harmonic maps* in differential geometry [110].

Harmonic maps are the generalization of geodesics and minimal surfaces to higher dimensional manifolds. They are given by the Euler functional/Nambu action that describes the (hyper-)area of a (hyper-)surface:

$$S = \int d^{n_\Sigma}\sigma \ g^{1/2}, \tag{2.108}$$

where $g^{1/2}$, the square root of the determinant of the image metric corresponds to the infinitesimal invariant-volume. The Euler functional (2.108) can be obtained from the Polyakov functional and the *pullback* procedure that consists in constructing the metric $[g_{\mu\nu}]$ on Σ from the metric on M and the map X such that:

$$g_{\mu\nu} = \partial_\mu X^i \partial_\nu X^j h_{ij}(X). \tag{2.109}$$

The metric (2.109) is called the *induced metric*. Given the metric (2.109), we introduce it into the Polyakov action (2.105) to get the Euler functional (2.108). Furthermore, the flow minimizing the Euler functional is the generalized mean curvature flow [167]:

$$\frac{\partial X^i}{\partial t} = g^{-1/2}\partial_\mu(g^{1/2}g^{\mu\nu}\partial_\nu X^i) + \Gamma^l_{jk}\partial_\mu X^j \partial_\nu X^k g^{\mu\nu} = \mathcal{H}^i, \tag{2.110}$$

where $\mathcal{H}$ is the generalized mean curvature vector. The Beltrami flow is illustrated on Figure 2.38 for color and texture images.

(a) Color image + Gaussian noise   **(b)** Restored image   **(c)** Texture image   **(d)** Restored image
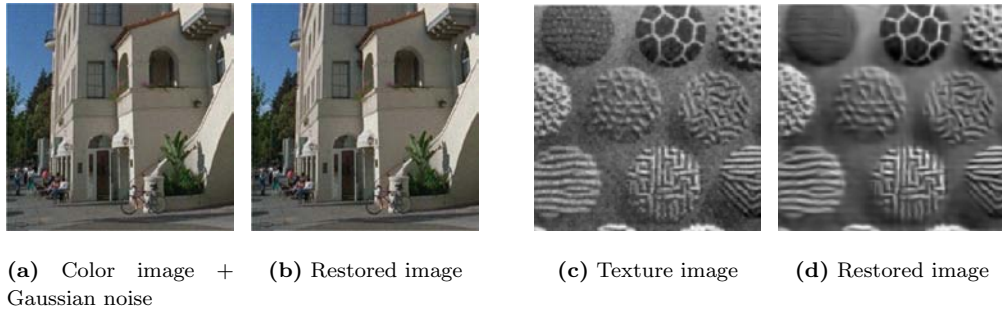
Figure 2.38: Denoising/Restoration of a gray-level and texture images with the Beltrami flow defined in [108, 166, 167] by Equation (2.107). Note that all figures are reproduced from [108, 167].

Let us finish our state-of-the-art chapter with the beautiful model of *image inpainting* proposed by Bertalmío-Sapiro-Caselles-Ballester in [17] and extended to texture images by Bertalmío-Vese-Sapiro-Osher in [18]. Inpainting is an old technique that aims at modifying a given image in an *undetectable form*. The previous authors proposed to carry out image inpainting with a PDE-based approach that fills-in regions to be inpainted in such as way that isophote lines, i.e. the curves with the same image intensity, arriving at the regions' boundaries are completed inside [17]. We illustrate this method on Figure 2.39.

(a) Original Image   **(b)** Corrupted Image   **(c)** Inpainting at t_k **(d)** Inpainting at $t_{l>k}$

(e) Original Image   **(f)** Corrupted Image   **(g)** Inpainting at t_k **(h)** Inpainting at $t_{l>k}$
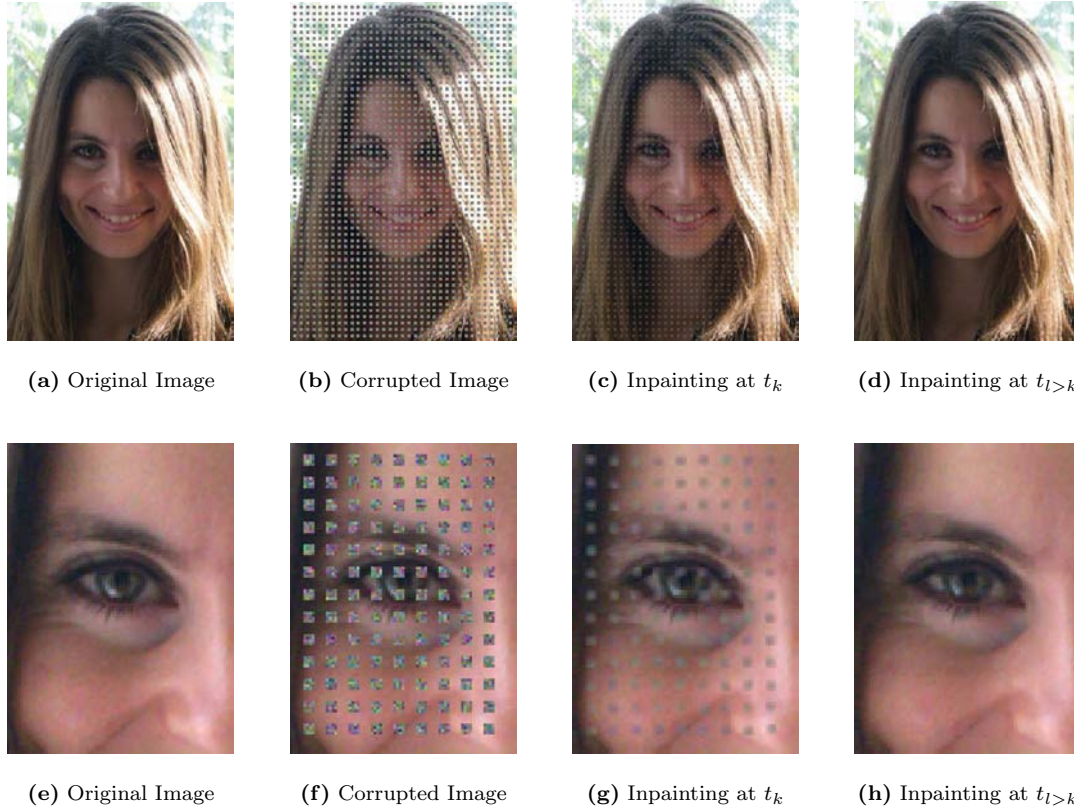
Figure 2.39: Image inpainting: Figures (a) and (e) present two color images that are corrupted by noise, Figures (b) and (f), and recovered on Figures (d) and (h) with the image inpainting model defined in [17].

2.6   Conclusion

This chapter introduced the state-of-the-art in the domain of image segmentation using variational models and partial differential equations. We analyzed and critized the most well-known models in order to present our contributions which will improve some existing solutions. In particular, Sections 2.1 and 2.2 emphasized the main drawback of the active contour/snake model. Many local minima exist in the energy functional of the active contour model, which makes the initial contour critical to get a satisfactory segmentation result. In the next chapter, we propose a new approach to handle this issue by determining a global minimum of the snake model.

Global Minimizers of The Active Contour/Snake Model

3

This chapter proposes to improve the image segmentation model of *snakes* defined by Kass-Witkin-Terzopoulos in [103], also called *geodesic active contours* by Caselles-Kimmel-Sapiro [35] and *geometric active contours* by Kichenassamy-Kumar-Olver-Tannenbaum-Yezzi [105]. As we explained in Section 2.1, the active contour/snake model is one of the most used segmentation models in image processing, such as in medical imaging, for its theoretical and practical advantages. However, this segmentation model suffers from the existence of *local minima* which makes the initial guess critical for getting satisfactory results. We propose to solve this problem by finding *global minimizers* of the active

contours model. We will see that our approach links different well-known methods to overcome the issue of local minima. We will relate the Rudin-Osher-Fatemi's image denoising model [155], based on the total variation norm of the given image, with the Chan-Vese's segmentation models of active contours [42, 179] based on the Mumford-Shah's functional [125].
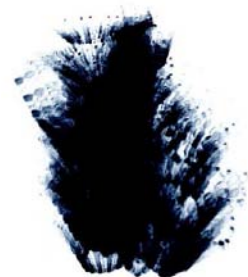
3.1 Introduction

The segmentation problem is fundamental in the computer vision and image processing fields since it is a core component towards e.g. automated vision systems and medical applications. Its aim is to find a partition of an image into a finite number of *semantically important regions.* As we saw in Sections 2.1, 2.2, 2.4.1 and 2.4.2, various variational and partial differential equations-based methods have been proposed to extract objects of interest in images such as the well-known active contours/snakes model defined by Kass-Witkin-Terzopoulos (KWT) in [103]. This method has been widely used in different image processing applications such as in medical imaging to extract

anatomical structures [101, 102, 115, 188].

Following the first model of active contours of KWT, Caselles-Kimmel-Sapiro (CKS) in [35] and Kichenassamy-Kumar-Olver-Tannenbaum-Yezzi (KKOTY) in [105] proposed the geometric (which means invariant w.r.t. the curve parametrization) minimization problem:

$$\min_{C \subset \Omega} F_{GAC}(C) = \int_0^{L(C)} f(|\nabla I_0(C(s))|) \, ds, \tag{3.1}$$

where ds is the Euclidean element of length, $L(C)$ is the length of the planar closed curve C, Ω is the image domain, $I_0 \in L^1(\Omega)$ is a given image and f is an edge detecting function that vanishes at object boundaries such as the one defined in Equation (2.3):

$$f(I_0) = \frac{1}{1 + \gamma |\nabla(I_0 * G_\sigma)|^2}, \tag{3.2}$$

where G_σ is the Gaussian function with standard deviation σ, $I_0 * G_\sigma$ is a smoothed version of the original image I_0 and γ is an arbitrary positive constant.

As said in Section 2.2, the calculus of variations provides the Euler-Lagrange equation of Functional F_{GAC} and the gradient descent method gives the flow that minimizes F_{GAC}:

$$\partial_t C = (\kappa f - \langle \nabla f, \mathcal{N} \rangle)\mathcal{N}, \tag{3.3}$$

where κ is the curvature and $\mathcal{N}$ the normal to the curve. Osher-Sethian introduced in [129] the implicit and intrinsic level set representation of contours to efficiently solve the contour propagation problem and to deal with topological changes. Equation (3.3) can be written in the level set form as follows:

$$\partial_t \phi = \left(\kappa f + \langle \nabla f, \frac{\nabla \phi}{|\nabla \phi|} \rangle \right) |\nabla \phi|, \tag{3.4}$$

where ϕ is the level set function embedding the active contour C.

The main drawback of this variational segmentation model, as many other variational models in image processing, is the existence of *local minima* in the energy F_{GAC}. Local minima are undesirable in optimization problems since they provide unsatisfactory results. For example, the initial active contour (embedded in a level set function) on Figure 3.1(a) can not fully segment both objects, Figure 3.1(b), because it gets stuck in a local minimum.

The approach proposed by Chan-Esedoḡlu-Nikolova (CEN) in [41] can help us to overcome the limitation of the standard active contours. In their paper, image segmentation and image denoising are closely related. We remind that image denoising aims at removing noise in images while keeping main features such as edges and textures. Two important variational models of image denoising are the Rudin-Osher-Fatemi (ROF) model [155] and the Mumford-Shah model [125] (even if the Mumford-Shah model is primarily a segmentation model). In [127, 180], Vese-Osher showed that the level set method links the ROF and the Mumford-Shah models.

(a) Initial Active Contour.
(b) Final Active Contour.
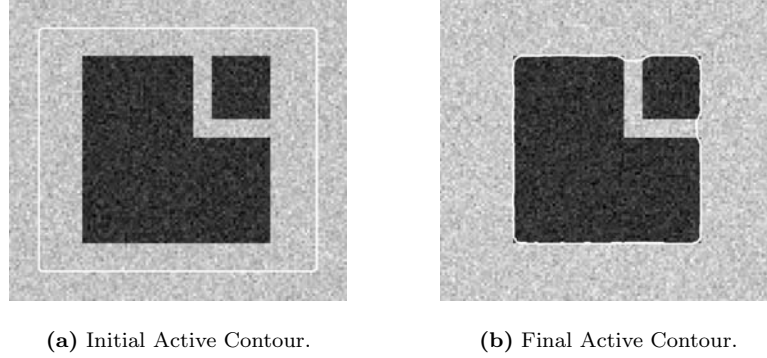
Figure 3.1: Standard active contour fails to segment both objects.

The authors in [41] proposed a method to find global minimizers of two well-known denoising and segmentation models. The first model is a *binary* image denoising model which removes the geometric noise in a given shape. And the second example is the powerful model of *active contours without edges* of Chan-Vese [42]. In this chapter, we propose three algorithms based on the work of CEN in [41] to find global minimizers of the standard active contour/snake model. Our first approach is based on the ROF model where the total variation (TV) norm of the unknown image is replaced by the weighted TV-norm and the L^2-norm for the fidelity term is changed into the L^1-norm [48]. We will show that the global minimizers of this new energy are the global minimizers of the active contour model subject to an intensity homogeneity constraint. Then, we will reconcile the standard active contours and the Chan-Vese's active contours defined from the Mumford-Shah functional in a global minimization framework.

3.2 Global Minimization of the Active Contours Model based on the ROF Model

3.2.1 Theoretical Approach

The Rudin-Osher-Fatemi model defined in [155] is one of the most famous and powerful variational and PDE-based image denoising models. This denoising technique removes the noise while preserving edges in images. The minimization problem of the convex ROF energy is as follows:

$$\min_u F_{ROF}(u, \lambda) = \int_\Omega |\nabla u| + \lambda \int_\Omega (u - I_0)^2 \, d\mathbf{x}, \tag{3.5}$$

where $\Omega \subset \mathbf{R}^N$ is an open set, I_0 is a given (possibly noisy) image and λ is an arbitrary positive parameter related to the scale of observation of the solution.

Based on [40, 41], we propose to minimize the following convex energy defined for any given observed image $I_0 \in L^1(\Omega)$ and any positive parameter λ:

$$F_1(u, \lambda) = \int_\Omega f|\nabla u| + \lambda \int_\Omega |u - I_0| d\mathbf{x}. \tag{3.6}$$

The difference between Energy (3.6) and the ROF model (3.5) is the introduction of the *weighted TV-norm* of u with the weighting function f and the L^1-*norm* as a fidelity measure. The L^1-norm, replacing the square L^2-norm of the original ROF model, has a big impact in the minimization process since it will allow us to find global minimizers of the snake model.

In [40], Chan-Esedoḡlu studied the differences between the standard ROF model and the ROF model that uses the L^1-norm as a fidelity measure. They showed that L^1-norm better preserves the contrast than L^2-norm and the order in which the features disappear is completely determined in terms of the geometry (such as area and length) of features and not in terms of the contrast. Figure 3.2 presents the difference between the ROF model with L^1-norm as a fidelity measure and our model, defined by energy F_1, that uses the weighted TV-norm. The parameter λ for both models is the largest value such that the four small circles in the original image (Figure 3.2(a)) are removed. The difference between both models is clear, the result generated by the weighted TV-norm and the L^1 fidelity term better preserves the geometry of the original features such as the corners and the largest circle.

The weighted total variation norm of the function u with the weight function f is defined as the following way:

Definition 1: Let $\Omega \subset \mathbf{R}^N$ be an open set and $u \in L^1(\Omega)$ and let f be a positive valued continuous and bounded function in Ω. Define the weighted total variation norm of u with the weight function f by

$$TV_f(u) := \int_\Omega f|\nabla u| = \sup_{\phi \in \Phi_f} \left\{ \int_\Omega u(\mathbf{x}) \mathrm{div}\phi(\mathbf{x}) \, d\mathbf{x} \right\}, \tag{3.7}$$

where

$$\Phi_f := \{\phi \in C^1(\Omega, \mathbf{R}) \mid |\phi(\mathbf{x})| \leq f, \text{ for all } \mathbf{x} \in \Omega\}. \tag{3.8}$$

The *coarea formula* for the TV_f-norm reads as follows (Strang [170]):

$$\int_\Omega f|\nabla u| = \int_{-\infty}^{\infty} \left(\int_{\gamma_\mu} f ds \right) \, d\mu, \tag{3.9}$$

$$= \int_{-\infty}^{\infty} \mathrm{Per}_f(E_\mu := \{\mathbf{x} : u(\mathbf{x}) > \mu\}) \, d\mu, \tag{3.10}$$

where γ_μ is the boundary of the set E_μ on which $u(\mathbf{x}) > \mu$. Hence, the term $\mathrm{Per}_f(E_\mu) = \int_{\gamma_\mu} f ds$ is the perimeter of the set E_μ weighted by the function f.

The relation between the minimization of Energy (3.6) and the active contour/snake model [35, 105] is as follows: If $\mathbf{1}_{\Omega_C}$ is the characteristic function of a set Ω_C which boundary is denoted C, then

$$F_1(u = \mathbf{1}_{\Omega_C}, \lambda) = \int_\Omega f|\nabla \mathbf{1}_{\Omega_C}| + \lambda \int_\Omega |\mathbf{1}_{\Omega_C} - I_0|d\mathbf{x}, \tag{3.11}$$

$$= \int_C f ds + \lambda \int_\Omega |\mathbf{1}_{\Omega_C} - I_0|d\mathbf{x}. \tag{3.12}$$
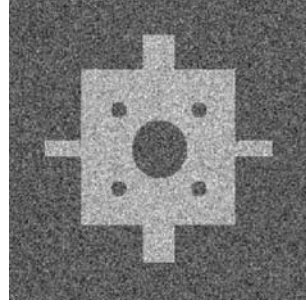
(a) Original image.
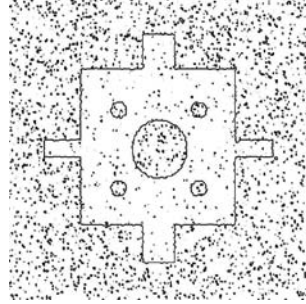
(b) Initial $\partial\{\mathbf{x} : u(\mathbf{x}) > 0.5\}$.
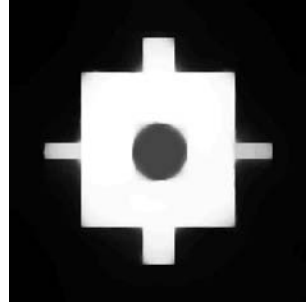
(c) Final u (TV-L^1).
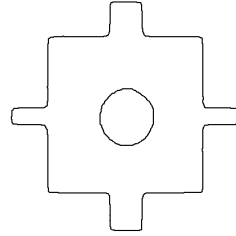
(d) Final $\partial\{\mathbf{x} : u(\mathbf{x}) > 0.5\}$ (TV-L^1).

(e) Final u (weighted TV-L^1).
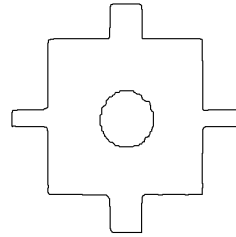
(f) Final $\partial\{\mathbf{x} : u(\mathbf{x}) > 0.5\}$ (weighted TV-L^1).

Figure 3.2: Comparison between the ROF model with L^1-norm as a fidelity measure and our model defined by the weighted TV-norm and the L^1-norm. $\partial\{\mathbf{x} : u(\mathbf{x}) > 0.5\}$ means the boundary of the set of points $\{\mathbf{x} : u(\mathbf{x}) > 0.5\}$ given $u \in [0, 1]$. The difference between both models is clear. The result generated by our model better preserves the geometry of the original features such as the corners and the largest circle.

Hence, minimizing Energy (3.12) is equivalent to

$$minimize \quad \int_C f ds = F_{GAC}(C) \;\; \text{(the active contour energy (3.1))} ,$$

while

approximating I_0 (in the L^1 sense) by a binary function of a set/region Ω_C. $\hspace{1cm}$ (3.13)

We now state Theorem 1:

Theorem 1: *Suppose that $f(\mathbf{x}) \in [0,1]$ and $I_0(\mathbf{x})$ is the characteristic function of a bounded domain in $\Omega_{I_0} \subset \Omega$, if $u_\lambda(\mathbf{x})$ is any minimizer of $F_1(.,\lambda)$, then for almost every $\mu \in [0,1]$ we have that the characteristic function*

$$\mathbf{1}_{\Omega_C(\mu)=\{\mathbf{x}:u_\lambda(\mathbf{x})>\mu\}} (\mathbf{x}), \hspace{2cm} (3.14)$$

where C is the boundary of the set Ω_C, is a global minimizer *of $F_1(.,\lambda)$.*

Proof. The proof of Theorem 1 is based on [40, 41, 169, 170] substituting the TV-norm by the weighted TV-norm. It basically consists of expressing Energy (3.6) in terms of the level sets of u and I_0:

$$F_1(u,\lambda) = \int_0^1 \text{Per}_f(\{\mathbf{x}:u(\mathbf{x})>\mu\})+ \hspace{3cm} (3.15)$$
$$\lambda \,|\{\mathbf{x}:u(\mathbf{x})>\mu\} \,\triangle\, \{\mathbf{x}:I_0(\mathbf{x})>\mu\}| \; d\mu,$$

then minimizing energy (3.15) point-wise in μ by solving a geometry problem.

Suppose that $f(\mathbf{x}) \in [0,1]$ and the original image I_0 is equal to $\mathbf{1}_{\Omega_{I_0}}$, i.e. I_0 is the characteristic function of a set Ω_{I_0}. It can be easily seen that any minimizer $u^\star(\mathbf{x})$ of F_1 will satisfy $u^\star(\mathbf{x}) \in [0,1]$ for almost every (a.e.) $\mathbf{x} \in \Omega$. Hence, the coarea formula (3.10) becomes:

$$TV_f(u) = \int_0^1 \text{Per}_f(\{\mathbf{x}:u(\mathbf{x})>\mu\}) \; d\mu, \hspace{2cm} (3.16)$$

and Energy $F_1(u,\lambda)$ can be written in terms of level sets as in [40, 41]:

$$F_1(u,\lambda) = \int_0^1 \left\{ \text{Per}_f(\{\mathbf{x}:u(\mathbf{x})>\mu\})+ \right. \hspace{2cm}$$
$$\left. \lambda|\{\mathbf{x}:u(\mathbf{x})>\mu\} \,\triangle\, \underbrace{\{\mathbf{x}:f(\mathbf{x})>\mu\}}_{\Omega_{I_0}}| \right\} d\mu,$$

where $S_1 \triangle S_2$ denotes the symmetric difference between the two sets S_1 and S_2 and $|.|$ is the N-dimensional Lebesgue measure. This suggests we consider for a.e. $\mu \in [0,1]$ the minimization problem:

$$\min_{\Omega_C(\mu)\subset\Omega} \text{Per}_g(\Omega_C(\mu)) + \lambda\,|\Omega_C(\mu) \,\triangle\, \Omega_{I_0}|, \hspace{2cm} (3.17)$$

which implies the following geometry problem for each level set of $u(x)$:

$$\min_{\Omega_C \subset \Omega} \text{Per}_g(\Omega_C) + \lambda \left| \Omega_C \triangle \Omega_{I_0} \right|. \tag{3.18}$$

Standard analysis tools and the weak lower semi-continuity property of the weighted BV-norm show the existence of minimizers for the previous minimization problem.

Let $\Omega_C^\star \subset \Omega$ be one of the minimizers of (3.18). Let $u_\lambda(\mathbf{x})$ be any minimizer of $F_1(., \lambda)$. Set

$$\Omega_C(\mu) := \{\mathbf{x} : u_\lambda(\mathbf{x}) > \mu\}. \tag{3.19}$$

Then,

$$\begin{aligned}
\text{Per}_f(\Omega_C(\mu)) + \lambda \left| \Omega_C(\mu) \triangle \Omega_{I_0} \right| & \\
\geq \text{Per}_f(\Omega_C^\star) + \lambda \left| \Omega_C^\star \triangle \Omega_{I_0} \right| & \quad \text{for a.e. } \mu \in [0, 1].
\end{aligned} \tag{3.20}$$

This implies that

$$F_1(u_\lambda(\mathbf{x}), \lambda) \geq F_1(\mathbf{1}_{\Omega_C^\star}(\mathbf{x}), \lambda), \tag{3.21}$$

which means that $\mathbf{1}_{\Omega_C^\star}(\mathbf{x})$ is also a minimizer of $F_1(., \lambda)$.
Furthermore, since u_λ is a minimizer, the inequality of (3.21) is in fact an equality for a.e. $\mu \in [0, 1]$. Thus, $\Omega_C(\mu)$ is a minimizer of the geometry problem (3.18) and $\mathbf{1}_{\Omega_C(\mu)}(\mathbf{x})$ is a minimizer of $E_1(., \lambda)$ for a.e. μ.

Since Energy functional F_1 is *not* strictly convex, it does not possess local minima that are not global minima. Therefore, we can look for *any* minimizer of Energy F_1, it will be a global minimizer. The gradient descent method is thus guaranteed to find a global minimizer of the segmentation model. The minimization flow of Functional F_1 is as follows:

$$\begin{aligned}
u_t &= \nabla \cdot \left(f \frac{\nabla u}{|\nabla u|} \right) + \lambda \frac{u - I_0}{|u - I_0|}, \tag{3.22} \\
&= f \, \nabla \cdot \left(\frac{\nabla u}{|\nabla u|} \right) + \langle \nabla f, \frac{\nabla u}{|\nabla u|} \rangle + \lambda \frac{u - I_0}{|u - I_0|}, \tag{3.23}
\end{aligned}$$

where the first term of the right-hand side is the curvature of the level sets of u multiplies by the weighting function f, the second term is a shock term which enhances the edges and the third term of the right-hand side is a data fidelity term w.r.t. the observed image I_0.

3.2.2 Results

In the standard model of active contours [35, 105], the solution was given by the steady-state solution of Flow (3.4). The evolution of the snake was represented by the evolution of the zero level set of function ϕ. In our new approach, the active contour/snake is computed in a different way.

We do not use a level set function but a function u which is solution of Flow (3.23). Hence, the new way of determining the active contour looks like more a denoising process than a segmentation process. One of the advantages of this new approach is to avoid to re-initialize regularly the level set function as a signed distance function.

The discretization of the evolution equation (3.23) is done with the numerical scheme:

$$
\begin{aligned}
\frac{u^{t+\Delta t} - u^t}{\Delta t} \;=\; & f\left(\sqrt{(D_x^0(I_0 * G_\sigma))^2 + (D_y^0(I_0 * G_\sigma))^2}\,\right) \cdot \\
& \left\{ D_x^-\left(\frac{D_x^+ u^t}{\sqrt{(D_x^+ u^t)^2 + (D_y^+ u^t)^2 + \varepsilon_1}}\right) \right. \\
& \left. + D_y^-\left(\frac{D_y^+ u^t}{\sqrt{(D_x^+ u^t)^2 + (D_y^+ u^t)^2 + \varepsilon_1}}\right) \right\} \\
& + \; \max(D_x^0 f, 0)\frac{D_x^- u^t}{\sqrt{(D_x^0 u^t)^2 + (D_y^0 u^t)^2 + \varepsilon_2}} \\
& + \; \min(D_x^0 f, 0)\frac{D_x^+ u^t}{\sqrt{(D_x^0 u^t)^2 + (D_y^0 u^t)^2 + \varepsilon_2}} \\
& + \; \max(D_y^0 f, 0)\frac{D_y^- u^t}{\sqrt{(D_x^0 u^t)^2 + (D_y^0 u^t)^2 + \varepsilon_2}} \\
& + \; \min(D_y^0 f, 0)\frac{D_y^+ u^t}{\sqrt{(D_x^0 u^t)^2 + (D_y^0 u^t)^2 + \varepsilon_2}} \\
& + \; \lambda\frac{u^t - I_0}{\sqrt{(u^t - I_0)^2 + \varepsilon_3}},
\end{aligned}
\tag{3.24}
$$

where u^t is the function at time t, Δt is the temporal step, D^0 is the central spatial derivative, D^+ is the forward spatial derivative, D^- is the backward spatial derivative and $\varepsilon_1, \varepsilon_2, \varepsilon_3$ are small positive constants. In all our experiments, we choose $\Delta t = 0.00005$, $\varepsilon_1 = 10^{-12}$, $\varepsilon_2 = 10^{-4}$ and $\varepsilon_3 = 10^{-4}$.

Let us now come back to the first image presented on Figure 3.1. However, we choose a new initial contour more challenging since it is the characteristic function of a small disk outside both objects (Figure 3.3(c)). Both objects are now successfully segmented on Figure 3.3(e).

The second example is the cameraman picture, Figure 3.4(a). This example illustrates the limitation of Theorem 1, which makes the *hypothesis* that the given image I_0 is a *binary function*. Unlike Figure 3.3(a) which is a noisy binary function, Figure 3.4(a) is very different from a characteristic function. This explains the important differences between the level contours $\mu = 0.4, 0.5$ and 0.6 (which are not global minimizers in this case) observed on Figure 3.5.

The next section will extend the global minimization of the active contour model to *non-binary* images I_0 with the Mumford-Shah model following [41].
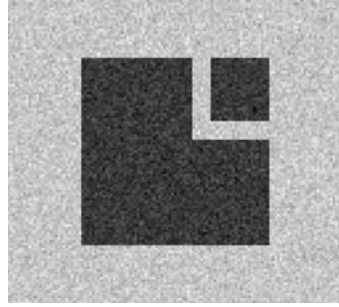
(a) Original image.
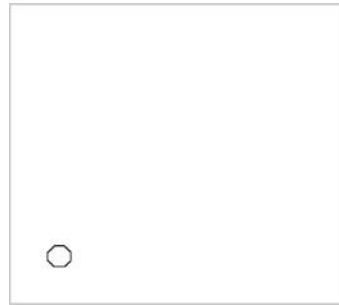
(b) Initial u.

(c) Initial $\partial\Omega_C(\mu = 0.5)$.

(d) Final u.
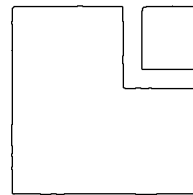
(e) Final $\partial\Omega_C(\mu = 0.5)$.

Figure 3.3: Our segmentation/denoising model has successfully extracted both objects on Figure (e) in the noisy image, Figure (a), whereas the initial guess, Figure (c), was a small circle outside both objects. This improves the standard active contour result obtained on Figure 3.1 where a good initial guess is needed to get the same result.

(a) Original image.

(b) Initial u.
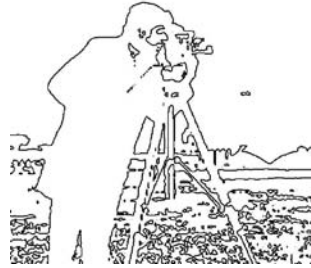
(c) Initial $\partial\Omega_C(\mu = 0.5)$.

(d) Final u.

(e) Final $\partial\Omega_C(\mu = 0.5)$.

Figure 3.4: Figure 3.4(e) presents the result obtained by the minimization the energy F_1. This example illustrates the limitation of the Theorem 1 which makes the hypothesis that the observed image I_0 is a binary function. Since this condition is not respected here, we get different isophotes/isolevel contours (which are not global minimizers) as we can observe on Figure 3.5.

(a) Final $\partial\Omega_C (\mu = 0.5)$.

(b) Final $\partial\Omega_C (\mu = 0.4)$.

(c) Final $\partial\Omega_C (\mu = 0.6)$.
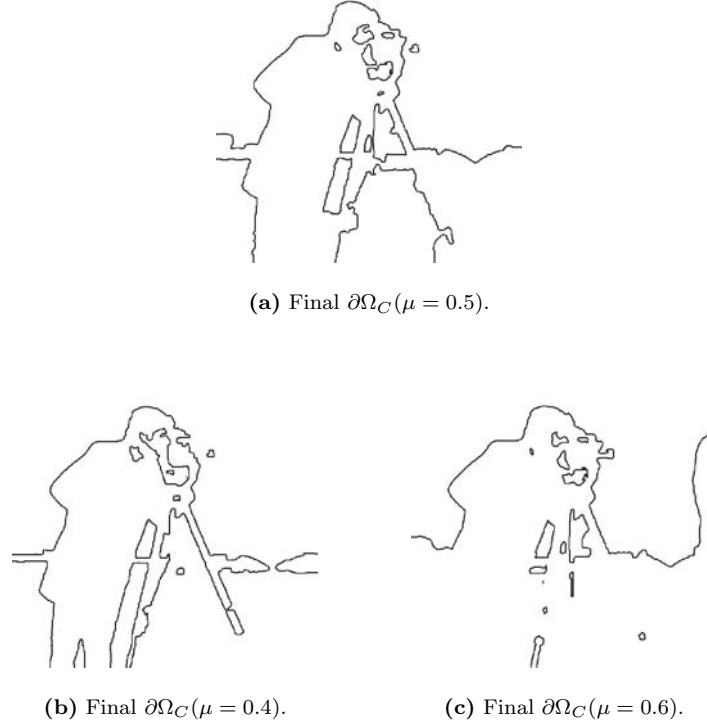
Figure 3.5: Since the cameraman picture is not a binary function, different isophotes/isolevel contours (which are not global minimizers) are obtained for $\mu = 0.4, 0.5$ and 0.6.

3.3 Global Minimization of the Active Contour Model based on the Mumford-Shah Model

3.3.1 The Piecewise-Constant Case

In this section we consider the global minimization of the active contour/snake model using the well-known Mumford-Shah's functional [125]. As we introduced in Section 2.4.1, Chan-Vese proposed in [42] the model of *active contours without edges* based on the detection of homogeneous regions. The name of their model underlines well the difference from the standard active contour model based on the detection of object edges. We propose to reconcile these two "complementary" (or "opposite" according to the point of view) segmentation models in a global minimization framework.

The variational segmentation model of the active contours without edges, i.e. the two-phase piecewise constant Mumford-Shah segmentation model, is as follows:

$$\min_{\Omega_C, c_1, c_2} F_{ACWE}(\Omega_C, c_1, c_2) = \mathrm{Per}(\Omega_C) +$$
$$\lambda \left(\int_{\Omega_C} (c_1 - I_0(\mathbf{x}))^2 \, d\mathbf{x} + \int_{\Omega \setminus \Omega_C} (c_2 - I_0(\mathbf{x}))^2 \, d\mathbf{x} \right), \tag{3.25}$$

where $I_0 \in L^1(\Omega)$ is any given image, $\Omega_C \subset \Omega$, $c_1, c_2 \in \mathbf{R}$ and $\mathrm{Per}(\Omega_C)$ is the perimeter of the set/region Ω_C, if C is the boundary of Ω_C then $\mathrm{Per}(\Omega_C) = \int_C ds$. The variational model (3.25) determines the best approximation, in the L^2 sense of the image I_0 as a set of regions with only two different values, c_1 and c_2. If Ω_C is fixed, the values of c_1 and c_2 which minimize Energy F_{ACWE} are the mean values inside and outside Ω_C. Finally the term $\mathrm{Per}(\Omega_C)$ imposes a smoothness constraint on the geometry of the set Ω_C which separates piecewise constant regions.

The minimization problem (3.25) is non-convex since minimization is carried over functions that take only the values c_1 and c_2, which is a non-convex collection. Hence, the optimization problem can have local minima, which implies solutions with wrong scales of details. Despite of the non-convex nature of (3.25), a natural way to determine a solution (Ω_C, c_1, c_2) is a two-step algorithm where c_1 and c_2 are firstly computed, then region Ω_C is updated to decrease Energy F_{ACWE}. Chan-Vese proposed in [42] a solution to determine an evolution equation for the region Ω_C based on a level set based approach. They represent the regions Ω_C and $\Omega \setminus \Omega_C$ with the Heaviside function of a level set function (which models a characteristic function). Hence Energy F_{ACWE} can be written according to a level set function ϕ:

$$F_{ACWE}(\phi, c_1, c_2) = \int_\Omega |\nabla H_\epsilon(\phi(\mathbf{x}))| d\mathbf{x} +$$
$$\lambda \int_\Omega \left(H_\epsilon(\phi) \left(c_1 - I_0(\mathbf{x})\right)^2 + H_\epsilon(-\phi) \left(c_2 - I_0(\mathbf{x})\right)^2 \right) d\mathbf{x}, \tag{3.26}$$

where H_ϵ is a regularization of the Heaviside function. The flow minimizing Energy (3.26) is then as follows:

$$\phi_t = H_\epsilon'(\phi) \left\{ \nabla.\left(\frac{\nabla \phi}{|\nabla \phi|} \right) - \lambda \underbrace{\left(\left(c_1 - I_0(\mathbf{x})\right)^2 - \left(c_2 - I_0(\mathbf{x})\right)^2 \right)}_{r_1(\mathbf{x})} \right\}, \tag{3.27}$$

Chan-Vese chose in [42] a non-compactly supported smooth strictly monotone approximation of the Heaviside function. As a result, the steady state solution of the gradient flow (3.27) is the same as:

$$\phi_t = \nabla.\left(\frac{\nabla \phi}{|\nabla \phi|} \right) - \lambda r_1(\mathbf{x}), \tag{3.28}$$

and this equation is the gradient descent flow of the energy:

$$\int_\Omega |\nabla \phi| + \lambda \int_\Omega r_1(\mathbf{x})\phi d\mathbf{x}. \tag{3.29}$$

As explained in [41], this energy is homogeneous of degree 1 in ϕ. This means that this evolution equation does not have a stationary solution if we do not restrict the minimization to ϕ such as $0 \le \phi(x) \le 1$.

Thus, we propose to minimize the following constrained minimization problem for any given observed image $I_0 \in L^1(\Omega)$ and any positive parameter λ:

$$\min_{0 \le u \le 1} F_2(u, \lambda) = \int_\Omega f|\nabla u| + \lambda \int_\Omega r_1(\mathbf{x})u d\mathbf{x}. \tag{3.30}$$

The relation between the standard active contour model [35, 105] and the model of active contours without edges [42] is as follows: If $\mathbf{1}_{\Omega_C}$ is the characteristic function of a set Ω_C which boundary is denoted C, then

$$
\begin{aligned}
F_2(u = \mathbf{1}_{\Omega_C}, \lambda) &= \int_\Omega f |\nabla \mathbf{1}_{\Omega_C}| + \lambda \int_\Omega r_1(\mathbf{x}) \mathbf{1}_{\Omega_C} d\mathbf{x}, && (3.31) \\
&= \int_C f ds + \lambda \int_\Omega ((c_1 - I_0(\mathbf{x}))^2 - (c_2 - I_0(\mathbf{x}))^2) \mathbf{1}_{\Omega_C} d\mathbf{x}. && (3.32)
\end{aligned}
$$

Hence, minimizing Energy (3.32) is equivalent to

$$
minimize \ \int_C f ds = F_{GAC}(C) \ \text{ (the active contour energy (3.1)) },
$$

while

approximating I_0 (in the L^2 sense) by

two regions Ω_C and $\Omega \setminus \Omega_C$ with two values c_1 and c_2.

We state the Theorem 2:

Theorem 2: *Suppose that $I_0(\mathbf{x}), f(\mathbf{x}) \in [0, 1]$, for any given $c_1, c_2 \in \mathbf{R}$, if $u_\lambda(\mathbf{x})$ is any minimizer of $F_2(., \lambda)$, then for almost every $\mu \in [0, 1]$ we have that the characteristic function*

$$
\mathbf{1}_{\Omega_C(\mu) = \{\mathbf{x} : u_\lambda(\mathbf{x}) > \mu\}} (\mathbf{x}), \tag{3.33}
$$

where C is the boundary of the set Ω_C, is a global minimizer of $F_2(., \lambda)$.

Proof. The proof of Theorem 2 is based on [41] with the weighted TV-norm replacing the TV-norm. Like Theorem 1, it basically consists of expressing Energy (3.30) in terms of the level sets of u and I_0:

$$
F_2(u, \lambda) = \int_0^1 \left\{ \mathrm{Per}_f(\{\mathbf{x} : u(\mathbf{x}) > \mu\}) + \right.
$$
$$
\left. \lambda \left(\int_{\{\mathbf{x} : u(\mathbf{x}) > \mu\}} (c_1 - I_0(\mathbf{x}))^2 \, d\mathbf{x} + \int_{\Omega \setminus \{\mathbf{x} : u(\mathbf{x}) > \mu\}} (c_2 - I_0(\mathbf{x}))^2 \, d\mathbf{x} \right) \right\} d\mu - \beta, \tag{3.34}
$$

where $\beta = \int_\Omega (c_2 - I_0(\mathbf{x}))^2 \, d\mathbf{x}$ is independent of u. If we define the set $\Sigma(\mu) := \{\mathbf{x} : u(\mathbf{x}) > \mu\}$ then Equation (3.34) can be re-written as follows:

$$
\begin{aligned}
F_2(u, \lambda) &= \int_0^1 \left\{ \text{Per}_f(\Sigma(\mu)) + \right. \\
&\left. \lambda \left(\int_{\Sigma(\mu)} (c_1 - I_0(\mathbf{x}))^2 \, d\mathbf{x} + \int_{\Omega \setminus \Sigma(\mu)} (c_2 - I_0(\mathbf{x}))^2 \, d\mathbf{x} \right) \right\} d\mu - \beta, \quad (3.35) \\
&= \int_0^1 F_{ACWE}^f(\Sigma(\mu), c_1, c_2) \, d\mu - \beta \quad (3.36)
\end{aligned}
$$

where

$$
F_{ACWE}^f(\Omega_C, c_1, c_2) := \text{Per}_f(\Omega_C) + \lambda \left(\int_{\Omega_C} (c_1 - I_0(\mathbf{x}))^2 \, d\mathbf{x} + \int_{\Omega \setminus \Omega_C} (c_2 - I_0(\mathbf{x}))^2 \, d\mathbf{x} \right). \quad (3.37)
$$

It follows that if $u(\mathbf{x})$ is a minimizer of the convex problem, then for a.e. $\mu \in [0, 1]$ the set $\Sigma(\mu)$ has to be a minimizer of the Functional $F_{ACWE}^f(\cdot, c_1, c_2)$.

Finally, the constrained problem (3.30) becomes an *unconstrained* minimization problem according to the following theorem [41]:

Theorem 3: *Let $r(\mathbf{x}) \in L^\infty(\Omega)$. Then the following convex constrained minimization problem*

$$
\min_{0 \leq u \leq 1} \int_\Omega f|\nabla u| + \lambda \int_\Omega r(\mathbf{x})u d\mathbf{x} \quad (3.38)
$$

has the same set of minimizers as the following convex and unconstrained minimization problem:

$$
\min_u \int_\Omega f|\nabla u| + \lambda \int_\Omega \alpha\nu(u) + \lambda r(\mathbf{x})u d\mathbf{x} \quad (3.39)
$$

where $\nu(\xi) := \max\{0, 2|\xi - \frac{1}{2}| - 1\}$ provided that $\alpha > \frac{\lambda}{2} \| r(\mathbf{x}) \|_{L^\infty(\Omega)}$.

Proof. The proof is in [41] with the weighted TV-norm replacing the TV-norm. We include it for completeness. The term $\alpha\nu(u)$ that appears in the second, unconstrained minimization problem (3.39) in the claim is an *exact penalty* term [92], see Figure 3.6 for a plot of its graph. Indeed, the two energies (3.38) and (3.39) agree for $\{u \in L^\infty(\Omega) | 0 \leq u(\mathbf{x}) \leq 1 \; \forall \mathbf{x}\}$. So we only need to show that any minimizer of the unconstrained problem automatically satisfies the constraint $0 \leq u \leq 1$. This is immediate: if $\alpha > \frac{\lambda}{2} \| r(\mathbf{x}) \|_{L^\infty(\Omega)}$, then

$$
|\lambda r(\mathbf{x})| \max\{|u(\mathbf{x})|, |u(\mathbf{x}) - 1|\} < \alpha\nu(u(\mathbf{x})) \quad \text{whenever } u(\mathbf{x}) \in [0, 1]^c, \quad (3.40)
$$

which means that the transformation $u \to \min\{\max\{0, u\}, 1\}$ always decreases the energy of the unconstrained problem (strictly if $u(\mathbf{x}) \in [0, 1]^c$ on a set of positive measure). That leads to the desired conclusion.

Energy functional F_2 is not strictly convex, it does not possess local minima that are not global minima. Thus, we can find any minimizer of Energy F_2 because it will be a global minimizer.
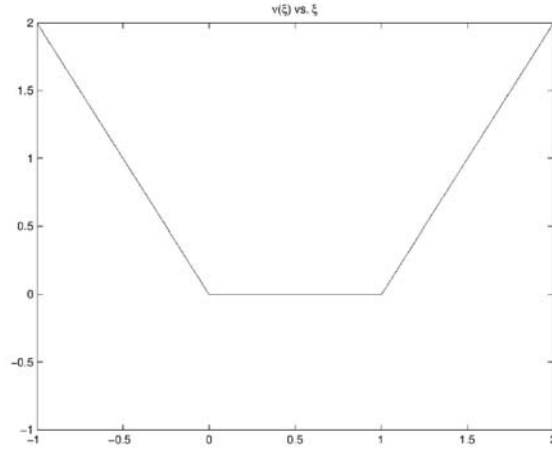
Figure 3.6: The function $\nu(.)$ is used for exact penalization as a method to impose the constraint $0 \leq u \leq 1$ in the minimization (3.38). Note that the figure is reproduced from [41].

Thus, we use the Euler-Lagrange technique and the gradient descent to determine the following minimization flow:

$$
\begin{aligned}
u_t &= \nabla.\left(f\frac{\nabla u}{|\nabla u|}\right) - \lambda r(\mathbf{x}) - \alpha\nu'(u), &(3.41)\\
&= f\ \nabla.\left(\frac{\nabla u}{|\nabla u|}\right) + \langle\nabla f, \frac{\nabla u}{|\nabla u|}\rangle - \lambda r(\mathbf{x}) - \alpha\nu'(u), &(3.42)
\end{aligned}
$$

where

$$
r(\mathbf{x}) = (c_1 - I_0(\mathbf{x}))^2 - (c_2 - I_0(\mathbf{x}))^2. \tag{3.43}
$$

3.3.2 Results

The discretization of the evolution equation (3.42) is done according to the numerical scheme:

$$
\begin{aligned}
\frac{u^{t+\Delta t} - u^t}{\Delta t} = \quad & f\left(\sqrt{(D_x^0(I_0 * G_\sigma))^2 + (D_y^0(I_0 * G_\sigma))^2}\,\right) \cdot \\
& \left\{ D_x^- \left(\frac{D_x^+ u^t}{\sqrt{(D_x^+ u^t)^2 + (D_y^+ u^t)^2 + \varepsilon_1}} \right) \right. \\
& \left. + D_y^- \left(\frac{D_y^+ u^t}{\sqrt{(D_x^+ u^t)^2 + (D_y^+ u^t)^2 + \varepsilon_1}} \right) \right\} \\
+ \quad & \max(D_x^0 f, 0) \frac{D_x^- u^t}{\sqrt{(D_x^0 u^t)^2 + (D_y^0 u^t)^2 + \varepsilon_2}} \\
+ \quad & \min(D_x^0 f, 0) \frac{D_x^+ u^t}{\sqrt{(D_x^0 u^t)^2 + (D_y^0 u^t)^2 + \varepsilon_2}} \\
+ \quad & \max(D_y^0 f, 0) \frac{D_y^- u^t}{\sqrt{(D_x^0 u^t)^2 + (D_y^0 u^t)^2 + \varepsilon_2}} \\
+ \quad & \min(D_y^0 f, 0) \frac{D_y^+ u^t}{\sqrt{(D_x^0 u^t)^2 + (D_y^0 u^t)^2 + \varepsilon_2}} \\
- \quad & \lambda r(\mathbf{x}) - \alpha \nu'_{\varepsilon_3}(u), \quad\quad\quad\quad (3.44)
\end{aligned}
$$

where $\Delta t = 0.00005$, $\varepsilon_1 = 10^{-12}$, $\varepsilon_2 = 10^{-4}$ and $\varepsilon_3 = 10^{-2}$ for all experiments and ν'_{ε_3} is a regularized version of ν' with $\nu_{\epsilon_3}(\xi)$ such that:

$$
\nu_{\epsilon_3}(\xi) = \begin{cases}
-\xi & \text{if} & & \xi & < -\epsilon_3/\sqrt{2}, \\
(1+\sqrt{2})\xi - \sqrt{\tan^2(3\pi/8)\xi^2 - (\xi - \epsilon_3)^2} & \text{if} & -\epsilon_3/\sqrt{2} \leq & \xi & < \epsilon_3, \\
0 & \text{if} & \epsilon_3 \leq & \xi & < 1 - \epsilon_3, \\
(1+\sqrt{2})\xi - \sqrt{\tan^2(3\pi/8)\xi^2 - (\xi - 1 + \epsilon_3)^2} & \text{if} & 1 - \epsilon_3 \leq & \xi & < 1 + \epsilon_3/\sqrt{2}, \\
\xi - 1 & \text{if} & 1 + \epsilon_3/\sqrt{2} \leq & \xi. &
\end{cases} \quad (3.45)
$$

The minimization flow (3.44) is applied to the cameraman picture presented on Figure 3.7(a). The two constants c_1 and c_2 are updated every 50 iterations. The final solution (Figure 3.7(e)) is close to a binary function which gives us, according to Theorem 2, similar global minimizers as we can see on Figure 3.8.

3.3.3   The Piecewise-Smooth Case

We extend the result of Section 3.3.1 to the two-phase piecewise *smooth* Mumford-Shah segmentation model. In this situation, the variational problem to solve is given in [179] by:

$$
\min_{\Omega_C, s_1, s_2} F_{VC}(\Omega_C, s_1, s_2) = \text{Per}(\Omega_C) +
$$
$$
\lambda \left(\int_{\Omega_C} (s_1(\mathbf{x}) - I_0(\mathbf{x}))^2 + \mu|\nabla s_1(\mathbf{x})|^2 d\mathbf{x} + \int_{\Omega \setminus \Omega_C} (s_2(\mathbf{x}) - I_0(\mathbf{x}))^2 + \mu|\nabla s_2(\mathbf{x})|^2 d\mathbf{x} \right), \quad (3.46)
$$

(a) Original image.

(b) Initial u.
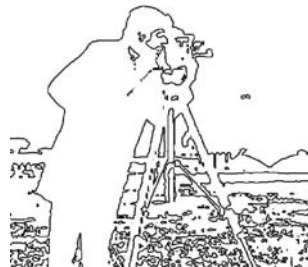
(c) Initial $\partial\Omega_C(\mu = 0.5)$.

(d) Final u.
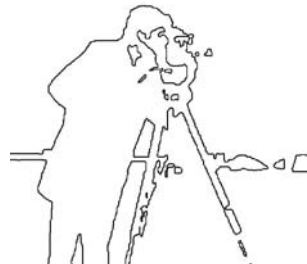
(e) Final $\partial\Omega_C(\mu = 0.5)$.

Figure 3.7: Figure 3.7(e) presents the contour obtained by the global minimization of the active contour energy subject to an intensity homogeneity constraint based on the Mumford-Shah energy (the 2-phase piecewise constant case defined in [42]). Our global minimization approach allows us to reconcile the standard active contours model with the model of Active Contours Without Edges.

(a) Final $\partial\Omega_C(\mu = 0.5)$.

(b) Final $\partial\Omega_C(\mu = 0.4)$.   (c) Final $\partial\Omega_C(\mu = 0.6)$.
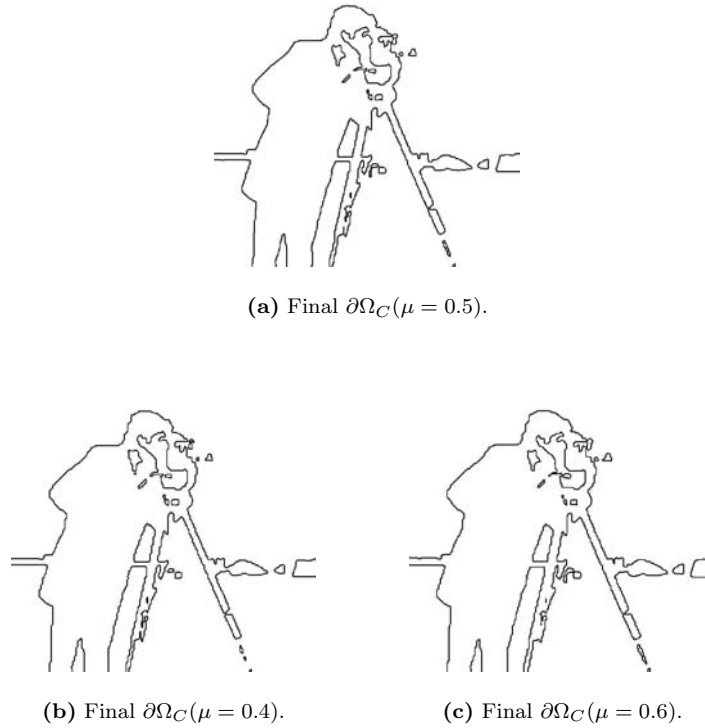
Figure 3.8: Unlike Figure 3.5 where isolevel contours are different from each other since the given image is not binary, the isolevel lines of Figure 3.7(d) are similar and correspond to global minimizers.

where $I_0 \in L^1(\Omega)$ is any given image, $\Omega_C \subset \Omega$, s_1, s_2 are two C^1 functions defined on Ω_C and on $\Omega \setminus \Omega_C$ respectively and $\mathrm{Per}(\Omega_C)$ is the perimeter of the set/region Ω_C. The variational problem (3.46) determines the best approximation, in the L^2 sense, of the image I_0 as a set of smooth regions represented by the function $s(\mathbf{x})$ such that

$$s(\mathbf{x}) = \left\{ \begin{array}{l} s_1(\mathbf{x}) \text{ if } \mathbf{x} \in \Omega_C, \\ s_2(\mathbf{x}) \text{ if } \mathbf{x} \in \Omega \setminus \Omega_C, \end{array} \right. \tag{3.47}$$

and $C = \partial\Omega_C = \partial(\Omega \setminus \Omega_C)$ is the boundary between smooth regions.

As (3.25), the minimization problem (3.46) is also non-convex, which implies the existence of local minima and possible unsatisfactory segmentation results.

As in Section 3.3.1, both regions Ω_C and $\Omega \setminus \Omega_C$ are represented by the Heaviside function of a level set function ϕ. This leads to the following energy:

$$F_{VC_2}(\phi, s_1, s_2) = \int_\Omega |\nabla H_\epsilon(\phi(\mathbf{x}))| d\mathbf{x} +$$
$$\lambda \left(\int_\Omega H_\epsilon(\phi)((s_1 - I_0)^2 + \mu|\nabla s_1|^2) d\mathbf{x} + \int_\Omega H_\epsilon(-\phi)((s_2 - I_0)^2 + \mu|\nabla s_2|^2) d\mathbf{x} \right). \quad (3.48)$$

E_{VC_2} is minimized with respect to functions s_1 and s_2 using the calculus of variations, ϕ being
fixed, which gives us the evolution equations of s_i and their Neumann boundary conditions:

$$\begin{cases} s_1 - I_0 = \mu \Delta s_1 \text{ in } \Omega_C, \\ \frac{\partial s_1}{\partial \mathcal{N}} = 0 \text{ on } \partial \Omega_C \cup \partial \Omega, \end{cases} \qquad \begin{cases} s_2 - I_0 = \mu \Delta s_2 \text{ in } \Omega \setminus \Omega_C, \\ \frac{\partial s_2}{\partial \mathcal{N}} = 0 \text{ on } \partial(\Omega \setminus \Omega_C) \cup \partial \Omega. \end{cases} \quad (3.49)$$

And the flow minimizing Energy (3.48) is as follows:

$$\phi_t = H'_\epsilon(\phi) \Bigg\{ \nabla \cdot \left(\frac{\nabla \phi}{|\nabla \phi|} \right) -$$
$$\lambda \underbrace{\left((s_1 - I_0)^2 - (s_2 - I_0)^2 + \mu|\nabla s_1|^2 - \mu|\nabla s_2|^2 \right)}_{r_2(\mathbf{x})} \Bigg\} \quad (3.50)$$

If a non-compactly supported smooth approximation of the Heaviside function is chosen, the
steady state solution of the gradient flow (3.50) is the same as:

$$\phi_t = \nabla \cdot \left(\frac{\nabla \phi}{|\nabla \phi|} \right) - \lambda r_2(\mathbf{x}) \quad (3.51)$$

and this equation is the gradient descent flow of the energy:

$$\int_\Omega |\nabla \phi| + \lambda \int_\Omega r_2(\mathbf{x}) \phi d\mathbf{x}. \quad (3.52)$$

As a result, the following constrained minimization problem is proposed for any given image
$I_0 \in L^1(\Omega)$ and any positive parameter λ:

$$\min_{0 \le u \le 1} F_3(u, \lambda) = \int_\Omega f|\nabla u| + \lambda \int_\Omega r_2(\mathbf{x}) u d\mathbf{x}. \quad (3.53)$$

We point out that in formulation (3.48) of the piecewise smooth functional the two functions s_1
and s_2 need to be defined only on their respective domains (namely Ω_C and $\Omega \setminus \Omega_C$) because of the
Heaviside function. However, in the relaxed formulation given in (3.53), these functions need to be
defined in the entire domain Ω (by a suitable extension).

*The relation between the standard active contour model [35, 105] and the model of active contours
based on the 2-phase Mumford-Shah functional [179] is as follows:*

$$
\begin{aligned}
F_3(u = \mathbf{1}_{\Omega_C}, \lambda) &= \int_\Omega g|\nabla \mathbf{1}_{\Omega_C}| + \lambda \int_\Omega r_2(\mathbf{x}) \mathbf{1}_{\Omega_C} d\mathbf{x}, && (3.54) \\
&= \int_C g\, ds + \lambda \int_\Omega \left((s_1 - f)^2 - (s_2 - f)^2 + \mu |\nabla s_1|^2 - \mu |\nabla s_2|^2 \right) \mathbf{1}_{\Omega_C} d\mathbf{x}. && (3.55)
\end{aligned}
$$

Hence, minimizing Energy (3.53) is equivalent to

$$
minimize \ \int_C f\, ds = F_{GAC}(C) \quad \text{(The active contour energy (3.1))} \, ,
$$

while

approximating I_0 (in the L^2 sense) by two piecewise smooth regions Ω_C and $\Omega \setminus \Omega_C$.

We state Theorem 4:

Theorem 4: *Suppose that $I_0(\mathbf{x}), f(\mathbf{x}) \in [0,1]$, for any given $s_1 \in C^1(\Omega)$, $s_2 \in C^1(\Omega)$, if $u_\lambda(\mathbf{x})$ is any minimizer of $F_3(.,\lambda)$, then for almost every $\mu \in [0,1]$ we have that the characteristic function*

$$
\mathbf{1}_{\Omega_C(\mu) = \{\mathbf{x} : u_\lambda(\mathbf{x}) > \mu\}} (\mathbf{x}), \tag{3.56}
$$

where C is the boundary of the set Ω_C, is a global minimizer of $F_3(.,\lambda)$.

Proof. The proof of Theorem 4 is similar to the proof of Theorem 2.

And finally, the constrained problem (3.53) becomes an unconstrained minimization problem according to the Theorem 3, Section 3.3.1. A minimizer of the convex energy F_3 can be found using the following minimization flow:

$$
u_t = \nabla . \left(f \frac{\nabla u}{|\nabla u|} \right) - \lambda r_2(\mathbf{x}) - \alpha \nu'(u), \tag{3.57}
$$

with $\alpha > \frac{\lambda}{2} \parallel r_2(\mathbf{x}) \parallel_{L^\infty(\Omega)}$.

3.3.4   Results

The minimization flow (3.57) is applied on the cameraman picture, Figure 3.9(a). The two functions s_1 and s_2 are initially chosen to I_0 and updated every 10 iterations according to Equation (3.49). The final solution (Figure 3.9(e)) is close to a binary function which gives us, according to Theorem 4, similar global minimizers.

We also propose to segment Figure 3.10(a) and simultaneously denoise it (Figure 3.10(b)). Finally we apply our segmentation/denoising model to the galaxy picture on Figure 3.11(a).

(a) Original image.

(b) Piecewise-smooth approximation.

(c) Initial u.

(d) Initial $\partial\Omega_C(\mu = 0.5)$.

(e) Final u.

(f) Final $\partial\Omega_C(\mu = 0.5)$.
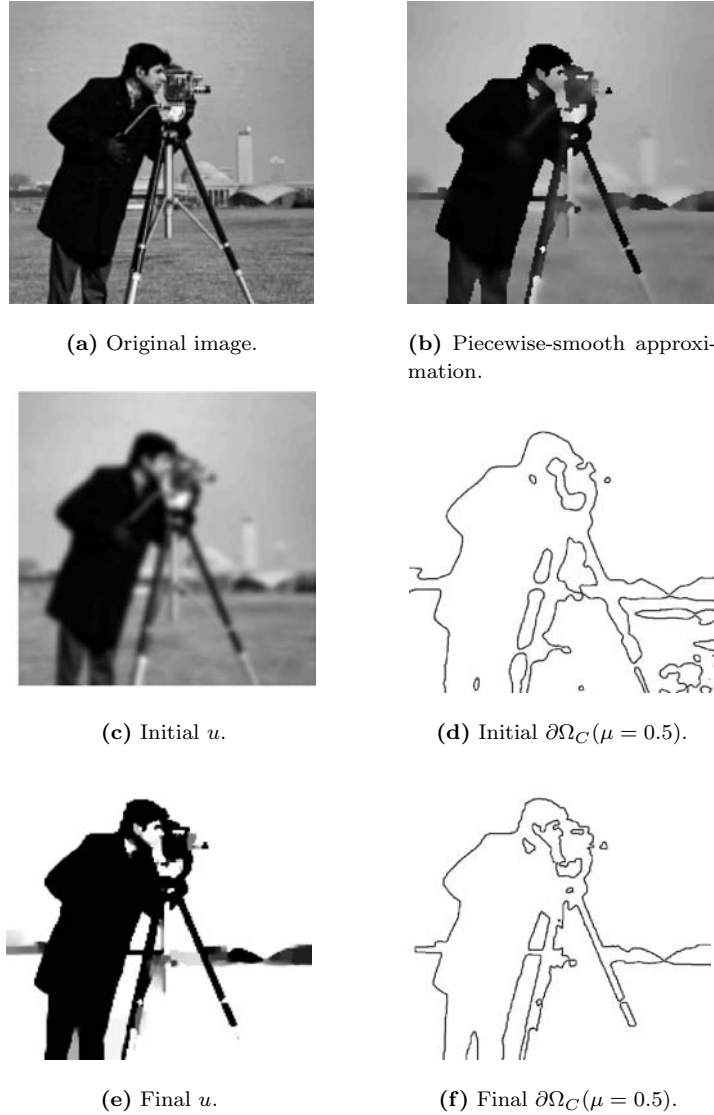
Figure 3.9: Figure 3.9(f) presents the contour obtained by the global minimization of the active contour energy subject to an intensity homogeneity constraint based on the Mumford-Shah energy (the 2-phase piecewise smooth case defined in [179]). Our global minimization approach allows us to reconcile the standard active contours model with the model of active contours based on the Mumford-Shah approach. Finally, Figure 3.9(b) shows the best piecewise smooth approximation of the original image (Figure 3.9(a))
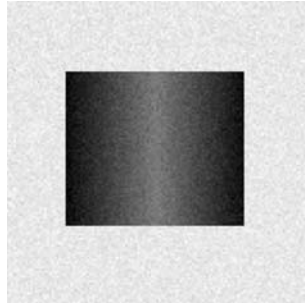
(a) Original image.

(b) Piecewise-smooth approximation.
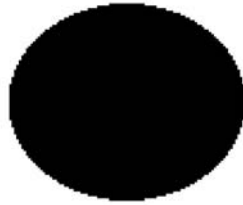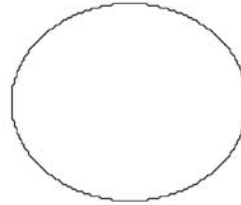
(c) Initial u.

(d) Initial $\partial\Omega_C (\mu = 0.5)$.

(e) Final u.
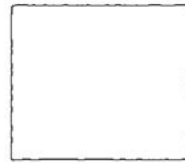
(f) Final $\partial\Omega_C (\mu = 0.5)$.

Figure 3.10: Figure 3.10(f) presents the contour obtained by the global minimization of the active contour energy subject to an intensity homogeneity constraint. Figure 3.10(b) shows the denoised image obtained with the minimization problem (3.53).
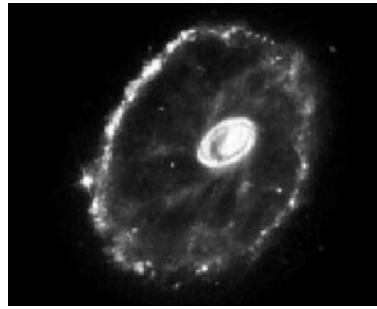
(a) Original image.
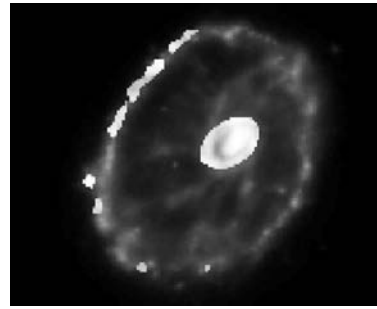
(b) Piecewise-smooth approximation.
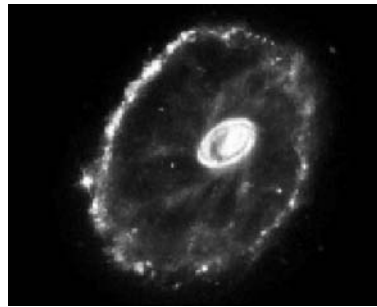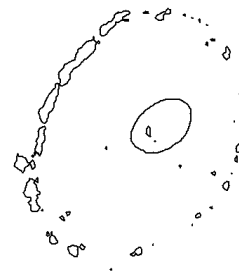
(c) Initial u.

(d) Initial $\partial\Omega_C(\mu = 0.5)$.

(e) Final u.
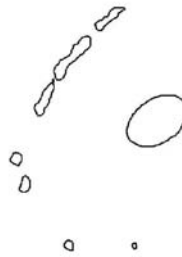
(f) Final $\partial\Omega_C(\mu = 0.5)$.

Figure 3.11: Figure 3.11(f) presents the contour obtained by the global minimization of the active contour energy subject to an intensity homogeneity constraint. Figure 3.11(b) shows the best piecewise smooth approximation of the original image (Figure 3.11(a)).

3.4   Conclusion

Based on [25], this chapter proposed three algorithms to find global minimizers of the active contour/snake variational model following the approach of Chan, Esedoḡlu and Nikolova [40, 41]. The first algorithm, defined from the ROF model [155], determines global minimizers of the snake model for any observed image close to a binary function. The two other algorithms, based on the Chan-Vese's version [42, 179] of the Mumford-Shah's model, find global minimizers (*when parameters c_1, c_2 or functions s_1, s_2 are fixed*) for any type of images, binary or non-binary.

It will not be surprising to see new applications of the approach introduced in [40, 41] to other image processing models to get global minima. The key idea is to express the energy functionals in terms of level sets as observed by Strang [169, 170].

In this work, we determined not one but several global minimizers of the active contour model, which looks to be a drawback. However, all global solutions are reasonable solutions and most of them are close to each other.

From a numerical point of view, the three algorithms are slow even if the standard re-initialization process of the level set function is not used in this approach. The non-linear nature of our PDEs requires to use a very small temporal step to guarantee a consistent evolution process. However, fast numerical schemes can be used to speed up the algorithms such as the second-order cone programming algorithm [3].

Let us mention the paper [50] of Cohen and Kimmel which also addresses the problem of determining a global minimum for the active contour model's energy. However, their approach is different from ours since it is focused on finding a minimal path between two given end points of an open curve. They have extended their method to closed curves but a topology-based saddle search routine is needed.

We also cite the paper [11] of Appleton and Talbot who proposed to determine a global minimum for the geodesic active contour model under the restriction that the contour contains a specified internal point. Authors introduced theorems and efficient graph-based algorithms to find a global minimum. However, unlike to our approach, their method needs a specified internal point, which means that no disconnected object can be extracted. For example, the two objects presented on Figure 3.3 can not be segmented with only one internal point. Their model needs to detect two internal points, which is not our case. Furthermore, the extension of their model to higher-dimension images is not straightforward whereas the extension is natural in our approach.

This chapter presented new image segmentation models based on the detection of object edges and homogeneous regions. The combination of boundary-based and region-based information to detect semantic objects in images is important to get good results. However, the proposed segmentation models use only the mean of intensities, i.e. the first statistical moments, which is limited with more complex semantic structures such as texture objects. Thus, we will introduce in the next chapter a new image segmentation model which will use probability density functions in the context of information theory and variational approaches.

ANACONDA: A New Active Contour Oriented Non Determinist Approach

<div style="text-align: right; font-size: 3em;">4</div>

This chapter introduces a new image segmentation model, called *anaconda**, that uses at the same time *determinist* and *statistic* concepts. We think that the active contours model, which is basically a determinist model developed from mechanics, can benefit from the powerful framework of *information theory*, which uses probabilities and statistics to efficiently carry out the image segmentation task. Thus, the goal of this chapter is to define an error probability of classification in the statistic context of information theory and to minimize it with the determinist shape gradient method. Then, a PDE, derived from the error probability functional, will partition any given image into several regions which probability densities are the most disjoint as possible.

© *Diego Porcel*

Thus, we will see that our image segmentation model is able to find regions in images differing just by statistic moments higher than mean and variance. Moreover, we will prove that our model improves some existing models using *mutual information* as segmentation criterion because mutual information is basically a *lower bound* of error probability. In our approach, we will directly work with the error probability of classification.

4.1 Introduction

In 1948, Shannon wrote two papers [165] concerning *a* mathematical theory of communication which has become *the* theory of communication called *information theory*. Information theory is the domain of mathematics which quantifies the concept of *information* and defines a rigorous way to

---

*Funny name from fun conversations, thanks Oli and Rosa!

determine how much information can be sent through a communication channel given a specific
transmission rate. The core of Shannon's theory is the *entropy* measure that rigorously determines
the information contained in a "message" which can be an image. The number of applications of
information theory is huge in the world of communication technology. They range from coding the-
ory, cryptography, economy, estimation theory to data compression, signal processing and recently
to quantum mechanics. In what follows, we will be obviously interested to apply information theory
to signal/image processing. More precisely, we will use powerful information theoretic concepts such
as stochastic processes, Markov chains, probability density estimation and error probability to carry
out the image classification problem.

We remind that the image classification task aims at splitting a data set into an *arbitrary num-
ber of classes* while conserving as much of the data structure as possible (see Figure 4.1). This
condition is closely related to information theory, and more precisely to data compression, where
the compression algorithm should also conserve as much information of the initial data as possible
while reaching a specific compression ratio [31, 32]. In the case of image classification, the analogue
of the compression ratio is the chosen number of classes.

(a) Original Image   (b) Classified Image
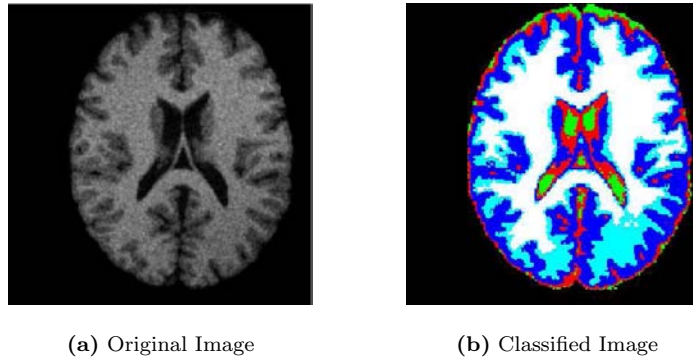
Figure 4.1: Figure (b) presents the classification of Figure (a) with 5 classes. Note that the figures
are reproduced from [31].

In [31, 32, 33], Butz-Thiran proposed a general mathematical framework, based on information
theory, to tackle a large class of signal processing problems including non-supervised image classifi-
cation, multi-modal medical image registration and audio-video joint processing. Their information
theoretical framework is based on *stochastic processes* for information transmission and the *error
probabilities* associated to these transmissions. The stochastic process models the signal processing
task and the error probability of the stochastic process drives the algorithm toward the solution of
the given image processing problem. We will describe their framework in the next section and we
will use it to determine an information theoretic model of image classification in Section 4.3. The
proposed classification model is basically a statistical model which admits several likely/possible so-
lutions. We propose to pick one solution with a determinist method based on a variational approach
and a partial differential equation (Section 4.4). This will allow us to combine probabilistic and de-
terministic approaches in a single framework and to exploit the advantages of each approach, since
statistical models usually offer a large number of possible solutions whereas deterministic methods
choose the best one with respect to (w.r.t.) geometric constraints.

4.2 A General Framework for Information Theoretic Signal Processing

Butz-Thiran proposed in [31, 33] a general framework for information theoretic signal and image processing. Their approach uses several information theoretic concepts to build different image processing algorithms. As commonly done in information theory, they use a stochastic process to model the consecutive steps of any given signal processing algorithm. A *stochastic process* is an indexed sequence of random variables (RV) $\{X_i\}_{i \in [1,..,N]}$ with in general arbitrary mutual dependencies [54]:

$$X_1 \to X_2 \to ... \to X_N, \tag{4.1}$$

The stochastic process (4.1) is entirely determined by the N sets of possible outcomes $\{\Omega_{X_i}\}_{i \in [1,..,N]}$ of the random variables $\{X_i\}$ and by the joint probability distribution $P(X_1, X_2, .., X_N)$. The RV $\{X_i\}$ represent the *consecutive steps* of the signal processing task. Let us take the example proposed in [31] to give a stochastic process associated to an image processing algorithm. The image processing algorithm consists of quantizing the edges of a given image, see Figure 4.2. This task can be modeled with the following stochastic process:

$$I \to E \to Q, \tag{4.2}$$

where I is the intensity RV, E is the edgeness RV and Q is the quantization RV. Computing the joint probability distribution $P(I, E, Q)$ implies to *transform deterministic signals/images into their corresponding probabilistic representations, i.e. probability and joint probability densities*, which can be estimated with the theory of probability density estimation [140, 148]. Figure 4.2 illustrates the signal/image space, the probability space and the probability density estimation which transforms spatial information into probabilistic information. The probabilistic "transformation" allows us to work in a probabilistic framework in order to use information theoretic concepts such as entropy, mutual information, maximum posterior estimation, etc.

After the transformation of signal/image processing tasks into a probability framework by probability density estimation, we now introduce the general information theoretic approach defined by Butz-Thiran in [31, 33] to define and solve any given signal/image processing problem. Firstly, the specific stochastic process which will form the information theoretic basis for any given image processing algorithm, including classification, is as follows:

$$X \to Y_1 \to Y_2 \to ... \to Y_N \to X^{est} \to E, \tag{4.3}$$

where the RV X represent with the *unknown variables* of the signal/image processing problem such as the class labels in classification, X^{est} is considered to be an estimate of the initial/input RV X, and both X and X^{est} are defined on the set of possible outcomes Ω_X. The N RVs $\{Y_i\}_{i \in [1,..,N]}$ represent the consecutive *observations* of X, they are defined on the sets of possible outcomes $\{\Omega_{Y_i}\}$ and finally E is an error measure to the stochastic process $X \to Y_1 \to Y_2 \to ... \to Y_N \to X^{est}$. E measures the accuracy of the estimation of X by X^{est}, and it is defined on $\Omega_E = \{0, 1\}$, which is 1 whenever the estimate X^{est} of X is considered an error and 0 otherwise.

The expectation of the RV E, namely $\mu_E = \langle E \rangle$, is a probabilistic measure of how well the output of the stochastic process, modeled by X^{est}, estimates the initial input, X. This expectation is an
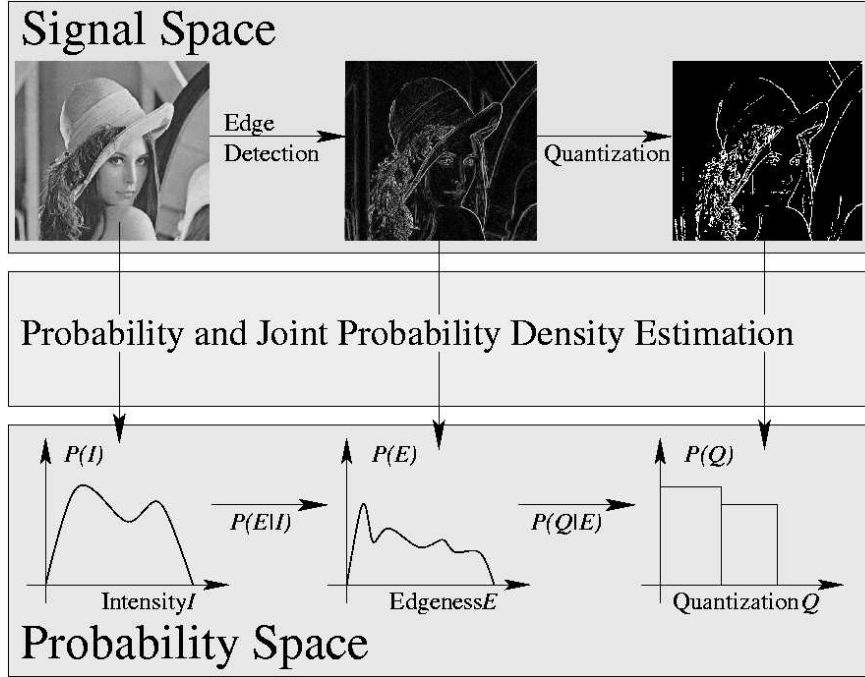
Figure 4.2: From image space to probability space: probability and joint probability density estimation are the basic tools used to transform signal processing algorithms from signal/image space to probability space. Thereafter information theoretic concepts can be applied to the resulting stochastic process. Note that the figure is reproduced from [31].

important quantity in information theory and is called the *error probability*, P_e, of the stochastic process. It is defined (in a discrete setting) by:

$$P_e = \mu_E = \sum_{x \in \Omega_X} \sum_{y_1 \in \Omega_{Y_1}} ... \sum_{y_N \in \Omega_{Y_N}} \sum_{x^{est} \in \Omega_X} P(x^{est}, y_N, .., y_1, x) \cdot$$
$$P(E = 1 | x^{est}, y_N, y_{N-1}, .., y_1, x). \tag{4.4}$$

All the transitions of the stochastic process (4.3) have, in general, arbitrary dependencies with all the other states in the process. In practice, this is too general, which makes it useful to consider the stochastic process (4.3) as a *Markov chain*. A stochastic process is a kth order Markov chain, or equivalently satisfies the kth order Markov condition, if the stochastic process is determined by transition probabilities that depend on the k previous states instead of the joint probability distribution, which means that

$$p(x_j | \{x_i\}_{i \in [1,..,N]}) = p(x_j | x_{j-1}, x_{j-2}, ..., x_{j-k}). \tag{4.5}$$

Butz-Thiran in [31, 33] proposed to consider that all the transitions of (4.3) fulfill the 1st order Markov condition, i.e. $P(y_j | y_{j-1}, y_{j-2}, ..., y_1, x) = P(y_j | y_{j-1})$, except for the last transition to the error probability E. The final transition depends on the initial input to the stochastic process, X,

and on its final output X^{est}, i.e. $P(E = 1|x^{est}, y_N, .., y_1, x) = P(E = 1|x^{est}, x)$. Thus, the error probability (4.4) can be re-written as follows:

$$P_e = \mu_E = \sum_{x \in \Omega_X} \sum_{y_1 \in \Omega_{Y_1}} ... \sum_{y_N \in \Omega_{Y_N}} \sum_{x^{est} \in \Omega_X} P(x) \cdot P(y_1|x) \cdot ... \qquad (4.6)$$
$$\cdot P(y_N|y_{N-1}) \cdot P(x^{est}|y_N) \cdot P(E = 1|x^{est}, x).$$

All the probability transitions of the stochastic process/Markov chain (4.3), except for the last one, model specific signal/image processing tasks such as transformations, segmentations, feature extractions, etc. Butz-Thiran call this the *signal processing block* of the process (Figure 4.3). Then, the expectation of the final random variable E, the error probability P_e, models an objective function that should be minimized w.r.t. the preceding processing block. This builds a general framework (Figure 4.3) for information theoretic signal processing which can incorporate a wide range of distinct algorithms, including image registration, segmentation, feature selection and image classification.
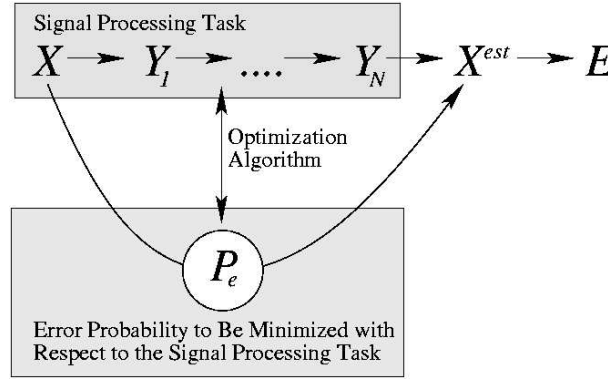
Figure 4.3: General framework for information theoretic signal processing: The signal processing tasks and the corresponding error probability estimation form a general approach to information theoretic signal processing. The error probability is the optimization objective to be minimized w.r.t. the signal processing tasks, such as classification or registration. Note that the figure is reproduced from [31].

In the next section, we will define an image classification algorithm built from this information theoretic framework. In other words, we will derive an expression for the error probability P_e specifically for the image classification task. We will later show that several existing information theoretic classification algorithms based on the active contours model are included in the proposed classification model.

4.3 Image Classification based on Information Theory

This section presents the *non-parametric* and *non-supervised* image classification model proposed in [31, 32]. It is derived from the previous information theoretic framework which defines an error probability of classification as an objective functional to be minimized. The proposed model introduces a new framework for *hidden Markov models* [31, 32, 190] which usually carries out image classification with a finite mixture model of Gaussian densities, one Gaussian per class. In [31, 32], authors made

no parametric assumption (such as Gaussian assumption) for the transition probabilities from the hidden states to the observable states. We will also make no parametric assumption in order to classify/segment images having semantic regions with no Gaussian probability density. Finally, this section will introduce the model of *Markov random fields* [190] which is basically used to model the statistical dependencies between neighboring samples in a given data set such as dependencies between pixels in a given image. Markov random field models will be used to regularize the image of class labels.

4.3.1   Non-Parametric Information Theoretic Image Classification

Let us consider a 2-D image, $I_0 \in L^1(\Omega)$, defined on a bounded open set $\Omega \subset \mathbf{R}^2$. The classification task aims at determining n_c classes which correspond to n_c regions in the 2-D image. Let us call $\Omega_1, \ldots, \Omega_{n_c}$ these n_c regions which must satisfy the equations

$$\bigcup_{i=1}^{n_c} \Omega_i = \Omega \quad \text{and} \quad \Omega_i \bigcap_{i \neq j} \Omega_j = \emptyset, \tag{4.7}$$

as shown on Figure 4.4.
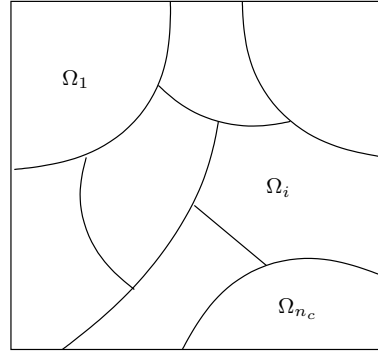
Figure 4.4: Partition of the image domain Ω into n_c regions.

Let us denote U_c a continuous random field, defined on the image domain Ω, which corresponds to the *field of the class labels*. The random field U_c at point $\mathbf{x} \in \Omega$ defines a discrete random variable, $C = U_c(\mathbf{x})$, which models a *class label*. The set of possible outcomes of the random variable C is $S_c = \{1, \ldots, n_c\}$.

Let us now denote U_Y a continuous random field, defined on Ω, which models the *image features* such as the gray level value I_0, the color intensity, the diffusion tensor in magnetic resonance images and so on. The random field U_Y at point $\mathbf{x} \in \Omega$ defines a continuous random variable, $Y = U_Y(\mathbf{x})$, which can be *multi-dimensional*. If we call n_Y the dimension of Y, the set of possible outcomes of Y is denoted $S_Y = \mathbf{R}^{n_Y}$. Finally, we introduce the class label γ which is associated to the feature subspace $S_Y^\gamma = \{y \in S_Y | \nexists \mathbf{x} \in \Omega \text{ with } U_Y(\mathbf{x}) = y\}$. Thus, the set of class labels becomes $S_c \cup \gamma = \{1, \ldots, n_c, \gamma\}$.

According to the information theoretic approach developed in Section 4.2, we consider the following stochastic process to carry out the classification task:

$$C \to Y \to C^{est} \to E, \qquad (4.8)$$

where C^{est} is a discrete RV, different from the RV C of class labels, also over S_c, which models an estimation of the initial/input RV C from the image features Y. E is an error ER being 1 whenever the estimated class label C^{est} is considered a wrong estimate of the initial class label C and 0 otherwise.

As we said in Section 4.2, all the transitions of the stochastic process (4.8) except for the last one are 1st order Markov transitions. The final transition depends only on the initial input to the process C and on its final output C^{est}. Therefore the whole stochastic process is defined by the following probability densities:

$$
\begin{aligned}
P(C = c), & \\
P(Y = y | C = c), & \\
P(C^{est} = c^{est} | Y = y, C = c) &= P(C^{est} = c^{est} | Y = y), \\
P(E = 1 | C = c, Y = y, C^{est} = c^{est}) &= P(E = 1 | C = c, C^{est} = c^{est}).
\end{aligned}
\qquad (4.9)
$$

The expectation of the error random variable E is a probabilistic measure which indicates how well the output of the stochastic process defined in (4.8), modeled by C^{est}, estimates the input C. Let us denote the error probabilistic measure by $P_e(U_c = u_c)$ where u_c is a possible outcome of the random field of the class labels. If we define the *class regions* as $\Omega_k = \{\mathbf{x} \in \Omega | u_c(\mathbf{x}) = k\}$ then

$$u_c(\Omega_1, \ldots, \Omega_{n_c}) = \sum_{k=1}^{n_c} k \cdot \chi_{\Omega_k}, \qquad (4.10)$$

where χ_{Ω_k} is the *characteristic function of the set* Ω_k which value is 1 whenever $\mathbf{x} \in \Omega_k$ and 0 otherwise. Thus, the expectation of E, $\mu_E = \langle E \rangle$, defines the following error probability of classification:

$$
\begin{aligned}
\mu_E =& P_e(u_c(\Omega_1, \ldots, \Omega_{n_c})) = \\
& \sum_{c^{est} \in S_c \cup \gamma} \int_{S_Y} \sum_{c \in S_c \cup \gamma} P(E = 1 | c, c^{est}) \cdot P(c^{est} | y) \cdot P(y | c) \cdot P(c) \, dy.
\end{aligned}
\qquad (4.11)
$$

Since no particular assumption is made about the transition probabilities in Equation (4.9), they are estimated non-parametrically for any given configuration of the class regions $\{\Omega_1, \ldots, \Omega_{n_c}\}$. Using *Gaussian kernel density estimation* [140, 148], also called *Parzen window density estimation*, we obtain the following transition probability densities:

$$P(y | c) = \frac{1}{|\Omega_c|} \int_{\Omega_c} G_\sigma(y - y(\mathbf{x})) \, d\mathbf{x} \qquad (4.12)$$

and

$$
P(c^{est} | y) = \begin{cases} \eta \cdot \int_{\Omega_{c^{est}}} \frac{G_\sigma(y - y(\mathbf{x}))}{H_{c^{est}}(y(\mathbf{x}))} \, d\mathbf{x} & \text{if } c^{est} \neq \gamma, \\ \int_{S_Y^\gamma} G_\sigma(y - y_2) dy_2 & \text{if } c^{est} = \gamma, \end{cases}
\qquad (4.13)
$$

where $G_b(x-a)$ denotes a Gaussian kernel with expectation a and standard variation b, $|\Omega_k|$ is the area of the class region Ω_k, $H_{c^{est}}(y(\mathbf{x})) = \int_{\Omega_{c^{est}}} \delta(y(\mathbf{x}) - y(\hat{\mathbf{x}}))d\hat{\mathbf{x}}$ is the histogram function where δ is the Dirac function and η is a normalization constant. Equation (4.13) justifies the introduction of the class label γ, which simply ensures that the tails of the Gaussian kernels are included in the probability estimations, i.e. that $\sum_{c\in S_c\cup\gamma} P(c|y) = 1, \ \forall y \in S_Y$. In addition to this, the probability $P(c)$ is chosen to be:

$$P(c) = \frac{|\Omega_c|}{n_c}. \tag{4.14}$$

Using the transitions of Equations (4.12) and (4.13), the error probability $P_e(u_c(\Omega_1,\ldots,\Omega_{n_c}))$ can be re-written for any configuration of the class regions $\{\Omega_1,\ldots,\Omega_{n_c}\}$ as follows (see [31] for the whole development):

$$P_e(u_c) = \sum_{c\in S_c} \sum_{c^{est}\in S_c} P(E=1|c,c^{est}) \cdot P(c,c^{est}) + P(\gamma), \tag{4.15}$$

where

$$P(c,c^{est}) \quad = \quad \frac{\eta}{n_c} \int_{\Omega_c} \int_{\Omega_{c^{est}}} \frac{G_{\sqrt{2}\sigma}(y_1(\mathbf{x}) - y_2(\hat{\mathbf{x}}))}{H_{c^{est}}(y_2(\hat{\mathbf{x}}))} \ d\mathbf{x}d\hat{\mathbf{x}} \tag{4.16}$$

is the probability that a point $\mathbf{x}\in\Omega$ with input class label c is transmitted to an output class label c^{est} and where

$$P(\gamma) = \frac{1}{n_c} \int_{S_Y} \int_{S_Y^\gamma} G_{\sqrt{2}\sigma}(y_1 - y_2) \ dy_1 dy_2 \tag{4.17}$$

is the probability that any point $\mathbf{x}$ gets transmitted into S_Y^γ. It is important to note that $P(\gamma)$ is independent of the specific class regions $\{\Omega_1,\ldots,\Omega_{n_c}\}$ and stays constant during the classification algorithm. Therefore, we omit this term in our classification algorithm.

The probabilities defined in Equation (4.16) can be compactly written in a matrix of size $n_c \times n_c$, noted Γ:

$$\Gamma_{c,c^{est}} = P(c,c^{est}), \quad \forall(c,c^{est}) \in S_c \times S_c, \tag{4.18}$$

where Γ is called the *transmission matrix* or *confusion matrix* of information theoretic classification since it represents a theoretical, non-parametrically determined probabilistic transmission matrix. Its trace, $\text{Tr}(\Gamma)$, gives the probability that the output c^{est} from the stochastic process of Equation (4.8) equals its input c. The sum of the off-diagonal elements plus $P(\gamma)$ gives the probability that the output region is a different class label than the input.

In [31, 33], authors showed that the probability of the final transition in (4.8), $P(E=1|c,c^{est})$ can be identified as a discrete *distortion measure*. Distortion is an important quantity in information theory. It accounts for the fact that not all errors in information transmission are of equal importance. For example in image compression, a large error in the pixel values is much more significant than a small one. In our case, we can associate similar properties to the factor $P(E=1|c,c^{est})$. In analogy to the transmission probability of Equation (4.16), we can re-write $P(E=1|c,c^{est})$ as a

matrix of size $n_c \times n_c$, noted Λ:

$$\Lambda_{c,c^{est}} = P(E = 1 | c, c^{est}), \quad \forall (c, c^{est}) \in S_c \times S_c. \tag{4.19}$$

Because of the close analogy to information theoretic distortion, we call Λ the *distortion matrix* of information theoretic classification. In the most general form, Λ has only to fulfill the condition that $0 \leq \Lambda_{i,j} \leq 1, \forall (i,j) \in S_c^2$. In practice though, a suitable choice allows for the penalization of more important classification errors and for the favoring of less significant ones. For example, it might be worse to misclassify elements of relatively small classes, while the misclassification of one single element of a large class is less significant.

Furthermore we normally consider that we do not commit an error when the output c^{est} equals the input to the stochastic process c. Therefore the diagonal elements of Λ are generally null: $\Lambda_{i,i} = 0, \forall i \in [1, .., n_c]$.

An interesting property about the distortion matrix is the possibility to *incorporate some prior information about the expected class sizes* in the classification task. Indeed, it is possible to bias the algorithm slightly towards the expected class sizes for poorly separated clusters by choosing a well adapted distortion matrix. A general form of such a biased distortion can be as follows:

$$\Lambda_{c,c^{est}} = (1 - \delta_{c,c^{est}}) \sum_{k \in S_c} \left(\frac{\alpha_k}{|\Omega_k|} \right)^l, \quad l \in \mathbf{R}_\star^+. \tag{4.20}$$

The unique minimum of the distortion (4.20) lies at $(|\Omega_1| = \alpha_1, |\Omega_2| = \alpha_2, .., |\Omega_{n_c}| = \alpha_{n_c})$. Therefore an appropriate choice of $\{\alpha_k\}$ incorporates some prior information, while the power l indicates the confidence about this prior information. In Figure 4.5, we show the behavior of the distortion (4.20) with respect to the choice of $\{\alpha_k\}$ and the parameter l for the case of $n_c = 2$ classes. If we use $\alpha_i = 1, \forall i \in [1, \ldots, n_c]$ in the distortion (4.20), we see that the minimum lies where the class sizes for all classes are equal. If the class sizes are very different, the algorithm can converge toward a bad optimum.

Finally, the matrix definitions of the transmission probabilities Γ and of the distortion matrix Λ result in a compact notation for the error probability $P_e(u_c)$:

$$P_e(u_c(\Omega_1, \ldots, \Omega_{n_c})) = \sum_{i,j=1}^{n_c} \Lambda_{ij} \cdot \Gamma_{ij}, \tag{4.21}$$

and the classification objective of finding the most representative configuration of the class regions $\{\Omega_1, \ldots, \Omega_{n_c}\}$ w.r.t. the error probability $P_e(u_c)$ can be written compactly by

$$\Omega_1^\star, \ldots, \Omega_{n_c}^\star = \min_{(\Omega_1, \ldots, \Omega_{n_c}) \in S_\Omega} P_e(\Omega_1, \ldots, \Omega_{n_c}), \tag{4.22}$$

where S_Ω is the set of all possible configurations of the class regions $\{\Omega_1, \ldots, \Omega_{n_c}\}$. Thus, solving the minimization problem (4.22) will carry out the classification of any given image into n_c classes. However the previous classification model does not use any prior spatial information regarding the configuration of the class regions. This could give unsatisfactory classification results because some outliers could appear in class regions. We avoid this problem by introducing a Markov random field in the classification model to regularize the image of class labels.

(a) $\alpha_1 = \alpha_2$ **(b)** $\alpha_1 \neq \alpha_2$
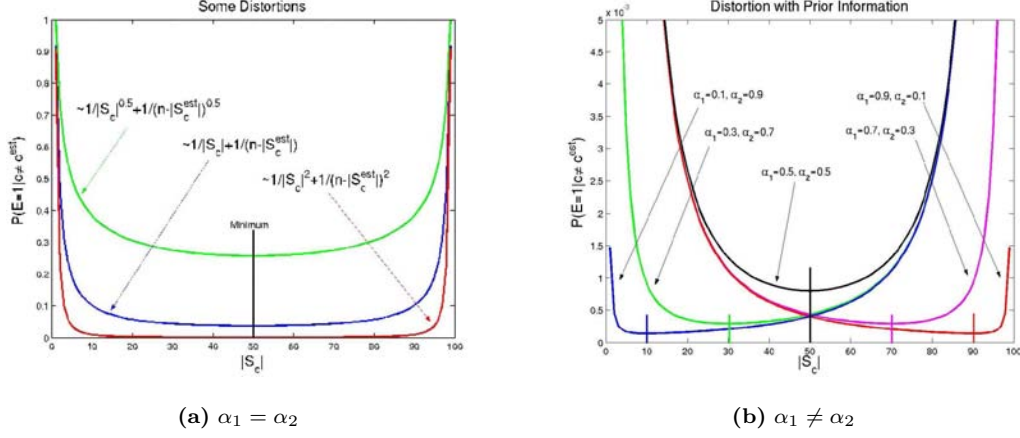
Figure 4.5: Figure (a) presents the distortion measure (4.20) *without* prior information, i.e. $\alpha_i = 1$, $\forall i \in [1, n_c = 2]$. The plots show clearly a consistent minimum for $l = 0.5, 1, 2$. Figure (b) presents the distortion measure (4.20) *with* prior information. The minimum of the distortion measure changes according to the values of α_i, $\forall i \in [1, n_c = 2]$, l being fixed. Thus, parameters α_i can incorporate some prior information about the expected class sizes of Ω_i, $\forall i \in [1, n_c = 2]$. Note that the figure is reproduced from [31].

4.3.2 Image Classification With Markov Random Fields

Markov random fields (MRF) are a well-known model used in signal/image processing algorithms to regularize the solution by introducing statistical dependencies between neighboring data in a given set. Following the model proposed by Butz-Thiran in [31, 32, 33], MRF are used to regularize the image of classification given by the minimization of the error probability defined in Equation (4.21).

Markov Random Fields

Let us consider a given image u_c defined on the domain Ω. This image can be modeled by a continuous random field U_c which u is a possible outcome of U_c. We denote $P(U_C = u_c)$ the prior probability density function for the image u_c. A random field is a Markov random field if it satisfies the two following conditions:

$$
\begin{aligned}
P(u_c(\mathbf{x})) &> 0, & \forall \mathbf{x} \in \Omega, & \quad (4.23) \\
P(u_c(\mathbf{x}) \mid u_c(\mathbf{x}' \neq \mathbf{x})) &= P(u_c(\mathbf{x}) \mid u_c(\mathbf{x}' \in N_{\mathbf{x}})), & \forall \mathbf{x} \in \Omega, & \quad (4.24)
\end{aligned}
$$

where $N_{\mathbf{x}}$ is a neighborhood of the point $\mathbf{x}$. The first condition (4.23) is technical and it implies that all possible outcomes are possible. The second condition (4.24) is very important since it means that *the neighborhood of* $\mathbf{x}$ *is sufficient to entirely define the probability of the site* $\mathbf{x}$. This is the reason for which MRF are famous in image processing since this technique fits well to model *images which intensity at a given point mainly depends on the intensities in its neighborhood and not in the whole image.*

The direct application of MRF to image processing is impossible since the transition probability (4.24) is very high dimensional. Fortunately, the *Hammersly-Clifford's theorem* [19, 81] proposes a

concrete way to use MRF. This theorem proves that a random field U_c is a MRF w.r.t. a system of neighborhoods N if and only if $P(u_c)$ has a *Gibbs distribution* w.r.t. N, that is

$$P_{MRF}(u_c) = \frac{1}{Z} \exp\left(-\frac{1}{T}E(u_c)\right),$$

(4.25)

where E, called the *energy/Gibbs function*, is equal to

$$E(u_c) = \sum_{c_l \in C_l} V_{c_l}(u_c).$$

(4.26)

Z is the normalization constant of the PDF which is called the partition function, T is a constant which controls the strength of the spatial dependencies (known as the temperature in the terminology of physical systems), C_l denotes the set of cliques, which are pixels connected according to the definition of the neighborhood N and V_{c_l} is a local potential function defined on cliques. In the case of image restoration, the absolute difference between intensities of two neighbor pixels is often used to regularize the image. In this situation, the cliques are defined as adjacent pairs of horizontal and vertical pixels.

A Specific Gibbs Function: The Total Variation Functional

The following idea is based on the paper written by Hamza-Krim in [88]. Let us consider an image u_c defined on the domain Ω. The Gibbs function with distribution defined in Equation (4.25), has to be chosen to regularize the image while preserving important features such as the boundaries of objects. Since the original work proposed by Perona-Malik in [141], several variational models have been defined to carry out the regularization while keeping important features. The main drawback of these variational integrals is the arbitrary determination of model parameters. Fortunately, the total variation (TV) functional is a model with powerful properties of regularization which does not need any choice of special parameters. The TV model was introduced in image processing by Rudin-Osher-Fatemi in [155] for image restoration. We remind that the total variation of a image/function u_c is defined by:

$$E(u_c) = TV(u_c) = \int_\Omega |\nabla u| d\mathbf{x}.$$

(4.27)

Information Theoretic Classification Combined with MRF

We defined in Section 4.3.1 an error probability of classification for any outcome of the class field u_c or equivalently the class regions $\{\Omega_1, \ldots, \Omega_{n_c}\}$. However, the class label at a given position $\mathbf{x}$ strongly depends on the classes in the neighborhood of $\mathbf{x}$. Thus, it is natural to introduce a MRF to model the spatial correlations between class labels. The random field U_c is from now on considered as a MRF, which means that the probability of a class label at a position $\mathbf{x}$ conditionally depends on the classes in the neighborhood of $\mathbf{x}$. Besides, the distribution of a particular outcome u_c is provided by a Gibbs distribution.

Now let us introduce the MRF model in the non-parametric information theoretic image classification model developed in Section 4.3.1. The spatial dependency of classes is introduced in the classification process via the following classification error probability

$$P_C(u_c(\Omega_1, \ldots, \Omega_{n_c})) = P_e(u_c) \cdot P_{MRF}(u_c), \tag{4.28}$$

where $P_e(u_c)$ is given by Equation (4.21) and $P_{MRF}(u_c)$ is the Gibbs distribution defined in Equation (4.25).

The final classification objective consist of finding the most representative configuration of the class regions $\{\Omega_1, \ldots, \Omega_{n_c}\}$ which minimizes the error probability of classification P_C:

$$\Omega_1^\star, \ldots, \Omega_{n_c}^\star = \min_{(\Omega_1, \ldots, \Omega_{n_c}) \in S_\Omega} P_C(\Omega_1, \ldots, \Omega_{n_c}). \tag{4.29}$$

The next step is to minimize the error probability (4.28) w.r.t. the class regions. We propose to carry out the minimization in a deterministic approach based on the shape gradient method.

4.4 Statistical Image Classification Combined with A Determinist Approach

Section 4.3 defined a statistical image classification model based on information theory, probability density estimation and an error probability of classification w.r.t. the n_c class regions $\{\Omega_1, \ldots, \Omega_{n_c}\}$. The next step is to determine the n_c class regions which minimize the error probability defined in Equation (4.28). Since the approach is basically probabilist many solutions are possible. We propose to pick a solution with a determinist variational approach. Variational approaches are the common framework between the image segmentation models proposed in this thesis. They are well-posed mathematical models which impose geometric constraints on the solution, such as smoothness. Moreover, when differentiability conditions are fulfilled, the minimum of the variational model is given by a partial differential equation that can be solved by efficient numerical schemes. In what follows, we will present the determinist tool of shape gradient introduced by Delfour-Zolesio in [69] which will be useful to determine evolution equations for the class regions to be classified by minimization of the error probability of classification (4.28).

4.4.1   Shape Gradient Method

As we said in Section 2.4.1, Jehan-Besson-Barlaud-Aubert in [99] and Aubert-Barlaud-Faugeras-Jehan-Besson in [13] proposed a general framework based on the *shape gradient method*, developed by Delfour-Zolesio in [69], to derivate a functional including *region and boundary features*. The shape gradient method consists of derivating a functional which depends on domains/regions that can continuously move. Let us introduce the basis of this theory in the following way. Let us denote $J(\Omega_i)$ a given functional which depends on a region Ω_i. We want to minimize J by deforming Ω_i. We thus need to derivate J w.r.t. Ω_i. This is done by introducing an artificial time t such that:

$$J(\Omega_i(t)) = \int_{\Omega_i(t)} f_R(x, \Omega_i(t))d\mathbf{x}, \tag{4.30}$$

where the function f_R is a general function which depends on the evolving region $\Omega_i(t)$. The derivative of J w.r.t. t is the *Eulerian derivative* of $J(\Omega_i(t))$ in the direction of $\mathbf{V}$ ([69, 99]) given by:

$$\frac{dJ}{dt} = \int_{\Omega_i(t)} \frac{\partial f_R}{\partial t} d\mathbf{x} - \int_{\partial\Omega_i(t)} f_R \ (\mathbf{V} \cdot \mathcal{N}_{\partial\Omega_i}) ds, \tag{4.31}$$

where $\mathbf{V}$ is the velocity field applied on the boundary $\partial\Omega_i(t)$ of the evolving region $\Omega_i(t)$ and $\mathcal{N}_{\partial\Omega_i}$ is the unit inward normal to $\partial\Omega_i(t)$ as shown on Figure 4.6.
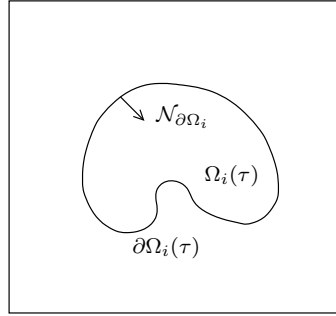
Figure 4.6: The evolving region Ω_i, its boundary $\partial\Omega_i$ and the inward normal $\mathcal{N}_{\partial\Omega_i}$ to $\partial\Omega_i$.

4.4.2   Shape Gradient of Classification Error Probability

The image classification task aims at finding the image of classes u_c or, equivalently, the n_c class regions $\Omega_k = \{\mathbf{x} \in \Omega | u_c(\mathbf{x}) = k\}$ which minimize the classification functional:

$$P_C := P_C(u_c(\Omega_1, \ldots, \Omega_{n_c})),$$

given in Equation (4.28). The final classification result does not change when we introduce a continuous strictly monotonous function $\varphi(.)$ such that:

$$J(u_c(\Omega_1, \ldots, \Omega_{n_c})) = \varphi(\ P_C(u_c)\ ), \tag{4.32}$$

Let us now introduce an artificial time t in the classification functional J:

$$J(t) = \varphi(\ P_C(t)\ ) = \varphi(P_e(t) \cdot P_{\mathrm{MRF}}(t)) \tag{4.33}$$

with

$$\begin{cases} P_e(t) & = \ \sum_{i,j=1}^{n_c} \Lambda_{ij}(\{\Omega_k\}, t) \cdot \Gamma_{ij}(\Omega_i, \Omega_j, t), \\ P_{\mathrm{MRF}}(t) & = \ \frac{1}{Z} \exp\left(-\frac{1}{T} E(u_c, t)\right), \end{cases} \tag{4.34}$$

and

$$
\begin{cases}
\Lambda_{ij}(\{\Omega_k\}, t) & = & (1 - \delta_{ij}) \sum_k^{n_c} \left(\frac{\alpha_k}{|\Omega_k(t)|} \right)^l, \\
|\Omega_k(t)| & = & \int_{\Omega_k(t)} d\mathbf{x},
\end{cases}
\tag{4.35}
$$

$$
\begin{cases}
\Gamma_{ij}(\Omega_i, \Omega_j, t) & = & \frac{\eta}{n_c} \int_{\Omega_i(t)} \int_{\Omega_j(t)} \frac{G_{\sqrt{2}\sigma}(y(\mathbf{x}) - y(\hat{\mathbf{x}}))}{H_{\Omega_j(t)}(y(\hat{\mathbf{x}}))} \, d\mathbf{x} d\hat{\mathbf{x}}, \\
H_{\Omega_j(t)}(y(\hat{\mathbf{x}})) & = & \int_{\Omega_j(t)} \delta(y(\hat{\mathbf{x}}) - y(\hat{\hat{\mathbf{x}}})) d\hat{\hat{\mathbf{x}}},
\end{cases}
\tag{4.36}
$$

$$
\begin{cases}
P_{\text{MRF}}(u_c, t) & = & \frac{1}{Z} \exp\left(-\frac{1}{T} E(u_c, t) \right), \\
E(u_c, t) & = & TV(u_c, t).
\end{cases}
\tag{4.37}
$$

The chain rule is used to derivate Functional J:

$$
\begin{aligned}
\frac{\partial J}{\partial t} & = & \frac{\partial \varphi}{\partial P_C} \cdot \frac{\partial P_C}{\partial t} \tag{4.38} \\
& = & \frac{\partial \varphi}{\partial P_C} \cdot \left(\frac{\partial P_e}{\partial t} P_{\text{MRF}} + P_e \frac{\partial P_{\text{MRF}}}{\partial t} \right), \tag{4.39}
\end{aligned}
$$

with

$$
\begin{cases}
\frac{\partial P_e}{\partial t} & = & \sum_{i,j=1}^{n_c} \left(\frac{\partial \Lambda_{ij}}{\partial t} \Gamma_{ij} + \frac{\partial \Gamma_{ij}}{\partial t} \Lambda_{ij} \right), \\
\frac{\partial P_{\text{MRF}}}{\partial t} & = & -\beta P_{\text{MRF}} \frac{\partial E}{\partial t},
\end{cases}
\tag{4.40}
$$

with $\beta = \frac{1}{T}$. Thus

$$
\frac{\partial J}{\partial t} = \frac{\partial \varphi}{\partial P_C} P_C \cdot \left[\sum_{i,j=1}^{n_c} \frac{1}{P_e} \left(\frac{\partial \Lambda_{ij}}{\partial t} \Gamma_{ij} + \frac{\partial \Gamma_{ij}}{\partial t} \Lambda_{ij} \right) - \beta \frac{\partial E}{\partial t} \right].
\tag{4.41}
$$

Then terms $\frac{\partial \Lambda_{ij}}{\partial t}$ and $\frac{\partial \Gamma_{ij}}{\partial t}$ are computed with the shape gradient method presented in Section 4.4.1:

$$
\begin{cases}
\frac{\partial \Lambda_{ij}}{\partial t}(\{\Omega_k\}, t) & = & (1 - \delta_{ij}) \sum_k^{n_c} \int_{\partial \Omega_k} A_k^\Lambda (\mathbf{V} \cdot \mathcal{N}_{\partial \Omega_k}) ds, \\
A_k^\Lambda(\Omega_k, t) & = & \frac{l \alpha_k^l}{|\Omega_k(t)|^{l+1}},
\end{cases}
\tag{4.42}
$$

$$
\begin{cases}
\frac{\partial \Gamma_{ij}}{\partial t}(\Omega_i, \Omega_j, t) & = & \int_{\partial \Omega_j} A_{ij}^\Gamma (\mathbf{V} \cdot \mathcal{N}_{\partial \Omega_j}) ds - \int_{\partial \Omega_i} B_j^\Gamma (\mathbf{V} \cdot \mathcal{N}_{\partial \Omega_i}) ds, \\
A_{ij}^\Gamma(s, \Omega_i, \Omega_j, t) & = & \frac{\eta}{n_c} \frac{1 - H_{\Omega_j(t)}(y(s))}{H_{\Omega_j(t)}(y(s))^2} \int_{\Omega_i(t)} G_{\sqrt{2}\sigma}(y(\mathbf{x}) - y(s)) d\mathbf{x}, \\
B_j^\Gamma(s, \Omega_j, t) & = & \frac{\eta}{n_c} \int_{\Omega_j(t)} \frac{G_{\sqrt{2}\sigma}(y(\hat{\mathbf{x}}) - y(s))}{H_{\Omega_j(t)}(y(\hat{\mathbf{x}}))} d\hat{\mathbf{x}}.
\end{cases}
\tag{4.43}
$$

The derivation of the Gibbs energy E w.r.t. t is not made with the shape gradient method but with the classic Euler-Lagrange technique as e.g. in the paper of Caselles-Kimmel-Sapiro [35]. This means that Functional E can be written as follows:

$$E(u_c) = \int_\Omega |\nabla u_c| d\mathbf{x}, \qquad (4.44)$$

with $u_c = \sum_{i=1}^{n_c} \chi_{\Omega_i}$ such that

$$E(u_c(\Omega_1, \ldots, \Omega_{n_c})) = \sum_{i=1}^{n_c} \int_{\Omega_i} |\nabla \chi_{\Omega_i}| d\mathbf{x}, \qquad (4.45)$$

using the Lemma of Samson-Blanc-Féraud-Aubert-Zerubia in [156], we obtain

$$E(\Omega_1, \ldots, \Omega_{n_c}) = \sum_{i=1}^{n_c} \int_{\partial\Omega_i} ds = \sum_{i=1}^{n_c} L_{\partial\Omega_i}, \qquad (4.46)$$

and with time t, E can be re-written in the following way:

$$E(\Omega_1, \ldots, \Omega_{n_c}, t) = \sum_{i=1}^{n_c} \int_{\partial\Omega_i(t)} ds. \qquad (4.47)$$

Finally, the Euler-Lagrange equations method is used and gives us:

$$\frac{\partial E}{\partial t} = \sum_{i=1}^{n_c} \int_{\partial\Omega_i} \kappa_i \ (\mathbf{V} \cdot \mathcal{N}_{\partial\Omega_i}) ds, \qquad (4.48)$$

where κ_i is the Euclidean curvature of the curve $\partial\Omega_i$.

Equation (4.48) *justifies* the choice of the Gibbs function as the TV function. Indeed, the gradient flow which minimizes E as fast as possible is given by:

$$\frac{\partial(\partial\Omega_i)}{\partial t} = \kappa_i \mathcal{N}_{\partial\Omega_i}, \quad \text{for } 1 \leq i \leq n_c, \qquad (4.49)$$

which is exactly the *mean curvature motion* that regularizes the curves $\partial\Omega_i$ in a natural and efficient way. Two important points arise here. The first one concerns the Markov random fields and the mean curvature motion. The surprising thing is that these two models are *equivalent* when the Gibbs function is equal to the TV function! In other words, the statistical regularization model of Markov random fields is equivalent to the determinist regularization model of mean curvature flow. The second point is that the curvature motion was not artificially added in the classification algorithm as it is done in most active contours-based works such as [91, 106]. The curvature term appears naturally in our evolution equation thanks to the statistical approach of the image classification task.

This section gave us the derivative of the error probability of classification w.r.t. n_c class regions $\{\Omega_1, \ldots, \Omega_{n_c}\}$. Since the general expression of the derivation is long, we did not write explicitly the complete expression of the form $\frac{\partial J}{\partial t} = \sum_i \int_{\Omega_i} F_{\Omega_i}(\mathbf{V} \cdot \mathcal{N}_{\partial\Omega_i}) ds$ that naturally gives the velocity vector field $\mathbf{V} = -F_{\Omega_i} \mathcal{N}_{\partial\Omega_i}$ which makes the boundary $\partial\Omega_i$ evolving as fast as possible toward a

minimum of the functional J. The next section will focuse on the image classification using $n_c = 2$ class regions. In this case, we will give the entire expression of the derivative of J and the velocity vector field $\mathbf{V}$.

4.4.3 Image Classification With Two classes

We consider the case of $n_c = 2$ classes. They are represented by a *level set function* ϕ such that $\Omega_1 = \{\mathbf{x} \in \Omega | \phi(\mathbf{x}) > 0\}$ and $\Omega_2 = \{\mathbf{x} \in \Omega | \phi(\mathbf{x}) < 0\}$. Then, the unit normal of boundaries of Ω_1 and Ω_2 are represented by $\mathcal{N} = \mathcal{N}_{\partial \Omega_1} = -\mathcal{N}_{\partial \Omega_2}$. We also define the curvature $\kappa = \kappa_1 = -\kappa_2$ and the contour $C = \partial \Omega_1 = \partial \Omega_2$. We choose the function $\varphi(\zeta) = \log(\zeta)$ and the parameters α_1, α_2 and l equal to 1. The image feature y is the gray level value, i.e. $y := I_0$. Finally, we denote $\Lambda = \Lambda_{12} = \Lambda_{21}$ and we remind that $\Lambda_{11} = \Lambda_{22} = 0$.

In this case, the derivative of J in Equation (4.41) is equal to:

$$\frac{\partial J}{\partial t}(\Omega_1, \Omega_2, t) = \frac{1}{P_e} \cdot \left[\frac{\partial \Lambda}{\partial t} (\Gamma_{12} + \Gamma_{21}) + \Gamma \cdot \left(\frac{\partial \Gamma_{12}}{\partial t} + \frac{\partial \Gamma_{21}}{\partial t} \right) \right] - \beta \frac{\partial E}{\partial t}. \tag{4.50}$$

Using the formula developed in the previous section, we obtain

$$\frac{\partial J}{\partial t} = \int_C \left\{ \frac{1}{P_e} \cdot \left[(A_1^\Lambda + A_2^\Lambda) \cdot (\Gamma_{12} + \Gamma_{21}) + \Lambda \cdot (A_{21}^\Gamma - A_{12}^\Gamma + B_1^\Gamma - B_2^\Gamma) \right] - 2\beta\kappa \right\} (\mathbf{V} \cdot \mathcal{N}) ds, \tag{4.51}$$

with

$$\begin{cases} A_1^\Lambda &= \frac{1}{|\Omega_1|^2}, \\ A_2^\Lambda &= \frac{1}{|\Omega_2|^2}, \end{cases} \tag{4.52}$$

$$\begin{cases} \Gamma_{12} &= \frac{\eta}{2} \int_{\Omega_1} \int_{\Omega_2} \frac{G_{\sqrt{2}\sigma}(I_0(\mathbf{x}) - I_0(\hat{\mathbf{x}}))}{H_{\Omega_2}(I_0(\hat{\mathbf{x}}))} \, d\mathbf{x} d\hat{\mathbf{x}}, \\ \Gamma_{21} &= \frac{\eta}{2} \int_{\Omega_2} \int_{\Omega_1} \frac{G_{\sqrt{2}\sigma}(I_0(\mathbf{x}) - I_0(\hat{\mathbf{x}}))}{H_{\Omega_1}(I_0(\hat{\mathbf{x}}))} \, d\mathbf{x} \, d\hat{\mathbf{x}}, \end{cases} \tag{4.53}$$

$$\begin{cases} A_{12}^\Gamma &= \frac{1}{2} \frac{1 - H_{\Omega_2}(I_0(s))}{H_{\Omega_2}(I_0(s))^2} \int_{\Omega_1} G_{\sqrt{2}\sigma}(I_0(\mathbf{x}) - I_0(s)) d\mathbf{x}, \\ A_{21}^\Gamma &= \frac{1}{2} \frac{1 - H_{\Omega_1}(I_0(s))}{H_{\Omega_1}(I_0(s))^2} \int_{\Omega_2} G_{\sqrt{2}\sigma}(I_0(\mathbf{x}) - I_0(s)) d\mathbf{x}, \end{cases} \tag{4.54}$$

$$\begin{cases} B_1^\Gamma &= \frac{1}{2} \int_{\Omega_1} \frac{G_{\sqrt{2}\sigma}(I_0(\hat{\mathbf{x}}) - I_0(s))}{H_{\Omega_1}(I_0(\hat{\mathbf{x}}))} \, d\hat{\mathbf{x}}, \\ B_2^\Gamma &= \frac{1}{2} \int_{\Omega_2} \frac{G_{\sqrt{2}\sigma}(I_0(\hat{\mathbf{x}}) - I_0(s))}{H_{\Omega_2}(I_0(\hat{\mathbf{x}}))} \, d\hat{\mathbf{x}}, \end{cases} \tag{4.55}$$

and

$$\frac{\partial E}{\partial t} = \int_C 2\kappa \, (\mathbf{V} \cdot \mathcal{N}) ds. \tag{4.56}$$

The derivative of J provides us the evolution equation of the active contour/*snake C* that we call *anaconda* (A New Active Contour Oriented Non Determinist Approach). According to the Cauchy-Schwartz inequality, the expression of the velocity vector field $\mathbf{V}$ that makes the curve C evolve as fast as possible toward a minimum of J is given by taking $\mathbf{V}$ as follows:

$$\mathbf{V} = \underbrace{\left(\frac{1}{P_e} \cdot \left[(A_1^\Lambda + A_2^\Lambda) \cdot (\Gamma_{12} + \Gamma_{21}) + \Lambda \cdot \left(A_{21}^\Gamma - A_{12}^\Gamma + B_1^\Gamma - B_2^\Gamma \right) \right] - 2\beta\kappa \right)}_{F_{CL}} \mathcal{N}, \qquad (4.57)$$

which gives us the evolution equation for the active contour/anaconda C minimizing the error probability of classification:

$$\frac{\partial C}{\partial t} = \mathbf{V} = F_{CL}\mathcal{N}. \qquad (4.58)$$

4.5 Results

We apply the evolution equation defined in Equation (4.58) to classify/segment different images. First of all, we test our classification algorithm with synthetic images, then with natural images.

Figure 4.7(a) is composed of four objects and the background having two different intensity means. We firstly apply the model of *active contours without edges* developed by Chan-Vese in [42] on Figures 4.7(b-e), then we apply our model on Figures 4.7(f-i). Both models successfully segment the four objects lying on Figure 4.7(a). Secondly, we apply the active contours without edges model on Figure 4.8(a) where the four objects and the background have the same intensity mean but two different intensity variances. The model of Chan-Vese is not able to segment the given image as shown on Figures 4.8(b-e) since this model is based on determining two sets of regions with *two different mean values*, which is not the case here. However, the model defined by Jehan-Besson-Barlaud-Aubert (JBA) in [99], based on a *variance criterion*, can correctly classify the figure, see Figures 4.8(f-i), as well as our model presented on Figure 4.8(j-m). Finally, the last synthetic image on Figure 4.9(a) is composed of the four objects and the background with the same mean value and the same variance. However, the two regions are different because they do not have the same statistic moments higher than the 2nd order. In this case, the model of JBA is not able to segment both regions as we can see on Figures 4.9(b-e) since both regions have the same variance value. However, our method manages to segment the four regions and the background, Figures 4.9(f-i), because our model is based on *probability densities* which are different for both regions as shown on Figures 4.9(j-m).

We also apply our classification/segmentation model to natural images. Figure 4.10(a) presents the zebra picture reproduced from Paragios-Deriche's paper [133] and Figure 4.10(e) shows the classification result given by our model. Contrary to Paragios-Deriche's approach, which needs three *texture patterns* taken from the zebra and the background, our classification algorithm is *unsupervised* since we do not need any image patches to carry out the classification task. We also try our model on the cameraman picture on Figure 4.11(a) and we get the final result on Figure 4.11(e). Finally, the segmentation model is applied on a x-ray picture, Figure 4.12(a), which gives the result

presented on Figure 4.12(e).

4.6 Relations With Other Statistical And Information Theoretic Models using Active Contours

In this section, we compare our classification/segmentation model with other active contour models. We how that our model, based on information theory, improves and includes several existing segmentation models.

4.6.1 Active Contours based on the Mumford-Shah Model

As explained in Section 2.4.1, Chan-Vese developed two models of active contours [42, 179] based on the Mumford-Shah's functional [125]. We used in Section 4.5 the model of active contours without edges [42] and we showed that this model efficiently segments two (no-connected) regions having two different intensity means, Figure 4.7(e), but fails to segment two regions with the same intensity mean but two different variances, Figure 4.8(e). However, our segmentation model is able to segment regions with the same intensity mean and the same variance value because our model is based on the shape of the density probabilities, i.e. statistical moments of higher order. Indeed, the active contour defined in Equation (4.58) evolves to find two regions having two probability densities as disjoint as possible as we can see on Figures 4.7(m), 4.8(q), 4.9(m), 4.10(i), 4.11(i) and 4.12(i). Each density probability is supposed to represent a semantic region/object in the given image as we observe on Figure 4.10(a).

4.6.2 Parametric And Non-Parametric Geodesic Active Regions

We now propose to show the connexion between our classification approach and the segmentation model of *geodesic active regions*, initially proposed by Paragios-Deriche in [132, 133, 134], then extended by Rousson-Deriche in [149, 151]. See Section 2.4.1 for more details.

Let us come back to the stochastic process/Markov chain defined in Equation (4.8) and let us consider the first part of the chain *only* (without C^{est}) and the error random variable of classification:

$$C \to Y \to E, \tag{4.59}$$

In this case, the previous stochastic process is defined by the following probability densities:

$$
\begin{aligned}
&P(C = c), \\
&P(Y = y | C = c), \\
&P(E = 1 | C = c, Y = y).
\end{aligned}
\tag{4.60}
$$

And the probabilistic measure of classification is:

$$\mu_E = P_e = \sum_{c \in S_c} \int_{S_Y} P(E = 1 | y, c) \cdot P(y | c) \cdot P(c) \, \mathrm{d}y. \tag{4.61}$$

We do not change the classification result by introducing a continuous monotone function φ such that:

$$P_e = \sum_{c \in S_c} \int_{S_Y} \varphi \left(P(E = 1|y, c) \cdot P(y|c) \cdot P(c) \right) \ \mathrm{d}y. \tag{4.62}$$

Besides, if no prior information concerning the probability density functions $P(E = 1|y, c)$ and $P(c)$ are available, we consider them as constant. Thus, we have:

$$P_e = \sum_{c \in S_c} \int_{S_Y} \varphi \left(P(y|c) \right) \ \mathrm{d}y. \tag{4.63}$$

It is interesting to note that the previous functional P_e is precisely the region-based functional used in the model of *geodesic active regions* defined in Equation (2.30) which region part is:

$$\sum_{i=1}^{N_R} \int_{\Omega_i} g_{R,i}(I_0(\mathbf{x})) d\mathbf{x}. \tag{4.64}$$

Equations (4.63) and (4.64) are equivalent if we replace the class index c by i, the number of classes N_R by n_c, the image feature y by I_0 and the function $\varphi \left(P(y|c) \right)$, which depends on the class c, by the function $g_{R,i}$, which also depends on i.

The last question concerns the conditional probability function $P(y|c)$ used in the geodesic active regions approaches. In the initial approach [132, 133], authors used a parametric approach. They supposed that any given image is composed of homogeneous regions which are represented by a Gaussian probability distribution. Hence, Functional (4.63) is equal to the original functional of the geodesic active regions if the conditional probability $P(y|c)$ is equal to the Gaussian distribution of each homogeneous region. We notice that the mixture of Gaussians in [132, 133] is computed in a stage separated from the evolution process, which is not our case. Thus, Rousson-Deriche in [151] integrated the computation of the Gaussian densities in the evolution process. Finally, they approximated in [149] the probability density function $P(y|c)$ with the non-parametric probability density estimation model of Parzen [140, 148] as we did in our approach.

The previous comments showed that the model of geodesic active regions are included in our image classification approach. More precisely, the model of Paragios-Deriche-Rousson corresponds to the first part of our stochastic process defined in Equations (4.59), and equal to (4.8), that carries out the classification task with the *maximum posterior probability* (MAP) approach. However, the MAP approach is less performant than the information theoretic approach presented in Section 4.2 since the MAP model does not validate its classification result. It is possible to validate the performance of the estimation with the second part of our stochastic process (4.8), $Y \rightarrow C^{est}$, which corresponds to a *validation part*. In fact, the stochastic process (4.8) can be interpreted with the general *cross-validation approach* which is composed of two steps [146]: one step to estimate assumptions of the given model about a set of data, such as classification, and a second step to validate the estimation of the classification. Cross-validation approaches have been applied to image restoration and to compute the optimal amount of smoothing in the ridge detection method [146]. Thus, in our case of classification, the first part of the Markov chain (4.8), $C \rightarrow Y$, estimates the candidate assumption, i.e. the candidate among the n_c classes by maximizing the transmission probability

which corresponds to the MAP approach, $P(c)P(y|c)$, and the second part of the Markov chain, $Y \rightarrow C^{est}$ validates the classification estimation made in the first part.

4.6.3 Non-Parametric Active Contours based on Shape Gradient Method

As presented in Section 2.4.1, Aubert-Barlaud-Faugeras-Jéhan-Besson (ABFJB) introduced in [13, 99] a new general framework to define active contours models based on boundary and region functionals thanks to the shape gradient method developed by Delfourd-Zolesion in [69]. In [99], they defined an active contour model which evolves according to the intensity variance to segment two (no-connected) regions having different variances. We used this segmentation model on Figures 4.8(f-i) to classify two regions having the same intensity mean but different variances. We also observed the limit of this model on Figures 4.9(b-e) where regions have the same intensity mean and variance.

Based on the framework of ABFJB, Herbulot-Jehan-Besson-Barlaud-Aubert (HJBA) presented in [90, 91] a segmentation model that used information theoretic concepts such as entropy and joint entropy. Their model also estimates probability densities non-parametrically with the non-parametric probability density estimation model of Parzen [140, 148]. Their approach is also included in ours because it also corresponds to the first part of the stochastic process (4.8) as in the previous section. The classification functional associates with (4.8) is given by Equation (4.63) where the function φ, in the case of HJBA, is equal to:

$$\varphi = -q(I_0(\mathbf{x}), \Omega_i) \ln q(I_0(\mathbf{x}), \Omega_i), \tag{4.65}$$

given in Equation (2.47).

Thus, conceptually speaking, the model of HJBA is also included in our classification approach. As in the case of Paragios-Deriche-Rousson, it does not validate its estimation of classification/segmentation because it does not use the cross-validation approach defined in the second part of the stochastic model (4.8).

4.6.4 Mutual Information

We finish the comparison of our model with other active contour models using statistical and information theoretic concepts with the *mutual information* tool. The mutual information (MI) concept is of huge interest in the image processing community since it has been widely and successfully used for e.g. multi-modal medical image registration, classification and feature extraction. MI is related to the classification task by *Fano's inequality* [77]. Indeed, let us consider again the stochastic process:

$$C \rightarrow Y \rightarrow C^{est} \rightarrow E.$$

If we apply Fano's inequality on the previous stochastic process, it gives us a *lower bound* of the error probability of classification:

$$\mu_E = P_e \geq \frac{\mathcal{H}_e(C|Y) - 1}{\log n_c} = \frac{\mathcal{H}_e(C) - I(C,Y) - 1}{\log n_c} \propto -MI(C,Y), \qquad (4.66)$$

where C is the class label, Y the image feature, $\mathcal{H}_e$ the entropy function and MI the mutual information function.

In [106, 107], Kim-Fisher-Yezzi-Cetin-Willsky proposed to use the mutual information between the class labels and the features to carry out the classification/segmentation process. They also used a non-parametric estimation of the probability density functions.

The mutual information concept has been used in many image processing problems because it is *not* always possible to directly compute the probability of classification P_e. In this case, the solution is to minimize the lower bound of the error probability by maximizing the mutual information $MI(C,Y)$ between the class labels C and the image features Y. However, it is obviously better to minimize directly the error probability rather than its lower bound to ensure a good classification result, which is possible with the framework introduced in Section 4.3.1.

4.7 Conclusion

This chapter presents a new image classification/segmentation model based on information theory and PDE-based approach. The proposed model benefits from statistic and deterministic approaches, which are used in a complementary way. Indeed, information theory, combined with a stochastic process and error probability, allowed us to define a functional of classification with respect to n_c class regions. As usual in statistical approaches, many solutions are likely and different methods exist to find one, such as the genetic algorithm [68] which is a probabilistic optimization method. We decided to determine the minimum of the classification functional in a deterministic way with a variational approach based on the shape gradient method. This allowed us to use efficient numerical schemes to deform the unknown class regions, based on the level set method, to determine the solution of the classification problem.

We also observed in our classification task that the statistical regularization model of Markov random fields is equivalent to the determinist regularization model of mean curvature flow when the Gibbs function is equal to the TV functional.

Experimental results, on synthetic and natural images, showed the promising performances of our segmentation model. Moreover, it is possible to improve this classification model by increasing the dimension of the image feature vector Y. In all our experiments, we only consider the grey-level value I_0 of the given image but we could also include the gradient and more interesting segment texture regions with the image decomposition based on the Gabor functions. This will be an interesting direction of research. Furthermore, we considered only $n_c = 2$ class regions in our experiments, which means that the proposed active contour model can segment only two semantic regions in a given image. Thus, it will also be interesting in the future to develop the model to segment more objects by considering the case $n_c > 2$.

We also compared our model to existing models that use active contours and statistical and information theoretic approaches. We analyzed several models and we proved that they are con-

ceptually included in our approach. The main difference between our approach and theirs relies on the cross-validation approach which consists of estimating a hypothesis, which is the classification in our case, and validating it afterward.

Finally, we also observed that our classification model can be interpreted and well-understood thanks to the information theory, which is also a way to validate the proposed segmentation model.

Thus, this chapter presented a new image segmentation model based on region-based information to detect semantic objects lying in images. However, this segmentation model is not able to extract important objects in the presence of occlusions or when some shape information are missing. Thus, we propose in the next chapter a new image segmentation model that uses a prior shape to handle occlusions and missing information.
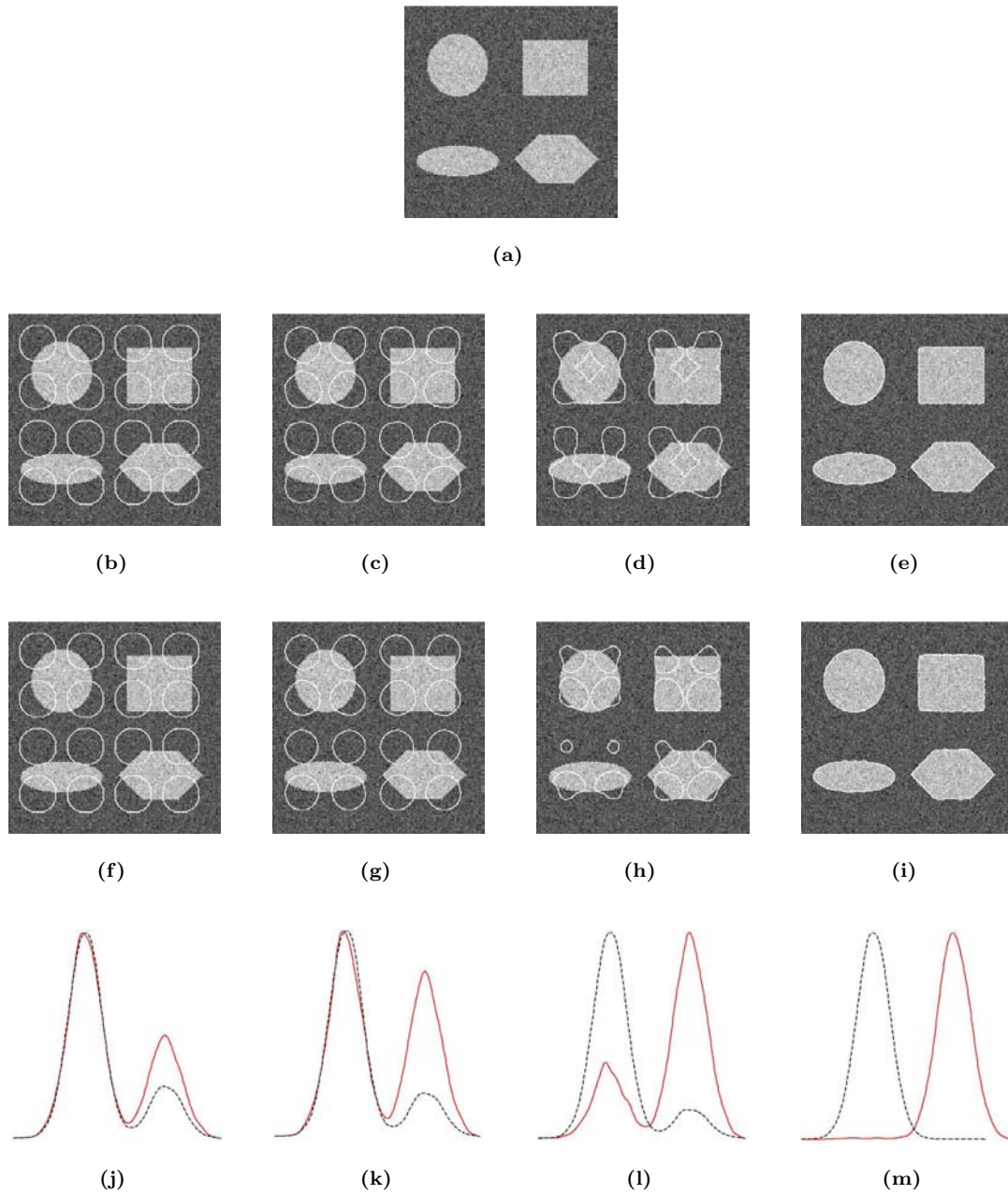
Figure 4.7: Figure (a) presents four objects and a background having two *different* intensity means. Figures (b-e) show the evolution of the active contours without edges model [42]. Figures (f-i) represent the evolution of our active contour/anaconda model and Figures (j-m) correspond to the probability densities inside and outside of the contour C during the evolution process.

(a)

(b)   **(c)**   **(d)**   **(e)**

(f)   **(g)**   **(h)**   **(i)**

(j)   **(k)**   **(l)**   **(m)**

(n)   **(o)**   **(p)**   **(q)**
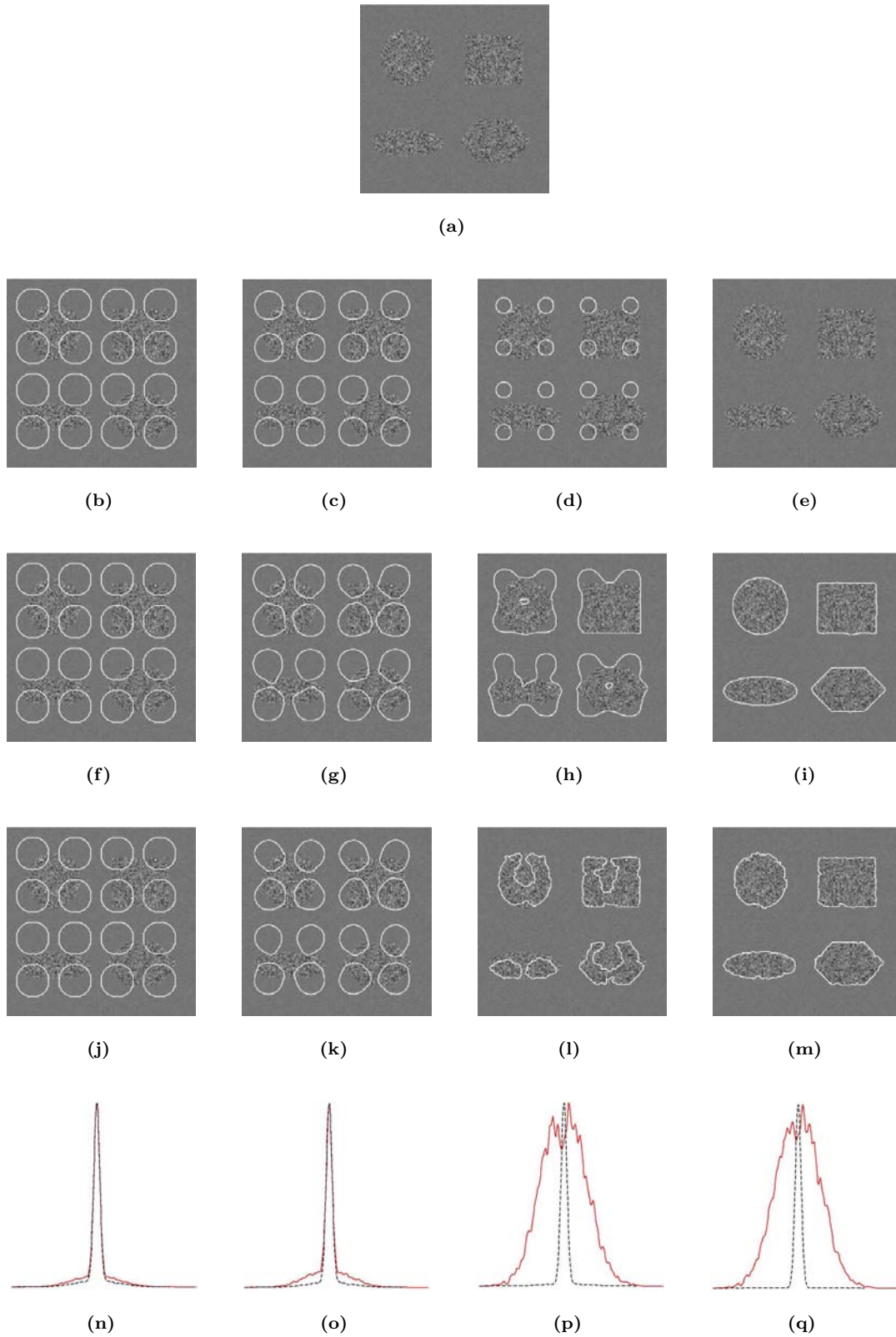
Figure 4.8: Figure (a) presents four objects and a background having the *same* intensity mean but *different* intensity variances. Figures (b-e) show the evolution of the active contours without edges model [42] which fails to segment the four objects because they have the same mean value as the background. Figures (f-i) represent the evolution of the active contour defined in [99] based on a variance criterion. Figures (j-m) show our active contour/anaconda model and Figures (n-q) correspond to the probability densities inside and outside of the contour C during the evolution process.
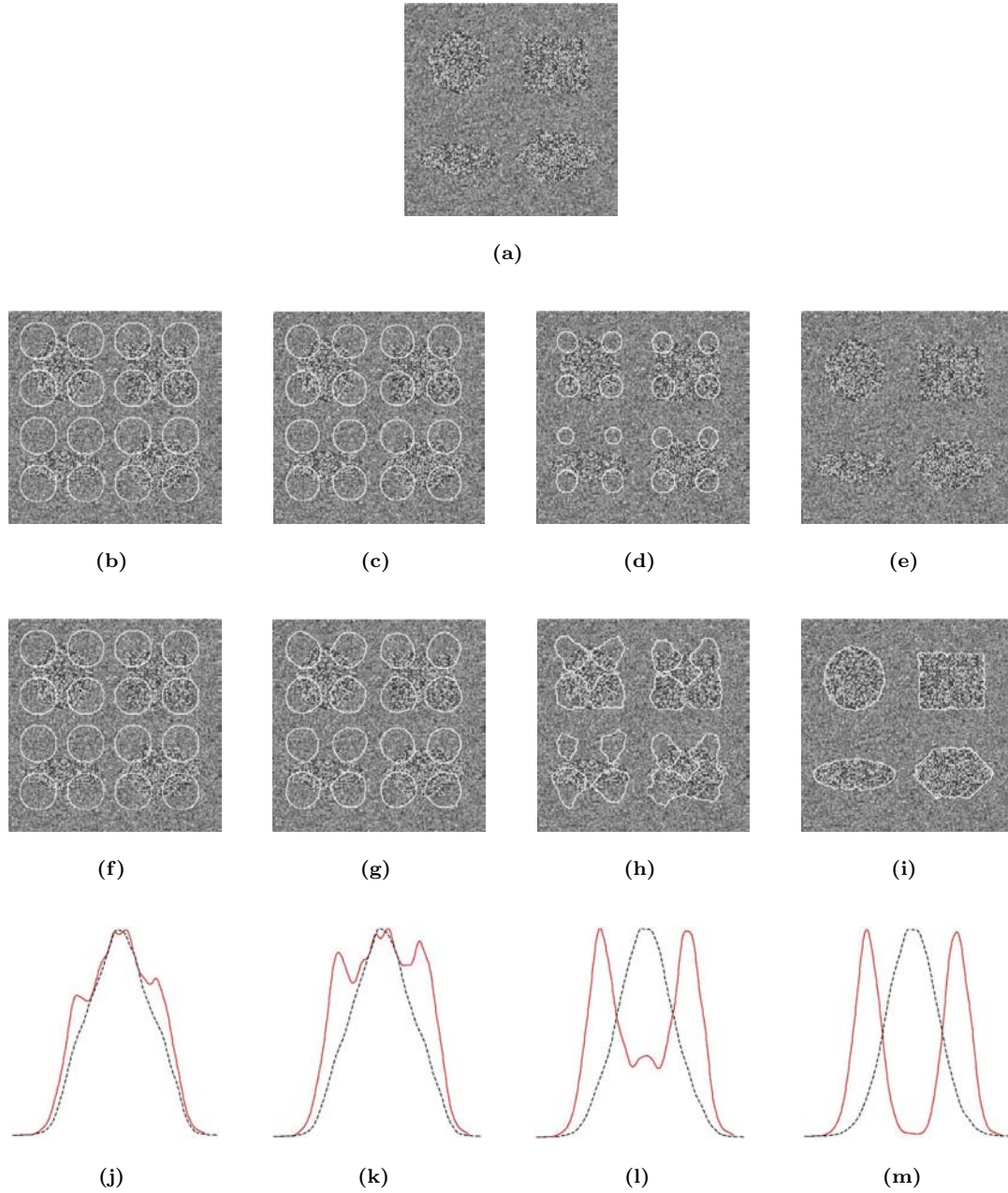
Figure 4.9: Figure (a) presents four objects and a background having the *same* intensity mean, the *same* variance but different statistic moments higher than the 2nd order. This figure is based on Kim's picture in [106]. Figures (b-e) show the evolution of the active contours defined in [99], based on a variance criterion, which fails to segment the four objects because they have the same variance value as the background. Figures (f-i) represent the evolution of our active contour/anaconda model and Figures (j-m) correspond to the probability densities inside and outside of the contour C during the evolution process. Our model manages to segment the four regions because our model is based on *probability densities* which are different for both regions as shown on Figure 4.9(m).

(a)

(b)   **(c)**   **(d)**   **(e)**

(f)   **(g)**   **(h)**   **(i)**
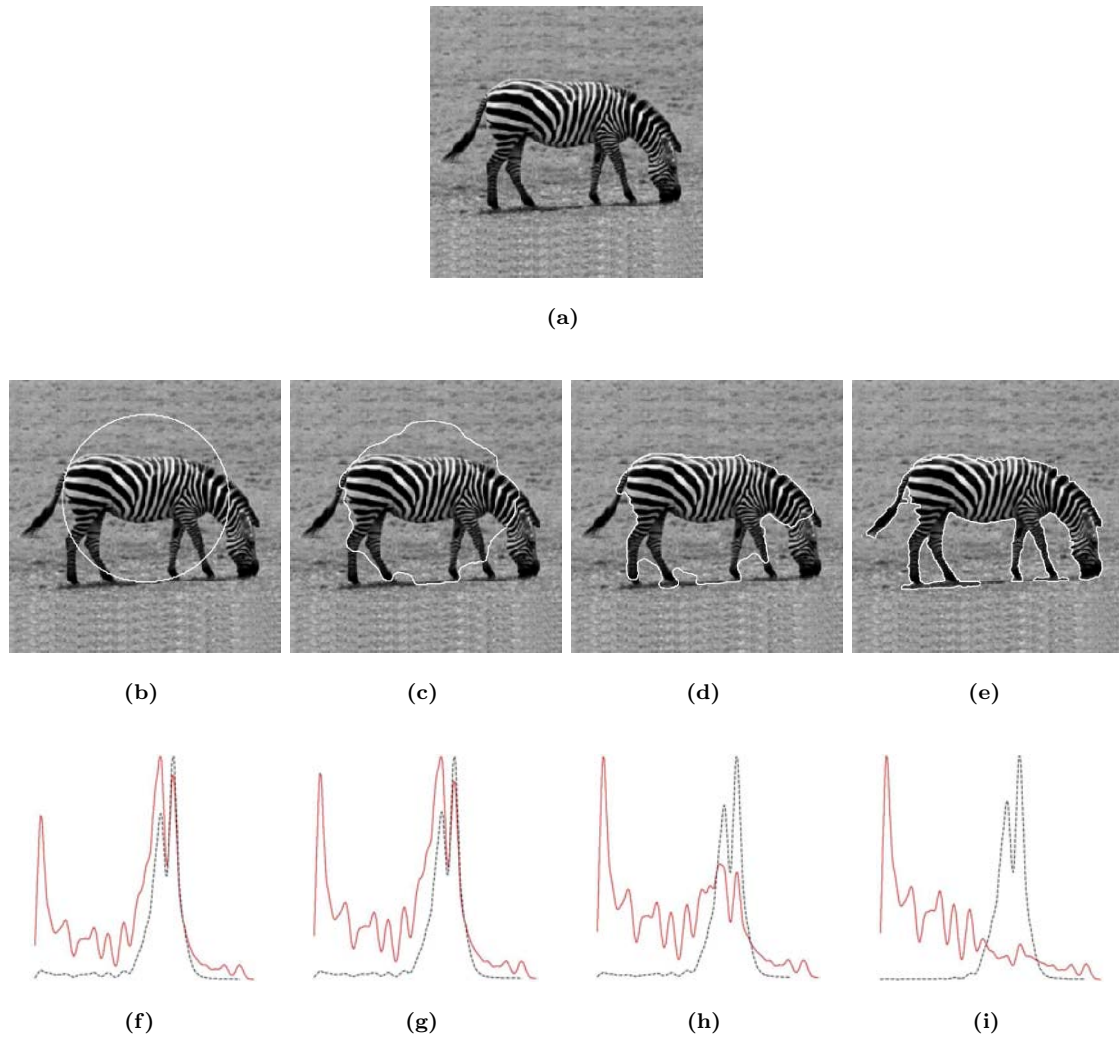
Figure 4.10: Figure (a) presents the zebra picture reproduced from Paragios-Deriche's paper [133]. Figures (b-e) show the evolution of our active contour/anaconda model and Figures (f-i) correspond to the probability densities inside and outside of the contour C during the evolution process.
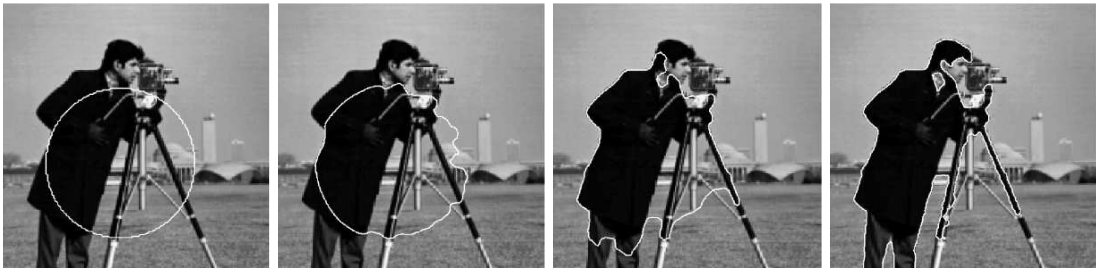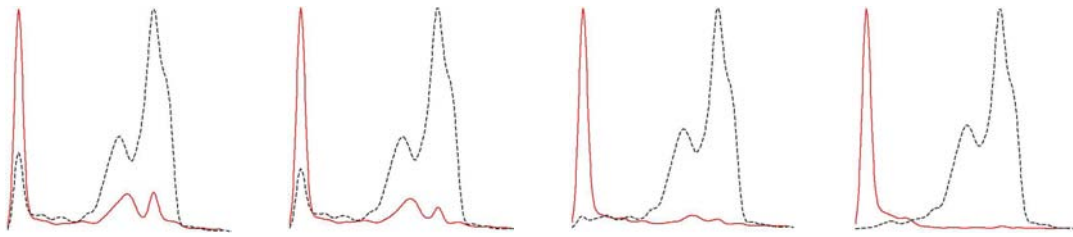
Figure 4.11: Figure (a) presents the cameraman picture. Figures (b-e) show the evolution of our active contour/anaconda model and Figures (f-i) correspond to the probability densities inside and outside of the contour C during the evolution process.

(a)

(b)   **(c)**   **(d)**   **(e)**

(f)   **(g)**   **(h)**   **(i)**
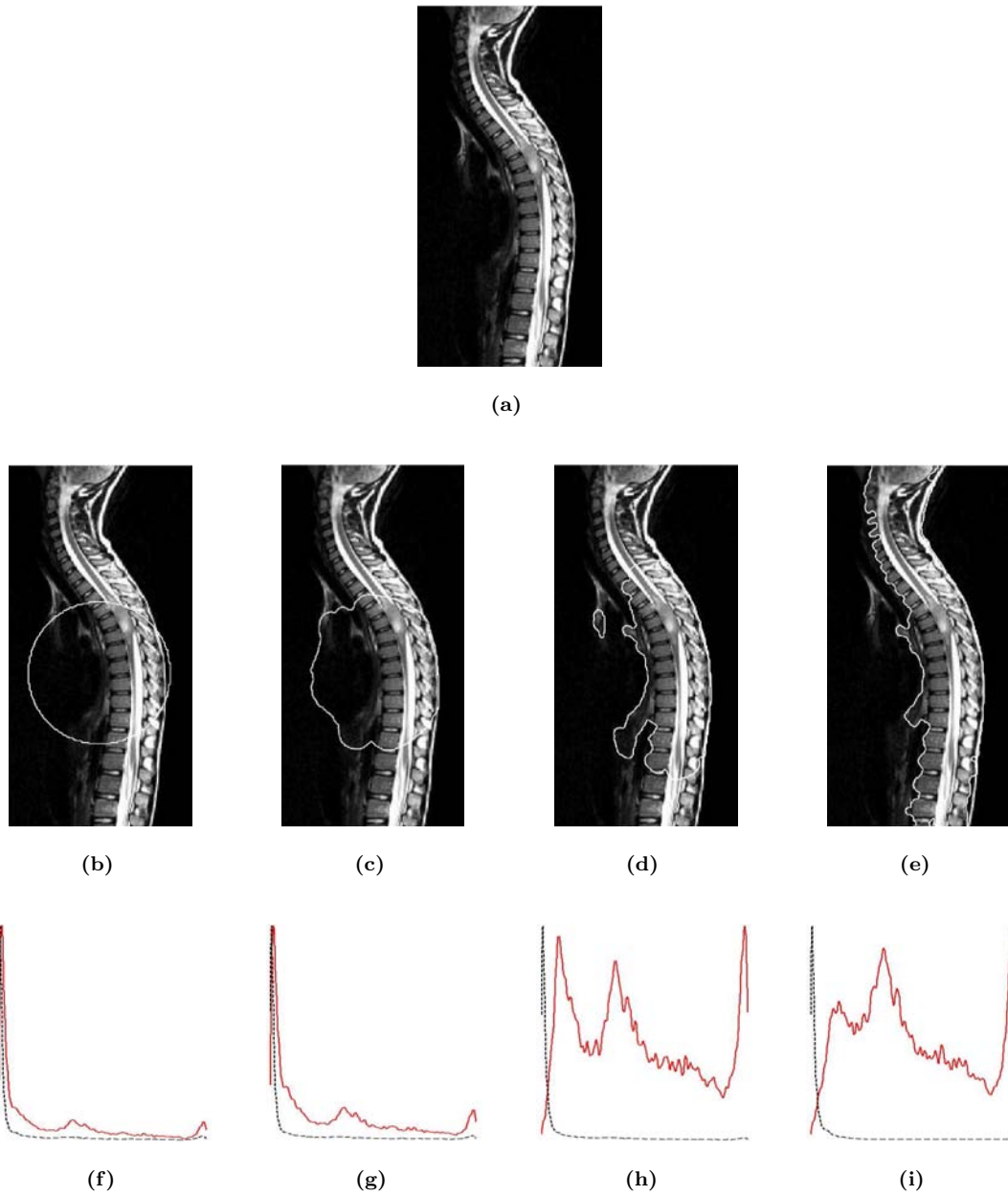
Figure 4.12: Figure (a) presents an x-ray picture. Figures (b-e) show the evolution of our active contour/anaconda model and Figures (f-i) correspond to the probability densities inside and outside of the contour C during the evolution process.

Variational Object Segmentation With Geometric Shape Prior

5

In this chapter, we propose a variational model to segment an object belonging to a given shape space using the active contour method [35, 103, 105], a geometric shape prior [113] and the Mumford-Shah functional [179]. The core of our model is an energy functional composed by three complementary terms. The first one is based on a shape model which constrains the active contour to get a shape of interest. The second term detects object boundaries from image gradients. Finally, the third term globally drives the shape prior and the active contour towards a homogeneous intensity region. The segmentation of the object of interest is given by the minimum of our energy functional. This minimum is computed with the calculus of variations and the gradient descent method that provide a system of evolution equations solved with the well-known level set method. We also prove the existence of this minimum in the space of functions with bounded variation. Applications of the proposed model are presented on synthetic and medical images.
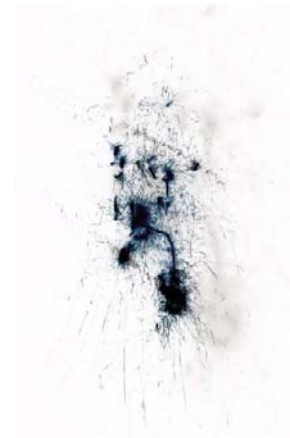
© *Diego Porcel*

5.1   Introduction and Motivations

This work aims at proposing a method to segment structures of interest with a given global shape. The segmentation problem remains fundamental in the computer vision and image processing fields since it is a core component toward automated vision systems and useful in medical applications.

Various methods have been proposed to extract objects of interest in images such as [51, 58, 59, 62, 66, 103]. However these methods employ parametric shape representations which are not as con-

103

veniently used as convenient as intrinsic representations such as the level set function [127, 129, 164]. Other models such as geodesic/geometric active contours [35, 105] use this intrinsic modeling of contours to for example detect fine real-world shapes such as medical structures [101, 115, 188]. As we observed in Chapter 2, level set-based methods are of growing interest since they are independent of the contour parametrization, and thus enable dealing with topological changes. They also benefit from efficient numerical schemes and are naturally extensible to higher dimensions. As we mentioned in Section 2.4, despite of these great advantages, the first-generation active contours, based on image gradients, are highly sensitive to the presence of noise and poor image contrast, which can lead to bad segmentation results. To overcome this drawback, some authors have incorporated robust region-based evolution criteria into the active contour energy functionals that are built from intensity statistics and homogeneity requirements [13, 42, 99, 106, 132, 151, 179], see Section 2.4.1 for more details. Yet the segmentation of *structures of interest* with these second-generation active contours is not able to deal with occlusion problems or presence of strongly cluttered background. The integration of prior shape knowledge about the objects in the segmentation task is therefore a natural way to solve occlusion problems [45, 60, 65, 66, 113, 138, 175] and can be considered as a third generation of active contours, see Section 2.4.2 for more details. In this chapter, we propose a model that exploits the advantages of three generations of active contours.

A geometric shape prior can be defined by different models such as Fourier descriptors, medial axis or atlas-based parametric models. Recently, the level set representation of shapes has been employed as a shape model [43, 113, 138]. This shape description presents strong advantages since being parametrization free, it can represent shapes of any dimension such as curves, surfaces and hyper-surfaces and basic geometric properties such as the curvature and the normal to contours are easily deduced. Finally, this shape representation is also naturally consistent with the level set framework of active contours. In [113], Leventon-Grimson-Faugeras have used a level set representation to model the shape prior. They have defined a shape model of the object of interest by computing a principal components analysis (PCA) of training shapes embedded in level set functions. They have then integrated this shape model in an evolution equation to globally drive the active contour towards the prior shape. However, their evolution equation is not expressed by a partial differential equation and there is no variational formulation associated with this evolution equation. In a general way, a variational formulation is useful both to understand and justify the proposed method. Moreover, evolution equations naturally appear from the variational model through the minimization of the proposed energy functional thanks to the calculus of variations. Finally, a variational formulation of a problem helps to prove the mathematical existence of solutions. Thus we propose a variational approach following the energy functional model of Chen *et al.* in [45] where we integrate the shape prior of Leventon-Grimson-Faugeras [113]. We then add a region-based energy term based on the Mumford-Shah functional [125, 179] to improve the robustness of our segmentation model w.r.t. noise, poor image contrast and initial position of the contour as showed in Section 2.4.1. We will also prove the existence of a solution for our variational segmentation problem.

The organization of this chapter is as follows. In the next section, we briefly review the statistical shape prior proposed by Leventon-Grimson-Faugeras in [113] based on the principal components analysis. Then, we will define our variational model to address the object segmentation problem with a prior shape knowledge and we will derive the system of evolution equations minimizing the proposed energy. We will prove the existence of a minimizer for our variational segmentation model. Then, we will present some results of the proposed method on 2-D synthetic and medical images. Finally, we will discuss our segmentation model and compare it with other ones.

5.2 The Statistical Shape Model of Leventon

5.2.1 Definition of the Principal Components Analysis

The statistical shape model of Leventon-Grimson-Faugeras defined in [113] is based on the PCA that aims at capturing the main variations of a training set while removing redundant information. In [51], Cootes and Taylor used this technique on parametric contours to segment different kinds of objects. The new idea introduced by Leventon-Grimson-Faugeras was to apply the PCA not on the parametric geometric contours but on the signed distance functions (SDFs) of these contours which are implicit and parameter free representations. They justified this choice in two ways: Firstly, SDFs provide a *stronger* tolerance than the parametric curves to slight misalignments during the alignment process of the training data since *the values of neighboring pixels are highly correlated in a SDF*. Secondly, this intrinsic contour representation also improves the shape registration process in terms of robustness, accuracy and speed. Indeed, the problem of the point-wise correspondence of contours (landmarks correspondence) is replaced by a problem of intensity correspondence on grid points which is easier to solve.

From a geometric point of view, the PCA determines the best orthonormal basis $\{\mathbf{e}_1...\mathbf{e}_m\}$ of $\mathbf{R}^m$ to represent a set of n m-dimensional points $\{\varphi_1...\varphi_n\}$ in the sense of the least squares fitting. Vectors $\{\mathbf{e}_i\}$ are given by the eigenvectors of the covariance matrix $\mathbf{\Sigma} = \frac{1}{n}MM^\top$ where M is a matrix which column vectors are the n aligned training SDFs $\{\varphi_j\}$. Vectors $\{\mathbf{e}_i\}$ correspond to the principal variation directions of the set of n points. They are called the *principal components*. Moreover, the first p principal axes define a reduced p-dimensional vector space in $\mathbf{R}^m$ equivalent to a hyper-plane minimizing the sum of squared distances between this hyper-plane and the set of n points. It is important to note that the accuracy of the fitting of this p-D hyper-plane in relation to the set of points can be measured in percentage by the formula $\beta = \sum_{k=1}^{p} \lambda_k / \sum_{k=1}^{n} \lambda_k$ where λ_k are the eigenvalues of $\mathbf{\Sigma}$. Thus, it is possible to arbitrarily fix the fitting percentage β and represent the data in a sub-vector space of dimension p. In practice, only the first principal modes are necessary to model the biggest variations present in our training set. These p principal components are sorted in a matrix $\mathbf{W}_p$. Then, the PCA can produce a new data set based on the training set $\{\varphi_j\}$:

$$\hat{\varphi} = \overline{\varphi} + \mathbf{W}_p\mathbf{x}_{pca}, \tag{5.1}$$

where $\overline{\varphi} = \frac{1}{n}\sum_{j=1}^{n}\varphi_j$ is the mean value and $\mathbf{x}_{pca}$ is called the vector of eigencoefficients, the shape vector or the eigenmodes of variation. Finally, if we suppose that the probability density function of the training set is a Gaussian function, which is often supposed when the PCA is used, then the probability to get $\hat{\varphi}(\mathbf{x}_{pca})$ is

$$P(\hat{\varphi}(\mathbf{x}_{pca})) = \frac{1}{(2\pi)^{p/2}|\mathbf{\Lambda}_p|^{1/2}} \; \exp(-\frac{1}{2}\mathbf{x}_{pca}^\top\mathbf{\Lambda}_p^{-1}\mathbf{x}_{pca}), \tag{5.2}$$

where $\mathbf{\Lambda}_p$ is a diagonal matrix containing the first p eigenvalues.

5.2.2 Applications of the PCA

In this work, we will consider two training sets of 2-D shapes of interest: an *ellipse* and a *left brain ventricle*. For the ellipse, we generate a training set of 30 ellipses by changing the size of a principal axis with a Gaussian probability function and apply the PCA on the SDFs of 30 training ellipses. We obtain one principal component that fits at 98% the set of ellipses. Figure 5.1 shows the aligned

training ellipses and the shape function corresponding to the mean and the eigenmode of variation of the training set.

(a)

(b) $\mathbf{x}_{pca} = -2\lambda_1$ **(c)** Mean **(d)** $\mathbf{x}_{pca} = 2\lambda_1$
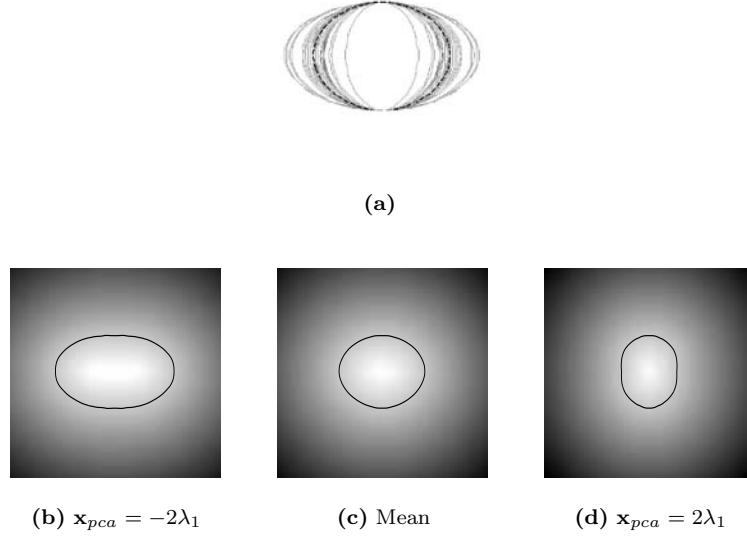
Figure 5.1: Figure (a) presents the 30 aligned training ellipses with the mean ellipse in dotted line. Figure (c) shows the mean value $\overline{\varphi}$. Figures (b) and (d) present $\overline{\varphi} \pm 2\lambda_1\mathbf{e}_1$, the unique eigenmode of variation of SDF ellipses which λ_1 is the eigenvalue. The zero level sets of the shape function $\hat{\varphi}$ is plotted in solid dark line.

For the left brain ventricle, we use 2-D medical images. We extract 45 2-D images of left ventricles from several coronal slices of T1-Weighted Magnetic Resonance images (MRI) of healthy volunteers (Figure 5.2) to build our shape model. Then, we rigidly register/align the training curves representing the object of interest by minimizing the shape similarity measure introduced by Chen *et al.* in [45]:

$$a(C_1, C_j^{new}) = \text{area of } (A_1 \cup A_j^{new} - A_1 \cap A_j^{new}) \quad \text{for } 2 \le j \le n, \tag{5.3}$$

where A_1 and A_j^{new} denote respectively the interior regions of the curves C_1 and C_j^{new} where C_j^{new} is the resulting curve from the rigid registration such that $C_j^{new} = s_j R_{\theta_j} C_j + T_j$ and n is the number of training curves. C_1 and C_j are aligned when the measure a is minimized for the appropriate values $s_j^\star$, $\theta_j^\star$ and $T_j^\star$. Figure 5.3 shows the aligned training ventricles.

After the registration/alignment process, we apply the PCA and we obtain three principal components that fit at 88.2% the set of 45 SDFs of ventricles. Figure 5.3 shows the shape function corresponding to the mean and the three main eigenmodes of variation of the training set.
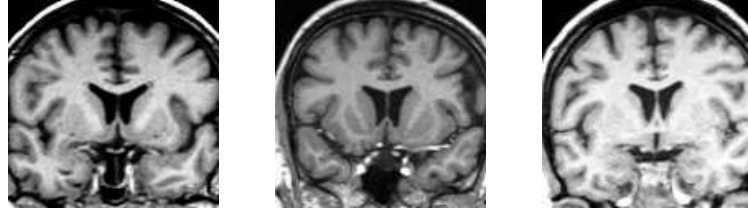
Figure 5.2: Three T1-Weighted Magnetic Resonance images of brain.

5.3 Variational Model for Object Segmentation

5.3.1 The Proposed Energy Functional

We propose the following energy functional to address the problem of object segmentation using a geometric shape prior with local and global image information:

$$F = \beta_s F_{shape}(C, \mathbf{x}_{pca}, \mathbf{x}_{ST}) + \beta_b F_{boundary}(C) + \beta_r F_{region}(\mathbf{x}_{pca}, \mathbf{x}_{ST}, u_{in}, u_{out}), \tag{5.4}$$

where

$$F_{shape} = \int_0^1 \hat{\varphi}^2(\mathbf{x}_{pca}, h_{\mathbf{x}_{ST}}(C(p)))|C_p|dp, \tag{5.5}$$

$$F_{boundary} = \int_0^1 f(|\nabla I(C(p))|)|C_p|dp, \tag{5.6}$$

$$F_{region} = \int_{\Omega_{in}(\mathbf{x}_{pca}, \mathbf{x}_{ST})} (|I_0 - u_{in}|^2 + \mu|\nabla u_{in}|^2)d\mathbf{x} +$$

$$\int_{\Omega_{out}(\mathbf{x}_{pca}, \mathbf{x}_{ST})} (|I_0 - u_{out}|^2 + \mu|\nabla u_{out}|^2)d\mathbf{x}, \tag{5.7}$$

where $d\mathbf{x} = dxdy$, Ω is the image domain, $C \subset \Omega$ is a planar closed curve representing the active contour, $\hat{\varphi} \in L^1(\Omega)$ is the shape function of the object of interest given by the principal components analysis (PCA) (see Equation (5.1)). Vector $\mathbf{x}_{pca} \in \mathbf{R}^p$ is the vector of PCA eigencoefficients, $h_{\mathbf{x}_{ST}}$ is an element of a group of spatial transformations (ST) parametrized by $\mathbf{x}_{ST} \in \mathbf{R}^{n_{ST}}$ (the vector of parameters) where n_{ST} is the number of transformation parameters, f is an edge detecting function such as Equation (2.3), Ω_{in} and Ω_{out} are the inside and outside regions of the zero level set of $\hat{\varphi}$, u_{in} and u_{out} are smooth approximations of the original image I_0 in Ω_{in} and Ω_{out} and β_b, β_s, β_r are arbitrary positive constants that balance the contributions of the boundary, shape and region terms.

The proposed functional F is an extension of the work of Chen *et al.* [45] where we have integrated the shape model of Leventon-Grimson-Faugeras [113] and the Mumford-Shah functional [125, 179]. The integration of the different cited models into one single model allows us to overcome the drawbacks and limitations of each model. We will develop this fact in Section 5.6. Let us now analyze the shape (5.5) and region (5.7) terms in the two following sections.

5.3.2 Shape Term F_{shape}

F_{shape} is a functional introduced by Bresson-Vandergheynst-Thiran in [29] which depends on the active contour C, the vector $\mathbf{x}_{pca}$ of PCA eigencoefficients and the vector $\mathbf{x}_{ST}$ of geometric trans-

(a)

(b) $\mathbf{x}_{pca} = (-2\lambda_1, 0, 0)$ **(c)** Mean   **(d)** $\mathbf{x}_{pca} = (2\lambda_1, 0, 0)$

(e) $\mathbf{x}_{pca} = (0, -2\lambda_2, 0)$ **(f)** Mean   **(g)** $\mathbf{x}_{pca} = (0, 2\lambda_2, 0)$

(h) $\mathbf{x}_{pca} = (0, 0, -2\lambda_3)$ **(i)** Mean   **(j)** $\mathbf{x}_{pca} = (0, 0, 2\lambda_3)$
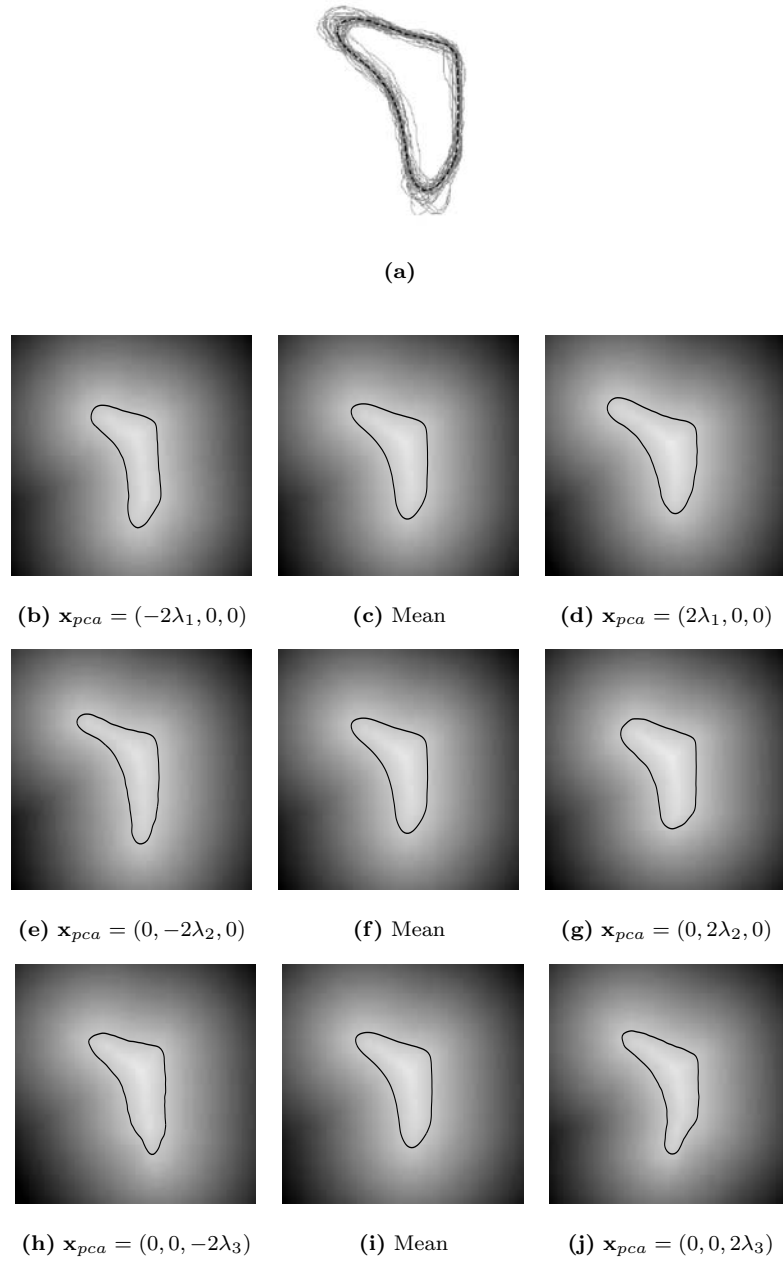
Figure 5.3: Figure (a) presents the 45 aligned training ventricles with the mean left ventricle in dotted line. The middle column is the mean value and the right and left columns present two eigenmodes of variation of the ventricle. The zero level sets of the shape function $\hat{\varphi}$ is plotted in solid dark line.

formations. This functional evaluates the shape difference between the contour C and the zero level set, $\hat{C}$, of the shape function, $\hat{\varphi}$, provided by the PCA. It is an extension of the shape-based term of Chen *et al.* [45] coupled with the shape model of Leventon-Grimson-Faugeras [113]. To give an interpretation of F_{shape}, let us take a rigid transformation with the scale parameter equal to one,

the angle and the vector of translations equal to zero, Thus, the function $\hat{\varphi}^2$ at point $C(q)$ is:

$$\hat{\varphi}^2(\mathbf{x}_{pca}, h_{\mathbf{x}_{ST}}(C(p))) = \hat{\varphi}^2(\mathbf{x}_{pca}, C(p)) \simeq |\hat{C}_{\mathbf{x}_{pca}}(p_{min}) - C(p)|^2, \tag{5.8}$$

where $|.|$ stands for the Euclidean norm. The equality is not strict since the shape function $\hat{\varphi}$ is not a SDF as Leventon noticed in [111, 113]. However, the PCA applied on aligned SDFs of a training set produces shape functions *very close* to SDFs. The case of a strict equality in Equation (5.8), i.e. the case of $\hat{\varphi}$ is a true SDF, will be discussed in Section 5.6. Figure 5.4 illustrates the function $\hat{\varphi}$ and $\hat{C}_{\mathbf{x}_{pca}}(p_{min})$. In practice, the point $\hat{C}_{\mathbf{x}_{pca}}(p_{min})$ and the value p_{min} are *not* computed. $\hat{C}_{\mathbf{x}_{pca}}(p_{min})$ corresponds to the closest point of $C(p)$ on the zero level set of $\hat{\varphi}$ and we use $\hat{C}_{\mathbf{x}_{pca}}(p_{min})$ to illustrate the shape function at point $C(p)$. Indeed, the shape function $\hat{\varphi}^2(\mathbf{x}_{pca}, h_{\mathbf{x}_{ST}}(C(p)))$ is equal to the distance $|\hat{C}_{\mathbf{x}_{pca}}(p_{min}) - C(p)|^2$, i.e. the value of the signed distance function $\hat{\varphi}$ at the point $C(p)$. Finally, F_{shape} is obtained by integrating $\hat{\varphi}^2$ along the active contour, which defines the shape similarity measure equivalent to the sum of square differences (SSD).
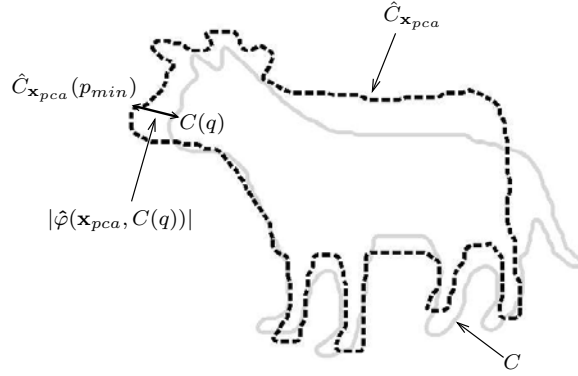
Figure 5.4: Illustration of the function $\hat{\varphi}(\mathbf{x}_{pca}, C(p))$: the square shape function is approximatively equal to the square Euclidean distance between the point $C(p)$ and the closest point $\hat{C}_{\mathbf{x}_{pca}}(p_{min})$ on the zero level set $\hat{C}_{\mathbf{x}_{pca}}$ of $\hat{\varphi}(\mathbf{x}_{pca})$.

The minimization of F_{shape} allows us to increase the similarity between the active contour and the shape model. The functional is minimized using the calculus of variations and the gradient descent method which provide three flows acting on the curve C, the vector of eigencoefficients $\mathbf{x}_{pca}$ and the vector of geometric transformations $\mathbf{x}_{ST}$. We analyze each of the three flows by fixing the two others. The flow minimizing F_{shape} w.r.t. the curve C is the classical geodesic flow [35, 105]:

$$\begin{cases} \partial_t C(t, p) & = & (\hat{\varphi}^2 \kappa - \langle \nabla \hat{\varphi}^2, \mathcal{N} \rangle)\mathcal{N} & \text{in }]0, \infty[\times[0, 1], \\ C(0, p) & = & C_0(p) & \text{in } [0, 1]. \end{cases} \tag{5.9}$$

The first term of the right-hand side of the flow (5.9), $\hat{\varphi}^2 \kappa \mathcal{N}$, is a mean curvature flow weighted by the square shape function $\hat{\varphi}$. The second term, $\langle \nabla \hat{\varphi}^2, \mathcal{N} \rangle \mathcal{N}$, is a flow which pushes the contour C toward the zero level set of $\hat{\varphi}$, i.e. the contour $\hat{C}$, thanks to the vector field $\nabla \hat{\varphi}^2$ which is close to the gradient of a square distance function. The PDE defined in Equation (5.9) changes the active

contour shape into any shape provided by the PCA model. This shape morphing has two main advantages. First, it is independent of the contour parametrization because of the intrinsic level set representation. This means that the landmarks correspondence problem is replaced by a grid point-wise intensity correspondence which is easier to solve. It is more accurate than parametrized shape morphing since the degree of deformation of level set functions is higher. Figure 5.5 presents the morphing between two curves.

(a)   **(b)**   **(c)**

(d)   **(e)**   **(f)**
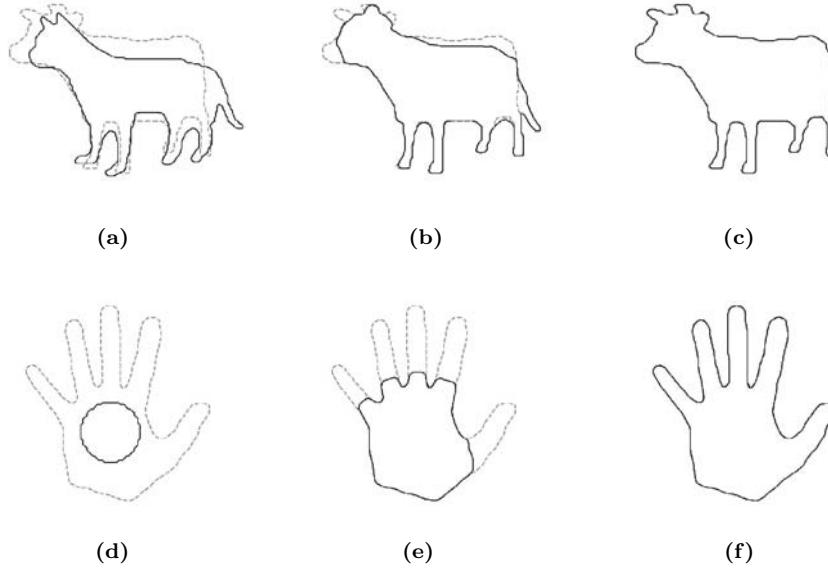
Figure 5.5: Minimization of F_{shape} with the flow given in Equation (5.9), $\mathbf{x}_{ST}$ and $\mathbf{x}_{pca}$ being fixed. Active contour is in solid line and the shape prior in dotted line. Figures (a)-(c) show the matching of a cat (initial active contour) into a cow (shape prior). Figures (d)-(f) present the matching of a circle into a hand.

The flow minimizing F_{shape} w.r.t. the vector of eigencoefficients $\mathbf{x}_{pca}$ is:

$$
\begin{cases}
d_t\mathbf{x}_{pca}(t) & = & -2\int_0^1 \hat{\varphi}\nabla_{\mathbf{x}_{pca}}\hat{\varphi} \ |C_p|dp & \text{in }]0,\infty[\times\Omega_{pca}, \\
\mathbf{x}_{pca}(t=0) & = & \mathbf{x}_{pca_0} & \text{in } \Omega_{pca}.
\end{cases}
\tag{5.10}
$$

$$
\text{with} \quad \nabla_{\mathbf{x}_{pca}}\hat{\varphi} = \begin{pmatrix} \mathbf{e}_{pca}^1 \\ \vdots \\ \mathbf{e}_{pca}^p \end{pmatrix},
$$

where $\mathbf{e}_{pca}^i$ is the ith principal component/eigenvector of the PCA presented in Section 5.2 and Ω_{pca} is the space of PCA variables defined by $\Omega_{pca} = [-3\lambda_1, 3\lambda_1] \times ... \times [-3\lambda_p, 3\lambda_p]$ which λ_i is the eigenvalue of the ith principal component. We choose a range of 3 standard deviations, λ_i, because we suppose that the probability density of training sets is Gaussian. The evolution Equation (5.10) changes the shape function $\hat{\varphi}$ to match its zero level set with the active contour. Figure 5.6 presents this shape matching.
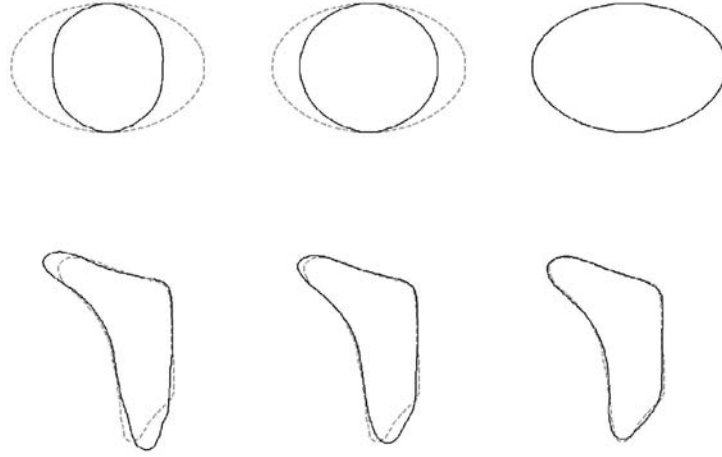
Figure 5.6: Minimization of F_{shape} with the flow given in Equation (5.10), φ and $\mathbf{x}_{ST}$ being fixed. The prior shape is in solid line and the active contour in dotted line. The first row presents the shape evolution of the PCA model of 30 ellipses (see Section 5.2.2). The zero level set of the shape function $\hat{\varphi}$ evolves to match with the active contour representing an ellipse taken in the training set. The second row shows the shape evolution of the PCA model of 45 left brain ventricles (see also Section 5.2.2). The shape model changes to match with the active contour representing a left brain ventricle taken in the training set.

The flow minimizing F_{shape} w.r.t. the vector of geometric transformations $\mathbf{x}_{ST}$ is:

$$\begin{cases} d_t \mathbf{x}_{ST}(t) & = -2 \int_0^1 \hat{\varphi} \langle \nabla \hat{\varphi}, \nabla_{\mathbf{x}_{ST}} h_{\mathbf{x}_{ST}}(C) \rangle |C_p| dp & \text{in }]0, \infty[\times \Omega_{ST}, \\ \mathbf{x}_{ST}(t=0) & = \mathbf{x}_{ST_0} & \text{in } \Omega_{ST}. \end{cases} \quad (5.11)$$

In our work, we consider the 2-D *rigid* (denoted by $h_{\mathbf{x}_{ST}^r}$) and *affine* (denoted by $h_{\mathbf{x}_{ST}^a}$) transformations:

$$h_{\mathbf{x}_{ST}^r} \quad : \quad \mathbf{x} \rightarrow h_{(s,\theta,T)}(\mathbf{x}) = sR_\theta \mathbf{x} + T, \quad (5.12)$$

$$h_{\mathbf{x}_{ST}^a} \quad : \quad \mathbf{x} \rightarrow h_{(s_x,s_y,\theta,s_h,T)}(\mathbf{x}) = R_{sc} R_\theta R_{sh} \mathbf{x} + T, \quad (5.13)$$

where

$$R_{sc} = \begin{pmatrix} s_x & 0 \\ 0 & s_y \end{pmatrix}, \quad R_\theta = \begin{pmatrix} \cos\theta & \sin\theta \\ -\sin\theta & \cos\theta \end{pmatrix},$$

$$R_{sh} = \begin{pmatrix} 1 & s_h \\ 0 & 1 \end{pmatrix} \text{ and } T = \begin{pmatrix} T_x \\ T_y \end{pmatrix}. \quad (5.14)$$

The vector of rigid transformations $\mathbf{x}_{ST}^r$ is composed of a scale (sc) parameter s, an angle of rotation θ and a vector of translations T and the vector of affine transformations $\mathbf{x}_{ST}^a$ is composed of two scale parameters s_x in x-direction and s_y in y-direction, an angle of rotation θ, a shearing (sh) parameter s_h and a vector of translations T. We will analyze the choice of the affine transformations in Section 5.6. Finally, the domain of the rigid/affine transformations is called Ω_{ST}.

As a consequence, the gradient term $\nabla_{\mathbf{x}_{ST}} h_{\mathbf{x}_{ST}}$ in Equation (5.11) depending on geometric transformations is:

$$\nabla_{\mathbf{x}_{ST}^r} h_{\mathbf{x}_{ST}^r}(\mathbf{x}) = \begin{pmatrix} \frac{\partial h_{\mathbf{x}_{ST}^r}}{\partial s}(\mathbf{x}) = R_\theta \mathbf{x} \\ \frac{\partial h_{\mathbf{x}_{ST}^r}}{\partial \theta}(\mathbf{x}) = s\partial_\theta R_\theta \mathbf{x} \\ \frac{\partial h_{\mathbf{x}_{ST}^r}}{\partial T}(\mathbf{x}) = \mathbf{1} \end{pmatrix}, \tag{5.15}$$

for 2-D rigid transformations and

$$\nabla_{\mathbf{x}_{ST}^a} h_{\mathbf{x}_{ST}^a}(\mathbf{x}) = \begin{pmatrix} \frac{\partial h_{\mathbf{x}_{ST}^a}}{\partial s_x}(\mathbf{x}) = (\partial_{s_x} R_{sc}) R_\theta R_{sh} \mathbf{x} \\ \frac{\partial h_{\mathbf{x}_{ST}^a}}{\partial s_y}(\mathbf{x}) = (\partial_{s_y} R_{sc}) R_\theta R_{sh} \mathbf{x} \\ \frac{\partial h_{\mathbf{x}_{ST}^a}}{\partial \theta}(\mathbf{x}) = R_{sc}(\partial_\theta R_\theta) R_{sh} \mathbf{x} \\ \frac{\partial h_{\mathbf{x}_{ST}^a}}{\partial s_h}(\mathbf{x}) = R_{sc} R_\theta (\partial_{s_h} R_{sh}) \mathbf{x} \\ \frac{\partial h_{\mathbf{x}_{ST}^a}}{\partial T}(\mathbf{x}) = \mathbf{1} \end{pmatrix}, \tag{5.16}$$

for 2-D affine transformations. The evolution equation (5.11) realizes the rigid and affine registration between the zero level set of the shape model $\hat{\varphi}$ and the active contour. Figures 5.7 and 5.8 present affine registrations.

Figure 5.7: Minimization of F_{shape} with the flow given in Equation (5.11), φ and $\mathbf{x}_{pca}$ being fixed. Images represents the affine registration process of a prior shape in solid line into an active contour in dotted line.

Note that the function $\hat{\varphi}$ is evaluated at $(\mathbf{x}_{pca}, h_{\mathbf{x}_{ST}}(C(q))$ in Equations (5.9-5.11).

Let us now express the previous equations in a variational level set formulation as presented in [45, 191]. The level set approach of [191], rather than [35, 105], will be used in Section 5.4 to prove the existence of solution minimizing our energy functional in the space of functions with bounded variation. The level set formulation of the shape functional from Equation (5.5) is:

$$F_{shape} = \int_\Omega \hat{\varphi}^2(\mathbf{x}_{pca}, h_{\mathbf{x}_{ST}}(\mathbf{x}))|\nabla \phi|\delta(\phi)d\mathbf{x}, \tag{5.17}$$

where ϕ is a level set function embedding the active contour C, $\delta(.)$ is the Dirac function and $\delta(\phi)$ is the contour measure on $\{\phi = 0\}$. The level set formulation of F_{shape} (5.17) is equivalent to the geometric formulation (5.5) because of the Coarea formula [73] which proves that $L_f(\phi) = \int_\Omega f(\mathbf{x})\delta(\phi)|\nabla \phi|d\mathbf{x} = \int_0^L f(C(s))ds = \int_0^1 f(C(p))|C_p|dp$ where L is the length of $C = \{\phi = 0\}$. Samson-Blanc Féraud-Aubert-Zerubia presented the proof in [156]. The level set formulation of

(d)   **(e)**   **(f)**
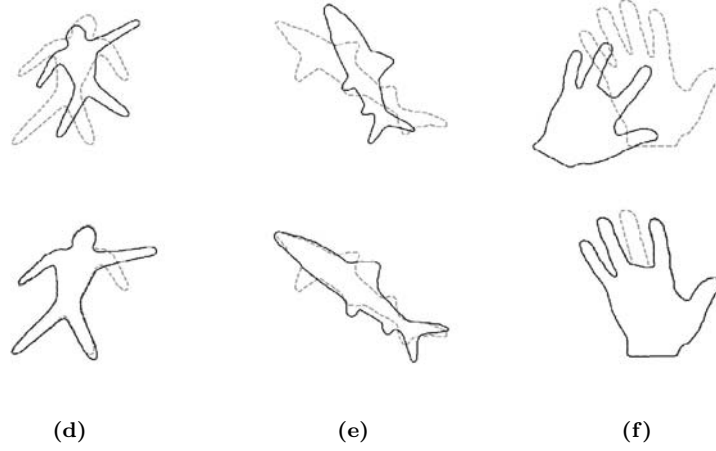
Figure 5.8: Minimization of F_{shape} with the flow given in Equation (5.11), φ and $\mathbf{x}_{pca}$ being fixed. Each column (c,d,e) presents the affine registration of a prior shape in solid line into an active contour in dotted line. The first row shows the initial position of the shapes and the second row the registered shapes. This registration process works with shapes having different local structures and missing information.

Equations (5.9-5.11) are:

$$\begin{cases} \partial_t \phi(t, \mathbf{x}) & = & \left(\hat{\varphi}^2 \kappa - \langle \nabla \hat{\varphi}^2, \frac{\nabla \phi}{|\nabla \phi|} \rangle \right) \delta(\phi) & \text{in }]0, \infty[\times \Omega, \\ \phi(0, \mathbf{x}) & = & \phi_0(\mathbf{x}) & \text{in } \Omega, \\ \frac{\delta(\phi)}{|\nabla \phi|} \partial_{\mathcal{N}_{\partial\Omega}} \phi & = & 0 & \text{on } \partial\Omega, \end{cases} \quad (5.18)$$

$$\begin{cases} d_t \mathbf{x}_{pca}(t) & = & -2 \int_\Omega \hat{\varphi} \nabla_{\mathbf{x}_{pca}} \hat{\varphi} |\nabla \phi| \delta(\phi) d\mathbf{x} & \text{in }]0, \infty[\times \Omega_{pca}, \\ \mathbf{x}_{pca}(t = 0) & = & \mathbf{x}_{pca_0} & \text{in } \Omega_{pca}, \end{cases} \quad (5.19)$$

$$\begin{cases} d_t \mathbf{x}_{ST}(t) & = & -2 \int_\Omega \hat{\varphi} \langle \nabla \hat{\varphi}, \nabla_{\mathbf{x}_{ST}} h_{\mathbf{x}_{ST}} \rangle |\nabla \phi| \delta(\phi) d\mathbf{x} & \text{in }]0, \infty[\times \Omega_{ST}, \\ \mathbf{x}_{ST}(t = 0) & = & \mathbf{x}_{ST_0} & \text{in } \Omega_{ST}. \end{cases} \quad (5.20)$$

In our segmentation model, the flows given by the Equations (5.18-5.20) are simultaneously used to constraint the active contour to get a shape of interest whatever the position of the active contour in the image.

We thus defined in this section a PDE-based process to force the active contour to get a particular shape. In the next section, we will introduce image information in our segmentation method to capture the object of interest in the given image.

5.3.3 Region Term F_{region}

In this section, we define a functional to drive the shape model towards an homogeneous intensity region with the shape of interest. If our objects of interest are supposed to have a smooth intensity

surface then the Mumford-Shah (MS) model is the most adapted model to segment these objects.

At this stage, we have the choice to apply the MS model either on the active contour or the shape prior. Since the general MS model extracts homogeneous regions [179] and our objective is to capture a homogeneous object *with a given shape* then the best solution is to apply the MS model on the shape prior. The MS model applied on the given shape prior will globally drive it toward a homogeneous intensity region with the shape of interest. An illustration of this choice will appear in Section **??**. We modify the MS functional [125] defined by Vese-Chan [179] in Section 2.4.1 to segment a smooth region which shape is described by the PCA model:

$$
F_{region}(\mathbf{x}_{pca}, \mathbf{x}_{ST}, u_{in}, u_{out}) = \int_{\hat{C}(\mathbf{x}_{pca}, \mathbf{x}_{ST})} ds +
$$
$$
\int_{\Omega_{in}(\mathbf{x}_{pca}, \mathbf{x}_{ST})}(|I_0 - u_{in}|^2 + \mu|\nabla u_{in}|^2)d\mathbf{x} + \int_{\Omega_{out}(\mathbf{x}_{pca}, \mathbf{x}_{ST})}(|I_0 - u_{out}|^2 + \mu|\nabla u_{out}|^2)d\mathbf{x}, \quad (5.21)
$$

where the curve $\hat{C}$ is the zero level set of the shape function $\hat{\varphi}$ given by the PCA process. The function $\hat{\varphi}$ defines an image partitioned into two regions Ω_{in} and Ω_{out}, representing respectively the object and the background, which common boundary is $\hat{C}$:

$$
\begin{cases}
\Omega_{in}(\mathbf{x}_{pca}, \mathbf{x}_{ST}) & = \{\mathbf{x} \in \Omega \mid \hat{\varphi}(\mathbf{x}, \mathbf{x}_{pca}, \mathbf{x}_{ST}) > 0\}, \\
\Omega_{out}(\mathbf{x}_{pca}, \mathbf{x}_{ST}) & = \{\mathbf{x} \in \Omega \mid \hat{\varphi}(\mathbf{x}, \mathbf{x}_{pca}, \mathbf{x}_{ST}) < 0\}, \\
\hat{C}(\mathbf{x}_{pca}, \mathbf{x}_{ST}) & = \{\mathbf{x} \in \Omega \mid \hat{\varphi}(\mathbf{x}, \mathbf{x}_{pca}, \mathbf{x}_{ST}) = 0\}.
\end{cases} \quad (5.22)
$$

The minimization of F_{region} determines the shape parameters $\mathbf{x}_{pca}$ and the parameters $\mathbf{x}_{ST}$ of spatial transformations which captures a region having the shape of interest (with $\mathbf{x}_{pca}$) whatever its position in images (with $\mathbf{x}_{ST}$). In our work, we do not considered the smoothing term, $\int_{\hat{C}} ds$, since shapes generated by the PCA are smooth enough. The functional F_{region} can be written with the shape function $\hat{\varphi}$:

$$
F_{region}(\mathbf{x}_{pca}, \mathbf{x}_{ST}, u_{in}, u_{out}) = \int_{\Omega} \Theta_{in} H(\hat{\varphi}(\mathbf{x}_{pca}, \mathbf{x}_{ST}) d\mathbf{x} + \int_{\Omega} \Theta_{out} H(-\hat{\varphi}(\mathbf{x}_{pca}, \mathbf{x}_{ST}) d\mathbf{x}, \quad (5.23)
$$

where $H(.)$ is the Heaviside function, $\Theta_r = |I_0 - u_r|^2 + \mu|\nabla u_r|^2$ and $r = in$ or out. The modified MS functional (5.23) is minimized using the gradient descent method on $\mathbf{x}_{pca}$ and $\mathbf{x}_{ST}$ and solving the Euler-Lagrange equations for u_{in} and u_{out}:

$$
\begin{cases}
d_t\mathbf{x}_{pca}(t) & = \int_{\Omega} (\Theta_{in} - \Theta_{out}) \frac{\partial\hat{\varphi}}{\partial\mathbf{x}_{pca}} \delta(\hat{\varphi})d\mathbf{x} & \text{in }]0, \infty[\times\Omega_{pca}, \\
& = \int_{\Omega} (\Theta_{in} - \Theta_{out}) \nabla_{\mathbf{x}_{pca}}\hat{\varphi} \, \delta(\hat{\varphi})d\mathbf{x}, & \\
\mathbf{x}_{pca}(t = 0) & = \mathbf{x}_{pca_0} & \text{in } \Omega_{pca},
\end{cases} \quad (5.24)
$$

$$
\begin{cases}
d_t\mathbf{x}_{ST}(t) & = \int_{\Omega} (\Theta_{in} - \Theta_{out}) \frac{\partial\hat{\varphi}}{\partial\mathbf{x}_{ST}} \delta(\hat{\varphi})d\mathbf{x} & \text{in }]0, \infty[\times\Omega_{ST}, \\
& = \int_{\Omega} (\Theta_{in} - \Theta_{out}) \langle\nabla\hat{\varphi}, \nabla_{\mathbf{x}_{ST}}h_{\mathbf{x}_{ST}}\rangle \, \delta(\hat{\varphi})d\mathbf{x}, & \\
\mathbf{x}_{ST}(t = 0) & = \mathbf{x}_{T_0} \text{ in} & \Omega_{ST},
\end{cases} \quad (5.25)
$$

$$\begin{cases} \partial_t u_{in}(t, \mathbf{x}) & = & u_{in} - I_0 - \mu \Delta u_{in} & \text{in }]0, \infty[\times \{\hat{\varphi} > 0\}, \\ u_{in}(0, \mathbf{x}) & = & I_0 & \text{in } \{\hat{\varphi} > 0\}, \\ \\ \partial_t u_{out}(t, \mathbf{x}) & = & u_{out} - I_0 - \mu \Delta u_{out} & \text{in }]0, \infty[\times \{\hat{\varphi} < 0\}, \\ u_{out}(0, \mathbf{x}) & = & I_0 & \text{in } \{\hat{\varphi} < 0\}. \end{cases} \tag{5.26}$$

Figure 5.9 shows that the minimization of F_{region} segments objects of interest when a part of information is missing and in presence of noise and occlusion. This model can also be used to segment the left brain ventricle on Figure 5.10.

(i)
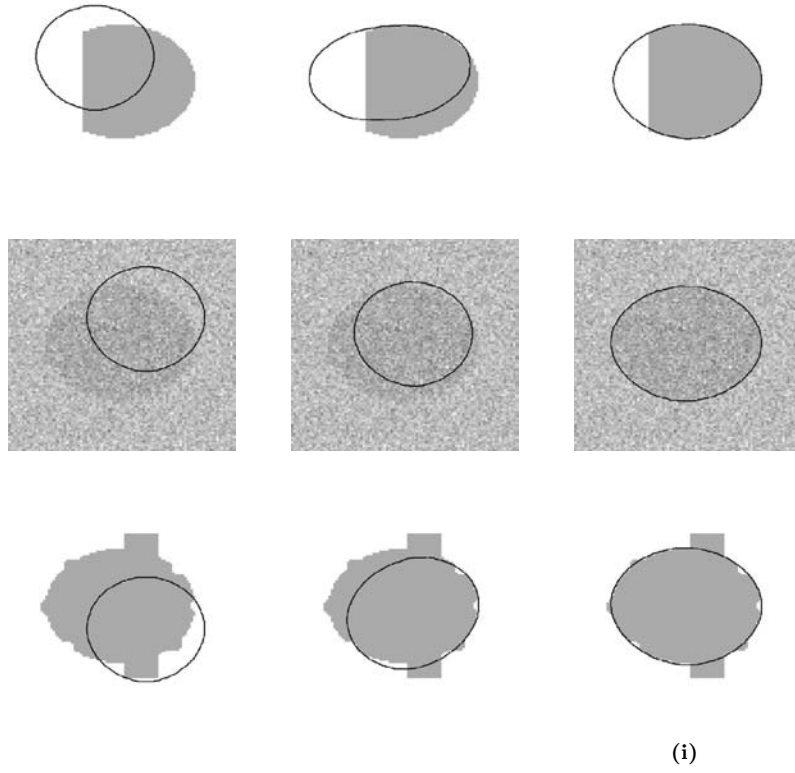
Figure 5.9: Minimization of F_{region} with the flows given by Equations (5.24-5.26). The first row presents the evolution of the segmentation process of an ellipse partially cut. The second row shows the segmentation of a noisy ellipse. And the third row is the segmentation of an occluded ellipse.

However, this segmentation method can not handle local structure variations (see Figure 5.9(i)) when e.g. an ellipse presents irregular boundaries. The model has not captured the local edge variations since it only deals with *global* shape variations provided by the PCA model. If we want to be able to capture the local variations around the global shape we found, we need to add a local criteria to our energy functional. We will consider for this purpose the classic geodesic active contour given by $F_{boundary}$.

Finally, we noticed that another segmentation method based on the Mumford-Shah functional and the PCA model of Leventon-Grimson-Faugeras was proposed by Tsai *et al.* [174, 175] but for a

Figure 5.10: Segmentation of the left ventricle with the flows given by Equations (5.24-5.26).

reduced model of the MS model. They used the *piecewise constant* approximation of the MS functional proposed by Chan-Vese in [42] to define a functional equal to Equation (5.21) when $\mu = 0$. Our model consider the general model of the MS model, i.e. the piecewise smooth approximation, as introduced by Vese-Chan in [179] in the context of active contours. We think that the piecewise smooth case of the MS model allows us to decrease the *intensity bias* present in the piecewise constant case. This bias, which can significantly affect the computation of the parameters $\mathbf{x}_{pca}$ and $\mathbf{x}_{ST}$, is due to the the inhomogeneity of the outside region, i.e. the background, with respect to the inside region, the object of interest. The reason is that the general MS model considers the grey value information by averaging *locally* the intensities in a neighborhood (which size depends on μ, Equation (5.26)) surrounding the contour by means of diffusion whereas the reduced MS model considers the grey value information by averaging *globally* the intensities over the background region and the object region. Cremers-Tischhäuser-Weickert-Schnörr in [62, 66] also compared the two cases of the MS functional and they noticed that the segmentation results are less accurate with the reduced model of MS because of the same reasons.

5.3.4   Combining Shape-Based, Boundary-Based and Region-Based Functionals

In Section 5.3.2, we studied a shape-based functional F_{shape} that evaluates the similarity between the active contour shape and the object shape prior to be segmented. In Section 5.3.3, we analyzed a region-based functional F_{region} which allows us to drive globally the shape prior toward a homogeneous intensity region. We now combine these two functionals with the boundary-based functional $F_{boundary}$ which captures the object edges to obtain a functional F (see Equation (5.4)) to segment objects with a shape model and with global and local image information.

The energy minimization of F is performed using the calculus of variations and the gradient descent method. We obtain a system of coupled evolution equations which steady-state solution gives the minimum of F, which means the solution of the segmentation problem. The existence of a minimum of F is proved in Section 5.4. Functional F is expressed in the Eulerian/level set framework as follows:

$$F = \int_{\Omega} f(x, \mathbf{x}_{pca}, \mathbf{x}_{ST})|\nabla\phi|\delta(\phi)d\mathbf{x} + \beta_r \int_{\Omega} (\Theta_{in} H(\hat{\varphi}(\mathbf{x}_{pca}, \mathbf{x}_T)) + \Theta_{out} H(-\hat{\varphi}))\, d\mathbf{x} \qquad (5.27)$$

where

$$f(\mathbf{x}, \mathbf{x}_{pca}, \mathbf{x}_{ST}) = \beta_s \hat{\varphi}^2(\mathbf{x}_{pca}, h_{\mathbf{x}_{ST}}(\mathbf{x})) + \beta_b g(|\nabla I(\mathbf{x})|). \qquad (5.28)$$

Thus, evolution equations minimizing F are:

$$\begin{cases} \partial_t \phi(t,x) &= \left(f\kappa - \langle \nabla f, \frac{\nabla \phi}{|\nabla \phi|} \rangle \right) \delta(\phi) & \text{in }]0,\infty[\times\Omega, \\ \phi(0,x) &= \phi_0(x) & \text{in } \Omega, \\ \frac{\delta(\phi)}{|\nabla \phi|} \partial_\mathcal{N} \phi &= 0 & \text{on } \partial\Omega, \end{cases}$$

(5.29)

$$\begin{cases} d_t \mathbf{x}_{pca}(t) &= -\int_\Omega \nabla_{\mathbf{x}_{pca}} \hat{\varphi} \; (2\beta_s \hat{\varphi} |\nabla \phi| \delta(\phi) + \beta_r(\Theta_{in} - \Theta_{out})\delta(\hat{\varphi}))d\mathbf{x} & \text{in }]0,\infty[\times\Omega_{pca}, \\ \mathbf{x}_{pca}(t=0) &= \mathbf{x}_{pca_0} & \text{in } \Omega_{pca}, \end{cases}$$

(5.30)

$$\begin{cases} d_t \mathbf{x}_{ST}(t) &= -\int_\Omega \langle \nabla \hat{\varphi}, \nabla_{\mathbf{x}_{ST}} h_{\mathbf{x}_{ST}} \rangle + \\ & \quad (2\beta_s \hat{\varphi} |\nabla \phi| \delta(\phi) + \beta_r(\Theta_{in} - \Theta_{out})\delta(\hat{\varphi}))d\mathbf{x} & \text{in }]0,\infty[\times\Omega_{ST}, \\ \mathbf{x}_{ST}(t=0) &= \mathbf{x}_{T_0} & \text{in } \Omega_{ST}, \end{cases}$$

(5.31)

$$\begin{cases} \partial_t u_{in}(t,\mathbf{x}) &= u_{in} - I_0 - \mu \Delta u_{in} & \text{in }]0,\infty[\times\{\hat{\varphi} > 0\}, \\ u_{in}(0,\mathbf{x}) &= I_0 & \text{in } \{\hat{\varphi} > 0\}, \\ \\ \partial_t u_{out}(t,\mathbf{x}) &= u_{out} - I_0 - \mu \Delta u_{out} & \text{in }]0,\infty[\times\{\hat{\varphi} < 0\}, \\ u_{out}(0,\mathbf{x}) &= I_0 & \text{in } \{\hat{\varphi} < 0\}. \end{cases}$$

(5.32)

5.4 Existence of a Solution For the Minimization Problem

This section deals with the mathematical study of

$$\min_{\phi, \mathbf{x}_{pca}, \mathbf{x}_T, u_{in}, u_{out}} \{ F = \\ \int_\Omega \left(\beta_s \hat{\varphi}^2(\mathbf{x}, \mathbf{x}_{pca}, \mathbf{x}_T) + \beta_b g(\mathbf{x}) \right) |\nabla H(\phi)| d\mathbf{x} + \beta_r F_{region}(\mathbf{x}_{pca}, \mathbf{x}_T, u_{in}, u_{out}) \}.$$

(5.33)

We follow the proofs of Chen *et al.* in [45] and Vese-Chan [178] to prove the existence of a minimizer for our proposed minimization problem using the direct method of the calculus of variations and compactness theorems on the space of functions with bounded variation.

The minimization problem is considered among characteristic functions χ_E of sets $E = \{\mathbf{x} \in \Omega | \phi(\mathbf{x}) \geq 0\}$ with bounded variation. The vector of PCA eigencoefficients $\mathbf{x}_{pca} = (\mathbf{x}_{pca_1}, ..., \mathbf{x}_{pca_p})$ is defined on $\Omega_{pca} = [-3\lambda_1, 3\lambda_1] \times ... \times [-3\lambda_p, 3\lambda_p]$ and the vector of geometric transformations $\mathbf{x}_T = (s_x, s_y, \theta, s_h, T_x, T_y)$ is defined on Ω_T. If $\Omega \subset \mathbf{R}^2$ is the domain of the original image I_0, say $\Omega =]0,255[^2$, then $\Omega_{ST} =]0,255[^2 \times [-\pi, \pi[\times [-127, 127] \times [-255, 255]^2$. Functions u_{in} and u_{out} from Section 5.3.3 are supposed in $C^1(\Omega)$ since they are smoothed versions of the original image I_0 ($u = I_0 + \mu \Delta u$ is the first order discretization of the linear heat diffusion equation $\partial_t u = \Delta u$ with $u(t=0) = I_0$).

We remind some definitions and theorems introduced in Evans-Gariepy [73], Giusti [85], Chen *et al.* in [45], Vese-Chan [178] and Ambrosio [6].

Definition 1: Let $\Omega \subset \mathbf{R}^N$ be an open set and let $f \in L^1(\Omega)$. The total variation norm of f is defined by

$$TV(f) = \int_\Omega |\nabla f| = \sup_{\psi \in \Phi} \left\{ \int_\Omega f(x) \text{div } \psi(x) \right\}, \tag{5.34}$$

$$\text{where} \quad \Phi = \left\{ \psi \in C_0^1(\Omega, \mathbf{R}^N) |\ |\psi(x)| \le 1, \text{on } \Omega \right\}. \tag{5.35}$$

Definition 2: A function $f \in L^1(\Omega)$ is said to have bounded variation in Ω if its distributional derivate satisfies $TV(f) < \infty$. We define $BV(\Omega)$ as the space of all functions in $L^1(\Omega)$ with bounded variation. The space $BV(\Omega)$ is a Banach space, endowed with the norm:

$$\|f\|_{BV(\Omega)} = \|f\|_{L^1(\Omega)} + TV(f). \tag{5.36}$$

Theorem 1 *A measurable subset E of $\mathbf{R}^N$ has finite perimeter in Ω if and only if the characteristic function $\chi_E \in BV(\Omega)$. We have $Per_\Omega(E) = TV(\chi_E) = \int_\Omega |\nabla \chi_E| < \infty$.*

Definition 3: Let $\Omega \subset \mathbf{R}^N$ be an open set and let $f \in L^1(\Omega)$ and $\alpha(x)$ be positive valued continuous and bounded functions on Ω. The weighted total variation norm of f is defined by

$$TV_\alpha(f) \quad = \quad \int_\Omega \alpha(x)|\nabla f| = \sup_{\psi \in \Phi_\alpha} \left\{ \int_\Omega f(x) \text{div } \psi(x) \right\}, \tag{5.37}$$

where

$$\Phi_\alpha = \left\{ \psi \in C_0^1(\Omega, \mathbf{R}^N) |\ |\psi(x)| \le \alpha(x), \text{on } \Omega \right\}. \tag{5.38}$$

If a function f has a finite weighted total variation norm in Ω then it also belongs to $BV(\Omega)$.

Definition 4: A function $f \in BV(\Omega)$ is a special function of bounded variation if its distributional derivative is given by

$$|Df| = TV(f) + \int_{\Omega \cap S_f} J_f d\mathcal{H}^{N-1}, \tag{5.39}$$

where J_f is the jump part defined on the set of points S_f and $\mathcal{H}^{N-1}$ is the (N-1)-dimensional Hausdorff measure. The space of special functions of bounded variation $SBV(\Omega)$ is a Banach space, endowed with the norm:

$$\|f\|_{SBV(\Omega)} = \|f\|_{L^1(\Omega)} + |Df|. \tag{5.40}$$

Theorem 2 *Let $\Omega \subset \mathbf{R}^N$ be an open set with a Lipschity boundary. If $\{f_n\}_{n \ge 1}$ is a bounded sequence in $BV(\Omega)$, then there exist a subsequence $\{f_{n_j}\}$ of $\{f_n\}$ and a function $f \in BV(\Omega)$, such that $f_{n_j} \to f$ strongly in $L^p(\Omega)$ for any $1 \le p < N/(N-1)$ and*

$$TV(f) \le \lim_{n_j \to \infty} \inf TV(f_{n_j}). \tag{5.41}$$

The following theorem is a generalization of the **main theorem** of Chen *et al.* in [45].

Theorem 3 *Let $\Omega \subset \mathbf{R}^N$ be an open set with a Lipschity boundary. If $\{f_n\}_{n \geq 1}$ is a bounded sequence in $BV(\Omega)$ and if $\{\alpha_n\}_{n \geq 1}$ is a sequence of positive valued continuous functions that uniformly converges to α on Ω, then there exists subsequences $\{f_{n_j}\}$ of $\{f_n\}$ and a function $f \in BV(\Omega)$ such that $f_{n_j} \to f$ strongly in $L^p(\Omega)$ for any $1 \leq p < N/(N-1)$ and*

$$TV_\alpha(f) \leq \lim_{n_j \to \infty} \inf TV_{\alpha_{n_j}}(f_{n_j}). \tag{5.42}$$

Theorem 4 *Let Ω be a bounded and open subset of $\mathbf{R}^2$ and I be a given image with $I \in L^\infty(\Omega)$. The minimization problem (5.33) re-written in the following form*

$$\min_{\chi_E, \mathbf{x}_{pca}, \mathbf{x}_T, u_{in}, u_{out}} \{ F = \int_\Omega \left(\beta_s \hat{\varphi}^2(\mathbf{x}, \mathbf{x}_{pca}, \mathbf{x}_T) + \beta_b g(\mathbf{x}) \right) |\nabla \chi_E| d\mathbf{x} + \beta_r F_{region}(\mathbf{x}_{pca}, \mathbf{x}_T, u_{in}, u_{out}) \}. \tag{5.43}$$

has a solution $\chi_E \in BV(\Omega)$, $\mathbf{x}_{pca} \in \Omega_{pca}$, $\mathbf{x}_T \in \Omega_{ST}$ and $u_{in}, u_{out} \in C^1(\Omega)$.

Proof: We use the direct method of the calculus of variations:
(A) Let $\{\chi_{E_n}, \mathbf{x}_{pca_n}, \mathbf{x}_{T_n}, u_{in_n}, u_{out_n}\}_{n \geq 1}$ be a minimizing sequence of (5.43), i.e.

$$\lim_{n \to \infty} F(\chi_{E_n}, \mathbf{x}_{pca_n}, \mathbf{x}_{T_n}, u_{in_n}, u_{out_n}) = \inf_{\chi_E, \mathbf{x}_{pca}, \mathbf{x}_T, u_{in}, u_{out}} F(\chi_E, \mathbf{x}_{pca}, \mathbf{x}_T, u_{in}, u_{out}). \tag{5.44}$$

(B) Since χ_{E_n} is a sequence of characteristic functions of E_n, then $\chi_{E_n}(x) \in \{0, 1\}$ - a.e. in Ω. A constant $M > 0$ exists such that $\|\nabla \chi_{E_n}\|_{L^1(\Omega)} \leq M, \forall n \geq 1$. Therefore, χ_{E_n} is a uniformly bounded sequence on $BV(\Omega)$.
Since $\{\mathbf{x}_{pca_n}\}$ and $\{\mathbf{x}_{T_n}\}$ are bounded sequences on compact spaces Ω_{pca} and Ω_{ST}, subsequences that converge to limits $\mathbf{x}_{pca}$ and $\mathbf{x}_T$ exist.
The integrand $f(x, \mathbf{x}_{pca}, \mathbf{x}_T) = \beta_s \hat{\varphi}^2 + \beta_b g$ is positive and bounded because both functions $\hat{\varphi}^2$ and g are bounded on Ω. Since the PCA is applied on continuous functions (SDFs) then the functions $\hat{\varphi}$ and f are also continuous and $f_n(\mathbf{x}) = f(\mathbf{x}, \mathbf{x}_{pca_n}, \mathbf{x}_{T_n})$ converges uniformly to f on Ω.
Following Theorem 3, a subsequence of χ_{E_n} that converges to a function χ_E strongly in $L^1(\Omega)$ exists.
Moreover , Theorem 3 also states that

$$\int_\Omega f|\nabla \chi_E| \leq \lim_{n_j \to \infty} \inf \int_\Omega f_{n_j}|\nabla \chi_{E_{n_j}}|, \tag{5.45}$$

(C) In the region-based functional defined in Equation (5.23):

$$F_{region}(\mathbf{x}_{pca}, \mathbf{x}_{ST}, u_{in}, u_{out}) = \int_\Omega (\Theta_{in} H(\hat{\varphi}(\mathbf{x}_{pca}, \mathbf{x}_T)) + \Theta_{out} H(-\hat{\varphi})) d\Omega, \tag{5.46}$$

the function $H(\hat{\varphi}(\mathbf{x}_{pca}, \mathbf{x}_T))$ is a characteristic function χ_G of sets $G = \{x \in \Omega | \hat{\varphi}(x) \geq 0\}$. So we have

$$F_{region}(\mathbf{x}_{pca}, \mathbf{x}_{ST}, u_{in}, u_{out}) = \int_\Omega (\Theta_{in}\chi_G(\mathbf{x}_{pca}, \mathbf{x}_T)) + \Theta_{out}(1 - \chi_G)) d\Omega \tag{5.47}$$

and we can define the function $u = u_{in}\chi_G + u_{out}(1 - \chi_G)$. The minimizing sequence of Equation (5.43) implies

$$\lim_{n \to \infty} F_{region}(\mathbf{x}_{pca_n}, \mathbf{x}_{T_n}, u_{in_n}, u_{out_n}) = \inf_{\mathbf{x}_{pca}, \mathbf{x}_T, u_{in}, u_{out}} F_{region}(\mathbf{x}_{pca}, \mathbf{x}_T, u_{in}, u_{out}). \tag{5.48}$$

Since the function χ_G depends continuously on variables $\mathbf{x}_{pca}$ and $\mathbf{x}_T$, we have $\chi_G(\mathbf{x}_{pca_n}, \mathbf{x}_{T_n}) = \chi_{G_n}$ and $u_n = u_{in_n}\chi_{G_n} + u_{out_n}(1 - \chi_{G_n})$. According to Ambrosio's lemma [6], we can deduce that there is a $u \in SBV(\Omega)$, such that a subsequence u_{n_j} converges to u a.e. in $BV - w*$ and

$$F_{region}(\mathbf{x}_{pca}, \mathbf{x}_{ST}, u_{in}, u_{out}) = F_{region}(u) \leq \liminf_{n_j \to \infty} F_{region}(u_{n_j}), \tag{5.49}$$

which means that u is a minimizer of F_{region}. Then, by combining Equations (5.45) and (5.49), χ_E, $\mathbf{x}_{pca}$, $\mathbf{x}_T$, u_{in} and u_{out} are minimizers of (5.43).

5.5   Experimental Results

5.5.1   Implementation issues

Concerning the PCA, the first stage consists in aligning rigidly the training curves representing the object of interest. As we said in Section 5.2.2, this is realized using the shape similarity measure introduced by Chen *et al.* [45]:

$$a(C_1, C_j^{new}) = \text{area of } (A_1 \cup A_j^{new} - A_1 \cap A_j^{new}) \quad \text{ for } 2 \leq j \leq n, \tag{5.50}$$

where A_1 and A_j^{new} denote respectively the interior regions of the curves C_1 and C_j^{new} where C_j^{new} is the resulting curve from the rigid registration such that $C_j^{new} = s_j R_{\theta_j} C_j + T_j$ and n is the number of training curves. C_1 and C_j are aligned when the measure a is minimized for the appropriate values $s_j^\star$, $\theta_j^\star$ and $T_j^\star$. These values are obtained by a global optimization algorithm called the genetic algorithm [68]. The second stage of the PCA consists in doing the singular values decomposition on the SDFs of the aligned training curves using the code provided by Numerical Recipes [1] on the matrix $\mathbf{\Sigma}^{dual} = \frac{1}{n}M^\top M$ (see section 5.2.1 for notations) to extract the n eigenvalues $\lambda_{pca}^{i,dual}$ and the corresponding eigenvectors $\mathbf{e}_{pca}^{i,dual}$. Note that the PCA is performed on $\mathbf{\Sigma}^{dual}$ rather than $\mathbf{\Sigma}$ to give faster and more accurate results. The eigenvectors $\mathbf{e}_{pca}^i$ and the eigenvalues λ_{pca}^i are then given by $\mathbf{e}_{pca}^i = M\mathbf{e}_{pca}^{i,dual}$ and $\lambda_{pca}^i = \lambda_{pca}^{i,dual}$.

Evolution equations (5.29) to (5.32) are numerically solved by iterating the following stages until convergence is reached:

1. Computation of the shape function $\hat{\varphi}(\mathbf{x}_{pca}, \mathbf{x}_{ST})$ using Equation (5.1) and performing the rigid and affine transformations (scaling, rotation, translations and shearing) with the B-splines interpolation method [177].

2. Calculation of the gradient $\nabla\hat{\varphi}$ using a central difference scheme. The term $\nabla_{\mathbf{x}_{pca}}\hat{\varphi}$ is given by the eigenvectors of the PCA model and $\nabla_{\mathbf{x}_{ST}}h_{\mathbf{x}_{ST}}$ is computed according to Equations (5.15) and (5.16).

3. Discretization of terms $|\nabla\phi|$ and $\langle\nabla f, \frac{\nabla\phi}{|\nabla\phi|}\rangle$ with e.g. the Osher-Sethian numerical scheme [129], see Section 2.3.2. Computation of the curvature with central difference schemes. The Dirac function δ and the Heaviside function H are computed by slightly regularized versions following [45, 191].

4. Computation of Functions u_{in} and u_{out} in $\{\hat{\varphi} > 0\}$ and $\{\hat{\varphi} < 0\}$ with the method proposed in [179].

5. Updating $\mathbf{x}_{pca}$, $\mathbf{x}_{ST}$ and ϕ using forward difference schemes of (5.30), (5.31) and (5.29).

   6. Re-distancing the level set function at every iteration with the Fast Marching Method of
      Adalsteinsson-Sethian [2, 117, 163].

5.5.2   Synthetic Image

In this first experiment, we consider an ellipse partially occluded with a noisy boundary and an
ellipse which part of the shape is missing. We applied the PCA on the training set of 30 ellipses
as proposed in Section 5.2.2. The alignment process, which performs the registration of shapes by
genetic programming, needed around 1 minute per 128×128 ellipse. Even if the alignment step is
not fast because the genetic optimization is a global optimization procedure, it is done *once* for all
experiments. The rest of the PCA is fast. The decomposition into principal components, which is
also done only once for all experiments, took a few seconds. And the most important procedures
(since they are used at each iteration) are very fast: the computation of a new shape according to
Equation (5.1) (with an arbitrary vector $\mathbf{x}_{pca}$) took around 10^{-3} second and the spatial transfor-
mations done with the B-splines programming also needed around 10^{-3} second. In all the following
experiments, from Figure 5.11 to Figure 5.16, the segmentation including shape and pose parameters
took around 5 minutes.

   We firstly used our segmentation model to segment an ellipse with irregular boundaries which is
partially occluded by a vertical bar. Figure 5.11 presents a geodesic active contour *without* a shape
prior and Figures 5.12 and 5.13 *with* a shape prior by taking $\beta_s = 1/3$, $\beta_b = 1$, $\beta_r = 10$, $\mu = 50$
and $\Delta t = 0.1$. The way of choosing the weighting parameters is as follows. β_b is always equal to 1.
μ determines the size of the neighborhood where the grey value information is averaged by means
of diffusion (5.32). Then, β_r is chosen such that the shape prior is attracted toward the region
to be segmented. Finally, β_s is selected in order to allow the active contour to move around the
shape prior in order to capture local boundaries. The active contours on Figures 5.12 and 5.13 have
captured high image gradients, i.e. the boundary variations (see Figure 5.12(d)), and also handled
the problem of occlusion thanks to the information contained in the prior shape model.

Figure 5.11: Evolution of the geodesic active contour *without* shape prior information.

   In the second example, our extraction model is applied to extract an ellipse which is partially
cut. Figure 5.14 presents a geodesic active contour *without* a shape prior and Figures 5.15 *with* a
shape prior by taking $\beta_s = 1/3$, $\beta_b = 1$, $\beta_r = 10$, $\mu = 50$ and $\Delta t = 0.1$. The active contour on
Figure 5.15 has captured high image gradients and also the missing part thanks to the information
contained in the prior shape model. Figure 5.16 illustrates what happens when only the *mean* shape
$\overline{\varphi}$ in the PCA model (Equation (5.1)) is used. In this experiment, the eigenmodes of variation are
essential to get a satisfactory result.

(a)   **(b)**   **(c)**

(d)
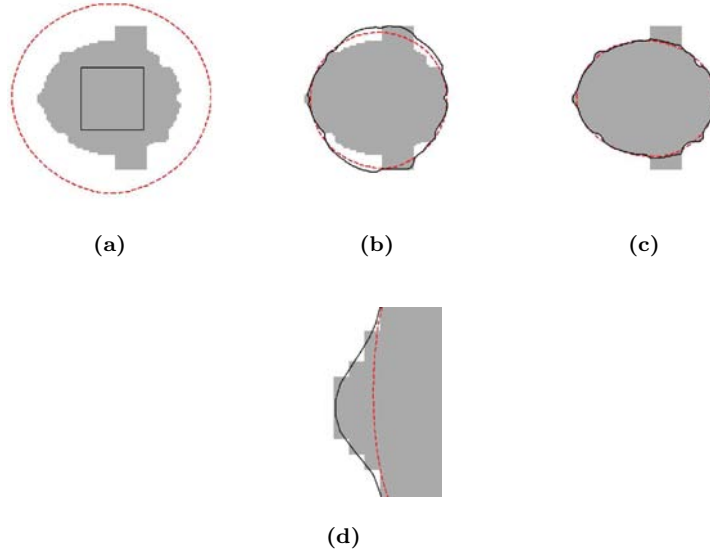
Figure 5.12: The first row presents the evolution of the active contour (in solid line) *with* a shape prior (in dotted line). In the second row, we zoom on the left point of the ellipse to show that our model is able to capture local deformations around the shape prior.
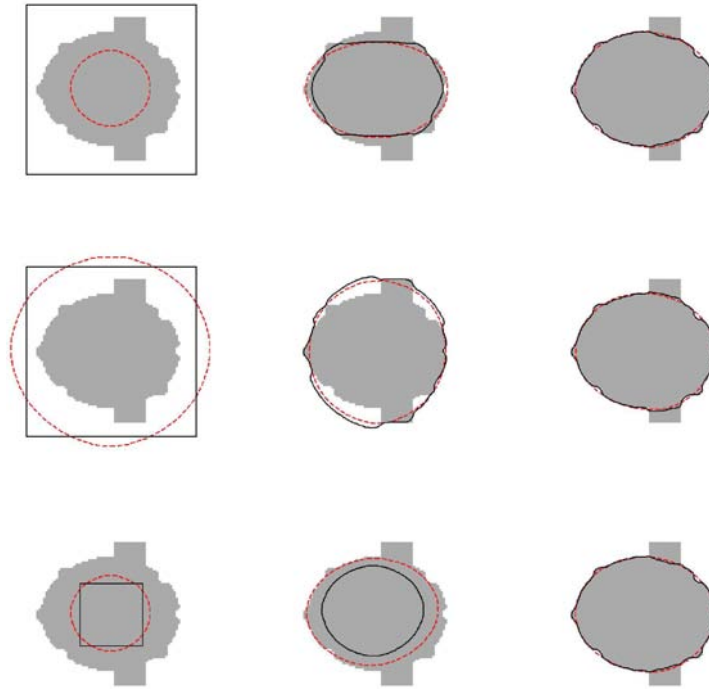
Figure 5.13: Our active contour model (in solid line) with a shape prior (in dotted line) is robust w.r.t. an initial active contour and an initial shape prior outside or inside the ellipse.
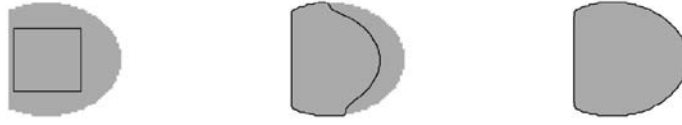
Figure 5.14: Evolution of the geodesic active contour *without* shape prior information.
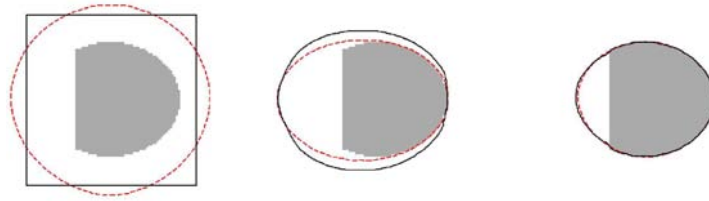
Figure 5.15: Evolution of the active contour (in solid line) *with* the shape prior (in dotted line).
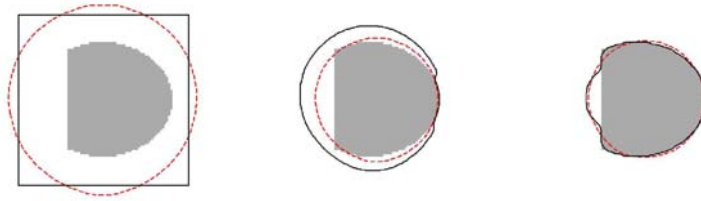
Figure 5.16: Result obtained using only the *mean* shape $\overline{\varphi}$ in the PCA model (Equation (5.1)) without the eigenmodes of variation.

Thus, our shape-based active contour model can segment objects with missing information, occlusion and local shape variations.

5.5.3 Medical Image

In this second experiment, we considered the left brain ventricle and its training set of 45 shapes. The alignment process, done by genetic programming, took around 1 minute per 128×128 ventricle. The decomposition into principal components needed a few seconds and, as in the case of ellipses described in the previous section, the computation of a new shape according to Equation (5.1) took around 10^{-3} second and the spatial transformations done with the B-splines programming around 10^{-3} second. In the experiments, from Figure 5.17 to Figure 5.21, the segmentation including shape and pose parameters took around 5 minutes.

We use our segmentation model to capture the left brain ventricle. Figure 5.17 presents the evolving geodesic active contour *without* a shape prior and Figure 5.18 *with* a shape prior by choosing $\beta_s = 2$, $\beta_b = 1$, $\beta_r = 100$, $\mu = 50$ and $\Delta t = 0.1$.

We observe on Figure 5.18 that the active contour has well captured the left ventricle whereas *the initial contour was around the two ventricles.* This segmentation result could not be obtained without a shape prior with the same initial contour as shown on Figure 5.17. The segmentation model has also provided the shape of the model which best fits the ventricle lying in the image.
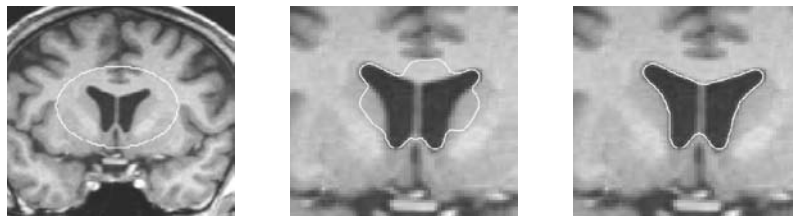
Figure 5.17: Evolution of the geodesic active contour *without* shape prior information.
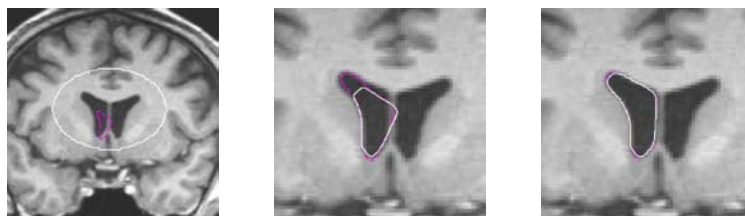
Figure 5.18: Evolution of the active contour (in solid line) *with* a shape prior (in dotted line).
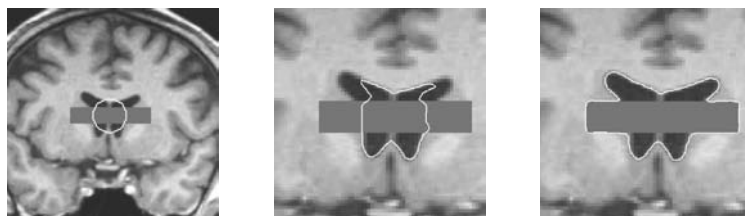
Figure 5.19: Evolution of the region-based active contour of Vese and Chan [179] in the presence of an occlusion.

Figure 5.18 illustrates the Section 5.3.3 remark: in this case, the MS model applied on the active contour will separate both ventricles (that form a homogeneous intensity region) from the rest of the white matter. The shape force will be then opposed to the region force since the shape force will pull the active contour inside the right ventricle towards the left ventricle whereas the MS force will constrain the active contour to stay on the border of ventricles. Our model avoids this situation since region-based forces are only applied on the contour of the shape prior and not on the active contour itself.

For Figures 5.19, 5.20 and 5.21, we followed the experiments done by Cremers-Tischhäuser-Weickert-Schnörr in [62, 66]. Indeed, we added an occlusion bar on Figures 5.19 and 5.20 and an
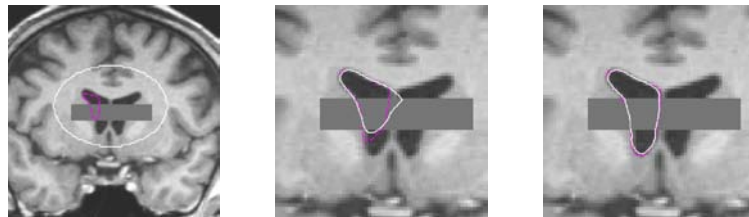
Figure 5.20: Evolution of the active contour (in solid line) *with* a shape prior (in dotted line) in the presence of an occlusion.
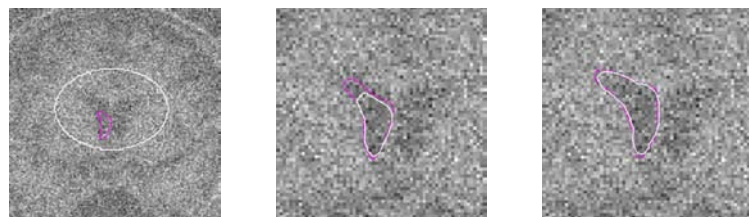
Figure 5.21: Evolution of the active contour (in solid line) *with* a shape prior (in dotted line) in the presence of an important quantity of noise.

important amount of noise on Figure 5.21. Figure 5.19 shows the evolution of the region-based active contour of Vese-Chan [179] which fails to segment the left ventricle. Hence, a shape-based term is essential to successfully segment the ventricle as shown on Figures 5.20 and 5.21.

5.6 Discussion

The active contour obtained from the minimization of the energy functional defined in Equation (5.4) is able to capture high image gradients and a homogeneous intensity region which shape matches the object of interest. We have seen on Figures 5.15 and 5.12 that the shape information allows us to solve the problems of missing information/occlusion while being sensitive to local shape variations. Indeed, small deformations are allowed around the zero level set of the shape function on a distance that depends on the relative weight β_s/β_b. These complex deformations are easier to handle in the level set framework, thanks to its intrinsic representation, than parametric ones [59, 66].

As we mentioned previously, the proposed segmentation model can be seen either as an extension of the model of Chen *et al.* [45] where we have introduced the shape model of Leventon-Grimson-Faugeras [113] and the Mumford-Shah model [179] or as an energy formulation of the model of Leventon with the MS energy functional. Using the variational formulation of Chen *et al.* enables us to prove in the previous section the existence of a solution minimizing our energy functional in the space of functions with bounded variation. Finally the region term based on the Mumford-Shah functional increases the speed of convergence toward the solution and also improves the robustness of the model w.r.t. the initial condition, noise and complex background.

The PCA shape model we use in our segmentation method presents a good compromise when compared to other models. First, the computation of the p principal components which are orthonor-

mal basis functions is straightforward and fast, using the singular values decomposition method. These functions are then used to produce new shapes of the object of interest according to a simple linear equation. The number p of principal components, i.e. the number of the shape model parameters, is often small as we have noticed for the ellipse (see Figure 5.1) that needs only one principal component or for the left brain ventricle (see Figure 5.3) with three principal components. Thus, global shape variations are modeled by a small number of variables which greatly reduces the complexity of the problem, when compared e.g. to Paragios-Rousson-Ramesh model [135, 138]. Indeed, their shape model generates more complex shapes than the PCA but the p shape parameters of the PCA model is replaced in their work by a local deformation field to be evaluated on a δ-band around the zero level set of the shape function.

Note that the shapes produced by the PCA are obviously implicit and intrinsic, i.e. independent of the parametrization, which facilitates the morphing and the registration processes. However, shape functions provided by the PCA are not exactly SDFs as proved by Leventon in [111]. Nevertheless, shape functions of the PCA are very close to SDFs, which allow us to use them in practice. The same remark holds for spatial transformation applied on the shape function. The shape function after an affine transformation is (in general) not a distance function. So, the family of shapes obtained by affine transformations is no longer an equivalent class w.r.t. Equation (5.1) and the shape term defined in Equation (5.5). The previous observations lead to the following *condition to successfully use the morphing and the registration processes* defined in Equation (5.5): a point belonging to the shape function constructed by the PCA or computed by a spatial transformation must see its height continuously decreasing when moving towards the zero level set even if its gradient is not exactly in the normal direction of the zero level set. Fortunately, we experimentally noticed that all shape functions generated by the PCA and changed by an affine transformation satisfy this condition. The shape functions given by the PCA are thus not accurate SDFs but there are two ways to obtain exact SDFs (and have a strict equality in Equation (5.1)). Either the shape function is projected in the SDFs space by re-distancing $\hat{\varphi}$ as a SDF or the framework of Charpiat-Faugeras-Keriven [43] can be used to define a mean and principal modes of variation for distance functions.

In our segmentation model, we have to compute the transformation and shape parameters. However, Cremers-Tischhäuser-Weickert-Schnörr-Kohlberger in [59, 66] have defined two shape energies independent of the rigid transformations and the shape parameters. This means that their segmentation model did *not* have to compute the vector of the rigid transformations $\mathbf{x}_{ST}$ and the vector of shape parameters $\mathbf{x}_{pca}$ with Equations (5.30) and (5.31) since the correct pose parameters are automatically estimated and the shape parameters can be extracted by projection on the respective eigenmodes. Thus, is it really useful to estimate the registration parameters $\mathbf{x}_{ST}$ and the shape parameters $\mathbf{x}_{pca}$? It depends on two questions: does the current application need to compute transformation and shape parameters and are affine or non-rigid transformations necessary? If the answer is positive for one of these questions, the estimation of these parameters will be imperative. Let us cite [20, 45] as examples, the transformation parameters are used to align time series images in order to minimize the effect of motion on the fMRI signal.

Recently and posterior to our publications [29] and [26], Rousson-Paragios-Deriche [154] presented a model to extract structures of interest similar to ours. Indeed, they also proposed to integrate the implicit shape prior of Leventon-Grimson-Faugeras [113] in a variational level set framework to derive two minimizing flows on the level set function representing the active contour and on the

spatial transformations. Finally, the shape vector is computed by solving a linear equation system. We notice that the shape-based functional of Rousson-Paragios-Deriche is similar to ours because it corresponds to the sum of square differences (SSD) between the active contour and the zero level set of the implicit shape prior. Indeed, their shape-based functional minimizes the difference between the level set function embedding the active contour and the level set-based shape prior weighted by the Dirac function applied to the level set function of the active contour. The difference between both works is the region-based functional. Rousson-Paragios-Deriche proposed to add the model of geodesic active regions to the shape-based functional. However, as explained in Section 5.3.3, since our objective is to capture an object belonging to a given shape space then we think that the best solution is to apply directly the region-based force on the contour of the shape prior as we did. Concerning the computation of the shape vector $\mathbf{x}_{pca}$, i.e. the mode weights of the PCA. The computation of the mode weights is probably more efficient with Rousson-Paragios-Deriche [154] than ours since their technique provides the optimal mode weights at each iteration which minimizes the shape difference between the active contour and the shape prior. Our model does not directly provide the optimal mode weights at each iteration since it is a gradient descent flow, i.e. a local minimization technique. However, at the end of the segmentation/registration process, our technique will provide the optimal mode weights which minimizes the difference between the active contour shape and the shape prior. Moreover, the way of computing the $\mathbf{x}_{pca}$ in the approach of [154] is given by an independent stage (solving a linear system) of the minimization energy functional w.r.t. $\mathbf{x}_{pca}$ which means that no mathematical theories can be applied to prove the existence of a solution by opposition to our approach (see Section 5.4).

Finally, by using a variational framework and the PDEs attached to it, we can consider other models such as [13, 42, 99, 106, 132, 151, 179] to segment objects by linearly combining energy functionals or the PDEs directly.

5.7 Conclusion

In this chapter, we proposed a new variational method to solve the fundamental problem of object segmentation using local and global image information with a geometric shape prior given by the model of PCA. To reach this objective, we have defined in Section 5.3.2 a shape-based functional to force the active contour to get a shape of interest whatever the position of the active contour in the image. Then in Section 5.3.3, we proposed a Mumford and Shah-based functional to drive globally the shape model toward a homogeneous intensity region with the shape of interest. Experimental results showed that our active contour is able to solve the problems of missing information and occlusion while being sensitive to local shape variations.

The shape model we used is the PCA model. As explained in Section 5.6, this model presents a good compromise between low complexity and acceptable shape priors. However, this model works well only if the probability density of the training set of the object of interest is Gaussian. If the true underlying probability density of the training set is not Gaussian (in presence of tumors in T1-WMR images for example) then more elaborated techniques such as non-parametric models are necessary.

We note that the proposed model can capture only one object, which is a limitation since we loose the powerful property of the level set approach that can segment several objects simultaneous-

ly. A first solution to handle multiple objects would consist in associating structures by coupling the evolution equations. Another solution would be to use the recent work of Cremers-Sochen-Schnörr [64, 65] who proposed in the context of variational level set methods a labeling function to indicate where to apply the shape prior in a given image.

This chapter introduced an image segmentation model to extract semantic objects which shape is known. In other words, we defined a new shape recognition algorithm. However, in some situations, some shape priors are very complex, such as the brain cortical surface, which makes difficult the shape recongition task. In this context, a multiscale representation of the shape prior could help to detect complex objects in a robust way. This multiscale shape recognition should have to be coupled with a multiscale image segmentation. Thus, we propose in the next chapter a multiscale segmentation model.

<div style="text-align: right;">

6

</div>

Multiscale Active Contours

In this chapter, we propose to define a *multiscale image segmentation model* to extract structures at different scales of observation/resolution *simultaneously*. The intrinsic multiscale nature of images is well-known since the original works of Iijima [183], Witkin [185] and Koenderink [109] who proposed a space to represent images at multiple scales of observation, called *scale space*. The segmentation model we will define is based on the active contour model, introduced in Sections 2.1 and 2.2. More precisely, we will introduce the concept of scale in the snake/active contour framework in order to define an evolution equation for the active contours in scale spaces which are basically non-Euclidean spaces. This non-Euclidean geometry and the special relation between space and

© *Diego Porcel*

scale/time is handled with the framework proposed by the *Polyakov action* [143] that was firstly defined in high energy physics for the *string theory*, which basically tries to unify the four fundamental forces of nature. Then, Sochen-Kimmel-Malladi [167] introduced this physics-based framework in image processing to efficiently denoise multi-dimensional images such as color and texture images. The mathematical framework used in the Polyakov action is the *differential geometry* that is efficient to intrinsically describe the scale spaces such as the linear/Gaussian scale space, the Perona-Malik scale space and the mean curvature scale space. Finally, potential applications of this technique is in shape analysis. For example, our multiscale segmentation technique can be coupled with the shape recognition and the shape registration algorithms to improve their robustness and their performance.

6.1 Multiscale Nature of Images

A very important concept in the physics world is the *scale*. When we look at real-world images, we realize that they are naturally composed of objects which are meaningful only at a given scale of

<div style="text-align: center;">

129

</div>

observation. As example [114], let us consider the forest picture 6.1.

Figure 6.1: Illustration of multiscale images. At fine scales (little white circle), leaves are significant, at intermediate scales, trees are relevant (large white circle) and finally at large scales, the whole forest is significant.

At very fine scales of observation (centimeter), the leaves are the significant objects, at intermediate scales of observation (meter), the trees are the meaningful objects and at the large scales of observation (kilometer), this is the whole forest which is significant. In other words, *the way we perceive the world depends on the scale of observation we use*, inspired by the scale principle of Morse [123]. This observation has a deep impact in physics because different theories have been developed to observe the very small and the very large scales of the physics world leading to quantum mechanics and relativity theory. Even the human visual system has integrated the concept of scale in its way to capture the real-world images since psychophysical and electro-physiological studies [95, 96, 189] have shown that the retina receives the image signal with a wide range of sampling apertures/scales [171].

Since natural images are composed of structures at different scales of observation, it is then natural to define a multiscale representation of an image in order to observe it at these different scales. Another motivation to develop such a representation is to design methods for automatically analyzing information and deriving specific applications in computer vision. How can we design a multiscale image representation or how can we decompose an image at different scales of observation/resolution? The answer of these questions are *scale spaces*. The main principle of scale spaces is to decrease the amount of information in images by simplifying/smoothing objects lying in them, starting from fine scales and ending to coarse scales. Mathematically speaking, scale spaces are hierarchical decompositions/representations at a continuum of scales, embedding the original image $I_0 : \mathbf{R}^N \to \mathbf{R}$ into a family $I : \mathbf{R}^N \times [0, \infty[\to \mathbf{R}$ of gradually more simplified versions.

The mathematical methods that generate scale spaces are generally based on partial differential equations coming from diffusion processes in physics and special mathematical properties and invariances. For instance, the first scale space that has been discovered by Iijima, Witkin, Koenderink [109, 183, 185] is the linear/Gaussian scale space produced by the linear diffusion equation: $\partial_t I = \Delta I$, $I(t = 0) = I_0$, which satisfies the conditions of linearity, causality, semi-group property, maximum principle, non-creation of local extrema at larger scales (this holds only for 1-dimensional signals), translation, rotation and scale invariances. Many other scale spaces can be defined from (non-linear) PDEs, satisfying different properties, such as the scale spaces produced by the Perona-Malik model [141], the mean curvature flow [4, 129, 159], the total variation functional [155] and others presented in Section 2.5.

Finally, let us mention that the theory of scale spaces is a young theory that is constantly under development but with strong mathematical bases. First applications of this theory have been to develop primitive differential operators which can change their scales of resolution to fit different unknown scales of real-world objects lying in images and thus extract specific local information from images such as edges, ridges and corners [78, 114, 172]. In the following work, we propose a multiscale image segmentation model to extract multiscale structures in scale spaces.

6.2 Why defining a Multiscale Image Segmentation Model?

In the previous section, we underlined the multiscale nature of real-world images that contain objects/structures meaningful at given scales of observation. These multiscale structures are *linked* through the scale because fine structures are included into coarser structures in a semantic way such as leaves are a part of trees, which are also a part of a forest, Figure 6.1. Hence, we propose to capture these structures at different scales of observation *simultaneously* to combine information from fine scales to coarse ones. This will be the objective of this chapter.

This chapter aims at defining a multiscale image segmentation model based on the *active contour* model and *scale spaces*. In other words, we want to introduce the concept of scale in the active contour formalism [35, 103, 105] to define an object multiscale segmentation model to capture fine characteristics at low scales and extract global shape at large scales. Two main questions arise when we want to design this model. Why do we propose such an image segmentation model? And how to mathematically define it?

As we said in Section 6.1, defining a multiscale image segmentation model makes sense because images are multiscale by nature. Moreover, any application such as image segmentation needs to use an appropriate scale to perform well. However, it is impossible to know a priori which is the proper scale to get satisfactory results. The appropriate scale can depend on many parameters such as the given image, the specific application, etc. For example, let us come back to the well-known segmentation model of active contours, introduced in Section 2.1, and let us consider the *standard deviation* σ of the Gaussian function G_σ in the edge detecting function $f(I_0) = \frac{1}{1+\gamma|\nabla(I_0 * G_\sigma)|^2}$ as the *scale parameter of the model*. Indeed, let us observe Figure 6.2. If the scale parameter σ is too small, the active contour gets stuck in noise (Figure 6.2(b)) and if the scale is too large, the snake is not able to capture corners (Figure 6.2(d)). However, an appropriate scale can give satisfactory result as shown on Figure 6.2(c). The problem is that the proper scale is not a priori known before the segmentation process. Hence, different results with different values of σ have to be tested to determine the correct scale. One solution to handle this issue is to work at different scales, which is possible with a multiscale image segmentation, and pick up a posteriori the scale (or several scales) that looks like the most interesting for the given application.

Another reason to develop a multiscale image segmentation model is to improve two classical applications in image analysis: the *shape recognition* task and the *shape registration* process. Indeed, the recognition of an object at different scales of observation would be able to improve the identification task. More precisely, combining a multiscale shape prior such as the multiscale medial axis called *cores* and developed by Pizer-Eberly-Morse-Fritsch [142], with our mutiscale segmentation model could provide an efficient multiscale recognition method. Moreover, a multiscale image segmentation model provides a multiscale shape representation that can be useful to register complex

(b) σ_1: small scale   **(c)** $\sigma_2 > \sigma_1$: *correct scale*   **(d)** $\sigma_3 > \sigma_2$: large scale
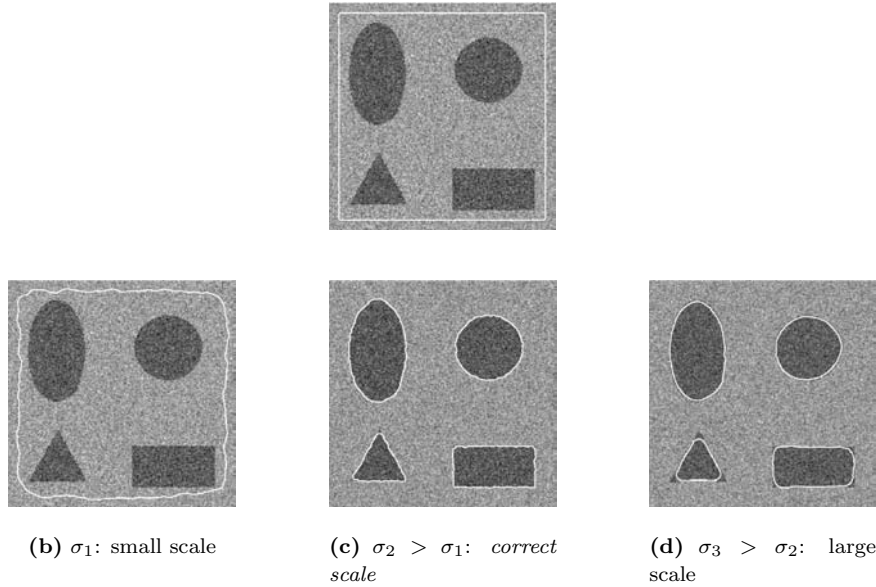
Figure 6.2: Illustration of the scale concept in the active contour model. If the scale parameter is too small, the contour gets stuck in noise, Figure 6.2(b) and if the scale is too large, the snake looses the corners , Figure 6.2(d). However, there exits a *correct scale* for this problem that gives us a satisfactory result, Figure 6.2(c).

geometric shapes such as the brain cortical surface. Special metrics defined in multiscale spaces can be used to efficiently compare shapes at different scales of resolution.

Many multiscale image segmentation models have already been proposed such as the one of Schnabel-Arridge in [161] who proposed a method to extract *scale by scale* the shape of objects. Then, they used the extracted multiscale shapes to localize and characterize shape changes at different levels of scale. They applied their model to segment 3-D brain magnetic resonance images in order to quantify the structural deformations for patients having epilepsy. However, the main issue concerning this approach is the *relation between space and scale/time* that is not taken into account in [161]. We propose to solve this issue by using special metric tensors to characterize the interdependence between space and scale.

As we previously wrote, the segmentation method that we will use in our work is the active contour model. If we want to define a multiscale image segmentation model based on the active contour framework, then we need to define an evolution equation for active contours evolving in scale spaces. The question is how to introduce the active contours into scale spaces. An answer is given by the fascinating work of Sochen-Kimmel-Malladi [167] concerning the *string theory* and the *Polyakov action.*

6.3   Weighted Polyakov Action

As we explained and developed in Section 2.5, Sochen-Kimmel-Malladi proposed in [166, 167] a new framework to deal with low level processing in vision. Their new point of view considers images as *surfaces embedded in higher dimensional space* such as on Figure 6.3.

(a) 2-D image

(b) Same image in 3-D
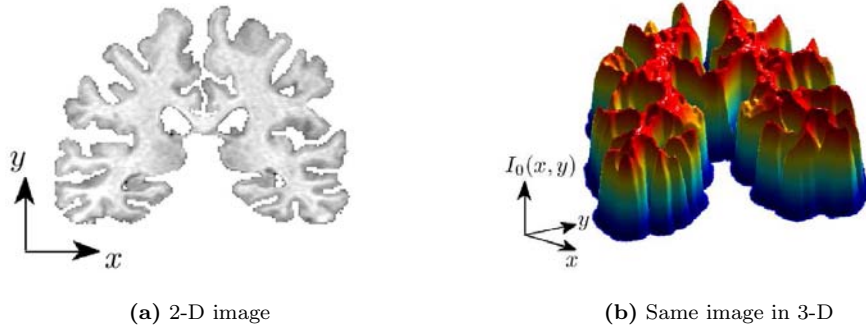
Figure 6.3: Figure (a) presents a classic 2-D grey-scale image and Figure (b) represents the same image as a surface embedded in a 3-D space.

They derived the Beltrami flow to efficiently denoise multi-dimensional images such as color and texture images [108]. The Polyakov action is basically a functional that measures the weight of a mapping X between an embedded manifold (the image manifold) Σ and the embedding manifold M (see Figure 6.4).
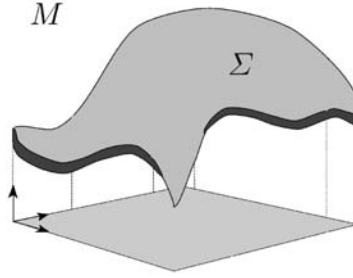
Figure 6.4: The manifold Σ embedded in M, reproduced from [167].

It is defined as follows:

$$
\begin{cases}
P(X, \Sigma, M) & = \quad \int d^{n_\Sigma} \varsigma \; g^{1/2} g^{\mu\nu} \partial_\mu X^i \partial_\nu X^j h_{ij} \\
X & : \quad (\Sigma, [g_{\mu\nu}]) \to (M, [h_{ij}])
\end{cases}
\tag{6.1}
$$

where $[g_{\mu\nu}]$ is the metric tensor/first fundamental form [110] of the manifold Σ, $d^{n_\Sigma}\varsigma$ is the integration element with respect to (w.r.t.) the local coordinates on Σ, $[h_{ij}]$ is the metric tensor of the embedding space M, n_Σ is the dimension of Σ, n_M the dimension of M, $[g^{\mu\nu}]$ is the inverse metric of $[g_{\mu\nu}]$, g is the determinant of $[g_{\mu\nu}]$, $\mu, \nu = 1, ..., n_\Sigma$, $i, j = 1, ..., n_M$ and $\partial_\mu X^i = \partial X^i / \partial \varsigma^\mu$. Moreover, when identical indices appear one up and one down, they are summed over according to the Einstein summation convention.

In [166, 167], Sochen-Kimmel-Malladi observed that the Polyakov action (6.1) is able to recover/generalize most of the existing scale spaces, from the linear scale space to the curvature scale space. This justifies the title of their paper since the Polyakov functional provides a *single equation* to generalize most of scale spaces fundamental in low level vision. In our work, we continue on investigating the Polyakov action. We will *extract* from it the well-known image segmentation model

of active contours/snakes evolving in Euclidean spaces. Then, we will extend the original model to scale spaces by defining an evolution equation for active contours propagating in these spaces.

First of all, a weighting function f is introduced in the functional (6.1) leading to the *weighted Polyakov action*:

$$P_f(X, \Sigma, M) = \int d^{n_\Sigma}\varsigma \ f(X, g_{\mu\nu}, h_{ij}) \ g^{1/2} g^{\mu\nu} \partial_\mu X^i \partial_\nu X^j h_{ij}, \tag{6.2}$$

Then, the weighted Polyakov action (6.2) is minimized w.r.t. the l-th embedding coordinate X^l using the Euler-Lagrange equations technique, $g_{\mu\nu}$ and h_{ij} being fixed. The flow acting on X^l is then as follows:

$$\begin{aligned} \frac{\partial X^l}{\partial t} &= f \cdot \left(g^{-1/2}\partial_\mu(g^{1/2}g^{\mu\nu}\partial_\nu X^l) + \Gamma^l_{jk}\partial_\mu X^j \partial_\nu X^k g^{\mu\nu} \right) \\ &\quad + \partial_k f g^{\mu\nu}\partial_\mu X^k \partial_\nu X^l - \frac{n_M}{2} h^{lk}\partial_k f \ g^{1/2}g^{\mu\nu}\partial_\mu X^i \partial_\nu X^j h_{ij}, \quad \text{for } 1 \le l \le n_M, \end{aligned} \tag{6.3}$$

where $g^{-1/2}\partial_\mu(g^{1/2}g^{\mu\nu}\partial_\nu X^l)$ is the Beltrami operator which generalizes the Laplace operator to non-flat manifolds and $\Gamma^l_{jk} = \frac{1}{2}g^{li}(\partial_j g_{ik} + \partial_k g_{ji} - \partial_i g_{jk})$ is the Levi-Civita connection coefficients [110].

The metric tensor $[g_{\mu\nu}]$ of the embedded manifold Σ is chosen to be the *induced metric tensor*: $[g_{\mu\nu}] = \partial_\mu X^i \partial_\nu X^j h_{ij}$, presented in Section 2.5. This choice of metric tensor means that the map X are *harmonic maps* such as geodesics and minimal surfaces and the weighted Polyakov action is reduced to the *weighted Euler functional/Nambu action* that describes the (hyper-)area of a (hyper-)surface Σ:

$$S_f = \int d^{n_\Sigma}\varsigma \ f \ g^{1/2}, \tag{6.4}$$

where $g^{1/2}$ is the square root of the determinant of $[g_{\mu\nu}]$ which corresponds to the infinitesimal invariant-area on Σ. It is consistent to work with harmonic maps when we try to recover the model of active contours/snakes [35] because this model also works with harmonic maps, more precisely with geodesics. The induced metric tensor is introduced in the flow (6.3), which yields to:

$$\begin{cases} \frac{\partial X^l}{\partial t} &= f\mathcal{H}^l + \partial_k f g^{\mu\nu}\partial_\mu X^k \partial_\nu X^l - \frac{n_M . n_\Sigma}{2}\partial_k f h^{kl}, \\ \mathcal{H}^l &= \left(g^{-1/2}\partial_\mu(g^{1/2}g^{\mu\nu}\partial_\nu X^l) + \Gamma^l_{jk}\partial_\mu X^j \partial_\nu X^k g^{\mu\nu} \right)_{g_{\mu\nu}=\partial_\mu X^i \partial_\nu X^j h_{ij}} \end{cases} \tag{6.5}$$

for $1 \le l \le n_M$ and $\mathcal{H}$ is the mean curvature vector generalized to any embedding manifold M.

Functional (6.4) and its minimization flow (6.5) are the general equations to recover the classical model of active contours and to derive the new model of *multiscale active contours*. Let us start by recovering the model of geodesic/geometric active contours and its level set version presented in Sections 2.2 and 2.3.2.

Application 1: The geodesic/geometric active contours model [35, 105] evolving in a 2-D Euclidean space is recovered by choosing the following mapping and metric tensor of the embedding space M:

$$\begin{cases} X := C : q \to (x(q), y(q)) \\ [h_{ij}] = [\delta_{ij}] \end{cases} \tag{6.6}$$

Introducing (6.6) in (6.4) and (6.5), we get:

$$\begin{cases} S_f = F_{GAC} = \int_C f \, ds \\ \partial_t C = (f\kappa - \langle \nabla f, \mathcal{N} \rangle) \, \mathcal{N}, \end{cases}$$

which corresponds to the energy (2.5) and the evolution equation (2.8) of the geodesic/geometric active contours model studied in Section 2.2.

Application 2: The evolution equation of the level set version of the geodesic/geometric active contours model can also be revisited by choosing

$$\begin{cases} X : (x_1, ..., x_n) \rightarrow (x_1, ..., x_n, \phi) \\ [h_{ij}] = [\delta_{ij}] \end{cases} \tag{6.7}$$

Introducing (6.7) in (6.4) and (6.5), we get:

$$\begin{cases} S_f = \int f \sqrt{1 + |\nabla \phi|^2} \prod_{1 \le i \le n} dx_i \\ \partial_t \phi = \frac{1}{\sqrt{1+|\nabla\phi|^2}} \nabla \cdot \left(f \frac{\nabla\phi}{\sqrt{1+|\nabla\phi|^2}} \right) = \frac{1}{\sqrt{1+|\nabla\phi|^2}} \left(f\mathcal{K}_{ES} + \langle \nabla f, \frac{\nabla\phi}{\sqrt{1+|\nabla\phi|^2}} \rangle \right), \end{cases} \tag{6.8}$$

where $\mathcal{K}_{ES} = \nabla \cdot \left(\frac{\nabla\phi}{\sqrt{1+|\nabla\phi|^2}} \right)$ corresponds to the mean curvature of the surface Σ embedded in an Euclidean space (ES). For 2-D surfaces Σ, it is equal to:

$$\mathcal{K}_{ES} = \frac{(1 + \phi_x^2)\phi_{yy} - 2\phi_x\phi_y\phi_{xy} + (1 + \phi_y^2)\phi_{xx}}{(1 + \phi_x^2 + \phi_y^2)^{3/2}}, \tag{6.9}$$

It is important to notice that the mean curvature $\mathcal{K}_{ES}$ is different to the mean curvature $\kappa = \nabla \cdot \left(\frac{\nabla\phi}{|\nabla\phi|} \right)$ of the level sets of ϕ in the classical model 2.3.1. We also observe that equations (6.8) are not exactly the corresponding formula of the level set version of the active contours model which are as follows:

$$\begin{cases} F = \int f |\nabla\phi| \prod_{1 \le i \le n} dx_i \\ \partial_t \phi = \nabla \cdot \left(f \frac{\nabla\phi}{|\nabla\phi|} \right) = f\kappa + \langle \nabla f, \frac{\nabla\phi}{|\nabla\phi|} \rangle. \end{cases} \tag{6.10}$$

However, the behavior of the segmentation model (6.8) is similar to the classical model (6.10) up to a function, called $r(\phi)$, that depends on the height variation on the surface Σ. Let us compute this function for 2-D surfaces Σ. The flow (6.8) acting on the level set component ϕ can be re-written in the following way:

$$\partial_t \phi = g_{ES}^{-1/2} \underbrace{(f\mathcal{K}_{ES} + \langle \nabla f, \nabla\phi \rangle)}_{=:F_{ES}}, \tag{6.11}$$

where $g_{ES} = 1 + |\nabla\phi|^2$. Equation (6.11), $\partial_t \phi = g_{ES}^{-1/2} F_{ES}$, implies that the surface Σ evolves according to $\partial_t X = F_{ES} \mathcal{N}_\Sigma$ where $\mathcal{N}_\Sigma = g_{ES}^{-1/2}(-\phi_x, -\phi_y, 1)$ is the unit normal to Σ. This means that the level sets of ϕ move according to the equation:

$$\partial_t C = P_\phi X_t = \underbrace{g_{ES}^{-1/2} |\nabla\phi|}_{=:r(\phi)} F_{ES} \, \mathcal{N} \tag{6.12}$$

$$= \left(f\mathcal{K}_{ES} r(\phi) - \langle \nabla f, \mathcal{N} \rangle r^2(\phi) \right) \mathcal{N} \tag{6.13}$$

where $P_\phi = I - \frac{\mathcal{N}_\phi \otimes \mathcal{N}_\phi}{|\mathcal{N}_\phi|^2}, \mathcal{N}_\phi = (0, 0, 1)$ is a projector operator onto the plane normal to the ϕ-axis, $\mathcal{N} = -\nabla\phi/|\nabla\phi|$ is the unit normal to the level sets and the function $r(\phi)$ is equal to $g_{ES}^{-1/2}|\nabla\phi|$. The equation (6.13) is close to the evolution equation (2.8) of the geodesic/geometric active contours $\partial_t C = (f\kappa - \langle \nabla f, \mathcal{N} \rangle)\mathcal{N}$ up to the surface mean curvature $\mathcal{K}_{ES}$ and the function r. However, both evolution equations have the same behavior, i.e. smoothing and attraction toward edges. Function r can be interpreted as an indicator of the height variation on the surface Σ (see [15]). Indeed, $g_{ES}^{-1/2}$ is the ratio between the area of an infinitesimal surface in the domain (x, y) and the corresponding area on the surface Σ. For flat surfaces, r is equal to 0 and it is close 1 near edges. Finally, the function r is constant almost everywhere when ϕ is a signed distance function.

Equations (6.4) and (6.5) allowed us to recover the model of active contours/snakes in the explicit and the implicit representations. Both representations, the contour C and the level set function ϕ, were embedded/evolved in Euclidean spaces defined by the Euclidean metric tensor $[h_{ij}] = [\delta_{ij}]$. However, Equations (6.4) and (6.5) were established for general embedding Riemannian manifolds M. Hence, it is possible to change the embedding space for the active contours and consider the scale spaces. The natural next question is *which scale spaces* can be used in our framework? The question was answered by Eberly in [70, 71] who defined a family of scale spaces that includes the linear scale space, the Perona-Malik scale space and the curvature scale space.

6.4   Scale Spaces

In [70, 71], Eberly studied the geometry of a large class of scale spaces and defined for them the general metric tensor:

$$[h_{ij}] = \ \text{diag}\left(\frac{1}{c^2}\mathcal{I}_n, \frac{1}{c^2\rho^2}\right), \tag{6.14}$$

where n is the spatial dimension, $\mathcal{I}_n$ is the $n \times n$ identity matrix, c and ρ are two functions that physically correspond to the *conductance* and the *density* functions in the general model of heat diffusion transfer. These functions can depend on space, scale and image data. As Eberly said in [70], the *natural diffusion equation* in any space defined by a metric tensor is obtained as follows: the left-hand side of the diffusion equation is given by one application of the scale derivative and the right-hand side by two applications of the spatial derivative. In the case of scale spaces, defined by the metric tensor (6.14), the scale derivative and the spatial derivative are given by the scale space (SS) gradient defined by the covariant derivative [110]:

$$\nabla_{SS} := \sqrt{[h^{ij}]^{-T}}\nabla^\star = \left(\underbrace{c\partial_{x_1}, \ldots, c\partial_{x_n}}_{\text{spatial derivative}}, \underbrace{\rho c\partial_\sigma}_{\text{scale derivative}}\right) = (c\nabla, \rho c\partial_\sigma) \tag{6.15}$$

where $[h^{ij}]$ is the inverse tensor of $[h_{ij}]$, T means the transpose operator, $[h^{ij}]^{-T} := ([h^{ij}]^{-1})^T$ and $\nabla^\star := (\partial_{x_1}, \ldots, \partial_{x_n}, \partial_\sigma) = (\nabla, \partial_\sigma)$ where ∇ stands for the Euclidean space gradient. Hence, the natural diffusion equation is defined by

$$(\rho c\partial_\sigma)\, I \ = \ (c\nabla) \cdot (c\nabla)\, I, \tag{6.16}$$

$$\partial_\sigma I \ = \ \frac{1}{\rho}\nabla \cdot (c\nabla I). \tag{6.17}$$

Equation (6.17) is the general model of *heat diffusion transfer* that generates different multiscale image representations, i.e. scale spaces, by applying a PDE which is a non-linear anisotropic diffu-

sion equation in its general expression.

Different choices of the functions c and ρ give different scale spaces with different diffusion equations (6.17). It is interesting to notice that most of popular scale spaces can be recovered, which emphasizes well the close relation between multiscale image analysis/scale space and diffusion processes that originate from physics. As a first example, let us consider the linear scale space obtained when $c = \sigma$ (the scale parameter) and $\rho = 1$. The diffusion equation is then:

$$\partial_\sigma I = \sigma \Delta I. \tag{6.18}$$

In [70], Eberly studied in details the linear scale space produced by the previous PDE and proved that it is hyperbolic and translation, rotation and scale invariant. Let us apply the scale space Equation (6.18) to the 2-D fractal image proposed by Von Koch on Figure 6.5. The linear scale space of the given image, corrupted with additive Gaussian noise, is presented on Figure 6.6.
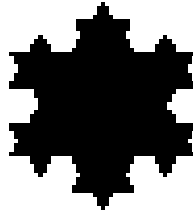
Figure 6.5: 2-D fractal image proposed by Von Koch.

Then, the linear scale space of the brain magnetic resonance images, Figure 6.7, is also generated on Figure 6.8.

Another well-known scale space can be derived from the metric tensor (6.14) and the associated multiscale generation process (6.17), this is the Perona-Malik scale space [141] obtained when $c = \exp(-\alpha|\nabla I|^2), \alpha > 0$ and $\rho = 1$:

$$\partial_\sigma I = \nabla.(c\nabla I), \tag{6.19}$$

which applies a non-linear anisotropic diffusion process which inhibits diffusion across edges, see Section 2.5. The third possible scale space is the space produced by the famous mean curvature flow which is one of the fundamental equation in image processing [4, 129, 159], Section 2.5. It is obtained by setting $c = \rho = \frac{1}{|\nabla I|}$, which yields to:

$$\partial_\sigma I = \nabla.\left(\frac{\nabla I}{|\nabla I|}\right)|\nabla I| = \kappa|\nabla I|, \tag{6.20}$$

where κ is the mean curvature of the level sets of I. Other scale spaces can be derived such as the scale space produced by the total variation flow [155] with $c = \frac{1}{|\nabla I|}$ and $\rho = 1$:

$$\partial_\sigma I = \nabla.\left(\frac{\nabla I}{|\nabla I|}\right) = \kappa. \tag{6.21}$$

Finally, let us finish with the scale space produced by the Beltrami flow of Sochen-Kimmel-Malladi

(a)

(b)   **(c)**   **(d)**   **(e)**
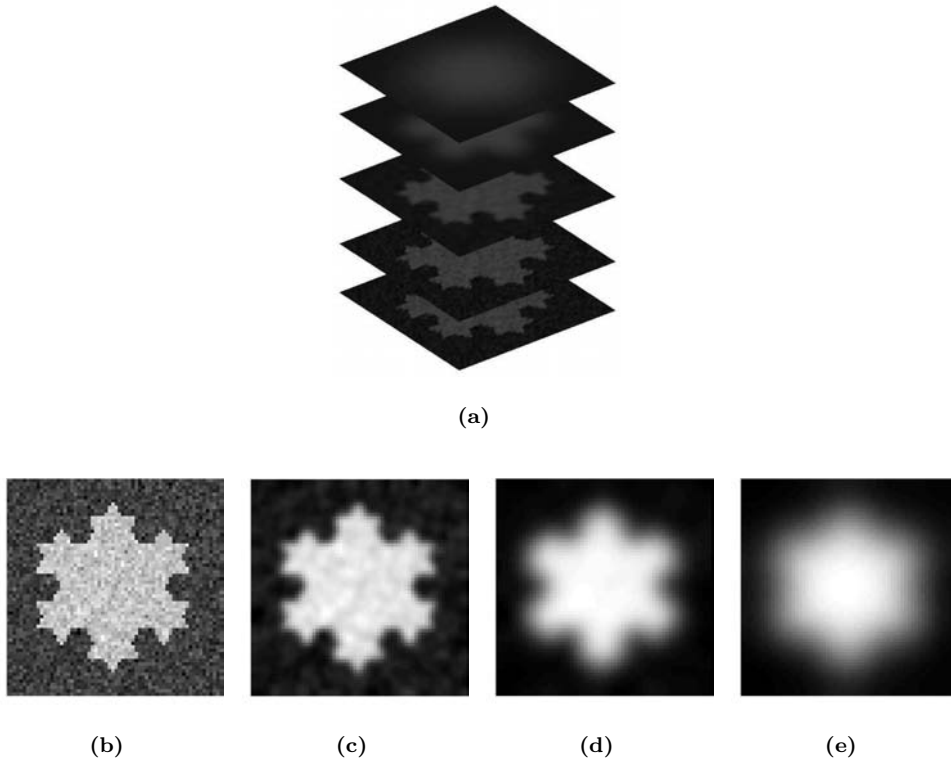
Figure 6.6: Figure (a) presents the linear scale space of the Von Koch's picture and Figures (b-e) show four different scales of observation.
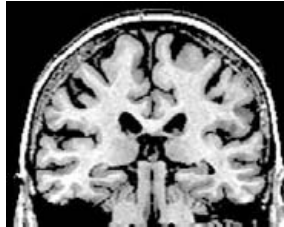
Figure 6.7: 2-D brain magnetic resonance image.

[166, 167] which naturally regularizes multi-dimensional images with $c = \rho = \frac{1}{\sqrt{1+|\nabla I|^2}}$, which gives:

$$\partial_\sigma I = \frac{1}{\sqrt{1 + |\nabla I|^2}} \nabla \cdot \left(\frac{\nabla I}{\sqrt{1 + |\nabla I|^2}} \right) = \Delta_g I, \tag{6.22}$$

which is equal for 2-D images to

$$\partial_\sigma I = \frac{(1 + I_x^2)I_{yy} - 2I_x I_y I_{xy} + (1 + I_y^2)I_{xx}}{(1 + I_x^2 + I_y^2)^2}. \tag{6.23}$$

(a)

(b)   **(c)**   **(d)**   **(e)**
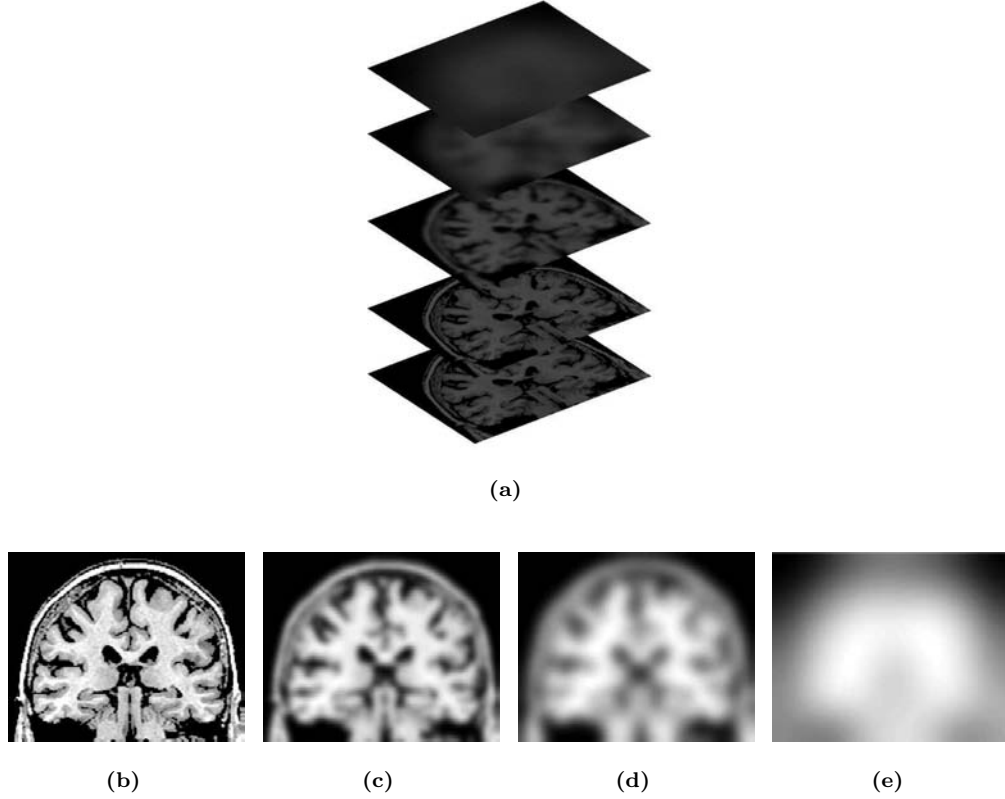
Figure 6.8: Figure (a) presents the linear scale space of the 2-D brain image and Figures (b-e) show four different scales of observation.

6.5 Multiscale Active Contours

In this section, we define the general evolution equation for the active contours in the scale spaces defined in the previous section. We use the results obtained in Section 6.3 on the weighted Polyakov action to determine this evolution equation and the associated energy variational model. The harmonic map X, the metric tensor $[h_{ij}]$ of the embedding scale space and the metric tensor $[g_{\mu\nu}]$ of the level set surface ϕ manifold representing the active contour are *arbitrary* chosen as follows:

$$\begin{cases} X : (x_1, ..., x_n, \sigma) \rightarrow (x_1, ..., x_n, \sigma, \phi) \\ [h_{ij}] = \text{diag}\left(\frac{1}{c^2}\mathcal{I}_n, \frac{1}{c^2\rho^2}, \frac{1}{c^2}\right) =: [h_{ij}^{SS}] \\ [g_{\mu\nu}] = \partial_\mu X^i \partial_\nu X^j h_{ij} =: [g_{\mu\nu}^{SS}] \end{cases} \tag{6.24}$$

where $x_1, ..., x_n$ are the n spatial components and σ is the scale parameter. Then, the previous Equations (6.24) are introduced in Functional (6.4) and its minimization flow (6.5):

$$\begin{cases} S_f = \int d^{n_\Sigma}\sigma \ f \ g^{1/2} \\ \partial_t X^l = f\mathcal{H}^l + \partial_k f g^{\mu\nu}\partial_\mu X^k \partial_\nu X^l - \frac{n_M.n_\Sigma}{2}\partial_k f h^{kl} \end{cases} \tag{6.25}$$

which leads to the energy functional and the evolution equation for the $(n+2)$-th component of X, i.e. the level set component ϕ, which embeds the *multiscale active contour* (MAC):

$$
\begin{cases}
E_{MAC} & = \quad \int f\sqrt{1+|\nabla\phi|^2+\rho^2\phi_\sigma^2} \prod_{1\leq i\leq n} \frac{dx_i}{c}\frac{d\sigma}{c\rho} \\
\partial_t\phi & = \quad g_{SS}^{-1/2}f\mathcal{K}_{SS} + \langle\nabla^{\mathbf{x},\sigma}f,\nabla^{\mathbf{x},\sigma}\phi\rangle_{[g_{SS}^{\mu\nu}]}
\end{cases}
\tag{6.26}
$$

where $f = f(x_1,...,x_n,\sigma)$, $g_{SS} = \frac{1}{c^{2(n+1)}\rho^2}(1+|\nabla\phi|^2+\rho^2\phi_\sigma^2)$ is the determinant of $[g_{\mu\nu}^{SS}]$, $\prod\frac{dx_i}{c}\frac{d\sigma}{c\rho}$ corresponds to the infinitesimal invariant volume in the scale spaces defined by the metric tensor (6.14), $\nabla^{\mathbf{x},\sigma} := (\nabla,\partial_\sigma)$, $\langle.,.\rangle_{[g_{SS}^{\mu\nu}]}$ is the inner product in manifolds $(\Sigma,[g_{SS}^{\mu\nu}])$ such that

$$
\langle V_1,V_2\rangle_{[g_{SS}^{\mu\nu}]} := V_1^T[g_{SS}^{\mu\nu}]V_2 = V_{1\mu}g_{SS}^{\mu\nu}V_{2\nu},
\tag{6.27}
$$

and $\mathcal{K}_{SS}$ is the $(n+2)$-th component of the mean curvature vector (6.5) (up to $g^{-1/2}$) generalized to scale spaces:

$$
\mathcal{K}_{SS} = \left(\partial_\mu(g^{1/2}g^{\mu\nu}\partial_\nu X^l) + g^{1/2}\Gamma_{jk}^l\partial_\mu X^j\partial_\nu X^k g^{\mu\nu}\right)_{g_{\mu\nu}^{SS}=\partial_\mu X^i\partial_\nu X^j h_{ij}^{SS}}.
\tag{6.28}
$$

By analogy with Section 6.3, we look for the evolution equation of the level sets of ϕ which zero level set represents the multiscale active contour. The evolution equation of the level set function ϕ can be re-written as follows:

$$
\begin{aligned}
\partial_t\phi & = \quad g_{SS}^{-1/2}f\mathcal{K}_{SS} + \langle\nabla^{\mathbf{x},\sigma}f,\nabla^{\mathbf{x},\sigma}\phi\rangle_{[g_{SS}^{\mu\nu}]} \tag{6.29} \\
& = \quad g_{ES}^{-1/2}\underbrace{\left(\sqrt{\frac{g_{ES}}{g_{SS}}}f\mathcal{K}_{SS} + \sqrt{g_{ES}}\langle\nabla^{\mathbf{x},\sigma}f,\nabla^{\mathbf{x},\sigma}\phi\rangle_{[g_{SS}^{\mu\nu}]}\right)}_{=:F_{SS}}, \tag{6.30}
\end{aligned}
$$

where $g_{ES} = 1+|\nabla^{\mathbf{x},\sigma}\phi|^2$. Same remark as in Section 6.3, Equation (6.30) of the level set function $\partial_t\phi = g_{SS}^{-1/2}F_{SS}$ implies that the surface Σ evolves according to $\partial_t X = F_{SS}\mathcal{N}_\Sigma$ where $\mathcal{N}_\Sigma$ is the unit normal to Σ and the level sets of ϕ move according to the equation:

$$
\partial_t C = P_\phi X_t = \left(f\mathcal{K}_{SS}r_{SS}(\phi,c,\rho) - \langle\nabla^\diamond f,\mathcal{N}\rangle r_{SS}^2(\phi,c,\rho)\right)\mathcal{N},
\tag{6.31}
$$

where operator $\nabla^\diamond = \frac{1}{c^2\rho^2}(\nabla,\rho^2\partial_\sigma)$, $\mathcal{N} = -\nabla^{\mathbf{x},\sigma}\phi/|\nabla^{\mathbf{x},\sigma}\phi|$ and the function r_{SS} is equal to $|\nabla^{\mathbf{x},\sigma}\phi|/g_{SS}$ in this case.

In the rest of this section, we develop some equations for $n=2$, i.e. 2-D images, that will use to experiment our multiscale segmentation model. The harmonic map X and the metric tensor $[h_{ij}^{SS}]$ of embedding scale spaces for $n=2$ have the following form:

$$
\begin{cases}
X : (x,y,\sigma) \rightarrow (x,y,\sigma,\phi) \\
[h_{ij}^{SS}] = \text{diag}\left(\frac{1}{c^2},\frac{1}{c^2},\frac{1}{c^2\rho^2},\frac{1}{c^2}\right)
\end{cases}
\tag{6.32}
$$

Then, the metric tensor $[g_{\mu\nu}^{SS}]$, its determinant g_{SS} and its inverse metric $[g_{SS}^{\mu\nu}]$ are as follows:

$$
\left\{
\begin{array}{rcl}
\left[g_{\mu\nu}^{SS}\right] & = & \dfrac{1}{c^2}\begin{pmatrix} 1+\phi_x^2 & \phi_x\phi_y & \phi_x\phi_\sigma \\ \phi_x\phi_y & 1+\phi_y^2 & \phi_y\phi_\sigma \\ \phi_x\phi_\sigma & \phi_y\phi_\sigma & \frac{1}{\rho^2}+\phi_\sigma^2 \end{pmatrix} \\[20pt]
g_{SS} & = & \dfrac{1}{c^6\rho^2}(1+\phi_x^2+\phi_y^2+\rho^2\phi_\sigma^2) \\[14pt]
\left[g_{SS}^{\mu\nu}\right] & = & \dfrac{1}{g}\dfrac{1}{c^4\rho^2}\begin{pmatrix} 1+\phi_y^2+\rho^2\phi_\sigma^2 & -\phi_x\phi_y & -\rho^2\phi_x\phi_\sigma \\ -\phi_x\phi_y & 1+\phi_x^2+\rho^2\phi_\sigma^2 & -\rho^2\phi_y\phi_\sigma \\ -\rho^2\phi_x\phi_\sigma & -\rho^2\phi_y\phi_\sigma & \rho^2(1+\phi_x^2+\phi_y^2) \end{pmatrix}
\end{array}
\right. \tag{6.33}
$$

The energy functional of the multiscale active contours for $n=2$ is

$$
E_{MAC}^{SS} = \int f\sqrt{1+\phi_x^2+\phi_y^2+\rho^2\phi_\sigma^2}\ \frac{dxdyd\sigma}{c^3\rho} \tag{6.34}
$$

The general evolution equation of multiscale active contours for $n=2$ is very long! Hence, it is easier to develop the evolution equation of active contours in specific scale spaces. In this work, we choose to use the most well-known scale space, i.e. the linear scale space. But other scale spaces can be used in our segmentation framework. In the future, it will be interesting to develop the curvature scale space which efficiently preserve multiscale edges to carry out the shape recognition task.

6.6 Active Contours in the Linear Scale Space

The first natural application of the previous multiscale segmentation model is in the linear scale space, obtained when the conductance function is equal to $c=\sigma$ (the scale parameter) and the density function equal to $\rho=1$. We consider the case $n=2$ of 2-D images. In this situation, the harmonic map X, the metric tensors $[h_{ij}^{LSS}]$, $[g_{\mu\nu}^{LSS}]$ and $[g_{LSS}^{\mu\nu}]$ are as follows:

$$
\left\{
\begin{array}{rcl}
X & : & (x,y,\sigma)\rightarrow(x,y,\sigma,\phi) \\[10pt]
\left[h_{ij}^{LSS}\right] & = & \dfrac{1}{\sigma^2}\mathcal{I}_4 \\[12pt]
\left[g_{\mu\nu}^{LSS}\right] & = & \dfrac{1}{\sigma^2}\begin{pmatrix} 1+\phi_x^2 & \phi_x\phi_y & \phi_x\phi_\sigma \\ \phi_x\phi_y & 1+\phi_y^2 & \phi_y\phi_\sigma \\ \phi_x\phi_\sigma & \phi_y\phi_\sigma & 1+\phi_\sigma^2 \end{pmatrix} \\[20pt]
g_{SS} & = & \dfrac{1}{\sigma^6}(1+\phi_x^2+\phi_y^2+\phi_\sigma^2) \\[14pt]
\left[g_{LSS}^{\mu\nu}\right] & = & \dfrac{1}{g}\dfrac{1}{\sigma^4}\begin{pmatrix} 1+\phi_y^2+\phi_\sigma^2 & -\phi_x\phi_y & -\phi_x\phi_\sigma \\ -\phi_x\phi_y & 1+\phi_x^2+\phi_\sigma^2 & -\phi_y\phi_\sigma \\ -\phi_x\phi_\sigma & -\phi_y\phi_\sigma & 1+\phi_x^2+\phi_y^2 \end{pmatrix},
\end{array}
\right. \tag{6.35}
$$

which implies that the energy of the multiscale active contour in the linear scale space is equal to:

$$
E_{MAC}^{LSS} = \int f\sqrt{1+\phi_x^2+\phi_y^2+\phi_\sigma^2}\ \frac{dxdyd\sigma}{\sigma^3}, \tag{6.36}
$$

and the flow applied on the level set function ϕ (embedding the active contour) is:

$$\partial_t \phi = g_{LSS}^{-1/2} f \mathcal{K}_{LSS} + g_{LSS}^{-1} \frac{1}{\sigma^2} \langle \nabla^{\mathbf{x},\sigma} f, \nabla^{\mathbf{x},\sigma} \phi \rangle_{LSS}, \tag{6.37}$$

where $\mathcal{K}_{LSS}$ is the mean curvature in the linear scale space computed using Equation (6.28):

$$\mathcal{K}_{LSS} = \underbrace{g_{LSS}^{-1/2} \frac{\phi_{\mu\nu}}{\sigma^6} g_{LSS}^{\mu\nu}}_{(1)} - \underbrace{3 g_{LSS}^{1/2} \frac{\phi_\mu}{\sigma} g^{\mu\sigma}}_{(2)}. \tag{6.38}$$

The first part of the mean curvature (6.38.1) in the linear scale space corresponds to the Euclidean part because the Euclidean mean curvature is equal to $g_{ES}^{-1/2} \phi_{\mu\nu} g_{ES}^{\mu\nu}$ when $\sigma = 1$, and the second term (6.38.2) corresponds to the Riemannian part. More explicitly, Equation (6.38) is equal to:

$$
\begin{aligned}
\mathcal{K}_{LSS} &= \frac{1}{\sigma} (1 + \phi_x^2 + \phi_y^2 + \phi_\sigma^2)^{-3/2} \cdot \big[\phi_{xx}(1 + \phi_y^2 + \phi_\sigma^2) + \phi_{yy}(1 + \phi_x^2 + \phi_\sigma^2) + \\
&\quad \phi_{\sigma\sigma}(1 + \phi_x^2 + \phi_y^2) - 2\phi_{xy}\phi_x\phi_y - 2\phi_{x\sigma}\phi_x\phi_\sigma - 2\phi_{y\sigma}\phi_y\phi_\sigma \big] \\
&\quad - 3 \frac{1}{\sigma^2} (1 + \phi_x^2 + \phi_y^2 + \phi_\sigma^2)^{-3/2} \cdot \phi_\sigma
\end{aligned} \tag{6.39}
$$

Finally, $\langle \cdot, \cdot \rangle_{LSS}$ in Equation (6.37) is the inner product in the linear scale space defined by $\langle V_1, V_2 \rangle_{LSS} = \frac{1}{\sigma^2} \langle V_1, V_2 \rangle$ such that:

$$\frac{1}{\sigma^2} \frac{1}{g_{LSS}} \langle \nabla^{\mathbf{x},\sigma} f, \nabla^{\mathbf{x},\sigma} \phi \rangle_{LSS} = \frac{\sigma^2}{1 + \phi_x^2 + \phi_y^2 + \phi_\sigma^2} (f_x \phi_x + f_y \phi_y + f_\sigma \phi_\sigma). \tag{6.40}$$

6.7   Multiscale Image Features

The previous sections introduced the segmentation model of *multiscale active contours* which is able to extract multiscale objects in multiscale images. The extraction process is based on a PDE (6.26) defining an evolution equation for hyper-surfaces in non-Euclidean manifolds, the scale spaces, which capture multiscale image features represented by the function f in the flow $\partial_t \phi = g_{SS}^{-1/2} f \mathcal{K}_{SS} + \langle \nabla^{\mathbf{x},\sigma} f, \nabla^{\mathbf{x},\sigma} \phi \rangle_{[g_{SS}^{\mu\nu}]}$. Which are the possible functions f to capture local multiscale edges?

6.7.1   Classical Multiscale Edge Detecting Function

By analogy with the classical model of geometric/geodesic active contours [35, 103, 105], the most common multiscale edge detecting function to capture multiscale structures is based on the norm of the image gradient:

$$f = \frac{1}{1 + \beta |\nabla_{SS} I(x_1, \ldots, x_n, \sigma)|^2}, \tag{6.41}$$

where β is an arbitrary positive parameter, ∇_{SS} is the scale space gradient defined in Equation (6.15) such as $|\nabla_{SS} I| = (c^2 I_{x_1}^2 + \ldots + c^2 I_{x_n}^2 + c^2 \rho^2 I_\sigma^2)^{1/2}$ and I is a multiscale image obtained by

applying a PDE such as (6.18),(6.19),(6.20), (6.21) or (6.22) on a given image I_0. The definition of the edge detecting function (6.41) is easy to establish without technical particularities. However, it is possible to define an enhanced multiscale edge detecting function with the work of Eberly [71] who studied many image features in a strong mathematical framework based on differential geometry. In our approach, we will consider special image features called *ridges*.

6.7.2 Multiscale Edge Detecting Function Based on Ridges

In [71], Eberly explored various ways to detect local image features, called ridges, in n-dimensional spaces. Ridges play an important role in the characterization of semantic local features. Generally speaking, ridges are image features of a function which have local maximum in f along the direction of the greatest concavity [123]. Thus, at a ridge point the direction of greatest curvature is the cross-ridge direction and the value of the function is greater than the neighboring points on either side of it. Figure 6.9 illustrates a line of ridge points.
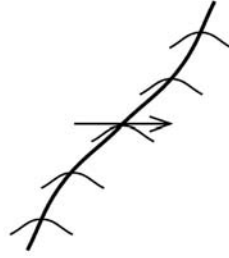
Figure 6.9: Ridges as maxima in the direction of the greatest curvature, reproduced from [123].

Ridges can be defined by different ways [71]. In our approach, we use the definition developed in Section 2.3 of [71]. A point in an n-D space is an m-D ridge ($m < n$) of a function $\mathcal{F}$ if:

$$
\begin{cases} \lambda_i < 0 \\ \langle e_i, \nabla \mathcal{F} \rangle = 0 \end{cases} \qquad \text{for all } i < n - m, \tag{6.42}
$$

where $(\lambda_1, \ldots, \lambda_n)$ with $|\lambda_1| \leq \ldots \leq |\lambda_n|$ and $(e_1, \ldots, e_n)$ are the eigenvalues and the corresponding eigenvectors of the *Hessian* of $\mathcal{F}$, which is the $n \times n$ matrix of the second derivatives of $\mathcal{F}$. The Hessian is a fundamental quantity in geometry because it is related with the intrinsic geometry of the n-graph independently of the surface parametrization. It is important to notice that the Hessian computed in an Euclidean space is different in a Riemannian space. The scale space Hessian ∇_{SS}^2 is obtained according to the following equation [110, 123]:

$$
\nabla_{SS}^2 := \sqrt{\left[h_{SS}^{ij} \right]^{-T}} \frac{d_c \nabla^{\mathbf{x}, \sigma} f}{d_c \xi_{SS}} \sqrt{\left[h_{SS}^{ij} \right]^{-1}}, \tag{6.43}
$$

where $\xi_{SS} = (x_1, \ldots, x_n, \sigma)$ and $\frac{d_c \nabla^{\mathbf{x}, \sigma} f}{d_c \xi_{SS}}$ is the covariant derivative of $\nabla^{\mathbf{x}, \sigma} f$, which is a second-order tensor defined by:

$$
\frac{d_c \nabla^{\mathbf{x}, \sigma} f}{d_c \xi_{SS}} = \left[\nabla^{\mathbf{x}, \sigma 2} f - \sum_{k=1}^{n+1} \Gamma^k (\nabla^{\mathbf{x}, \sigma} f)_k \right], \tag{6.44}
$$

where $\nabla^{\mathbf{x},\sigma\,2}$ stands for the Euclidean Hessian, $(\nabla^{\mathbf{x},\sigma} f)_k$ is the k-th component of $\nabla^{\mathbf{x},\sigma} f$ and Γ^k is the k-th Levi-Civita connection coefficient of $[h_{SS}^{ij}]$. In the practical case of 2-D images, i.e. when $n = 2$, and considering the linear scale space with $c = \sigma$ and $\rho = 1$, then the Hessian, which takes into account the particular interdependence between space and scale, is equal to [123]:

$$\nabla^2_{LSS} = \left[\begin{array}{ccc} \sigma^2 \frac{\partial^2 \mathcal{F}}{\partial x^2} - \sigma \frac{\partial \mathcal{F}}{\partial \sigma} & \sigma^2 \frac{\partial^2 \mathcal{F}}{\partial x \partial y} & \sigma^2 \frac{\partial^2 \mathcal{F}}{\partial x \partial \sigma} + \sigma \frac{\partial \mathcal{F}}{\partial x} \\ \sigma^2 \frac{\partial^2 \mathcal{F}}{\partial x \partial y} & \sigma^2 \frac{\partial^2 \mathcal{F}}{\partial y^2} - \sigma \frac{\partial \mathcal{F}}{\partial \sigma} & \sigma^2 \frac{\partial^2 \mathcal{F}}{\partial y \partial \sigma} + \sigma \frac{\partial \mathcal{F}}{\partial y} \\ \sigma^2 \frac{\partial^2 \mathcal{F}}{\partial x \partial \sigma} + \sigma \frac{\partial \mathcal{F}}{\partial x} & \sigma^2 \frac{\partial^2 \mathcal{F}}{\partial y \partial \sigma} + \sigma \frac{\partial \mathcal{F}}{\partial y} & \sigma^2 \frac{\partial^2 \mathcal{F}}{\partial \sigma^2} + \sigma \frac{\partial \mathcal{F}}{\partial \sigma} \end{array} \right]. \tag{6.45}$$

Equations (6.42) and (6.45) allow us to compute multiscale ridges for a function $\mathcal{F}$ to be chosen. In our approach, we decide to extract ridges from the norm of the scale space gradient of the multiscale image I:

$$\mathcal{F} = |\nabla_{LSS} I(x, y, \sigma)| = \sigma \cdot (I_x^2 + I_y^2 + I_\sigma^2)^{1/2}, \tag{6.46}$$

using Equation (6.42). The result of this process is a binary function, namely $\mathbf{1}_{ridges}(x, y, \sigma)$ which is equal to 1 for ridge points and 0 otherwise. Then, the function $\mathbf{1}_{ridges}$ is multiplied by the multiscale norm $|\nabla_{LSS} I|$ to weight the ridge points. Finally, our edge detecting function is given by the equation:

$$f = \frac{1}{1 + \beta \left(\mathbf{1}_{ridges} \cdot |\nabla_{LSS} I|\right)}, \tag{6.47}$$

which means that f is equal to 1 on homogeneous regions as in the classical model of geometric/geodesic active contour [35, 103, 105].

Let us detect some ridge points in the linear scale space of the 2-D fractal image proposed by Von Koch on Figure 6.5. First of all, the linear scale space of the given image, corrupted with additive Gaussian noise, is computed and presented on Figure 6.6. Then, the multiscale image gradient norm is determined on the first row of Figure 6.10. The multiscale ridges of the scale space norm are determined according to the eigenvalues and the eigenvectors of the Hessian (6.45) and multiplied by the norm of the scale space image gradient, see second row of Figure 6.10.

6.8   Multiscale Gradient Vector Flow

Section 6.5 proposed a multiscale segmentation flow (6.26) which is able to capture structures (6.41) and (6.47) in scale spaces defined in Section 6.7. The segmentation process is completely defined however it is very *slow* as the process of geometric/geodesic active contours. This is due to the edge detecting function f and its gradient $\nabla^{\mathbf{x},\sigma} f$ in (6.26) which are only *"active" close to object edges*. Indeed, when the active contour is far from edges, the gradient of f is close to zero and f is nearly equal to 1, which means that only the curvature acts, which is a slow evolution process. When the active contour is close to edges, then the gradient of f becomes active and attract the snake toward the edges. The evolution process could be speed up if the active contour was attracted by the edges in homogeneous/smooth regions. This issue was solved by Xu-Prince in [186] who proposed a method called the *gradient vector flow* (GVF) which can *extend* the multiscale gradient field of f
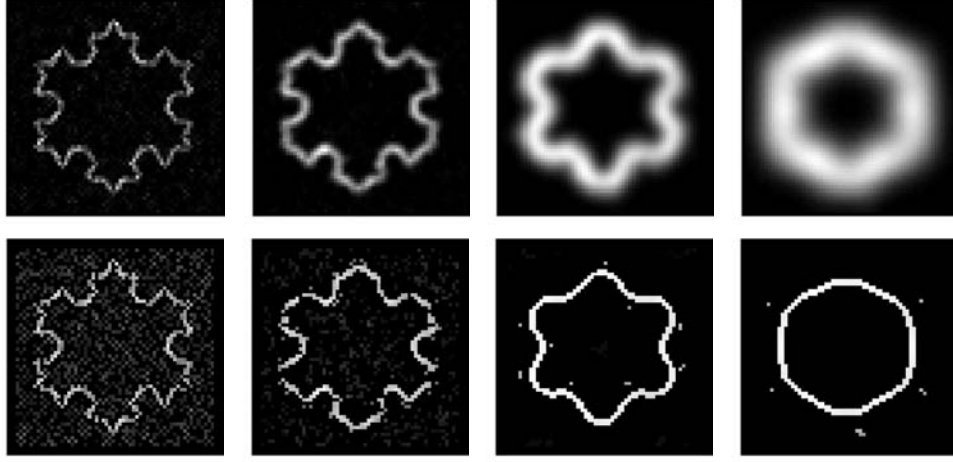
Figure 6.10: The first row represents the norm of the scale space gradient of the multiscale image computed on Figure 6.6 at four scales of observation and the second row presents the ridges of the scale space image gradient norm.

into smooth regions and also deal with the problem of *concave regions*. In the following, we firstly present the original model of Xu-Prince who is designed to work in Euclidean spaces. Then, we will extend the model to scale spaces.

6.8.1 Gradient Vector Flow in Euclidean Spaces

The gradient vector flow model was originally developed to overcome the issues of contour initialization and poor convergence to boundary concavities in the geometric/geodesic active contours model [35, 103, 105]. For example, Figure 6.13 presents an object with concave concavities which can not be fully segmented with classical geometric/geodesic active contours (even with a balloon force [49]) since the snake can not go inside concave parts of the given object. Moreover, the convergence of the classical active contours model is slow compared with the method proposed by Xu-Prince in [186] even if the initial contour is satisfactory. Xu-Prince propose to *diffuse/extend the image gradients* into smooth regions while preserving edge forces. Their method is defined in a variational framework since the GVF field minimizes the following energy functional in the n-D Euclidean space:

$$F_{ES}^{GVF}(\mathbf{V}) = \int \ \mu \underbrace{\left(\sum_{i=1}^{n} |\nabla V_i|^2 \right)}_{(1)} + \underbrace{|\nabla f|^2 |\mathbf{V} - \nabla f|^2}_{(2)} \ d\mathbf{x}, \tag{6.48}$$

where $f(x_1, \ldots, x_n)$ is the initial data n-D function, $\mathbf{V}(x_1, \ldots, x_n) = (V_1, \ldots, V_n)$ is the *gradient vector field* minimizing Functional (6.48) and extending the original gradient of f in homogeneous/smooth regions, μ is an arbitrary constant which balances the contributions between the diffusion and regularization term (6.48.1) and the data fidelity term (6.48.2). Indeed, if $\mu \to 0$ then the solution is $\mathbf{V} = \nabla f$ and if $\mu \to \infty$ then $\mathbf{V}$ is solution of the classic isotropic diffusion equation $\int \sum_{i=1}^{n} |\nabla V_i|^2$. Moreover, when the norm of gradient $|\nabla f|$ is small in (6.48), i.e. in smooth regions, the term (6.48.2) is also small and Energy (6.48) minimizes the diffusion-based term (6.48.1) by propagating the vector field $\mathbf{V}$. Inversely, when the norm of gradient $|\nabla f|$ is large, i.e. on edges, the

second term (6.48.2) dominates and constraints the vector field $\mathbf{V}$ to be equal to the original data ∇f.

The minimization of Energy functional (6.48) is done using the calculus of variations and the gradient descent method which provide n flows, one per component of the GVF field. The Frechet derivative of F_{ES}^{GVF} w.r.t. V_i in the ξ-direction is

$$\langle \frac{\partial F_{ES}^{GVF}}{\partial V_i}, \xi \rangle = \int \xi \cdot \left[-\mu \left(\sum_{j=1}^{n} \partial_{x_j}^2 V_i \right) + |\nabla f|^2 (V_i - \partial_{x_i} f) \right] d\mathbf{x}, \quad \text{for } 1 \le i \le n. \qquad (6.49)$$

Then, the flow minimizing F_{ES}^{GVF} w.r.t. V_i is

$$\frac{\partial V_i}{\partial t} = \mu \left(\sum_{j=1}^{n} \partial_{x_j}^2 V_i \right) - |\nabla f|^2 (V_i - \partial_{x_i} f), \quad \text{for } 1 \le i \le n. \qquad (6.50)$$

Let us apply the GVF model to the picture 6.11. Figure 6.12 presents the gradient of the image 6.11 and the extended image gradient computed with Equations (6.50). Finally, Figure 6.13 illustrates the usefulness of the GVF method since the geodesic/geometric active contours model which uses the classic image gradient can not fully segment the harmonic boundary whereas the gradient vector flow allows us to completely segmented the boundary.
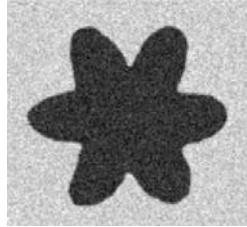
Figure 6.11: Object which boundary is an harmonic curve.

(a)	(b)	(c)	(d)
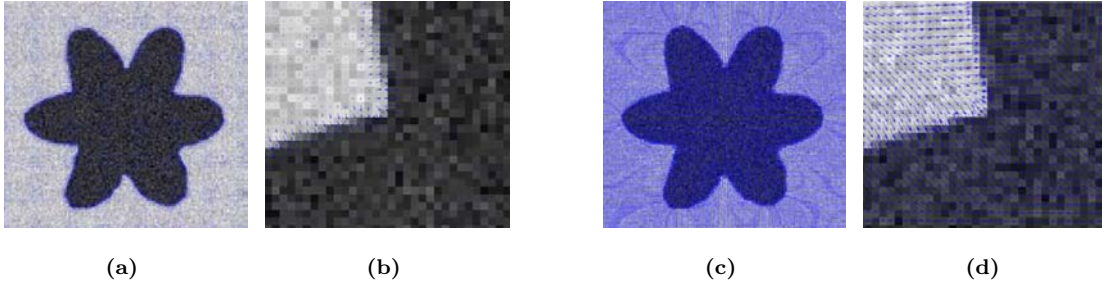
Figure 6.12: Figure (a) and (b) present the gradient of the given image. Figure (c) and (d) show the extended image gradient using the GVF method. Note that Figures (a) and (d) respectively are zooms of Figures (a) and (c) respectively.

(a)   **(b)**   **(c)**
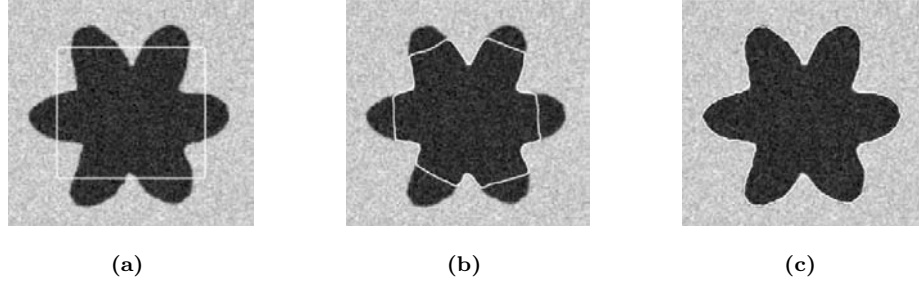
Figure 6.13: Figure (a) presents the initial active contour. Figure (b) is the final contour using the classic image gradient on Figure 6.12(a) and Figure (c) is the final contour using the GVF method on Figure 6.12(c).

6.8.2   Gradient Vector Flow in Scale Spaces

The previous section introduced the GVF method which basically extends the image gradient in homogeneous/smooth regions to faster capture image edges and to deal with concave and convex object boundaries. The previous method was defined in n-D Euclidean spaces but we will *generalize* it into scale spaces by taking account the special relation between space and scale using the metric tensor (6.14). We will use the multiscale gradient vector flow model to extend the multiscale edge detecting function (6.41) or (6.47) into smooth regions to efficiently capture multiscale objects in multiscale images.

The Euclidean GVF model is extended to scale spaces by simply "updating" the Euclidean quantities to their Riemannian equivalents. Thus, the Euclidean gradient ∇ is replaced by the scale space gradient ∇_{SS} and the Euclidean infinitesimal invariant volume element $d\mathbf{x}$ by the scale space one $d\mathbf{x}_{SS}$, Energy functional (6.48) then becomes:

$$F_{SS}^{GVF}(\mathbf{V}) = \int \mu \left(\sum_{i=1}^{n} |\nabla_{SS} V_i|^2 \right) + |\nabla_{SS} f|^2 (\mathbf{V} - \nabla_{SS} f)^2 \ d\mathbf{x}_{SS}, \qquad (6.51)$$

Considering the scale space gradient $\nabla_{SS} = (c\nabla, \rho c \partial_\sigma)$ and $d\mathbf{x}_{SS} = \prod_{1 \le i \le n} \frac{dx_i}{c} \frac{d\sigma}{c\rho}$, the Frechet derivative of F_{SS}^{GVF} w.r.t. V_i in the ξ-direction is:

$$\langle \frac{\partial F_{SS}^{GVF}}{\partial V_i}, \xi \rangle = \int \xi \cdot$$
$$\left[-\mu \left(\sum_{j=1}^{n} \partial_{x_j}(c^2 \partial_{x_j} V_i) + \partial_\sigma(c^2 \rho^2 \partial_\sigma V_i) \right) + |\nabla_{SS} f|^2 (V_i - (\nabla_{SS} f)_i) \right] \frac{1}{c^{n+1}\rho} \ d\mathbf{x}, \ (6.52)$$

for $1 \le i \le n+1$. Then, the flow minimizing F_{SS}^{GVF} w.r.t. V_i is

$$\frac{\partial V_i}{\partial t} = \mu \left(\sum_{j=1}^{n} \partial_{x_j} \left(\frac{\partial_{x_j} V_i}{c^{n-1}\rho} \right) + \partial_\sigma \left(\frac{\rho \partial_\sigma V_i}{c^{n-1}} \right) \right) - \frac{|\nabla_{SS} f|^2}{c^{n+1}\rho} (V_i - (\nabla_{SS} f)_i), \qquad (6.53)$$

for $1 \leq i \leq n + 1$. For our application, we consider the linear scale space, i.e. $c = \sigma, \rho = 1$ and 2-D images, i.e. $n = 2$:

$$\frac{\partial V_i}{\partial t}(x, y, \sigma) = \mu(\sigma^{-1} \nabla^{\mathbf{x},\sigma 2} V_i - \sigma^{-2} \partial_\sigma V_i) - \sigma^{-1} |\nabla^{\mathbf{x},\sigma} f|^2 (V_i - \sigma \partial_i f), \quad \text{for } i = x, y, \sigma, \quad (6.54)$$

where $\nabla^{\mathbf{x},\sigma 2} = \nabla^2 + \partial_\sigma^2$ and $\nabla^{\mathbf{x},\sigma} = (\nabla, \partial_\sigma)$.

Let us apply the GVF method in the linear scale space of the fractal image of Von Koch shown on Figure 6.5. The initial vector field is chosen to be the scale space gradient of the edge detecting function (6.47), i.e. $\mathbf{V}(t = 0) = \nabla_{LSS} f$, and the resulting GVF is presented on Figure 6.15.
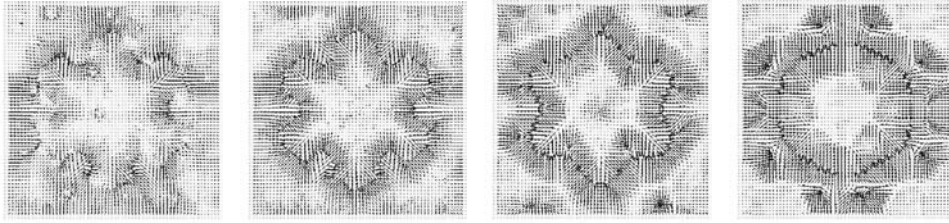
Figure 6.14: Multiscale GVF of the edge detecting function (6.47) at four different scales of observation in the linear scale space of the Von Koch's picture.

The multiscale GVF can also be applied to the classic edge detecting function defined on Equation (6.41). We apply the GVF in the linear scale space of the brain image, Figure 6.7. The norm of the multiscale image gradient and the GVF field are shown on Figure 6.15.
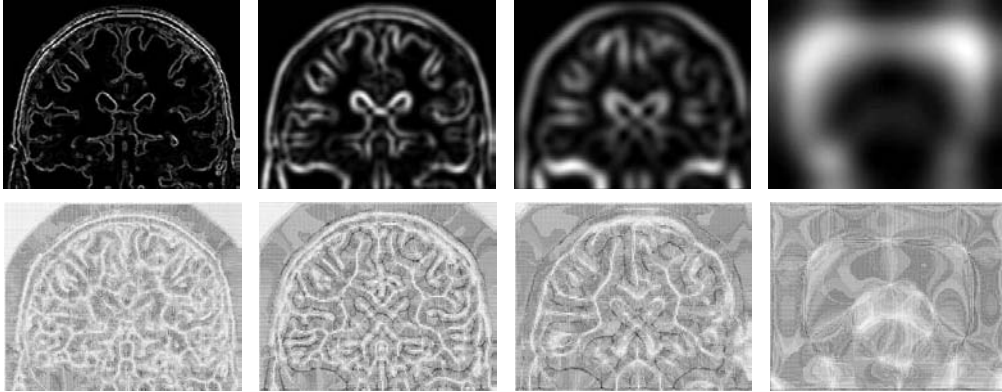
Figure 6.15: First row presents the linear scale space norm of the multiscale brain image, Figure 6.8, and the second row is the multiscale GVF of the classic edge detecting function (6.41) at four different scales of observation.

6.9   Results

In this section, we apply our multiscale image segmentation model (6.26) in the linear scale spaces of images proposed on Figures 6.5 and 6.7. The segmentation process is given by the flow (6.37)

and the multiscale GVF defined in Equation (6.54) is used to extend the attraction of multiscale edges in the scale space.

First of all, we apply the multiscale active contours model to the picture of Von Koch. First top row of Figure 6.16 presents the evolution of the contour, which is a surface in this case, in the linear scale space and the last four rows of Figure 6.16 shows the evolution process of the multiscale snake at four scales of observation, i.e. on four slices of the linear scale space.

We also apply the multiscale active contours model to the brain picture. Note that the brain cortical surface was initially segmented in the original image and the result was used as initial contour for all scales, see second row of Figure 6.17. This prior segmentation is necessary to avoid bad local minima and produce better result. We remind that the active contours method is solved with an evolution equation which captures the closest local minimum in the energy. The GVF model can not allow to avoid local minima, it is only useful to increase the speed of convergence and to capture concave and convex regions. First top row of Figure 6.17 presents the evolution of the multiscale active contour in the linear scale space and the last four rows of Figure 6.17 shows the evolution process of the multiscale snake at four scales of observation, i.e. on four slices of the linear scale space.

6.10   Toward A Mathematical Correctness of the Multiscale Active Contours Model

The multiscale active contours model defined in Equation (6.26) is basically a variational model which solution is given by a *parabolic partial differential equation*. The proposed segmentation model is the generalization of the geometric/geodesic active contours model [35, 105] which mathematical solutions are *viscosity solutions*. Hence, it is natural to ask if the solutions of our multiscale segmentation model are also viscosity solutions?

The theory of viscosity solutions was developed by Crandall-Lions [57] in 1983 for first order PDE and later for second order PDE explained in a didactic way in the "user's guide to viscosity solutions" of Crandall-Ishii-Lions [56]. Generally speaking, viscosity solutions are solutions of PDEs that can be *not smooth*. However, they are consistent with classical smooth solutions since they coincide with them when classical solutions exist. In computer vision, one of the most well-known viscosity solution is the *distance function* [118]:

$$d_K(\mathbf{x}) = \inf_{\mathbf{y} \in K} d(\mathbf{x}, \mathbf{y}), \tag{6.55}$$

where K is a closed subset of $\mathbf{R}^n$ and d is the Euclidean distance. The distance function is solution of the following hyperbolic problem:

$$\begin{cases} |\nabla \phi| = 1 & \text{in } \mathbf{R}^n \setminus K, \\ \phi = 0 & \text{on } \partial K, \end{cases} \tag{6.56}$$

which can be used to re-distance the level set function or to compute geodesics, i.e. paths with minimal length, when $|\nabla \phi| = F$ which function F characterizes the "space weighting".

Unfortunately, the theory of viscosity solutions was designed for solutions defined in Euclidean spaces. But the solutions of our multiscale model are defined in scale spaces, i.e. in *Riemannian*
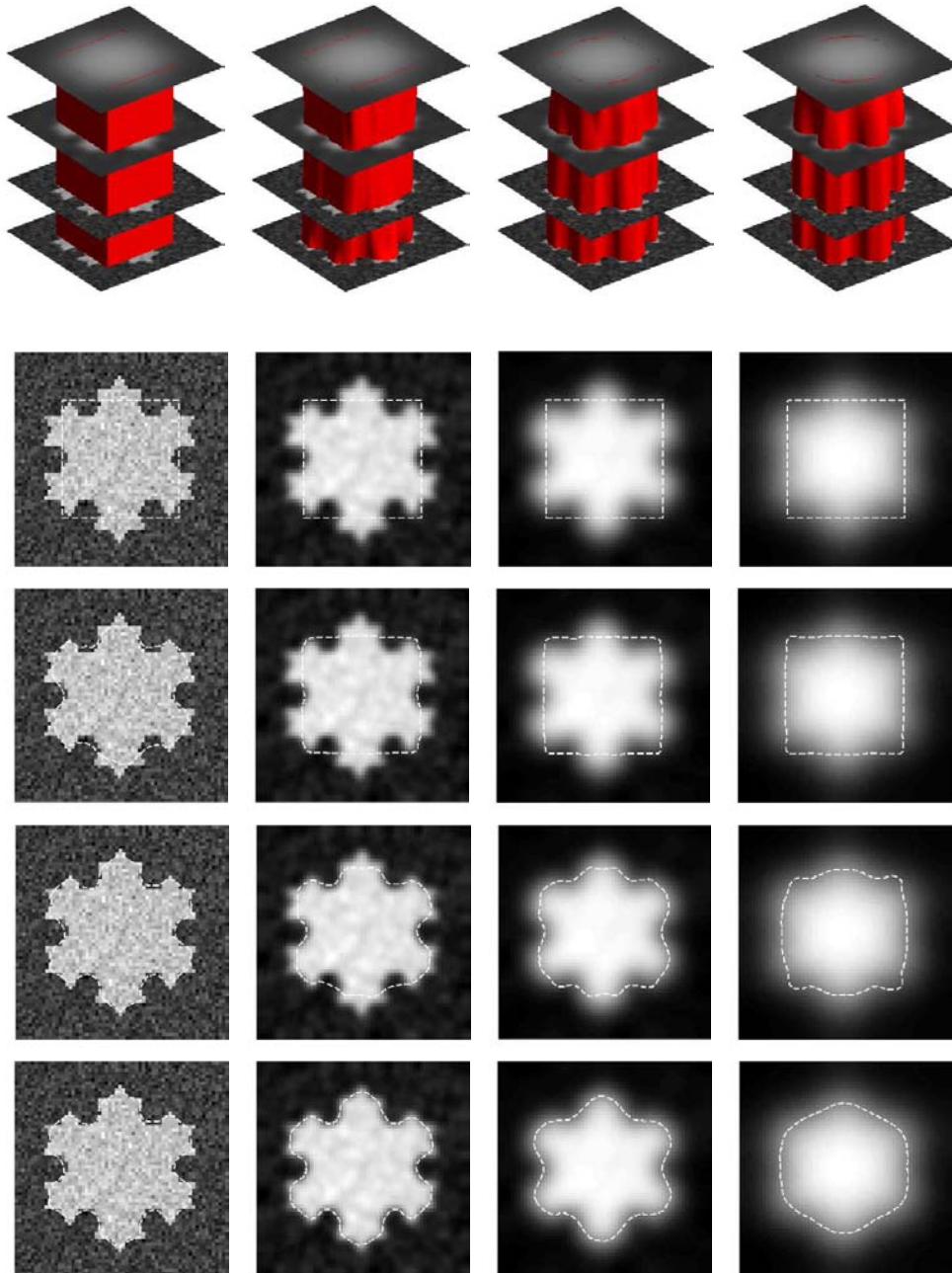
Figure 6.16: First top row presents the multiscale active contour evolving in the linear scale space and the last four row show the active contour propagating at four different scales.
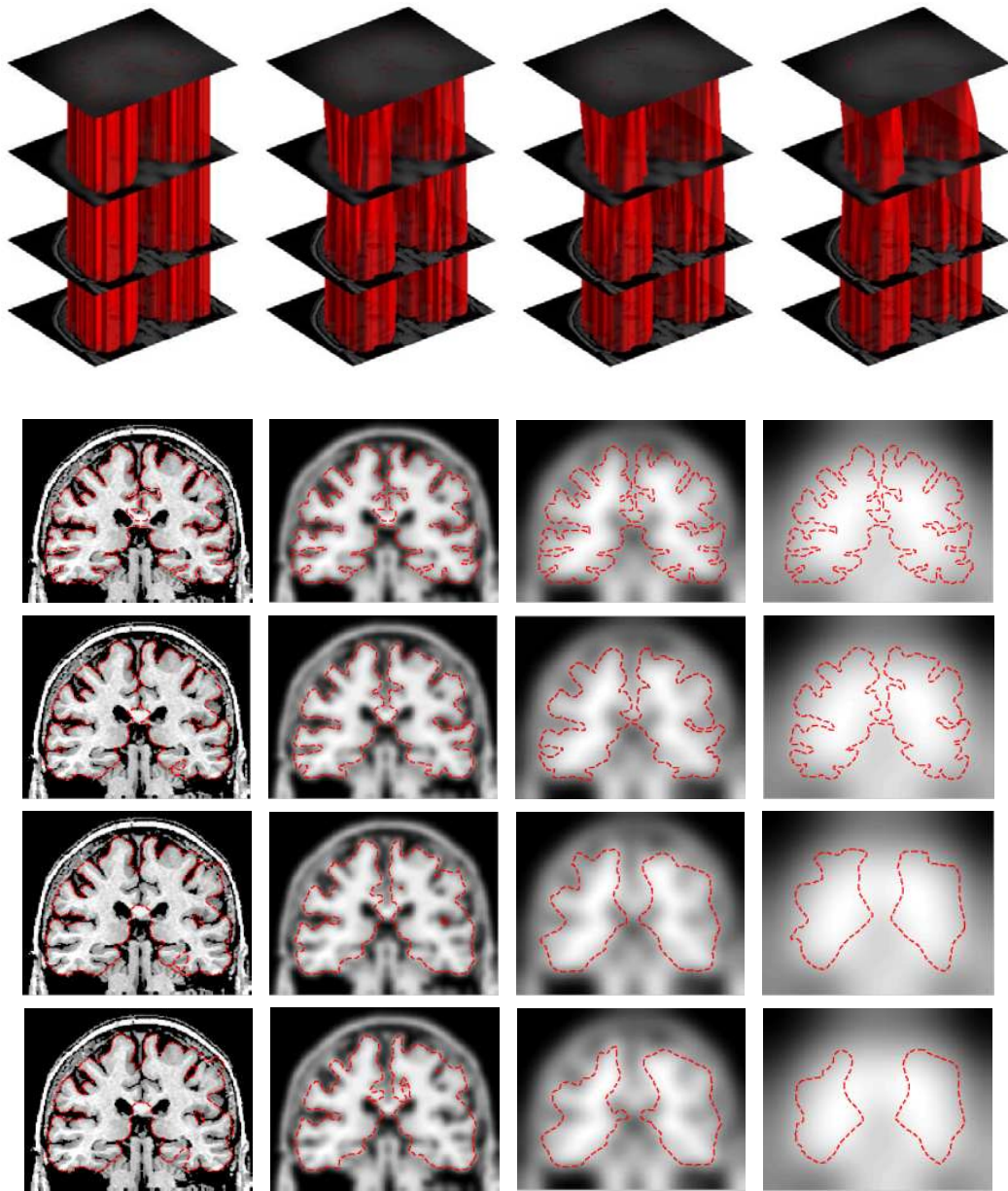
Figure 6.17: First top row presents the multiscale active contour evolving in the linear scale space and the last four row show the active contour propagating at four different scales.

manifolds. If we want to use the theory of viscosity solutions to prove that the solutions of our multiscale problem are viscosity solutions then we have to answer to the fundamental question: is the theory of viscosity solutions valid in Riemannian manifolds? The answer is beyond the scope of this section since it is difficult to prove it. However we propose to define what are viscosity solutions on Riemannian manifolds and to show that our Hamilton-Jacobi equation satisfies the classical *proper* condition to prove the existence of viscosity solutions.

The following definitions are based on the works of Crandall-Ishii-Lions [56] for second order elliptic and hyperbolic equations in Euclidean spaces and Mantegazza-Mennucci [118] who studied the hyperbolic problem (6.56) in Riemannian manifolds. Let M be a compact, smooth, connected n-dimensional differentiable Riemannian manifold defined by the metric tensor $[g_M]$. The following Hamilton-Jacobi problem is considered in a locally compact set $\Omega \subset M$:

$$H(\mathbf{x}, \phi(\mathbf{x}), D_M\phi(\mathbf{x}), D_M^2\phi(\mathbf{x})) = 0 \quad \text{in } \Omega, \tag{6.57}$$

where $H : \Omega \times \mathbf{R} \times T^\star\Omega \times S(n) \to \mathbf{R}$ where $T^\star$ is the cotangent bundle and $S(n)$ is the set of symmetric $n \times n$ matrices, D_M is the covariant differentiation operator on (M, g_M) and D_M^2 is the second order covariant differentiation operator on (M, g_M). We suppose that H is *degenerate elliptic*, which means that

$$H(\mathbf{x}, r, p, X) \leq H(\mathbf{x}, r, p, Y) \text{ whenever } X \leq Y. \tag{6.58}$$

Following the papers [16, 57], we will give two definitions of viscosity solutions for hyperbolic PDEs in Riemannian manifolds. The first definition is based on the maximum principle.

Theorem 1: Maximum Principle and Regular Solutions
$\phi \in C^2(\Omega)$ *is a classic solution of (6.57) in the Riemannian Manifold* (M, g_M) *if and only if:*

$\forall \eta \in C^2(\Omega)$, *if* $\mathbf{x}_0 \in \Omega$ *is a local maximum of* $\phi - \eta$, *we have:*
$H(\mathbf{x}_0, \phi(\mathbf{x}_0), D_M\eta(\mathbf{x}_0), D_M^2\eta(\mathbf{x}_0)) \leq 0,$

and

$\forall \eta \in C^2(\Omega)$, *if* $\mathbf{x}_0 \in \Omega$ *is a local minimum of* $\phi - \eta$, *we have:*
$H(\mathbf{x}_0, \phi(\mathbf{x}_0), D_M\eta(\mathbf{x}_0), D_M^2\eta(\mathbf{x}_0)) \geq 0.$

The proof of this theorem is as follows. Suppose that $\mathbf{x}_0 \in \Omega$ is a local maximum of $\phi - \eta$. It implies that $D_M\phi(\mathbf{x}_0) = D_M\eta(\mathbf{x}_0)$ and $D_M^2\phi(\mathbf{x}_0) \leq D_M^2\eta(\mathbf{x}_0)$ and using the property of degenerate ellipticity of H defined in Equation (6.58), Theorem 1 is proved. Hence, the maximum principle implies that a solution to an elliptic equation can be defined without using regularity properties because Theorem 1 does not need the existence of $D_M\phi$ and $D_M^2\phi$ to determine the solution. Following Theorem 1, we can define a viscosity solution in the Riemannian manifold (M, g_M) as follows:

Definition 1: Viscosity Solutions in Riemannian Manifolds based on the Maximum Principle
$\phi \in C(\Omega)$ *is a viscosity solution of (6.57) in the Riemannian Manifold* (M, g_M) *if and only if:*

$\forall \eta \in C^2(\Omega)$, if $\mathbf{x}_0 \in \Omega$ is a local maximum of $\phi - \eta$, we have:
$H(\mathbf{x}_0, \phi(\mathbf{x}_0), D_M \eta(\mathbf{x}_0), D_M^2 \eta(\mathbf{x}_0)) \leq 0$,

and

$\forall \eta \in C^2(\Omega)$, if $\mathbf{x}_0 \in \Omega$ is a local minimum of $\phi - \eta$, we have:
$H(\mathbf{x}_0, \phi(\mathbf{x}_0), D_M \eta(\mathbf{x}_0), D_M^2 \eta(\mathbf{x}_0)) \geq 0$.

If ϕ only satisfies the first (respectively second) inequation, then ϕ is said to be a viscosity subsolution (resp. viscosity supersolution).

An equivalent definition of viscosity solutions can be given based on the notion of superjet and subjet, which plays an important role in the second order PDEs.

Definition 2: Superjet and Subjet of Second Order Continuous Functions.
Let $\phi \in C(\Omega)$. The second order superjet of ϕ at $\mathbf{x} \in \Omega$ is the convex subset of $T^\star\Omega \times S(n)$, namely $J_\Omega^{2,+}\phi(\mathbf{x})$, which elements (p, X) satisfy:

$$\phi(\mathbf{y}) - \phi(\mathbf{x}) - \langle p, \mathbf{y} - \mathbf{x} \rangle - \tfrac{1}{2}\langle X(\mathbf{y} - \mathbf{x}), \mathbf{y} - \mathbf{x} \rangle \leq o(|\mathbf{y} - \mathbf{x}|^2),$$

for $\mathbf{y} \in \Omega$ near $\mathbf{x}$.
The second order subjet of ϕ at $\mathbf{x} \in \Omega$ is the convex subset of $T^\star\Omega \times S(n)$, namely $J_\Omega^{2,-}\phi(\mathbf{x})$, which elements (p, X) satisfy:

$$\phi(\mathbf{y}) - \phi(\mathbf{x}) - \langle p, \mathbf{y} - \mathbf{x} \rangle - \tfrac{1}{2}\langle X(\mathbf{y} - \mathbf{x}), \mathbf{y} - \mathbf{x} \rangle \geq o(|\mathbf{y} - \mathbf{x}|^2),$$

for $\mathbf{y} \in \Omega$ near $\mathbf{x}$.

In this definition, we implicitly used the Taylor development on the Riemannian manifold (M, g_M):

$$\phi(\mathbf{x}) = \phi(\mathbf{y}) + \langle D_M\phi|_{\mathbf{x}=\mathbf{y}}, \mathbf{y} - \mathbf{x} \rangle + \frac{1}{2}\langle D_M^2\phi|_{\mathbf{x}=\mathbf{y}}(\mathbf{y} - \mathbf{x}), \mathbf{y} - \mathbf{x} \rangle + o(|\mathbf{y} - \mathbf{x}|^2), \qquad (6.59)$$

for $\mathbf{y} \in \Omega$ near $\mathbf{x}$.

Let us propose a new definition of viscosity solutions in the Riemannian manifold (M, g_M):

Definition 3: Viscosity Solutions in Riemannian Manifolds based on the Superjet and Subjet.
A viscosity subsolution of (6.57) in the Riemannian Manifold (M, g_M) is a function $\phi \in USC(\Omega)$ such that:

$$H(\mathbf{x}, \phi(\mathbf{x}), p, X) \leq 0, \quad \forall \mathbf{x} \in \Omega, \forall (p, X) \in J_\Omega^{2,+}\phi(\mathbf{x}).$$

A viscosity supersolution of (6.57) in the Riemannian Manifold (M, g_M) is a function $\phi \in LSC(\Omega)$ such that:

$$H(\mathbf{x}, \phi(\mathbf{x}), p, X) \geq 0, \quad \forall \mathbf{x} \in \Omega, \forall (p, X) \in J_\Omega^{2,-}\phi(\mathbf{x}).$$

ϕ is a viscosity solution if it is both a subsolution and a supersolution. $USC(\Omega)$ is the set of upper semi-continuous functions on Ω and $LSC(\Omega)$ is the set of lower semi-continuous functions on Ω.

Finally, we consider the associated parabolic problem to (6.57):

$$\phi_t + H(t, \mathbf{x}, \phi(\mathbf{x}), D_M\phi(\mathbf{x}), D_M^2\phi(\mathbf{x})) = 0 \qquad (6.60)$$

where now ϕ is a function of $(t, \mathbf{x})$ and $D_M\phi, D_M^2\phi$ mean $D_{M\mathbf{x}}\phi, D_{M\mathbf{x}}^2\phi$. Instead of working on Ω, we introduce $\Omega_T = (0, T) \times \Omega$ and $P_\Omega^{2,+}$, $P_\Omega^{2,-}$ the parabolic variants of the semijets $J_\Omega^{2,+}$, $J_\Omega^{2,-}$. Then, $P_\Omega^{2,+}\phi$ is defined by $(a, p, X) \in \mathbf{R} \times T^\star\Omega \times S(n)$ lies in $P_\Omega^{2,+}\phi(s, \mathbf{y})$ if $(s, \mathbf{y}) \in \Omega_T$ and

$$\phi(t, \mathbf{x}) \leq \phi(s, \mathbf{y}) + a(t - s) + \langle p, \mathbf{x} - \mathbf{y}\rangle + \frac{1}{2}\langle X(\mathbf{x} - \mathbf{y}), \mathbf{x} - \mathbf{y}\rangle + o(|t - s| + |\mathbf{x} - \mathbf{y}|^2), \quad (6.61)$$

for $(t, \mathbf{x}) \in \Omega_T$ near $(s, \mathbf{y})$, which implies the new definition:

Definition 4: Viscosity Solutions of Parabolic Equations in Riemannian Manifolds.
A viscosity subsolution of the parabolic equation (6.60) in the Riemannian Manifold (M, g_M) is a function $\phi \in USC(\Omega_T)$ such that:

$$a + H(\mathbf{x}, \phi(\mathbf{x}), p, X) \leq 0, \quad \forall (t, \mathbf{x}) \in \Omega_T, \forall (a, p, X) \in P_\Omega^{2,+}\phi(t, \mathbf{x}).$$

A viscosity supersolution of the parabolic equation (6.60) in the Riemannian Manifold (M, g_M) is a function $\phi \in LSC(\Omega_T)$ such that:

$$a + H(\mathbf{x}, \phi(\mathbf{x}), p, X) \geq 0, \quad \forall (t, \mathbf{x}) \in \Omega_T, \forall (a, p, X) \in P_\Omega^{2,-}\phi(t, \mathbf{x}).$$

ϕ is a viscosity solution if it is both a subsolution and a supersolution. $USC(\Omega_T)$ is the set of upper semi-continuous functions on Ω_T and $LSC(\Omega_T)$ is the set of lower semi-continuous functions on Ω_T.

As we said at the beginning of this section, we will not attempt to develop the theory of viscosity solutions in Riemannian manifolds which is obviously a difficult task. However, we think that the solution of the parabolic PDE (6.26), representing the multiscale active contours model, might be a viscosity solution defined on scale spaces which are Riemannian manifolds. This idea comes from the expression of the PDE (6.37) which can be re-written in a new shape useful in the theory of viscosity solutions. Indeed, the steady state solution $\phi_1^\star$ of Flow (6.37):

$$\left(g_{LSS}^{-1/2} f\mathcal{K}_{LSS} + g_{LSS}^{-1}\frac{1}{\sigma^2}\langle\nabla^{\mathbf{x},\sigma} f, \nabla^{\mathbf{x},\sigma}\phi\rangle_{LSS}\right)_{\phi_1^\star} = 0, \qquad (6.62)$$

has the same steady state solution when we multiply it by $g_{LSS} > 0$:

$$\left(g_{LSS}^{1/2} f\mathcal{K}_{LSS} + \frac{1}{\sigma^2}\langle\nabla^{\mathbf{x},\sigma} f, \nabla^{\mathbf{x},\sigma}\phi\rangle_{LSS}\right)_{\phi_2^\star = \phi_1^\star} = 0. \qquad (6.63)$$

Hence, the equivalent flow of (6.37) is considered:

$$\phi_t = g_{LSS}^{1/2} f \mathcal{K}_{LSS} + \frac{1}{\sigma^2} \langle \nabla^{\mathbf{x},\sigma} f, \nabla^{\mathbf{x},\sigma} \phi \rangle_{LSS}, \qquad (6.64)$$

which can be re-written in the *attractive* form:

$$\phi_t = \mathrm{Tr}\left[\left(\mathcal{I}_{n+2} - \frac{\nabla_{[h_{LSS}]}\phi \otimes \nabla_{[h_{LSS}]}\phi}{|\nabla_{[h_{LSS}]}\phi|^2} \right) \nabla_{[h_{LSS}]}^2 \phi \right] - \langle V, \nabla_{[h_{LSS}]}\phi \rangle, \qquad (6.65)$$

for a certain V and

$$\begin{cases} \nabla_{[h_{LSS}]}\phi = \sqrt{h_{LSS}^{-T}} \nabla\phi, \\ \nabla_{[h_{LSS}]}^2 \phi = \sqrt{h_{LSS}^{-T}} \left(\nabla^2\phi - \sum_{k=1}^{n+2} \Gamma_{LSS}^k \phi_k \right) \sqrt{h_{LSS}^{-1}}, \end{cases} \qquad (6.66)$$

and setting $p = \nabla_{[h_{LSS}]}\phi$ and $X = \nabla_{[h_{LSS}]}^2 \phi$, we find:

$$\phi_t = \underbrace{\mathrm{Tr}\left[\left(\mathcal{I} - \frac{p \otimes p}{|p|^2} X \right) \right] - \langle V, p \rangle}_{H(t,\mathbf{x},p,X)}, \qquad (6.67)$$

which is the *expression of the Hamilton-Jacobi equation H in the geometric/geodesic active contours model [34, 35, 56]!*

In other words, the shape of our PDE is consistent with the classical theory of viscosity solutions because H is *proper*. Hence, the future directions of research will be to

- attempt to generalize the theory of viscosity solutions to Riemannian manifolds in order to prove the mathematical correctness of Equation (6.65).

and if the theory is valid in Riemannian manifolds, then it will be interesting to

- check if Equation (6.65) can be generalized to any scale spaces:

$$\phi_t = \mathrm{Tr}\left[\left(\mathcal{I}_{n+2} - \frac{\nabla_{[h_{SS}]}\phi \otimes \nabla_{[h_{SS}]}\phi}{|\nabla_{[h_{SS}]}\phi|^2} \nabla_{[h_{SS}]}^2 \phi \right) \right] - \langle V, \nabla_{[h_{SS}]}\phi \rangle, \qquad (6.68)$$

  with

$$\begin{cases} \nabla_{[h_{SS}]}\phi = \sqrt{h_{SS}^{-T}} \nabla\phi, \\ \nabla_{[h_{SS}]}^2 \phi = \sqrt{h_{SS}^{-T}} \left(\nabla^2\phi - \sum_{k=1}^{n+2} \Gamma_{SS}^k \phi_k \right) \sqrt{h_{SS}^{-1}}, \end{cases} \qquad (6.69)$$

- verify if the generalized mean curvature flow embedding in a space $(M, [h_{ij}])$ and acting on the component I of the mapping $X : (x_1, \ldots, x_n) \to (x_1, \ldots, x_n, I)$, defined by Sochen-Kimmel-Malladi [167], can be expressed by (multiply by $g > 0$):

$$g \cdot \left(g^{-1/2} \partial_\mu (g^{\mu\nu} \partial_\nu I) + \Gamma_{jk}^{l=I} \partial_\mu X^j \partial_\nu X^k g^{\mu\nu} \right)_{g_{\mu\nu} = \partial_\mu X^i \partial_\nu X^j h_{ij}} = \qquad (6.70)$$

$$\mathrm{Tr}\left[\left(\mathcal{I}_{n+2} - \frac{\nabla_{[h_{ij}]}I \otimes \nabla_{[h_{ij}]}I}{|\nabla_{[h_{ij}]}I|^2} \nabla_{[h_{ij}]}^2 I \right) \right], \qquad (6.71)$$

  which would prove the existence of a viscosity solution for the generalized mean curvature flow.

6.11   Conclusion and Future Research

In this chapter, we defined a method to extract multiscale objects lying in images. As we said in Section 6.1, the multiscale nature of images makes this image segmentation method relevant.

The *multiscale paradigm* implies that all solutions to a given image analysis problem, corresponding to different scales of observation, are valid! The choice of a "correct" scale is significant only for a given application, which "fixes" the scale, but all solutions are relevant. That is why we considered all scales in our approach, i.e. all possible solutions, to the segmentation problem.

This also allows us to use the important multiscale information given by the scale spaces. Scale spaces were defined in Section 6.4 from the general heat diffusion equation, which provided us the metric tensor of the embedding spaces. Then, we used the framework of Polyakov [143] and Sochen-Kimmel-Malladi [167] to introduce the concept of scale in the active contour model by defining an evolution equation for the active contours in scale spaces. We also chose the metric tensor of the embedded manifold as the induced metric tensor in order to work with harmonic maps as in classical works. This gives us the model of *multiscale active contours*, which attempts to generalize the model of geometric/geodesic active contours to Riemannian manifolds.

Future works will be focused on integrating this multiscale segmentation technique into shape analysis methods such as the shape recognition task with a multiscale shape prior such as the cores [142], and the shape registration method to improve their robustness and their performance. We will also change the linear scale space [27, 28] which does not preserve well the edges. We will use the curvature scale space that is one of the fundamental equation in image processing. Finally, Section 6.10 introduced the issue of viscosity solutions in Riemannian manifolds. We observed that the shape of our Hamilton-Jacobi equation fits well with the Euclidean case. A future direction can be also centered on extending the theory of viscosity solutions to Riemannian manifolds to prove the correctness of our segmentation model.

7

Conclusion
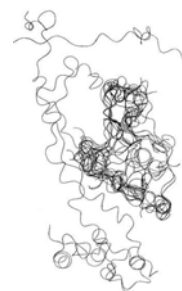
© *Diego Porcel*

7.1 Achievements

This thesis presented four segmentation models to tackle the image segmentation problem.

The first model [25] used the weighted total variation functional to relate the geodesic/geometric active contours model [35, 103, 105] with the ROF image denoising model [155] and the image segmentation models of Chan-Vese [42, 179] based on the Mumford-Shah's functional [125]. *Theoretic proofs, based on [41], were given to show that the minimizers of the proposed variational models are global, which is an important result of this dissertation.* Indeed, the classical geodesic/geometric active contours model is based on important mathematical properties such as invariance w.r.t. the parametrization, well-posed model thanks to the theory of viscosity solutions. However this model suffers from the existence of local minima, which makes the initial active contour critical to get satisfactory results. By coupling two "opposite" image segmentation models we succeeded both to reconcile active contours without and with edges and to determine global minimizers of the initial snake problem. The global minimizers, given by our approach, are not unique, which seems to be a

drawback, but all global solutions are close to each other. Finally, the active contours model defined in this approach did not use classical evolution schemes based on the level set method, which allowed us not to re-initialize the signed distance function embedding the active contour. Instead, we used a PDE-based scheme based on image denoising algorithms and determined global minimizers by thresholding.

The second image segmentation model defined in this thesis combined at the same time determinist and statistical concepts. We used the statistic approach of information theory to define an error probability of classification based on stochastic process and probability densities estimation. This error probability functional was defined by Butz-Thiran's information theoretic approach [32, 33]. This approach provided us a variational model of non-parametric and non-supervised image classification that was minimized with the determinist shape gradient method [13, 69, 99]. *The combination of statistical and determinist approaches in a single framework to carry out the image classification/segmentation task is another important result of this thesis.* Moreover, the information theoretic approach of the classification also allowed us to interpret and better understand other existing models that use information theoretic concepts such as mutual information. We showed that several existing models are conceptually included in our approach. Finally, our model used the cross-correlation approach which both estimates and validates the estimation of the classification result, which is not the case with other models.

The third model [26, 29] proposed a variational model which extracts an object of interest which geometric shape is given by the principal components analysis defined on level set functions by Leventon [113]. Our segmentation model also used the geodesic/geometric active contours model [35, 105] to detect object boundaries and the model of Vese-Chan [179] to capture a smooth intensity region having the shape of interest. *The contribution given by this model is the combination of three families of active contours which capture object boundaries, homogeneous regions and a geometric shape prior in a single segmentation framework in order to combine all advantages of each family.* We also proved that our variational model is mathematically well-posed since there exists a solution in the special space with bounded variation (SBV).

Finally, the fourth and last contribution of this dissertation is the multiscale active contours model [27, 28]. *This model proposed to generalize the active contours model into multi-scale spaces, the scale spaces, in order to define a multiscale image segmentation technique to simultaneously extract structures at different scales of observation.* The main difficulty of this approach is to introduce the active contours into scale spaces that are Riemannian spaces. The solution was given with the Polyakov action [143] that was first used in string theory to reconcile quantum mechanics and gravitation, then in image processing by Sochen-Kimmel-Malladi [167] to naturally denoise multi-dimensional images. Thus, we used the Polyakov framework to define the energy and the evolution equation of the multiscale active contours model. We applied our model on the linear/Gaussian scale space but our framework also works with other well-known scale spaces such as the curvature scale space. Finally, we tried to open a way toward the mathematical correctness of our evolution equation. *We noticed that the shape of the Hamilton-Jacobi equation is exactly the shape of the Hamilton-Jacobi in the Euclidean spaces, which means that if the theory of viscosity solutions can be extended to Riemannian spaces then our model has a viscosity solution.*

7.2   Future Works

Some directions of research can be investigated. The most natural are the following:

- Concerning the first proposed model that determines global minimizers of the active contours/snakes model, the interesting future work will be to apply our framework on the two-phase model of Vese-Chan defined in [179]. Their multiphase segmentation model can partition any given image with triple junctions according to the Four-Color theorem [79] using two level set functions (see Section 2.4.1). We could combine their model with the global minimization framework introduced in Chapter 3 to define a general image segmentation variational model having global solutions.

- The model introduced in Chapter 4 can be extended to multi-dimensional images such as color and texture images. It will also be useful to extend the number of (not necessary connected) regions having same probability densities to more than two regions. It is possible to realize this extension by coupling the level set functions such as in [132, 179].

- The third proposed image segmentation model can also be improved by extending the shape prior model based on the principal components analysis to non-parametric shape density estimations such as the model of Cremers-Osher-Soatto [60]. It should also be interesting to investigate a multi-level set approach to capture more objects having the same shape of interest such as in [64, 65].

- As we said previously, the final segmentation model presented in Chapter 6 should be considered deeply. A future work will be to change the linear scale space with the curvature scale space in order to realize a better multiscale segmentation and above all to carry out a multiscale shape recognition task in good conditions. But one of the most important future work will be to investigate if the theory of viscosity solutions developed by Crandall-Ishii-Lions [56] could be extended to Riemannian manifolds. If it is the case then our multiscale active contours model will be mathematically well-posed as the classical active contours model is.

The previous future directions of research are naturally derived from the four image segmentation models proposed in this thesis. But as we said at the beginning of this thesis image segmentation is not an easy task. However, if we could define a model that merges the four previous models into a single model then we would get close to a general image segmentation model. Indeed, if we could define a multiscale image segmentation model that incorporates statistical/probabilistic concepts such as information theory and multiscale shape priors and if the solution was unique, which means it is provided by a global minimizer, then we would have an efficient model to segment any natural images close to human visual system. But long is the road...

Bibliography

[1] *Numerical Recipies in C++ and C.* Cambridge University Press, 2002.

[2] D. Adalsteinsson and J. Sethian. A Fast Level Set Method for Propagating Interfaces. *Journal of Computational Physics*, 118:269–277, 1995.

[3] F. Alizadeh and D. Goldfarb. Second-Order Cone Programming, Technical Report 51-2001, RUTCOR, Rutgers University, 2001.

[4] L. Alvarez, F. Guichard, P.L. Lions, and J.M. Morel. Axioms and Fundamental Equations of Image Processing. *Archives For Rational Mechanics*, 123(3):199–257, 1993.

[5] L. Alvarez, P.L. Lions, and J.M. Morel. Image Selective Smoothing and Edge Detection by Nonlinear Diffusion (II). *SIAM Journal of Numerical Analysis*, 29(3):845–866, 1992.

[6] L. Ambrosio. A Compactness Theorem for a Few Class of Functions of Bounded Variation. *Bolletino Della Unione Matematica Italiana*, VII(4):857–881, 1989.

[7] L. Ambrosio. Variational Problems in SBV and Image Segmentation. *Acta Applicandae Mathematicae*, 17:1–40, 1989.

[8] L. Ambrosio. Existence Theory for a New Class of Variational Problems. *Archive for Rational Mechanics and Analysis*, 111:291–322, 1990.

[9] L. Ambrosio and H.M. Soner. Level Set Approach to Mean Curvature Flow in Arbitrary Codimension. *Journal of Differential Geometry*, 43:693737, 1996.

[10] L. Ambrosio and V.M. Tortorelli. Approximation of Functionals Depending on Jumps by Elliptic Functionals via Γ-Convergence. *Communications on Pure Applied Mathematics*, 43: 999–1036, 1990.

[11] B. Appleton and H. Talbot. Globally Optimal Geodesic Active Contours. *Journal of Mathematical Imaging and Vision*, 23(1):67–86, 2005.

[12] G. Aubert, M. Barlaud, O. Faugeras, and S. Jehan-Besson. Image Segmentation using Active Contours: Calculus of Variations or Shape Gradients, Technical Report INRIA/I3S RR-4483, 2002.

[13] G. Aubert, M. Barlaud, O. Faugeras, and S. Jehan-Besson. Image Segmentation using Active Contours: Calculus of Variations or Shape Gradients. *SIAM Applied Mathematics*, 63(6): 2128–2154, 2003.

[14] G. Aubert and L. Blanc-Féraud. Some Remarks on the Equivalence Between 2-D and 3-D Classical Snakes and Geodesic Active Contours. *International Journal of Computer Vision*, 34(1):19–28, 1999.

[15] G. Aubert and P. Kornprobst. *Mathematical Problems in Image Processing: Partial Differential Equations and the Calculus of Variations*, volume 147. Springer, 2001.

[16] G. Barles. Solutions de Viscosité et Equations Elliptiques du Deuxième Ordre, 1997.

[17] M. Bertalmío, G. Sapiro, V. Caselles, and C. Ballester. Image Inpainting. In *International Conference on Computer Graphics and Interactive Techniques*, pages 417–424, 2000.

[18] M. Bertalmío, L. Vese, G. Sapiro, and S. Osher. Simultaneous Structure and Texture Image Inpainting. *IEEE Transactions on Image Processing*, 12(8):882 –889, 2003.

[19] J. Besag. Spatial Interaction And The Statistical Analysis Of Lattice Systems. *Journal Of Royal Statistical Society*, 36:192–236, 1974.

[20] B.B. Biswal and J.S. Hyde. Contour-based Registration Technique to Differentiate Between Task-activated and Head Motion-induced Signal Variations in fMRI. *Magnetic Resonance in Medecine*, 38(3):470–476, 1997.

[21] P. Blomgren and T.F. Chan. Color TV: Total Variation Methods for Restoration of Vector Valued Images. *IEEE Transactions on Image Processing*, 7(3):304–309, 1998.

[22] A. Bonnet. On the Regularity of the Edge Set of Mumford-Shah Minimizers. *Progress in Nonlinear Differential Equations*, 25:93–103, 1996.

[23] A. Braides. *Approximation of Free-Discontinuity Problems*. Volume 1694 of Lectures Notes in Mathematics, Springer-Verlag, 1998.

[24] A. Braides and G. Dal Maso. Non-Local Approxiamtion of the Mumford-Shah Functional. *Calculus Variational Partial Differential Equations*, 5(4):293–322, 1997.

[25] X. Bresson, S. Esedoḡlu, P. Vandergheynst, J.-P. Thiran, and S. Osher. Global Minimizers of The Active Contour/Snake Model, UCLA CAM Report 05-04, 2005.

[26] X. Bresson, P. Vandergheynst, and J.Thiran. A Variational Model for Object Segmentation Using Boundary Information, Statistical Shape Prior and the Mumford-Shah Functional, ITS Technical Report 08.04, Signal Processing Institute, Swiss Federal Institute of Technology, Lausanne, Switzerland, http://itswww.epfl.ch, February 2004.

[27] X. Bresson, P. Vandergheynst, and J.-P. Thiran. Multiscale Active Contours. In *Proceedings of 5th International Conference on Scale Space and PDE methods in Computer Vision*, pages 167–178, 2005.

[28] X. Bresson, P. Vandergheynst, and J.-P. Thiran. Multiscale Active Contours. *International Journal of Computer Vision, Special Issue on Scale Space and Vision Applications*, 2005.

[29] X. Bresson, P. Vandergheynst, and J.P. Thiran. A Priori Information in Image Segmentation: Energy Functional Based on Shape Statistical Model and Image Information. In *IEEE International Conference on Image Processing*, pages 425–428, 2003.

[30] P. Burchard, L.-T. Cheng, B. Merriman, and S. Osher. Motion of Curves in Three Spatial Dimensions Using a Level Set Approach. *Journal of Computational Physics*, 170:720–741, 2001.

[31] T. Butz. From Error Probability To Information Theoretic Signal and Image Processing - PhD Thesis, 2003.

[32] T. Butz, P. Hagmann, E. Tardif, R. Meuli, and J.-P. Thiran. A New Brain Segmentation Framework. In *International Conference on Medical Image Computing and Computer Assisted Intervention (MICCAI), Lecture Notes in Computer Science, Vol. 2879*, pages 586–593, 2003.

[33] T. Butz and J.-P. Thiran. From Error Probability to Information Theoretic (Multi-Modal) Signal Processing. *Signal Processing*, 85(5):875–902, 2005.

[34] V. Caselles, F. Catte, T. Coll, and F. Dibos. A Geometric Model for Active Contours in Image Processing. *Numerische Mathematik*, 66:1–31, 1993.

[35] V. Caselles, R. Kimmel, and G. Sapiro. Geodesic Active Contours. *International Journal of Computer Vision*, 22(1):61–79, 1997.

[36] V. Caselles, R. Kimmel, G. Sapiro, and C. Sbert. Minimal Surfaces: A Three Dimensional Segmentation Approach. *IEEE Transactions on Pattern Analysis and Machine Intelligence*, 19(4):394–398, 1997.

[37] F. Catté, T. Coll, P.L. Lions, and J.M. Morel. Image Selective Smoothing and Edge Detection by Nonlinear Diffusion. *SIAM Journal of Numerical Analysis*, 29(3):182–193, 1992.

[38] A. Chambolle. Image Segmentation by Variational Methods: Mumford and Shah Functional and the Discrete Approximation. *SIAM Journal of Applied Mathematics*, 55(3):827–863, 1995.

[39] A. Chambolle and G. Dal Maso. Discrete Approximations of the Mumford-Shah Functional in Dimension Two, Technical Report 9820, Université Paris Dauphine, Ceremade, 1998.

[40] T.F. Chan and S. Esedoḡlu. Aspects of Total Varation Regularized L^1 function Approximation, UCLA CAM Report 04-07, 2004.

[41] T.F. Chan, S. Esedoḡlu, and M. Nikolova. Algorithms for Finding Global Minimizers of Image Segmentation and Denoising Models, UCLA CAM Report 04-54, 2004.

[42] T.F. Chan and L.A. Vese. Active Contours Without Edges. *IEEE Transactions on Image Processing*, 10(2):266–277, 2001.

[43] G. Charpiat, O. Faugeras, and R. Keriven. Shape Metrics, Warping and Statistics. In *IEEE International Conference on Image Processing*, pages 627–630, 2003.

[44] Y. Chen, W. Guo, F. Huang, D. Wilson, and E.A. Geiser. Using Prior Shape and Points in Medical Image Segmentation. In *Energy Minimization Methods in Computer Vision and Pattern Recognition, LNCS 2683*, page 291305, 2003.

[45] Y. Chen, H.D. Tagare, S. Thiruvenkadam, F. Huang, D. Wilson, K.S. Gopinath, R.W. Briggsand, and E.A. Geiser. Using Prior Shapes in Geometric Active Contours in a Variational Framework. *International Journal of Computer Vision*, 50(3):315–328, 2002.

[46] Y. Chen, S. Thiruvenkadam, H.D. Tagare, F. Huang, D. Wilson, and E.A. Geiser. On the incorporation of shape priors into geometric active contours. In *Workshop on Variational and Level Set Methods in Computer Vision*, pages 145–152, 2001.

[47] Y.-G. Chen, Y. Giga, and S. Goto. Uniqueness and Existence of Viscosity Solutions of Generalized Mean Curvature Flow Equations. *Journal of Differential Geometry*, 33(3):749–786, 1991.

[48] E. Cheon and A. Paranjpye. Noise removal by total variation minimization, UCLA MATH 199 project report, Adviser: L. Vese, 2002.

[49] L.D. Cohen. On Active Contour Models and Balloons. *Computer Vision Graphics Image Processing*, 53:211–218, 1991.

[50] L.D. Cohen and R. Kimmel. Global Minimum for Active Contour Models: A Minimal Path Approach. *International Journal of Computer Vision*, 24(1):57–78, 1997.

[51] T. Cootes and C. Taylor. Statistical Models of Appearance For Computer Vision. *Technical Report, University of Manchester*, 1999.

[52] T. Cootes, C. Taylor, D. Cooper, and J. Graham. Active Shape Models - their Training and Application. *Computer Vision and Image Understanding*, 61:38–59, 1995.

[53] R. Courant and D. Hilbert. *Methods of Mathematical Physics, Vol. 1*. Interscience Publishers, Inc., New York, 1953.

[54] T.M. Cover and J.A. Thomas. *Elements of Information Theory*. John Wiley & Sons, 1991.

[55] M.G. Crandall, L.C. Evans, and P.L. Lions. Some Properties of Viscosity Solutions of Hamilton-Jacobi Equations. *Transactions of the American Mathematical Society*, 282:487–502, 1984.

[56] M.G. Crandall, H. Ishii, and P.L. Lions. Users' guide to viscosity solutions of second order partial differential equations. *Bulletin of the American Mathematic Society*, 27(1):1–69, 1992.

[57] M.G. Crandall and P.L. Lions. Viscosity Solutions of Hamilton-Jacobi Equations. *Transactions on American Mathematics Society*, 277:1–42, 1983.

[58] D. Cremers, T. Kohlberger, and C. Schnörr. Nonlinear Shape Statistics in Mumford-Shah Based Segmentation. In *European Conference on Computer Vision*, pages 93–108, 2002.

[59] D. Cremers, T. Kohlberger, and C. Schnörr. Shape Statistics in Kernel Space for Variational Image Segmentation. *Pattern Recognition*, 36:1929–1943, 2003.

[60] D. Cremers, S.J. Osher, and S. Soatto. Kernel Density Estimation and Intrinsic Alignment for Knowledge-driven Segmentation: Teaching Level Sets to Walk. In *Annual Pattern Recognition Symposium DAGM, Springer Verlag LNCS Vol. 3157*, pages 36–44, 2004.

[61] D. Cremers, S.J. Osher, and S. Soatto. Kernel Density Estimation and Intrinsic Alignment for Knowledge-driven Segmentation: Teaching Level Sets to Walk, CAM Report 04-44, 2004.

[62] D. Cremers, C. Schnörr, and J. Weickert. DiffusionSnakes: Combining Statistical Shape Knowledge and Image Information in a Variational Framework. In *IEEE Workshop on Variational and Levelset Methods*, page 137144, 2001.

[63] D. Cremers and S. Soatto. A Pseudo-Distance for Shape Priors in Level Set Segmentation. In *IEEE Workshop on Variational, Geometric and Level Set Methods in Computer Vision*, pages 169–176, 2003.

[64] D. Cremers, N. Sochen, and C. Schnörr. Towards Recognition-Based Variational Segmentation Using Shape Priors and Dynamic Labeling. In *Scale-Space'03, LNCS 2695*, pages 388–400, 2003.

[65] D. Cremers, N. Sochen, and C. Schnörr. Multiphase Dynamic Labeling for Variational Recognition-Driven Image Segmentation. In *European Conference on Computer Vision*, pages 74–86, 2004.

[66] D. Cremers, F. Tischhäuser, J. Weickert, and C. Schnörr. Diffusion Snakes: Introducing Statistical Shape Knowledge into the Mumford-Shah Functional. *International Journal of Computer Vision*, 50(3):295–313, 2002.

[67] Daniel Cremers. Statistical Shape Knowledge in Variational Image Segmentation, Ph.D. Thesis, 2002.

[68] L. Davis. *Handbook of Genetic Algorithms*. Van Nostrand, 1991.

[69] M.C. Delfour and J.P. Zolésio. *Shapes and Geometries: Analysis, Differential Calculus, and Optimization*. Advances in Design and Control, SIAM, 2001.

[70] D. Eberly. A Differential Geometric Approach to Anisotropic Diffusion in Geometry-Driven Diffusion in Computer Vision. *Computational Imaging and Vision*, 1:371–392, 1994.

[71] D. Eberly. Geometric Methods For Analysis Of Ridges In n-Dimensional Images, Ph.D Thesis, University of North Carolina, 1994.

[72] C.L. Epstein and M. Gage. The curve shortening flow. *in Wave Motion: Theory, Modeling, and Computation, A. Chorin and A. Majda, Editors, Springer-Verlag, New York*, MR 89f:58128, 1987.

[73] L.C. Evans and R.F. Gariepy. *Measure Theory and Fine Properties of Functions*. Studies in advanced Mathematics, CRC Press, 1992.

[74] L.C. Evans and J. Spruck. Motion of Level Sets by Mean Curvature I. *Journal of Differential Geometry*, 33(3):635–681, 1991.

[75] L.C. Evans and J. Spruck. Motion of Level Sets by Mean Curvature II. *Transactions of the American Mathematical Society*, 330:321–332, 1992.

[76] L.C. Evans and J. Spruck. Motion of Level Sets by Mean Curvature III. *Journal of Geometric Analysis*, pages 121–150, 1992.

[77] R.M. Fano. Class Notes For Transmission Of Information, MIT, Cambridge, MA, Course 6.574, 1952.

[78] L. Florack. The Syntactical Structure of Scalar Images, Ph.D Thesis, University of Utrecht, 1993.

[79] R. Fritsch and G. Fritsch. *The Four-Color Theorem. History, Topological Foundations and Idea of Proof.* Springer, 1998.

[80] D. Gabor. Information Theory in Electron Microscopy. *Laboratory Investigation*, 14(6):801–807, 1965.

[81] S. Geman and D. Geman. Stochastic Relaxation, Gibbs Distributions, And The Bayesian Restoration Of Images. *IEEE Transaction on Pattern Analysis And Machine Intelligence*, 6:721–741, 1984.

[82] G. Gerig, O. Kübler, R. Kikinis, and F.A. Jolesz. Nonlinear Anisotropic Filtering of MRI data. *IEEE Transactions on Medical Imaging*, 11:221–232, 1992.

[83] E. De Giorgi and L. Ambrosio. New Functionals in the Calculus of Variations. *Atti. Accad. Naz. Lincei Rend. Cl. Sci. Fis. Mat. Natur.*, 82(2):199–210, 1988.

[84] E. De Giorgi, E. Magenes, and U. Mosco. Convergence Problems for Functionals and Operators. In *International Meeting on Recent Methods in Nonlinear Analysis*, pages 131–188, 1978.

[85] E. Giusti. *Minimal Surfaces and Functions of Bounded Variation*. Birkhauser, Basel, 1985.

[86] M.B. Green, J.H. Schwarz, and E. Witten. *Superstring Theories, volume I and II*. Cambridge University Press, 1987.

[87] F. Guichard, L. Moisan, and J.-M. Morel. A Review of P.D.E. Models in Image Processing and Image Analysis. *Journal de Physique IV*, 12(1):137–156, 2002.

[88] A.B. Hamza, H. Krim, and G.B. Unal. Unifying Probabilistic And Variational Estimation. *IEEE Signal Processing Magazine*, 19(5):37–47, 2002.

[89] R.M. Haralick, S. R. Sternberg, and X. Zhuang. Image Analysis using Mathematical Morphology. *IEEE Transactions on Pattern Analysis and Machine Intelligence*, 9(4):532–550, 1987.

[90] A. Herbulot, S. Jehan-Besson, M. Barlaud, and G. Aubert. Shape Gradient For Image Segmentation Using Information Theory. In *IEEE International Conference on Acoustics, Speech, and Signal Processing (ICASSP)*, pages 21–24, 2004.

[91] A. Herbulot, S. Jehan-Besson, M. Barlaud, and G. Aubert. Shape Gradient For Multi-Modal Image Segmentation Using Joint Intensity Distributions. In *International Workshop on Image Analysis for Multimedia Interactive Services (WIAMIS)*, 2004.

[92] J.-B. Hiriart-Urruty and C. Lemarechal. *Convex Analysis and Minimization Algorithms*. Grundlehren der mathematischen Wissenschaften vol. 305-306, Springer-Verlag, 1993.

[93] X. Huang, N. Paragios, and D. Metaxas. Establishing Local Correspondences towards Compact Representations of Anatomical Structures. In *International Conference on Medical Image Computing and Computer Assisted Intervention, MICCAI03*, pages 926–934, 2003.

[94] X. Huang, N. Paragios, and D. Metaxas. Registration of Structures in Arbitrary Dimensions: Implicit Representations, Mutual Information And Free Form Deformations, Technical Report DCS-TR-520, Division of Computer and Information Sciences, The State Univiversity Of NJ, 2003.

[95] D.H. Hubel. *Eye, Brain and Vision*. Scientific American Press, New York, 1988.

[96] D.H. Hubel and T.N. Wiesel. Brain Mechanisms of Vision. *Scientific American Press*, 241: 45–53, 1979.

[97] R. Hummel. Representations based on Zero-Crossings in Scale-Space. In *Conference On Computer Vision and Pattern Recognition*, pages 204–209, 1986.

[98] S. Jehan-Besson, M. Barlaud, and G. Aubert. DREAM2S: Deformable Regions driven by an Eulerian Accurate Minimization Method for Image and Video Segmentation, Technical Report I3S RR-2001-14, 2001.

[99] S. Jehan-Besson, M. Barlaud, and G. Aubert. DREAM2S: Deformable Regions driven by an Eulerian Accurate Minimization Method for Image and Video Segmentation. *International Journal of Computer Vision*, 53(1):45–70, 2003.

[100] G.-S. Jiang and D. Peng. Weighted ENO Schemes for Hamilton-Jacobi Equations. *Journal of Scientific Computing*, 21(6):2126–2143, 1999.

[101] L. Jonasson, X. Bresson, P. Hagmann, O. Cuisenaire, R. Meuli, and J.P. Thiran. White Matter Fiber Tract Segmentation in DT-MRI Using Geometric Flows. *Medical Image Analysis*, 9(3): 223–236, 2004.

[102] L. Jonasson, P. Hagmann, X. Bresson, J.P. Thiran, and V. Wedeen. Submitted: Representing Diffusion MRI in 5D for Segmentation of White Matter Tracts with a Level Set Method. In *Information Processing in Medical Imaging*, 2005.

[103] M. Kass, A. Witkin, and D. Terzopoulos. Snakes: Active Contour Models. *International Journal of Computer Vision*, pages 321–331, 1987.

[104] S. Kichenassamy, A. Kumar, P. Olver, A. Tannenbaum, and A.J. Yezzi. Gradient Flows and Geometric Active Contour Models. In *International Conference on Computer Vision*, pages 810–815. IEEE, 1995.

[105] S. Kichenassamy, A. Kumar, P. Olver, A. Tannenbaum, and A.J. Yezzi. Conformal Curvature Flows: From Phase Transitions to Active Vision. In *Archive for Rational Mechanics and Analysis*, volume 134, pages 275–301, 1996.

[106] J. Kim, J.W. Fisher III, A. Yezzi, Jr.M. Cetin, and A.S. Willsky. Nonparametric Methods For Image Segmentation Using Information Theory And Curve Evolution. In *IEEE International Conference on Image Processing (ICIP)*, pages 797–800, 2002.

[107] J. Kim, J.W. Fisher III, A. Yezzi, Jr.M. Cetin, and A.S. Willsky. Incorporating Complex Statistical Information In Active Contour-Based Image Segmentation. In *IEEE International Conference on Image Processing (ICIP)*, 2003.

[108] R. Kimmel, R. Malladi, and N. Sochen. Images as Embedded Maps and Minimal Surfaces: Movies, Color, Texture, and Volumetric Medical Images. *International Journal of Computer Vision*, 39(2):111–129, 2000.

[109] J. J. Koenderink. The Structure of Images. *Biological Cybernetics*, 50:363–370, 1984.

[110] Erwin Kreyszig. *Differential Geometry*. Paperback, 1991.

[111] M. Leventon. Statistical Models for Medical Image Analysis, Ph.D Thesis, 2000.

[112] M. Leventon, O. Faugeras, W.E.L. Grimson, and W.M. Wells III. Level Set Based Segmentation with Intensity and Curvature Priors. *Mathem. Meth. in Biomed. Image Anal.*, 2000.

[113] M. Leventon, W.E.L. Grimson, and O. Faugeras. Statistical Shape Influence in Geodesic Active Contours. In *IEEE International Conference of Computer Vision and Pattern Recognition*, pages 316–323, 2000.

[114] T. Lindeberg. *Scale-Space Theory in Computer Vision*. Kluwer Academic Publishers, Netherlands, 1994.

[115] R. Malladi, R. Kimmel, D. Adalsteinsson, G. Sapiro, V. Caselles, and J.A. Sethian. A Geometric Approach to Segmentation and Analysis of 3D Medical Images. In *Mathematical Methods in Biomedical Image Analysis Workshop*, 1996.

[116] R. Malladi, J. Sethian, and B. Vemuri. Shape Modeling with Front Propagation: A Level Set Approach. *IEEE Transactions on Pattern Analysis and Machine Intelligence*, 17:158175, 1995.

[117] R. Malladi, J. Sethian, and B. Vemuri. A Fast Level Set Based Algorithm for Topology-independent Shape Modeling. *Journal of Mathematical Imaging and Vision*, 6(2/3):269–289, 1996.

[118] C. Mantegazza and A.C. Mennucci. Hamilton-Jacobi Equations and Distance Functions on Riemannian Manifolds. *Applied Mathematics*, 47:1–25, 2003.

[119] D. Marr and E. Hildreth. Theory of Edge Detection. In *Proceedings of Royal Society London, B207*, pages 187–217, 1980.

[120] G. Dal Maso. An introduction to Γ-convergence. In *Progress in Linear Differential Equations and their Applications, Birkhäuser, Boston*, 1993.

[121] G. Matheron. *Random Sets and Integral Geometry*. Wiley, New York, 1975.

[122] J.M. Morel and S. Solimini. *Variational Methods in Image Segmentation*. Progress in Nonlinear Differential Equations and Their Applications, 1995.

[123] B. Morse. Computation of Object Cores From Grey-Level Images, Ph.D Thesis, University of North Carolina, 1994.

[124] D. Mumford and J. Shah. Boundary Detection by Minimizing Functionals. In *Proceedings of the International Conference on Computer Vision and Pattern Recognition*, pages 22–26, 1985.

[125] D. Mumford and J. Shah. Optimal Approximations of Piecewise Smooth Functions and Associated Variational Problems. *Communications on Pure and Applied Mathematics*, 42:577–685, 1989.

[126] CMLA Laboratory of the Ecole Normale Supérieure de Cachan. Megawave2, http://www.cmla-ens.cachan.fr/Cmla/Megawave/.

[127] S. Osher. "Level Set Methods", in Geometric Level Set Methods in Imaging, Vision and Graphics. *eds. S. Osher and N. Paragios, Springer-Verlag, NY*, pages 3–20, 2003.

[128] S. Osher and N. Paragios. *"Level Set Methods", in Geometric Level Set Methods in Imaging, Vision and Graphics*. Springer-Verlag, NY, 2003.

[129] S. Osher and J.A. Sethian. Fronts Propagating with Curvature-Dependent Speed: Algorithms Based on Hamilton-Jacobi Formulations. *Journal of Computational Physics*, 79(1)(12-49), 1988.

[130] S. Osher and C.-W. Shu. High-Order Essentially Nonsocillatory Schemes for Hamilton-Jacobi Equations. *Journal of Computational Physics*, 28(4):907–922, 1991.

[131] S.J. Osher and L.I. Rudin. Feature-Oriented Image enhancement using Shock Filters. *SIAM Journal of Numerical Analysis*, 27:919–940, 1990.

[132] N. Paragios and R. Deriche. Geodesic Active Regions: A New Paradigm to Deal with Frame Partition Problems in Computer Vision. *Journal of Visual Communication and Image Representation*, 13(1-2):249–268, 2002.

[133] N. Paragios and R. Deriche. Geodesic Active Regions and Level Set Methods for Supervised Texture Segmentation. *International Journal of Computer Vision*, 46(3):223–247, 2002.

[134] N. Paragios and R. Deriche. Geodesic Active Regions and Level Set Methods for Motion Estimation and Tracking. *Computer Vision and Image Understanding (In Press)*, 97(3):259–282, 2005.

[135] N. Paragios and M. Rousson. Shape Priors for Level Set Representations. In *European Conference on Computer Vision*, 2002.

[136] N. Paragios, M. Rousson, and V. Ramesh. Knowledge-based Registration & Segmentation of the Left Ventricle: A Level Set Approach. In *IEEE Workshop in Applications on Computer Vision*, 2002.

[137] N. Paragios, M. Rousson, and V. Ramesh. Matching Distance Functions: A Shape-To-Area Variational Approach for Global-To-Local Registration. In *European Conference on Computer Vision*, page 775790, 2002.

[138] N. Paragios, M. Rousson, and V. Ramesh. Non-rigid Registration using Distance Functions. *Journal of Computer Vision and Image Understanding*, 89(2-3):142–165, 2003.

[139] Nikos Paragios. Geodesic Active Regions and Level Set Methods: Contributions and Applications in Artificial Vision, PhD Thesis, Université de Nice-Sophia Antipolis/I.N.R.I.A., 2000.

[140] E. Parzen. On the Estimation of a Probability Density Function and the Mode. *Annals of Mathematical Statistics*, 1962:10651076, 33.

[141] P. Perona and J. Malik. Scale-Space and Edge Detection Using Anisotropic Diffusion. *IEEE Transactions on Pattern Analysis and Machine Intelligence*, 1252(629-639), 1990.

[142] S.M. Pizer, D. Eberly, B.S. Morse, and D.S. Fritsch. Zoom-Invariant Vision of Figural Shape: The Mathematics of Cores. *International Journal of Computer Vision and Image Understanding*, 69:55–71, 1998.

[143] A.M. Polyakov. Quantum Geometry of Bosonic Strings. *Physics Letters B*, 103:207–210, 1981.

[144] F. Precioso, M. Barlaud, T. Blu, and M. Unser. Smoothing B-spline Active Contour for Fast and Robust Image and Video Segmentation. In *IEEE International Conference on Image Processing*, page 137140, 2003.

[145] M.H. Protter and H.F. Weinberger. *Maximum Principles in Differential Equations*. Prentice-Hall, Englewood Cliffs, 1967.

[146] S.J. Reeves. A Cross-Validation Approach to Image Restoration and Blur Identification, Ph.D. Thesis, Georgia Institute of Technology, 1990.

[147] T. Riklin-Raviv, N. Kiryati, and N. Sochen. Unlevel-Sets: Geometry and Prior-based Segmentation. In *European Conference on Computer Vision*, pages 50–61, 2004.

[148] F. Rosenblatt. Remarks on some Nonparametric Estimates of a Density Function. *Annals of Mathematical Statistics*, 27:832837, 1956.

[149] M. Rousson, T. Brox, and R. Deriche. Active Unsupervised Texture Segmentation on a Diffusion Based Feature Space. In *Conference on Computer Vision and Pattern Recognition (CVPR)*, pages 699–704, 2003.

[150] M. Rousson, T. Brox, and R. Deriche. Active Unsupervised Texture Segmentation on a Diffusion Based Feature Space, Technical Report INRIA, RR-4695, 2003.

[151] M. Rousson and R. Deriche. A Variational Framework for Active and Adaptative Segmentation of Vector Valued Images. In *Workshop on Motion and Video Computing (WMVC)*, pages 56–61, 2002.

[152] M. Rousson and R. Deriche. Variational Framework for Active and Adaptative Segmentation of Vector Valued Images, Technical Report INRIA, RR-4515, 2002.

[153] M. Rousson, N. Paragios, and R. Deriche. Active Shape Models from a Level Set Perspective, Technical Report RR-4984, 2003.

[154] M. Rousson, N. Paragios, and R. Deriche. Implicit Active Shape Models for 3D Segmentation in MR Imaging. In *International Conference on Medical Image Computing and Computer Assisted Intervention, MICCAI04*, pages 209–216, 2004.

[155] L. I. Rudin, S. Osher, and E. Fatemi. Nonlinear Total Variation Based Noise Removal Algorithms. *Physica D*, 60(1-4):259 – 268, 1992.

[156] C. Samson, L. Blanc-Féraud, G. Aubert, and J. Zerubia. A Level Set Model for Image Classification. *International Journal of Computer Vision*, 40(3):187–197, 2000.

[157] B. Sandberg, T.F. Chan, and L.A. Vese. A Level-Set and Gabor-based Active Contour Algorithm for Segmenting Textured Images, UCLA CAM Report 02-39, 2002.

[158] G. Sapiro. *Geometric Partial Differential Equations and Image Analysis*. Cambridge University Press, 2001.

[159] G. Sapiro and A. Tannenbaum. Affine Invariant Scale-Space. *International Journal of Computer Vision*, 11(1):25–44, 1993.

[160] G. Sapiro and A. Tannenbaum. On Affine Plane Curve Evolution. *Journal of Functional Analysis*, 119(1):79–120, 1994.

[161] J. A. Schnabel and S.R. Arridge. Active Shape Focusing. *Image and Vision Computing*, 17(5-6):419–428, 1999.

[162] J. Serra. *Image Analysis and Mathematical Morphology, Vol.I*. Academic Press, London, 1982.

[163] J. Sethian. Fast Marching Methods. *SIAM Review*, 41:199–235, 1999.

[164] J.A. Sethian. *Level Set Methods and Fast Marching Methods: Evolving Interfaces in Computational Geometry, Fluid Mechanics, Computer Vision and Material Sciences*. Cambridge University Press, 1999.

[165] C.E. Shannon. A Mathematical Theory of Communication. *Bell System Technical Journal*, 27:379–423 and 623–656, July and October 1948.

[166] N. Sochen, R. Kimmel, and R. Malladi. A General Framework For Low Level Vision, Technical Report LBNL-39243, Physics Department, Berkeley, 1996.

[167] N. Sochen, R. Kimmel, and R. Malladi. A General Framework For Low Level Vision. *IEEE Transactions on Image Processing*, 7(3):310 – 318, 1998.

[168] M. Sonka, V. Hlavac, and R. Boyle. *Image Processing, Analysis, and Machine Vision*. 2nd ed. Brooks/Cole Publishing Company, 1998.

[169] G. Strang. L^1 and L^∞ Approximation of Vector Fields in the Plane. In *Nonlinear Partial Differential Equations in Applied Science*, pages 273–288, 1982.

[170] G. Strang. Maximal Flow Through A Domain. *Mathematical Programming*, 26(2):123–143, 1983.

[171] B.M. ter Haar Romeny. *Front-End Vision and Multiscale Image Analysis: Introduction to Scale-Space Theory*. Kluwer Academic Publishers, Netherlands, 1997.

[172] B.M. ter Haar Romeny (Editor). *Geometry Driven Diffusion in Computer Vision*. Kluwer Academic Publishers, Netherlands, 1994.

[173] A. Tsai, W. Wells, C. Tempany, E. Grimson, and A. Willsky. Mutual Information in Coupled Multi-Shape Model for Medical Image Segmentation. *Medical Image Analysis*, 8(4):429–445, 2004.

[174] A. Tsai, A. Yezzi, W. Wells, C. Tempany, D. Tucker, A. Fan, W.E. Grimson, and A. Willsky. Model-based Curve Evolution Techniques for Image Segmentation. In *IEEE International Conference of Computer Vision and Pattern Recognition*, pages 463–468, 2001.

[175] A. Tsai, A. Yezzi, W. Wells, C. Tempany, D. Tucker, A. Fan, W.E. Grimson, and A. Willsky. A Shape-Based Approach to the Segmentation of Medical Imagery Using Level Sets. *IEEE Transactions on Medical Imaging*, 22(2):137–154, 2003.

[176] A. Tsai, A. Yezzi, and A.S. Willsky. Curve Evolution Implementation of the MumfordShah Functional for Image Segmentation, Denoising, Interpolation and Magnification. *IEEE Transactions on Image Processing*, 10(8):1169–1186, 2001.

[177] M. Unser. Splines: A Perfect Fit for Signal and Image Processing. *IEEE Signal Processing Magazine*, 16(6):22–38, 1999.

[178] L. Vese and T. Chan. A Multiphase Level Set Framework for Image Segmentation Using the Mumford and Shah Model, UCLA CAM Report 01-25, 2001.

[179] L.A. Vese and T.F. Chan. A Multiphase Level Set Framework for Image Segmentation Using the Mumford and Shah Model. *International Journal of Computer Vision*, 50(3):271–293, 2002.

[180] L.A. Vese and S.J. Osher. The Level Set Method Links Active Contours, Mumford-Shah Segmentation, and Total Variation Restoration, UCLA CAM Report 02-05, 2002.

[181] V.J. Wedeen, T.G. Reese, D.S. Tuch, M. R. Wiegell, T.G. Weisskoff, and D. Chessler. Mapping Fiber Orientation Spectra in Cerebral White Matter with Fourier-Transform Diffusion MRI. In *Proceedings of 8th Annual Meeting ISMRM*, page 82, 2000.

[182] J. Weickert. Coherence-Enhancing Diffusion Filtering. *International Journal of Computer Vision*, 31(2/3):111–127, 1999.

[183] J. Weickert, S. Ishikawa, and A. Imiya. Linear Scale-Space has First been Proposed in Japan. *Journal of Mathematical Imaging and Vision*, 10:237–252, 1999.

[184] Joachim Weickert. *Anisotropic Diffusion in Image Processing*. ECMI Series, Teubner-Verlag, Stuttgart, Germany, 1998.

[185] A.P. Witkin. Scale-space filtering. In *International Joint Conference Artificial Intelligence*, pages 1019–1022, 1983.

[186] C. Xu and J. Prince. Snakes, shapes and gradient vector flow. *IEEE Transaction on Image Processing*, 7:359–369, 1998.

[187] A. Yezzi, A. Tsai, and A. Willsky. A Statistical Approach to Snakes for Bimodal and Trimodal Imagery. In *International Conference of Computer Vision*, page 1999, 898-903.

[188] A.Jr. Yezzi, S. Kichenassamy, A. Kumar, P.J. Olver, and A. Tannenbaum. A Geometric Snake Model for Segmentation of Medical Imagery. *IEEE Transactions on Medical Imaging*, 16(2): 199–209, 1997.

[189] S. Zeki. *A Vision of the Brain*. Blackwell Scientific Publications, 1993.

[190] Y. Zhang, M. Brady, and S. Smith. Segmentation of Brain MR Images Through a Hidden Markov Random Field Model And the Expectation-Maximization Algorithm. *IEEE Transactions on Medical Imaging*, 20(1):4557, 2001.

[191] H.-K. Zhao, T. Chan, B. Merriman, and S. Osher. A variational level set approach to multi-phase motion. *Journal of Computational Physics*, 127(1):179–195, 1996.

[192] S. C. Zhu and A. Yuille. Region Competition: Unifying Snakes, Region Growing, and Bayes/MDL for Multiband Image Segmentation. *IEEE Transactions on Pattern Analysis and Machine Intelligence*, 18(9):884–900, 1996.

Curriculum Vitae

Full name:	**Xavier BRESSON**
Degrees:	Bachelor of Science in Theoritical Physics
	Engineering Diploma from École Supérieure d'Électricité
	Master of Science in Control and Signal Processing
Address:	Signal Processing Institute (ITS)
	Swiss Federal Institute of Technology (EPFL)
	CH-1015 Lausanne
	Switzerland
Contact numbers:	Tel. (+41 21) 693 46 22
	Fax. (+41 21) 693 76 00
	E-mail: xavier.bresson@epfl.ch
	xavierbresson@yahoo.com
Civil status:	Single
Date and place of birth:	July 6$^{\text{th}}$ 1976, Vendôme, France
Nationality:	French

Education

Since 2001	Ph.D. Student in Computer Vision Signal Processing Institute (ITS) Swiss Federal Institute of Technology (EPFL), Lausanne, Switzerland
1999-2000	Master of Science (DEA) in Control and Signal Processing Signal and System Laboratory (LSS) University of Paris XI, France
1998-2000	Electrical Engineer École Supérieure d'Électricité (Supélec), Paris, France
1994-1998	Bachelor of Science (Maîtrise) in Theoritical Physics University of Provence, Marseilles, France

Work Experience

Since 2001	Ph.D. Student at the Signal Processing Institute (ITS) Lecture Assistant of pattern recognition and information theory Research Assistant of three diploma projects and two semester projects
Oct-Dec 2004	Visit in University of California (UCLA) under supervision of Prof. Stanley Osher
Apr-Aug 2000	Internship in Alcatel-Paris on the estimation of perceived speech quality in a GSM network
May-Jul 1998	Internship in Laboratory of Ion Storage and Laser Manipulation on ion trapping

Languages

French:	mother tongue
English:	fluent oral and written
Spanish:	basics

Computer Skills

Operating systems:	Windows, Unix, Linux
Programming & Applications:	C, C++, Visual Basic, Matlab

Hobbies

Sports, cooking, traveling, cinema

Publications

Journal Papers

- X. Bresson, P. Vandergheynst and J. Thiran, "Multiscale Active Contours", Invited for a Special Issue on Scale Space & Vision Applications in *International Journal of Computer Vision*, 2005

- L. Jonasson, X. Bresson, P. Hagmann, O. Cuisenaire, R. Meuli and J. Thiran, "White Matter Fiber Tract Segmentation in DT-MRI Using Geometric Flows", *Medical Image Analysis*, Vol. 9, No. 3, pp. 223-236, 2005

- L. Jonasson, P. Hagmann, C. Pollo, X. Bresson, C. Richero Wilson, R. Meuli and J. Thiran, "A Level Set Method For Segmentation of The Thalamus And Its Nuclei in DT-MRI", *Special Issue of Signal Processing on Diffusion Tensor Imaging*, Submitted, 2005

- X. Bresson, P. Vandergheynst and J. Thiran, "A Variational Model for Object Segmentation Using Boundary Information and Statistical Shape Prior Driven by the Mumford-Shah Functional", *International Journal of Computer Vision*, Submitted, 2004

Conference Papers

- X. Bresson, S. Esedoglu, P. Vandergheynst, J. Thiran and S. Osher, "Global Minimizers of The Active Contour/Snake Model", *International Conference on Free Boundary Problems: Theory and Applications*, Invited, 2005

- X. Bresson, P. Vandergheynst and J. Thiran, "Multiscale Active Contours", *5th International Conference on Scale Space and PDE methods in Computer Vision*, LNCS Vol. 3459, pp. 167-178, 2005

- L. Gui, X. Bresson and J. Thiran, "Multiscale Image Segmentation Using Active Contours", *IEEE Workshop on Variational, Geometric and Level Set Methods in Computer Vision*, Submitted, 2005

- L. Jonasson, P. Hagmann, X. Bresson, J. Thiran and V. Wedeen, "Representing Diffusion MRI in 5D for Segmentation of White Matter Tracts with a Level Set Method", *Information Processing in Medical Imaging*, 2005

- L. Jonasson, P. Hagmann, C. Richero Wilson, X. Bresson, C. Pollo, R. Meuli and J. Thiran, "Coupled Region Based Level Sets for Segmentation of the Thalamus and its Subnuclei in DT-MRI", *International Society for Magnetic Resonance in Medicine (ISMRM)*, 2005

- S. Roy, J. Broquet, X. Bresson and J. Thiran, "Semi-Automatic contour Analysis of the Optic Nerve Head", *15th International Meeting of International Neuro-Ophthalmology Society*, 2004

- X. Bresson, P. Vandergheynst and J. Thiran, "A Priori Information in Image Segmentation: Energy Functional based on Shape Statistical Model and Image Information", *International Conference on Image Processing (ICIP)*, Vol. 3, pp. 428-428, 2003

- L. Jonasson, P. Hagmann, X. Bresson, R. Meuli, O. Cuisenaire and J. Thiran, "White Matter Mapping in DT-MRI Using Geometric Flows", *Computer Aided Systems Theory (EURO-CAST)*, Vol. 2809, pp. 585-596, 2003

- X. Bresson, P. Vandergheynst and J. Thiran, "Geometric Moments in Scale-Spaces", *16th International Conference on Pattern Recognition (ICPR)*, Vol. 4, pp. 418-421, 2002